Experimental Study of Isothermal and Evaporative Sprays

Srikrishna Sahu

Multiscale Flow Dynamics Group
Thermofluids Division
Mechanical Engineering Department
Imperial College London
London SW7 2BX
United Kingdom

Submitted in partial fulfilment of the requirements for the degree of Doctor of Philosophy of the Imperial College London.

Abstract

The present research focuses on studying an isothermal spray to understand the mechanism of interaction between droplets and turbulent air flow, and an evaporative spray to evaluate the group evaporation of droplets as opposed to single droplet evaporation. The thesis describes the development and application of two novel experimental techniques for simultaneous characterization of droplet and gaseous phases in isothermal and evaporative sprays respectively. Both approaches use the out-of-focus imaging technique, Interferometric Laser Imaging for Droplet Sizing (ILIDS), for planar measurements of droplet size and velocity. The in-focus imaging techniques Particle Image Velocimetry (PIV) and Planar Laser Induced Fluorescence (PLIF) are respectively combined with ILIDS for simultaneous measurement of gas flow characteristics in an isothermal spray and vapour concentration distribution in an evaporative spray.

Combination of either of the two optical arrangements results in a discrepancy in the location of the centre of a droplet leading to erroneous identification of the droplets in the PIV/PLIF images. This issue has been addressed and a method is proposed to reduce the droplet positioning error.

The coupling between the droplet and gas phases in the isothermal spray is explained by evaluating several statistical quantities, the most important being the spatial correlation coefficients of the droplet-gas velocity fluctuations obtained conditional on droplet size classes. The effect of anisotropy and gravity on the momentum transfer between the two phases are studied. The gas flow eddy structures are extracted by applying Proper Orthogonal Decomposition (POD) on the instantaneous gas velocity data and the selective influence of the large scale eddy structures of the gas phase

flow on the droplet-gas flow interaction are examined.

In order to study the effect of inter droplet spacing on the droplet evaporation rate, experiments are first performed for the mono-sized droplet stream. The smaller inter droplet spacing of the larger droplet sizes causes the vapour to surround the droplet stream leading to droplet group evaporation. The smaller magnitude of the mean group evaporation number, evaluated at different radial locations in the evaporative acetone spray, suggests the mode of evaporation is in the range of regimes of individual to group evaporation. It is shown that the assumption of uniform droplet spacing in the theoretical expressions for the evaluation of the group evaporation number always leads to overestimation of the group evaporation number.

Acknowledgements

First and foremost I offer my sincere gratitude to my supervisors Prof. Yannis Hardalupas and Prof. Alex Taylor for rendering their valuable knowledge, guidance and generous help at all the stages of my research work. They supported me throughout my thesis with their patience and knowledge whilst allowing me the room to work in my own way. I enjoyed the stimulating discussions with both of them on diverse subjects from experimental techniques to physics of fluid mechanics. The days spent with them form the best period of my professional training and satisfying achievement.

I am deeply indebted to the Department of Mechanical Engineering, Imperial College London, for providing financial assistance over the period of my doctoral study. I am grateful to my supervisors during masters at IIT Kanpur, Prof. K.Muralidhar and Prof. P.K. Panigrahi for their encouragement and motivating me for research.

In my daily work I have been blessed with a friendly and cheerful group of fellow students and I am indebted to each of them for all their help and support. I am especially grateful to my colleagues and dear friends, Kostas, Nikos and George for their timely discussions and generous help. My special thanks to Panos and Flo, who have been very close, and have always provided a friendly and cheerful environment. I wish to thank all of the academic visitors from Japan, who were so kind, friendly and humble. Especially the days I had spent with Aida-San and Asai-San will remain memorable forever. Matsura-San's enthusiasm and dedication for research will always remain inspirational for me. The assistance received from Phil, John, Guljar and Eddy for building up the experimental set–up is acknowledged with deep regards. Outside

office, I wish to thank my friends Sandeep, Aditya G, Aditya K, Davendu, Linash, Jibu and Rajagopal for their affection, cooperation and wonderful friendship.

I am grateful to my sister Chinmayee and brother Abinash for helping me get through the difficult times, and for all the emotional support, and caring they provided. I am thankful to my wife and soulmate, Kalyani, for her unconditional love, support and patient. My parents receive my deepest gratitude for their dedication, love and support, which go beyond words. I dedicate this thesis to them.

The silent support, best wishes and blessings of all my family members have been the constant source of inspiration throughout my research programme. Even to think of thanking them is to trivialise all that they have done for me. My profound debt to them therefore, remain silent and unacknowledged.

This work, unless where the reference is mentioned, is the result of the study carried out by Srikrishna Sahu

Srikrishna Sahu

London, May 2011

Advances in science are not made by one discovery or another, or writing and publishing paper, but by earnest study and a lot of work.

Subrahmanyan Chandrasekhar

Nobel laureate

Dedicated to my parents

Mr. Bijaya Kumar Sahu

&

Mrs. Kumudini Sahu

Contents

Abstract **2**

Acknowledgements **4**

Declaration **6**

1 Introduction **25**

1.1 Motivation 25

1.2 Droplet-gas interaction in a spray 30

1.2.1 Particle-fluid correlation terms 31

1.2.2 Contribution from Numerical studies 35

1.2.3 Experiments in two-phase flows 36

1.3 Measurement of evaporative spray 38

1.4 Aim of this work 43

1.5 Outline of the thesis 46

2 Combined ILIDS and PIV Technique **48**

2.1 Interferometric Laser Imaging for Droplet Sizing (ILIDS) 49

2.1.1 Background 49

2.1.2 Principle 51

2.1.3 Image Processing 55

2.1.4 Important notes for the application of ILIDS 61

2.2 Particle Image Velocimetry (PIV) 64

2.2.1 Image Processing 66

2.3 Combining ILIDS with PIV 77
2.3.1 Principle 77
2.3.2 Experimental Set–up 79
2.4 Droplet Centre Discrepancy 89
2.4.1 Theoretical prediction of the centre discrepancy 90
2.4.2 Quantification of droplet centre discrepancy 97
2.4.3 Application to a polydisperse spray with no gas phase seeding 103
2.5 Combined ILIDS and PIV measurements 106
2.5.1 Droplet filtering from PIV images 107
2.5.2 Calculation of the gas velocity through PIV and integration of the result with ILIDS 109
2.5.3 Application to a Spray 111
2.6 Summary 113

3 Two phase interaction 115
3.1 Measurement location 116
3.2 Drop size distribution 118
3.3 Droplet/gas instantaneous, mean and turbulent velocity 121
3.4 Spatial correlation of droplet and gas velocity fluctuations 130
3.4.1 Method of calculation of spatial correlations 131
3.4.2 Droplet-Gas velocity correlation 134
3.4.3 Droplet-Droplet velocity correlation 138
3.4.4 Comparison of Droplet-Gas, Droplet-Droplet and Gas correlation 140
3.5 PDF of droplet-gas relative velocity 146
3.6 Effect of the flow field on the droplet concentration 149
3.6.1 Scale of droplet clustering 152
3.6.2 Radial distribution Function (RDF) 154
3.6.3 Correlation between fluctuations in droplet concentration and gas velocity 156
3.7 Summary 158

4 Influence of large scale flow structures **161**

4.1 Proper Orthogonal Decomposition (POD) 162

4.2 Application of POD 166

4.2.1 Modal Contributions to droplet-gas velocity correlation 169

4.2.2 Modification of turbulent kinetic energy at various length scales 171

4.3 Summary 177

5 Combined ILIDS and PLIF technique **179**

5.1 Combining ILIDS with PLIF 180

5.1.1 Principle and Experimental Set-up 180

5.1.2 Droplet centre discrepancy 186

5.2 Application of the combined technique to mono-sized droplet stream 189

5.2.1 Quantification of the droplet centre discrepancy 191

5.2.2 Vapour phase measurement around the droplet stream 194

5.3 Application of the combined technique to a polydispersed spray . . . 200

5.3.1 Image processing 202

5.3.2 Dispersed phase measurement 206

5.3.3 Vapour phase measurement 215

5.4 Summary 223

6 Conclusions **227**

6.1 Conclusions 227

6.1.1 Combined ILIDS and PIV technique 228

6.1.2 Droplet-gas interaction in sprays 229

6.1.3 Measurement of evaporative spray 232

6.2 Scope for future work 234

Bibliography **236**

List of publications **244**

List of Figures

1.1 Depiction of preferential concentration (a) Particle Centrifuging occurs due to the vortical structure of the flow, which increases the local particle concentration (contours of grey levels show particle concentration - black colour corresponds to zero particle concentration), Hardalupas and Horender (2003a) (b) Instantaneous fluid and particle velocity vectors from a single plane of a direct numerical simulation of forced isotropic turbulence. Particle positions are shown by the circles, the symbol size in each frame and particle velocity vectors, Fevrier *et al.* (2005). 26

1.2 Effect of group combustion number on the type of spray combustion, Chiu and Kim (1983). 28

2.1 (a) Intensity of scattered light around a single droplet ($D = 100\mu m$) as a function of scattering angle and contribution from the first three scattering orders for an incident plane wave ($\lambda = 532\ nm$) for vertically polarized light (b) Schematic of the optical paths of external reflection and first order refraction through the transparent spherical droplet. . 50

2.2 (a) Principle of the interferometric laser imaging technique (b) A typical ILIDS image using the conventional technique. 51

2.3 (a) Schematic of the optical configuration of ILIDS including the optical compression unit introduced by Maeda *et al.*, 2000 (b) A typical compressed ILIDS image. 53

2.4 (a) top: Intensity variation for a fringe pattern in the ILIDS image of a droplet and bottom: its corresponding continuous wavelet transform spectrum at two different scales (b) Fourier spectrum of the fringe pattern. 57
2.5 Demonstation of droplet velocity estimation in ILIDS processing . . . 59
2.6 Location of the image plane with Scheimpflug condition. 62
2.7 Schematic of the Particle Image Velocimetry technique. 65
2.8 Correlation based PIV and the two approaches for evaluating the correlation. 67
2.9 Mean velocity plot of the flow field corresponding to the Okamoto *et al.* (2000)'s images processed using the modified direct method using FFT. 71
2.10 Probability density functions of PIV displacement data in vertical direction obtained by processing the full sequence of the Okamoto images using various algorithms for computing the cross-correlation: (a) Direct estimation, (b) FFT based estimation and (c) Modified direct method using FFT. 72
2.11 A pair of simulated PIV images: Original, Cropped and the corresponding Mask. 75
2.12 Principle of the combined ILIDS and PIV technique. 78
2.13 Schematic of the Experimental Rig (a) Elevation view and (b)Plan view. 80
2.14 Generation of the laser sheet using series of lenses. 82
2.15 Possible optical arrangements for the combined ILIDS and PIV measurements. 83
2.16 Depiction of the discrepancy in droplet centre. 89

2.17 (a) Schematic of the optical system for theoretical prediction of discrepancy in droplet centres between the focused and defocused planes (b) Images along the axis of the lens of a droplet in the focussed and defocused planes and the corresponding coordinate systems (c) A simplified schematic of the same optical system shown in Figure 2.17(a) (but with the laser sheet, focused plane and defocused plane normal to the lens axis) in order to depict the dependency of the centre discrepancy on the droplet position. 91

2.18 (a) Deviation of the geometric centre from the derived centre of the droplet image as a function of z position in the object plane (b) Discrepancy in derived centre and geometrical centre between in-focus and defocus planes as a function of z position in the object plane (c) Relative change in centre discrepancy as a function of position x in the object plane for a droplet situated at three positions z = -7, 0 and 7 mm, respectively (d) Comparison of the centre discrepancy for two droplet sizes of 200 and 20 μm as a function of position y. Focal length was 135 mm, magnification was 0.6 and aperture size was 40 mm. . . 94

2.19 (a) Intensity distribution of the glare points in the PIV image of the mono-sized droplet stream and its corresponding wavelet transform spectrum (b) Intensity distribution and wavelet transform spectrum of the glare points and seeding particles corresponding to the polydisperse spray. 98

2.20 Fringe patterns and corresponding glare points for a stream of mono-dispersed droplets without gas phase seeding at three different positions in the object plane, $y = -5.0$, $+1.0$ and $+5.0$ mm, respectively. The ILIDS images are superimposed on the PIV image. Note that the origin of the coordinate system ($x = 0$ and $y = 0$) lies in the centre of the CCD array, which coincides with the centre of the image of the figure. 100

2.21 (a) top: Centre discrepancy between ILIDS and PIV images in the horizontal (y) direction as a function of y position in the object plane. The straight line is a linear fit to the original data. bottom: The remaining droplet centre discrepancy after subtracting the estimated error. (b) top: Centre discrepancy in the vertical (x) direction as a function of x position in the object plane and the estimated error. The straight line is a linear fit to the original data. bottom: The remaining droplet centre discrepancy after subtracting the estimated error. . . . 101
2.22 Simultaneous ILIDS (left) and PIV (right) images of droplets in a polydisperse spray without seeding particles. 103
2.23 (a) top: Centre discrepancy between ILIDS and PIV images in the horizontal (y) direction as a function of y position in the object plane for the spray. The discrepancy was obtained after subtracting the estimated error (resulting from linear fit of the measured discrepancy for the mono-disperse droplet stream) from droplet centres in the ILIDS image. bottom: The same information without correction. (b) top: Centre discrepancy in the vertical (x) direction as a function of x position in the object plane. The discrepancy was obtained after subtracting the estimated error from droplet centres in the ILIDS image. bottom: The same information without correction. 104
2.24 (a) Remaining droplet centre discrepancy in horizontal direction (y) as a function of droplet size. (b) Remaining droplet centre discrepancy in vertical direction (x) as a function of droplet sizes. 105
2.25 Simultaneous ILIDS (left) and PIV (right) images corresponding to the monodispersed droplet stream surrounded by co flowing air seeded with aluminium oxide particles. 106
2.26 (Left) Demonstration of identification of glare points in PIV image using the wavelet transform. (Right) The PIV image after removal of the glare points (the boundaries associated with the removed glare points are shown as dotted circles). 107

2.27 Simultaneous droplet and gas velocity vector plots for the case of the mono-sized droplet stream surrounded with seeding particles at a given instant. Bold vectors represent droplet velocity, which is scaled down by a factor of 5. 110
2.28 Illustration of the image processing details of the combined ILIDS and PIV technique. Boundaries of the removed glare points from the PIV image are shown as dotted circles. In the plot of simultaneous droplet and gas velocities, the blocked disks represent droplets and the associated bold vectors represent droplet velocity. 112
2.29 Droplet positions and velocities from ILIDS (open circles) and PIV (blocked circles). Droplet positions from ILIDS are plotted without correction for centre discrepancy. 113

3.1 Measurement locations in the spray and the coordinate system. . . . 116
3.2 Probability of droplet size in the measurement region at the cross-stream location, (a) $R = 0\ mm$, (b)$R = 50\ mm$, (c)$R = 100\ mm$, (d)$R = 150\ mm$ and (e)$R = 185\ mm$. 119
3.3 Instantaneous velocity plot of simultaneously measured droplet and gas velocities at the cross-stream measurement location, $R = 0\ mm$. The bold vectors in red represent droplet velocity. 121
3.4 Mean velocity for droplet size classes of 20-35μm, 35-50μm, and 50-65μm and for the gas flow for various cross-stream measurement locations, R. 123
3.5 Area-averaged (a) mean and (b) rms velocity, for droplet (size class 20–35μm) and gas flow for various cross-stream measurement locations, R. 125
3.6 Scatter plot of instantaneous fluctuating droplet velocity, $u_d \sim v_d$, for droplet size class 20–35μm at $R = 0\ mm$. 127
3.7 Normalized shear stress obtained from the gas velocity for various cross-stream locations, R. 127

3.8 The method of calculation of the spatial correlation of the velocity fluctuations. The formula corresponds to the droplet-gas velocity correlation in axial direction, as an example. 131
3.9 Spatial correlation coefficent of gas velocity fluctuations of axial and cross-stream velocity components along both directions at the measurement location, $R = 0\ mm$. 133
3.10 Spatial correlation coefficients of droplet-gas velocity fluctuations for various droplet size classes for (a) axial component of velocity and (b) cross-stream component of velocity , at $R = 0\ mm$. Error bars indicate the statistical uncertainty of the correlation coefficient for 95% confidence interval. 135
3.11 Comparison of spatial correlation coefficients of droplet-gas velocity fluctuations in (a) axial direction, R_{ud*ug} and (b) cross-stream direction, R_{vd*vg} for the three droplet size classes for the cross-stream measurement locations $R = 0$, 100 and 185 mm, respectively. 136
3.12 Spatial correlation coefficients of droplet-gas velocity fluctuations for (a) droplet axial velocity with gas cross-stream velocity and (b) droplet cross-stream velocity with gas axial velocity, for different droplet size classes, at $R = 0\ mm$. 137
3.13 Spatial correlation coefficients of droplet-droplet velocity fluctuations for various droplet size classes for (a) axial component of velocity and (b) cross-stream component velocity, at $R = 0\ mm$. Error bars indicate the statistical uncertainty of the correlation coefficient for 95% confidence interval. 139
3.14 Comparison of spatial correlation coefficients of droplet-droplet (R_{dd}) and droplet-gas (R_{dg}) velocity fluctuations for droplet size class 20–35μm and gas velocity correlation (R_{gg}) for both axial and cross-stream velocity components at the cross-stream measurement locations (a) $R = 0\ mm$, (b) $R = 100\ mm$ and (c) $R = 185\ mm$, respectively. 142

3.15 Probability density functions of droplet-droplet relative fluctuation of (a) axial component of velocity and (b) cross-stream components of velocity for various radius of separation, r and three droplet size classes at $R = 0\ mm$. 148
3.16 Various statistics of the PDFs of the relative axial component of velocity of droplets corresponding to Figure 3.15. a) Mean, (b) Standard deviation, (c) Skewness and (d) Kurtosis. 149
3.17 Probability density functions of droplet-gas relative velocity for (a) axial component of velocity and (b) cross-stream component of velocity for various radius of separation, r and three droplet size classes at $R = 0\ mm$. 150
3.18 Various statistics of the PDFs of the relative axial component of velocity of droplets and gas corresponding to Figure 3.17. a) Mean, (b) Standard deviation, (c) Skewness and (d) Kurtosis. 151
3.19 Comparison of PDF of the number of droplets per box with a binomial distribution for the cross-stream measurement location at $R = 0\ mm$ for three different box sizes with dimensions (a) $H/8 \times L/10$, (b) $H/4 \times L/5$ and (c) $H/2 \times L/2$ where the measurement area is $H \times L$. . . . 153
3.20 Evaluation of RDF for the cross-stream measurement locations at (a) $R = 0\ mm$, (b) $R = 100\ mm$ and (c) $R = 185\ mm$ respectively. . . . 155

4.1 Cumulative contributions of the eigen-values of the respective POD modes for the measurement locations at $R = 0\ mm$, 100 mm and 185 mm respectively. 166
4.2 Flow structures associated with 1st, 2nd, 3rd and 4th POD modes for the cross-stream measurement locations $R = 0\ mm$, 100 mm and 185 mm respectively. 168

4.3 Contributions of various POD modes to the spatial correlation of droplet-gas velocity fluctuations for droplet size class 20-35μm at the measurement location $R = 0\ mm$ for (a) axial velocity component (R_{ud*ug}) and (b) cross-stream velocity component (R_{vd*vg}). 170

4.4 Comparison of the spatial gas correlation coefficient R_{gg} and the modified droplet-gas coefficient RN_{gg} for both axial (left) and cross-stream (right) velocity components evaluated for (a) Mode 1, (b) Mode 2, (c) Mode 3 and (d) Mode 4 for the measurement location $R = 0\ mm$.175

5.1 Experimental arrangement of the combined ILIDS and PLIF technique. 182

5.2 Timing diagram of the combined ILIDS and PLIF technique. 184

5.3 (a) Schematic of the optical system for theoretical prediction of discrepancy in droplet centres between the focused plane in PLIF imaging and defocused plane in ILIDS imaging (b) Discrepancy in geometric centre of the fringe pattern in the ILIDS defocus plane and centre of the droplet image in the PLIF focal plane as a function of the y position in the object plane. The discrepancy for the case of combined ILIDS with PIV arrangement is also plotted for comparison. 187

5.4 Simultaneous ILIDS (left) and PLIF (right) images of the mono-sized droplet stream with size (a) $D_d = 235\mu m$ and (b) $D_d = 122\mu m$ respectively. The color on the right represents the pixel intensity values (linear scale, min = and max =). 190

5.5 (a) Superimposed ILIDS and PLIF images for a stream of monodispersed droplets (D_d = 235 μm) at two different positions in the object plane, $y = -3.5$ and $+3.5$ mm, respectively. Note that the origin of the coordinate system ($x = 0$ and $y = 0$) lies in the centre of the CCD array, which coincides with the centre of the image of the figure. (b) top: Centre discrepancy between ILIDS and PLIF images in the horizontal (y) direction as a function of y position in the object plane. The straight line is a linear fit to the original data. bottom: The remaining droplet centre discrepancy after subtracting the estimated error. 191

5.6 Depiction of error in droplet position due to centre discrepancy. Instantaneous contour plot of vapour concentration around a monodispersed droplet stream with droplet size of 235μm is shown along with the droplet positions obtained from both ILIDS and PLIF images. 193

5.7 Contour plots of instantaneous vapour concentration corresponding to evaporating monodispersed droplet streams of size 235μm (left) and 122μm (right) respectively. 197

5.8 Radial profiles of acetone vapour concentration around droplets in the mono-sized droplet stream for droplet size (a) $D_d = 235\mu m$ and (b) $D_d = 122\mu m$ respectively, averaged over 50 instantaneous images. The error bars indicate the root mean square of vapour concentration fluctuations. 198

5.9 Axial profile of acetone vapour concentration around droplets in the mono-sized stream of droplets with size $D_d = 122\mu m$ averaged over 50 instantaneous images. The error bars indicate root mean square of vapour concentration fluctuations. 200

5.10 Measurement locations in the evaporative spray and the coordinate system. 201

5.11 Illustration of the image processing details of the combined ILIDS and PLIF technique. A pair of typical instantaneous ILIDS and PLIF images are shown along with the droplet filtered PLIF image. In the plot of simultaneous vapour concentration and droplet velocities, the dark blue regions are the removed droplet positions and the bold vectors in white represent the droplet velocity. 203
5.12 Probability of droplet size distribution for the acetone spray (left) and water spray (right) for the radial measurement locations (a) $R = 0$ mm, (b) $R = 15$ mm, (c) $R = 30$ mm and (d) $R = 45$ mm. 207
5.13 probability of variation in instantaneous and total SMD for the radial measurement location at $R = 45$ mm. 208
5.14 Mean velocity for droplet size class of 15–30μm for various radial measurement locations, R. 209
5.15 Area-averaged (a) mean and (b) rms velocity, for droplet size classes of 15–30μm, 30–45μm and 45–60μm for various radial measurement locations, R. 210
5.16 Radial distribution function (RDF) for the three droplet size classes for the radial measurement locations, at (a) $R = 0$ mm and (b) $R = 45$ mm. 211
5.17 Probability of variation in average inter droplet distance for the radial measurement location at $R = 45$ mm. 213
5.18 Contour plots of (a) mean vapour concentration and (b) ratio of rms of fluctuations to the local mean value for the radial measurement locations at $R = 45$ mm. 216
5.19 Local coordinate system for evaluation of distribution of the mean and the fluctuations of vapour concentration around a droplet. 218
5.20 Comparison of mean vapour concentration distribution in y^+ direction with the theoretically predicted trend in case of an isolated droplet as described by the d^2-law (Spalding, 1951). 219

5.21 Variation in fluctuations of vapour concentration (R_c) for the droplet size class of 15–30 μm in (a) x^- and x^+, and (b) y^- and y^+ directions respectively, at the radial measurement location $R = 45\ mm$. R_c is shown for various windows with in the measurement area. The dashed line represents the position of the droplet centre. 221

5.22 Variation in fluctuations of vapour concentration (R_c) in y^+ direction for the three droplet size classes and for various windows with in the measurement area, at the radial measurement location $R = 45\ mm$. . 222

5.23 Spatially averaged correlation coefficients between fluctuations in droplet velocity and vapour concentration (R_{c*u_d} or R_{c*v_d}) for the three droplet size classes for (a) axial and (b) radial directions respectively, at the radial measurement location $R = 45\ mm$. 224

List of Tables

2.1 Error in mean velocity and rms velocity for both velocity components for the three PIV algorithms with respect to the LES calculations. The error is spatially averaged over the viewing area. The interrogation window size was $32 \times 32\ pixel^2$. 71

2.2 Error in mean velocity and rms velocity for both velocity components with respect to the LES calculations for the 12% cropped simulated PIV images for the modified PIV algorithm both with and without consideration of the masking technique. The error is spatially averaged over the viewing area. The interrogation window size was $32 \times 32\ pixel^2$. 76

3.1 Area-averaged statistics of velocity of various droplet size classes and gas flow for the first cross-stream measurement location, $R = 0\ mm$. The viewing area was $8{\times}12\ mm^2$. 124

3.2 Ratio of the terminal velocity to the mean and rms of the droplet velocity for various droplet sizes for the cross-stream measurement locations, $R = 0\ mm$ and $185\ mm$ respectively. 128

3.3 The parameters $D1$ and $D2$ for the different box sizes corresponding to Figure 3.19. 154

3.4 Spatial correlation coefficients of fluctuations of droplet concentration and axial component of gas velocity evaluated for each of the four boxes (of size $H/2 \times L/2$) for the measurement locations at $R = 0$, 100 and $185\ mm$. 157

3.5 Spatial correlation coefficients of fluctuations of droplet concentration and cross-stream component of gas velocity evaluated for each of the four boxes (of size $H/2 \times L/2$) for the measurement locations at $R =$ 0, 100 and 185 mm. 158

5.1 The mean and rms of the group combustion number for the different measurement locations, R. G_1 is according to Equation (5.6) and G_2 is according to Equation (5.7). 214

Chapter 1

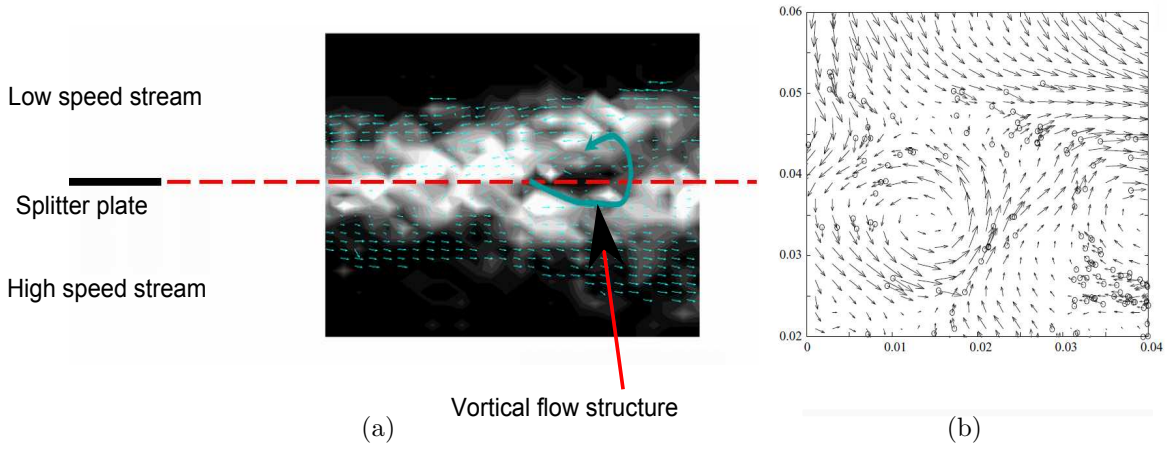
Introduction

1.1 Motivation

Spray plays an important role in today's world of technology with a wide range of applications including internal combustion engines, spray painting, spray drying, powder metallurgy, agricultural and pharmaceutical applications. In spray research, the researchers often confront a lot of complexities since spray formation, droplet breakup, and the corresponding turbulent two-phase flows represent some of the most challenging problems in Fluid Mechanics. Especially, in case of spray combustion, addition of heat transfer, evaporation, and turbulence in the environment makes the understanding of the physics very demanding. Thus, there is a need to study these processes separately and prescribe or even predict the spatial and temporal variations in the spray characteristics of a basic steady spray. This would minimize the coupling between the different effects and provide parametric understanding of the complex process of spray combustion.

A spray is generated in a flow field induced by the spray dynamics. The interaction of the spray with the entrained turbulent flow is an important part of the evolution of the spray. This may lead to different dynamic behaviour of droplet dispersion and redistribution of the droplets due to difference in droplet inertia, momentum and drag. It is well known that a turbulent flow is characterized by the existence of several length scales of characteristic eddies or flow structures, some of which assume very

specific roles in the description and analysis of the flow (Tennekes and Lumley, 1972). A droplet motion can have varying degree of response to an eddy which depends on the droplet size, relative droplet-fluid velocity and length scale of the eddy. For



(a) (b)

Figure 1.1: Depiction of preferential concentration (a) Particle Centrifuging occurs due to the vortical structure of the flow, which increases the local particle concentration (contours of grey levels show particle concentration - black colour corresponds to zero particle concentration), Hardalupas and Horender (2003a) (b) Instantaneous fluid and particle velocity vectors from a single plane of a direct numerical simulation of forced isotropic turbulence. Particle positions are shown by the circles, the symbol size in each frame and particle velocity vectors, Fevrier *et al.* (2005).

instance, when the particle relaxation time becomes of the order of the turbulent time scale, a phenomenon known as 'preferential concentration' (Figure 1.1) is called up on. This issue has been addressed by many researchers over the last two decades. As shown in the figure, the particles tend to flung away from the vortex cores of the eddies and in many cases get collected in rings surrounding the vortices. This may lead to local relative void regions: the number density of certain size classes will be lower than the local mean. Hence the instantaneous spatial distribution of droplets in sprays might have dense and dilute regions, characterized by the appearance of clusters of droplets, Zimmer *et al.* (2003). In liquid-fuelled combustion, such interactions strongly influence the process of air-fuel mixture preparation. Uneven spatial distribution of droplets leads to regions with very different fuel concentration, which may affect the underlying progress. These processes have a direct impact on the combustion efficiency and exhaust gas emission.

The droplet-gas interaction mechanism in a spray—or in general the particle-fluid interaction in a dispersed two-phase flow—is not yet well understood even without considering evaporation or combustion. In spite of considerable progress in this subject on both experimental and numerical fronts, many important issues (for instance, turbulence modulation at different length scales of the flow and the effect of distribution of particle sizes, gravity, anisotropy etc.) remains to be addressed. Therefore, in order to ensure efficient burning of the fuel during combustion, it is essential to gain a physical understanding of the underlying mechanism of the droplet-gas interaction in a non-evaporative or isothermal sprays, as a first step.

Evaporation of the droplets further increases complexity of the problem since new challenges appear. For the combustion of liquid fuelled sprays, the droplet vaporization can be critical since the vaporization can be the slowest process determining the overall burning rate. The evaporation of a single droplet is well described by the classical $d^2 - law$: the square of the droplet diameter (D_d) varies linearly with time (Spalding, 1951). This theory is based on the assumption that the droplet is isolated and still in a quiescent atmosphere, and the evaporation process is quasi-steady. It also assumes the evaporation process is controlled by a mass diffusion process exterior to the droplet and leads to a total droplet lifetime $t_l = {D_d}^2\rho/8\tau_d\Delta C$ (where ρ is the density of the evaporating media, τ_d is the mass diffusion coefficient of the droplet vapour in the exterior gas, and ΔC is the concentration change of the droplet vapour from the droplet surface to the ambient concentration far away from the droplet). However, this situation can never be representative of polydispersed sprays in combustion engines which are submitted to highly turbulent conditions. Because of the appearance of clustering of droplets, as described before, the inter particle spacing may become sufficiently small and interaction between droplets sets in which prevents the oxidizer penetration in the innermost region of the spray. Consequently, a fuel rich mixture is formed in which droplets do not burn individually, but rather in a group. This phenomenon was characterized, in the theoretical analysis of Chiu and Kim (1983), by the Group combustion number, G. For the case of a

mono-disperse cloud, G can be expressed as:

$$G = 3(1 + 0.276Re^{0.5}Sc^{0.33})LeN^{2/3}\frac{D_d}{l_d} \tag{1.1}$$

where Re is the droplet Reynolds number, Sc and Le are the gas Schmidt number and the Lewis number respectively, N is the total number of droplets in the cloud, l_d is the mean inter-droplet spacing, and D_d is the droplet diameter. This dimensionless number may be seen as the ratio between the characteristic evaporation speed and the molecular diffusion speed, or the convective speed of the hot gases inside the cloud.

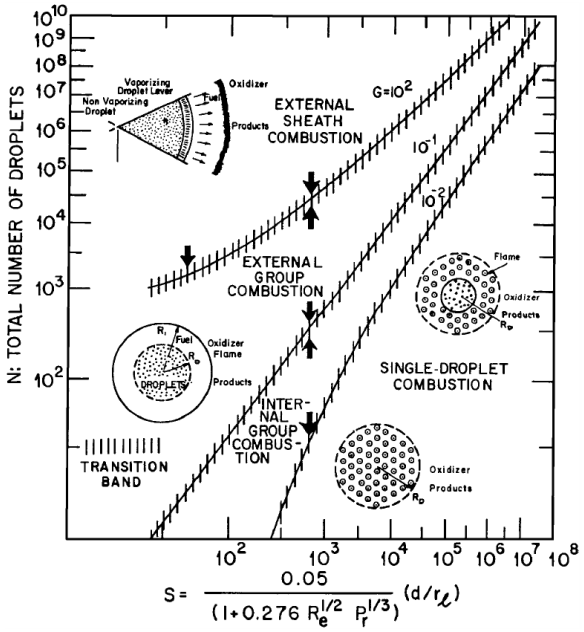


Figure 1.2: Effect of group combustion number on the type of spray combustion, Chiu and Kim (1983).

The magnitude of G has been shown to have profound effect on the flame location and distributions of temperature, fuel vapour and oxygen. Four types of behaviour are found, as shown in Figure 1.2. For large G ($\gg 1$), the droplets are too close to each other to allow diffusion of heat inside the cloud and external sheath combustion occurs. In such case, only an external layer of droplets is evaporated and the resulting flame remains at a stand-off distance from the spray boundary. Under the other limiting condition, $G \ll 1$, the droplets are sparse enough so that the hot gases reach the core of the spray. Hence, evaporation and combustion processes take

place around every individual droplets. Chiu and Kim (1983) anticipated a smooth transition between these limit regimes, leading to intermediate submodes depending on the magnitude of G. When G is slightly above unity, the flame stays around the droplet group with a temperature rise of the liquid phase affecting the core of the cloud (external group combustion). For G smaller than unity, a first ring of individual burning droplets is centred on a droplet cloud surrounded by a diffusion flame (internal group combustion). However, experimental verification of the cloud burning regimes are limited to either qualitative observations or quantitative studies on systems with small number of droplets or droplet arrays. Therefore, before stepping into the study of spray combustion, it is important to realise the conditions which promote this collective behaviour of droplets in an evaporative spray and identify the regimes in the spray where it is going to prevail.

The field of two-phase interaction in dispersed two-phase flows both with and without considering evaporation is rich, in terms of physics of the problem, and has been attracting researchers from a diversified areas of interest since a long time. However there is still lack of understanding which can be attributed to a number of causes. First of all there is an issue of understanding turbulence itself. The non-linearity of the Navier-Stokes equations makes most problems difficult or even impossible to solve. For any sensible predictions, parts of the equation need to be modelled. However, this modelling often encounters the so-called 'closure problem' because of the appearance of one or more extra terms which have to be modelled too. So no analytical solution is yet possible. Addition of particles/droplets to the flow further increases the complexity, since the effect of the droplets on the fluid again needs modelling.

Though numerical simulations have become immensely popular for studying the single phase flow, today's computational capability puts a restriction on doing 'exact calculations' or Direct Numerical Simulation (DNS) of two phase flows. For a dispersed two-phase flow, the only way to exactly describe the system, including the interaction of the phases, is to fully resolve the particle surfaces. This dramatically increases the number of required cells for doing DNS and, thus memory and processing

speed. So, at the moment only very simple geometries with limited numbers of particles can be studied at low Reynolds numbers. Most numerical work uses simplifications, for example, by assuming the particle to be a point-force and choosing a model for the particle equation of motion. Moreover, two phase flows with distribution of particle/droplet sizes are yet to be examined numerically.

The other way to gain insight is to rely on experiments. Classical single point techniques (*e.g.* Phase Doppler Anemometer) and planar techniques like Particle Image Velocimetry have been widely used for the two phase flow studies since decades. However, each has its own limitation. While the single point techniques can not address the issues of preferential concentration and/or flow structure identification, Particle Image Velocimetry can not provide the information on droplet size. Therefore there is a need of developing experimental techniques for detailed characterization of the two phase flows.

1.2 Droplet-gas interaction in a spray

In a dispersed two-phase flow, the carrier phase is described by density, temperature, pressure and velocity field. The droplet or particle phase is described by size, concentration, temperature and velocity field. The coupling takes place through mass, momentum and energy transfer between phases. Mass coupling is the addition of mass through evaporation or removal of mass from the carrier stream by condensation. Momentum coupling is the result of the drag force on the dispersed and continuous phase. Energy coupling occurs either through the transfer of thermal or kinetic energy between the phases. For a non-evaporative spray, it is the momentum and energy coupling which play key role in the interaction mechanism between the droplets and gas motion.

The interaction between the dispersed phase and carrier phase in sprays can be broadly categorized as $one - way\ coupling$ (droplet dispersion by turbulence) or $two - way\ coupling$ (mutual effect between the phases or turbulence modification by droplets also), Crowe *et al.* (1998). In case of one-way coupling, the effect of the

particles on the fluid phase is negligible. The particles may follow all, a part or none of the fluid structures in turbulent flow. As far as numerical computation is concerned, it is sufficient to calculate the fluid phase behaviour and subsequently integrate the particle equations of motion. With a higher load (or with heavier particles), the particle phase starts influencing the fluid phase resulting in two-way coupling between the phases. The fluid phase and particle phase equations should be solved simultaneously. The turbulence level can be attenuated or augmented, depending on the particle characteristics. Despite numerous suggestions, there is no single parameter that seems capable of predicting this behaviour. In literature, the use of Stokes number[1] (St), volume load (ϕ_v), ratio of particle size (D_p) to a characteristic fluid length scale ($\wedge$) and particle Reynolds number (Re_p) have been suggested as parameters, which determine if the fluid turbulence to be attenuated or enhanced. However, contradictory results have been found.

1.2.1 Particle-fluid correlation terms

An important goal of researchers examining particle-laden flows is to develop models for both particle dispersion by turbulence and turbulence attenuation by particles. Consider such a particle flow with negligible particle loading so that the inter particle collisions can be neglected. As per Chen and Wood (1985), the turbulent kinetic energy (TKE) equation for the continuous phase, considering the drag force between the particles and the carrier fluid and using a $k-\epsilon$ closure scheme, can be written as:

$$\frac{dk}{dt} = \left(\frac{dk}{dt}\right)_{sp} - \frac{\overline{C}}{\rho_f \tau_d}\left(\overline{u_{ig}u_{ig}} - \overline{u_{ig}u_{id}}\right) - \frac{1}{\rho_f \tau_d}\left(\overline{cu_{ig}u_{ig}} - \overline{cu_{ig}u_{id}}\right) - \frac{1}{\rho_f \tau_p}\left(\overline{U_{ig}} - \overline{U_{id}}\right)\overline{cu_{ig}} \tag{1.2}$$

where U and u denote the instantaneous and fluctuating velocity respectively, subscript i refers to the component of the Cartesian reference system, C and c are the instantaneous and fluctuating particle concentration, overbar denotes time-averaging,

[1]Stokes number of particles, St, is defined as the ratio of particle relaxation time (τ_p) to some time scale of the fluid flow (τ_f).

and τ_p is the particle relaxation time. It should be noted that Equation (1.2) refers to only one particle size and its application to polydisperse sprays requires additional effort. The first term on the right hand side comprises the production, dissipation and transport terms in single phase fluid. The remaining terms, derived by assuming a linear drag law for particles, include correlations of the particle concentration and velocity fluctuations of the fluid and/or particle-fluid velocity correlations and represents an 'extra' modification of turbulent kinetic energy due to particles. This equation describes only the attenuation of fluid turbulence, since it was derived for particles much smaller than the large eddy scale in the flow. When the fluctuating particle concentration is uncorrelated to that of the fluid velocity, the last two terms are negligible. Though this is usually true when turbulent attenuation is large, strong correlation may be expected when the particle Stokes number tends to 'one'. Thus, we see that the feasibility of incorporation of the effect of two-way coupling (*i.e.* modification of turbulence by the particles through interfacial momentum transfer) depends on successful modelling of the cross-correlation terms appearing in the TKE equation and it is essential to find a way to measure these correlations.

Evaluation of the fluid-particle velocity correlations in particle/droplet laden flows is rare in the literature. This is not due to lack of interest rather the difficulties in obtaining such measurements. The most important limiting factor is the measurement of both fluid and particle velocities at the same time. Since the particle occupies a finite volume and causes a local disturbance to the flow, the correlation is defined between the particle velocity and the fluid velocity in a small neighbourhood surrounding the particle. For the case of polydisperse size distribution of particles in the flow, such as in a polydispered spray, the velocity correlations need to be evaluated conditional on droplet size or size classes.

Prevost *et al.* (1996) reported measurements of fluid-particle velocity correlations in an axisymmetrical polydispersed particle laden tube jet at 30 jet diameters from the nozzle exit. They used Phase Doppler Annemometer (PDA) which allowed measuring the particle (glass beads) size/velocity and fluid velocity (tracer particles) at a single point, in the spray. Since the fluid velocity could not be measured at the same time

and location as the particle velocities, in order to obtain the fluid velocity 'seen' by the droplets, they reconstructed the signal of the continuous phase using an interpolation scheme. The correlations were obtained for various size classes. The measured radial kinetic stress was found to lie very close to the measured radial fluid-particle correlation and both were shown to decrease significantly for larger particles. On the contrary, the longitudinal kinetic stress is significantly greater than the measured longitudinal fluid-particle correlation and the difference between these terms increased for larger particles. However, it is essential to evaluate the inaccuracies introduced because of the interpolation of the fluid velocity. This work was later extended by Ferrand *et al.* (2003) to analyse a more concentrated jet (mass loading $\phi_m = 73\%$ compared to 8% in the previous work) where the fluid-particle correlations were expected to contribute actively to the magnitude of the turbulence modulation. They calculated the attenuation terms relative to the turbulent kinetic energy transfer from the particles to the gas with the knowledge of the correlation terms and the particle concentration per size class (obtained by coupling PDA with laser induced fluorescence). It was concluded that neglecting the fluid-particle correlated motion leads to overestimation of the magnitude of the attenuation terms appearing in the TKE equation of the carrier phase.

Sakakibara *et al.* (1996) used particle image velocimetry (PIV) for simultaneous planar measurements of the fluid and particle velocities in a jet laden with mono-sized glass beads. Two different particle sizes were considered. They adjusted the camera so that scattered light from the tracers never exceeded 70% of saturation, and then eliminated the tracers from the image with a suitable threshold. The resulting image was processed to measure the particle phase velocity, and also was subtracted from the original image to give a tracer-image field. The particle velocity was correlated with the average velocity of the nearest-neighbour, carrier-phase PIV measurement points. The direct measurements produced correlation values which were too low which was attributed to the uncertainty in velocity estimation. A problem with this technique is that it leaves low-intensity halos around the hole where each particle was eliminated. So, it is important to mention the uncertainties associated with the

correlation estimation.

Hardalupas and Horender (2003b) developed a new method for the estimation of gas-droplet velocity cross-correlation function in a spray from an air blast atomiser using PDA. In order to obtain the correlation at non-zero time delay, the method combined time dependent velocity measurements of droplets in sprays and a droplet eddy interaction model. It was found that the droplet-gas velocity cross-correlation function was asymmetric around zero time delay and the presence of a mean slip velocity between the two phases shifted its maximum to non-zero time delays.

Apart from the correlation between particle and fluid velocity, it is also essential to quantify the correlations that involve particle concentration in the equation describing the carrier phase turbulence modification, which are usually omitted as negligible. Although, in literature, the use of PDA has been reported for the measurement of particle concentration fluctuations, such measurement was shown to depend on a choice of the sampling time. This makes the interpretation of the results difficult. Imaging techniques have also been used for this purpose. Longmire and Eaton (1992) used phase-locked digital imaging to measure spatial distribution of particle number density in a pulsed jet laden with glass beads. The size of the probe volume was kept smaller than the length scale of the observed preferential particle concentration distribution. Therefore, they measured the random and non-random fluctuations of particle concentration. However, the effect of relative size of the interrogation window on the measurement of particle concentration was not considered. Hardalupas and Horender (2003a) pointed out that this may result to inappropriate measurements of the correlations between particle concentration and fluid velocity. They reported measurements of cross-correlation coefficients of two particle velocity components and concentration fluctuations in a horizontal plane shear layer laden with glass beads. Velocity measurements were obtained by PIV and instantaneous particle concentration by counting the number of particles in each interrogation cell of the PIV images. The effect of interrogation cell size on instantaneous particle concentration was assessed and an appropriate cell size (which showed maximum deviation from randomness) was chosen to quantify the non-random

contribution of particle concentration fluctuations.

1.2.2 Contribution from Numerical studies

Along side the experiments, considerable contributions from the numerical works on the two-phase interaction have been documented (Squires and Eaton (1990); Boivin *et al.* (1998); Sundaram and Collins (1999); Ferrante and Elghobashi (2003); to name a few). The numerical calculations, mostly based on direct numerical simulation (DNS) of particles suspended in isotropic and homogeneous turbulent flow, focused on the prediction of the modification of turbulent kinetic energy of the carrier phase by the dispersed phase and/or the issue of preferential concentration in the two-phase flows. The significant conclusions that can be derived from such investigations are that for a suspension of particles with response time much larger than the Kolmogorov time scale, the main effect of the particles is to suppress the energy of eddies of all sizes as compared to the particle-free case. But, for a suspension with particles with a response time smaller than the Kolmogorov time, the turbulent kinetic energy of almost all sizes increases. For a suspension of particles with a response time between the two limiting cases mentioned above, the energy of the larger eddies is suppressed, whereas the energy of the smaller ones is enhanced.

However, it should be noted that in almost all of the numerical works, the particles are treated as 'point-particles' because it is impossible to resolve the flow field around individual particles, since this demands enormous computational power (which is unavailable at present). This results in a significant simplification, since the turbulence generation due to particle wakes and vortices shed by the particles could not be taken into account (Poelma and Ooms, 2006). Also, most numerical studies do not consider the effect of gravity which can be a source of turbulence production and can generate a strongly anisotropic system. Moreover, examining two phase flows laden with distribution of particle sizes is yet to be examined numerically. Nevertheless, the simulations provide a parametric study of the two phase interaction process to gain fundamental insights of the complex physical processes.

1.2.3 Experiments in two-phase flows

Considering the limitations often encountered in the numerical simulations of dispersed two phase flows, the experimental approach has been encouragingly acknowledged. However, as mentioned before, only few experiments have reported the measurement of particle-fluid velocity cross-correlation. The measurement difficulty arises from the following challenging factors:

1. The estimation of the above mentioned correlation terms require *simultaneous* and *planar* measurement of velocity of both phases. This is because both the particle and fluid velocity around each particle have to be determined at the same instant. PIV is suitable for this purpose because it allows the simultaneous measurement of the velocity of both phases over an imaged area. The dispersed phase velocity can be obtained by tracking the same particle in both pair of images while the image of tracer particles can be used to measure the velocity of the carrier phase. However, the difficulty arises in separating the contributions of both phases. The so called "cross-talk" between the two phases should be avoided, especially, to minimize the influence of the presence of particles on the evaluation of the cross-correlation spectrum of the tracer images.

2. Since the velocity correlations appearing in Equation (1.2) is based on a given droplet/particle size or size class, the estimation of the velocity correlations ($\overline{u_{ip}u_{ig}}$) has to be done *conditional* on that droplet size (or size class). However, the current literature is restricted to single-point measurements and/or mono-sized particle experiments.

3. Along with the velocities of both phases and size of the particles, the instantaneous particle concentration should be measured to evaluate the correlation between them. Though PIV is suitable for this purpose (as mentioned before), the effect of relative size of the interrogation windows on these correlations should be considered.

For estimation of the correlation terms in a spray, all of the aforementioned conditions needs to be satisfied. Several attempts have been made in the past for two-phase measurements in dispersed flows. In planar, image-based techniques with laser illumination, this is usually done either by acquiring images of both phases on a single camera followed by image processing to separate the phases or by using two cameras each arranged to acquire images from individual phases in some way. A popular approach is to tag the gas phase seeding with a fluorescent dye in conjunction with an adequate optical filter that attenuates the Mie scattered signal from the spray droplets.

For example, Lindken and Merzkirch (2002) used only one camera for bubbly flow measurement based on a combination of PIV with fluorescent tracer particles and shadowgraphy and digital phase separation with a masking technique. Similarly, Rottenkolber *et al.* (2002) acquired consecutive images from the spray alone and of the induced gas flow alone using fluorescent seeding particles to trace the gas phase. They described two different algorithms for phase discrimination known as 'mask' and 'peak' separation techniques. In order to avoid the presence of the two phases on the same image, Kosiwczuk *et al.* (2005) tagged both phases, instead of only one, with two different fluorescent dyes. Two cameras were used, one for each phase, along with suitable optical filter set. They could obtain simultaneous and independent velocity fields of the two phases by processing each image containing only one phase by standard PIV or particle tracking velocimetry (PTV) algorithms. Most phase-discrimination systems eliminate noise, including tracer images near the particle surfaces. Tanaka and Eaton (2010) solved this problem by using a very-high resolution PIV system with an imaged area of only 3.7 mm by 4.7 mm. Phase discrimination based only on particle image size resulted in essentially zero cross talk. However, the small measurement area required a large number of image pairs to obtain converged turbulence statistics.

We see that the literature on two-phase planar measurements in sprays does not yet provide either extensive information on droplet size-velocity correlation simultaneous in space or the gas phase velocity in presence of the dispersed phase.

Classical single point techniques cannot identify reliably issues such as preferential concentration or coherent flow structure identification in sprays. Since knowledge of the droplet size is equally important as the droplet and gas velocity, PIV alone is not sufficient for the task. The fluorescence approach can provide velocities of the gas flow and/or droplet phase. But it is always associated with the possibility of cross-contamination due to Mie scattering, which needs to be quantified, and, moreover, it is relatively expensive to use.

Considering the limitations in the above experimental approaches, the importance of *planar* measurement of droplet/particle sizes can be realized. The droplet size measurement over a two-dimensional area would facilitate the evaluation of the correlation between fluid and particle velocity if the gas velocity can be simultaneously measured in the same area. Use of the optical technique known as Interferometric Laser Imaging for Droplet Sizing (ILIDS) offers such an opportunity. ILIDS (also known as Interferometric Particle Imaging, IPI) is an optical technique for instantaneous measurements of the spatial distribution of individual droplet size and velocity in polydisperse sprays. It makes use of the spacing of the interference fringes formed due to reflected and first order refracted scattered light from individual droplets, when collected by 'defocused optics', to determine the droplet size (Glover *et al.*, 1995). The incorporation of image compression optics by Maeda *et al.* (2000, 2002) reduces fringe overlapping in dense sprays and avoids the complexity of the evaluation of fringe spacing (Damaschke *et al.*, 2005) and thus extends the applicability of ILIDS to relatively dense sprays. Hence, ILIDS was opted for planar droplet characterization in the present study.

1.3 Measurement of evaporative spray

Spray vaporization and combustion are very complex topics, that require the understanding of physical processes such as spray atomization and transport, turbulence, chemistry, and also interaction of all these quantities with each other. Since in an industrial-type combustor, all the aforementioned parameters are generally

coupled to each other, it is difficult to determine the separate influence of each of them. As a result, idealized sprays are studied to minimize the coupling between the different effects and to provide parametric results. In this thesis, the focus will be on the measurement evaporative sprays with specific objectives of studying the collective behaviour of droplets and the interaction between the droplet and vapour phases.

In an evaporating spray, the interaction between droplets can have a strong impact on the evaporation rate. The evaporating neighbouring droplets changes the vapour mass fraction of the air/vapour mixture and thus decrease the vaporizing rate and also, modify the flow properties, such as velocity or temperature. Depending on parameters such as droplet diameter and spacing, the vapour spatial distribution around droplets may change leading to various combustion regimes, such as group combustion or individual droplet burning. As was described earlier, Chiu and Kim (1983) formulated a quasi-steady analysis of droplet clouds and identified a characteristic group combustion number G as a controlling parameter dictating the combustion mode (see Figure 1.2). For the case of a monodisperse cloud, G is defined as:

$$G = 3(1 + 0.276Re^{0.5}Sc^{0.33})LeN^{2/3}\frac{D}{L} \tag{1.3}$$

where Re is the droplet Reynolds number, Sc and Le are the gas Schmidt number and the Lewis number, N is the total number of droplets in the cloud, L is the mean inter-droplet spacing, and D is the droplet diameter. By further assuming uniform spherical cloud, $Le = 1$, and neglecting the convective enhancement effect to the droplet vaporization process, Equation (1.3) can be simplified to:

$$G = 2\pi nDR_c^2 \tag{1.4}$$

where n is the droplet number density and R_c is the cloud radius. The magnitude of G determines the prevailing modes of combustion.

This model has the significant drawback that its assumptions are virtually impossible to satisfy in a laboratory experiment. Consequently, experimental verification of cloud-burning regimes has been limited to either qualitative observations in

practical, turbulent sprays or more quantitative studies on systems with a small number of droplets or droplet arrays. In particular, many studies were performed using monodisperse droplet streams to study droplet evaporation or combustion (Connon *et al.*, 1997; Castanet *et al.*, 2003; Frackowiak *et al.*, 2009; Orain *et al.*, 2006). This simple geometry is particularly attractive because it generates a temporally and spatially repeatable stream of droplets with well-controlled injection frequency, droplet size and velocity, and droplet spacing, which allows us to study the individual influence of each of these parameters on droplet vaporization. In order to bridge the gap on knowledge between the droplet combustion and on spray combustion, several studies were performed on model droplet clusters with two and three dimensional array of droplets *e.g.* Silvermann and Dunn-Rankin (1994), Segawa *et al.* (2007) and Watanabe *et al.* (2007). Although these were much better controlled than a spray, they are an oversimplification of actual droplet clouds in sprays, and testing of cloud burning in more realistic situations, perhaps intermediate between these extremes, is necessary (Chen and Gomez, 1997).

Apart from the collective combustion of the droplets, spatial and temporal inhomogeneities of fuel vapour distribution due to interaction of the spray with the turbulent air have been identified as key factors leading to increased pollutant emissions or combustion oscillations. The carrier flow turbulence can also have a strong impact on vaporization either directly by modifying mass and heat transfers or indirectly through droplet dispersion. Birouk and Gokalp (2006) provide a review of the studies on the direct effect of turbulence on single droplets. Most of these studies point out that with increasing turbulence levels the evaporating rate of a single droplet will be increased. Several authors have dealt with the vaporization rate of a droplet mist in turbulent conditions; however, these studies are rather rare. One example is Sornek *et al.* (2000), who experimentally studied effect of turbulence properties on dispersion and evaporation of an industrial spray. The fine scale fluctuations were imposed on the spray by placing a grid in front of the spray nozzle. They found that the effect of the turbulence was to produce more uniform spatial distribution of droplets and reduce the inter-droplet interactions leading to an increase in the global

vaporization rate. The evaporated fuel disperses slower than the liquid droplets.

Thus we see, in order to characterize an evaporative spray several quantities must be measured which includes droplet size, velocity, temperature, flux, fuel vapour distribution and the crucial parameter, inter droplet spacing. Physical models can be derived from such experiments and can be subsequently implemented in calculation codes to examine more complex situations. Advanced laser diagnostic techniques that are crucial to progress in such challenging environments have been introduced though at a slower pace, principally because of difficulties associated with the presence of the dispersed phase. For measuring the dispersed phase (droplet size/velocity), most of the previous studies relied on phase Doppler anemometer (PDA) for example Chen and Gomez (1997), Sornek *et al.* (2000) and Karpetis and Gomez (2000). However, for the evaluation of the group combustion number, G, by PDA one has to rely on Equation (1.4) which assumes the droplets to be uniformly spaced. But this assumption may not be true. The mean droplet size and inter-droplet distance may vary with time. Also, evaluation of the instantaneous group combustion number and its variation with time would shed light on the probability of occurrence of the various combustion modes, an important issue which has been always neglected. PDA being a single-point-technique can not address these issues and planar measurement of droplet position and size is essential.

Measurement of fuel vapour concentration in a spray requires the use of non-intrusive techniques which do not disturb the flow and gather instantaneous phenomena. In particular, laser-based diagnostics are well suited for this type of measurement and have largely been developed over the past two decades. The most common techniques are planar laser-induced fluorescence (PLIF), and spontaneous Raman scattering. PLIF is particularly interesting because it allows us to determine the spatial distribution of liquid and vapour phases. Laser diagnostics based on elastic interactions are practically inapplicable as the scattered intensities, which are emitted at the laser wavelength, are about six orders of magnitude lower for the gas phase (Rayleigh range) than for the droplets (upper Mie range). The huge dynamic range of the emitted light makes it impossible to detect the vapour or the smallest

droplets when bigger drops are present. The laser techniques based on Raman or absorption/fluorescence interactions provide emissions at specific wavelengths whose frequency shifts are practically insensitive to the phase in which the probed molecules are found. Thus these techniques can reject the elastic light scattering by the droplets but they cannot discriminate spectrally between liquid and vaporized phase contributions of a given molecule.

However, owing to the strong density differences between condensed and gaseous phases, the laser induced emissions from the vaporized phase are very difficult to extract from the strong liquid contribution. The main limitation of optical diagnostics is due to the finite dynamic range of the detectors compared to the large range of signal levels that have to be detected especially if the measurement has to be performed with high time and space resolutions. Either the signal from the droplets will saturate the intensified camera, or the vapour signal will be below noise level. Bazile and Stepowski (1995) suggested using a molecule with a strong absorption coefficient which makes the droplet fluorescence limited to a surface contribution while the contribution of the gas phase scales as the mass of vapour. The necessary camera dynamic is thus reduced and vapour phase concentration can be obtained in regions where liquid is diluted enough. In this respect, they found acetone to be the ideal choice. Its strong absorption coefficient at the laser wavelength (ultra violet) and its low dependence of fluorescence properties on pressure and temperature (constant quenching) makes it ideal for studies under various thermal conditions. By analysing the histogram of the signal level in the spray, they set a cut-off threshold to reject the contribution of the liquid phase. However, their study did not provide information on the instantaneous droplet size and velocity distribution. Kurosawa *et al.* (2002) combined ILIDS with PLIF for simultaneous characterization of both droplet and vapour phases in an evaporative spray. While ILIDS provided the droplet size and velocity, PLIF measured the vapour concentration around droplets. However, the results were limited to the mean droplet velocity and mean vapour concentration distribution. Moreover, there was a positioning error between the droplet centre and the surrounding vapour concentration distribution.

The above discussion confirms the necessity of using a planar measurement technique for simultaneous characterization of both droplet and vapour phases in an evaporative spray.

1.4 Aim of this work

The present research has two goals related to the physics of isothermal and evaporative sprays respectively. For the former case, the aim is to develop an experimental technique for simultaneous and planar characterization of both droplet and gas phases in a spray, and apply the technique to understand the interaction mechanism between a non-evaporating spray and its entrained gas flow field. The study of an evaporative spray aims to develop an experimental technique for simultaneous and planar measurement of the droplet and vapour phases in an evaporative spray and, subsequently, apply it to obtain measurements that provide physical insight on the collective behaviour of evaporating droplets and the interaction between the droplets and vapour phase.

There is lack of experimental data on droplet-fluid velocity correlations in isothermal sprays, which is essential not only for modelling the turbulence modulation of the carrier phase by the droplets in a spray but also, to provide insight into the physics of the momentum transfer between the two phases. The measurement difficulties arise because of the limitations of the existing techniques to obtain simultaneous and planar measurements of droplet size, velocity and number density, and the fluid velocity around the droplets. Hence the first aim is to develop a novel experimental technique by combining Interferometric Laser Imaging for Droplet Sizing (ILIDS) with Particle Image Velocimetry (PIV) which can facilitate measurement of all the above mentioned quantities in a isothermal spray. While ILIDS provides planar droplet size and velocity, the gas velocity in the vicinity of individual droplets is obtained by PIV. Thus, the same droplet is imaged as a set of fringes in the defocused ILIDS image and a pair of glare points in the focused PIV image. The advantage of this approach lies in the fact that the position of droplets in a spray, obtained by

ILIDS beforehand, helps in identifying the images of the same droplets in the PIV image, thus making it possible to associate the droplet size/velocity to the glare-points. The glare-points are removed from the PIV image retaining only 'seeding' particles, which follow the gas phase flow. The PIV images are then processed to obtain the gas velocity in the vicinity of each droplet.

An unexpected difficulty with the combined technique is the presence of a discrepancy in droplet centres when calculated independently through ILIDS and PIV images. The "droplet centre discrepancy" is a crucial factor which needs to be accounted for, since this would lead to incorrect estimation of the droplet-gas velocity correlation terms, like those appearing in Equation (1.2). For a detailed description of the cause of this positioning error in droplet centre and a proposed method to minimize it, one is referred to Chapter 2. Straightforward application of the conventional PIV algorithm to process non-ideal PIV images (now devoid of droplets) may result in inaccurate estimation of the gas velocity. Hence, special care will be given to this topic.

Measurements are performed with the combined ILIDS/PIV technique in a model co-flowing isothermal spray dryer with a water spray injected from a single air-assist solid cone atomizer. Using the data obtained by this set-up, the following statistical quantities appearing in Equation (1.2) are determined to gain more insight into coupling effects between the two phases:

- droplet-gas spatial velocity correlation coefficients.
- droplet-droplet and gas-gas spatial velocity correlation coefficients.
- probability density functions of the fluctuating velocity relative between droplets and gas .
- instantaneous droplet concentration.
- radial distribution function, *i.e.* probability of finding a second particle at a given separation distance from a test particle.
- correlation coefficients of gas velocity-droplet concentration fluctuations.

The droplet-gas and droplet-droplet spatial velocity correlations are measured conditionally on droplet size classes. Also, for each droplet size class, the correlations are obtained as a function of distance of separation from the reference droplet. This will exemplify the influence of gas motion away from a droplet on the droplet motion, an important aspect which the existing models for two-phase coupling do not take into account. The focus of the study will be on the following questions:

1. How does the momentum transfer take place between the droplet and gas phase?

2. What is the effect of droplet size and anisotropy in droplet motion on the momentum exchange between the two phases?

3. Does the flow show any sign of preferential concentration?

4. Can we study the contribution of individual flow structures (each corresponding to a specific length scale of the gas flow) on droplet-gas interaction mechanism?

5. If so, can we say something about the turbulence modulation at a specific length scale of the flow: whether turbulence attenuation or augmentation is going to be prominent?

The first two questions can be answered by considering the behaviour of the droplet-gas, droplet-droplet and gas spatial velocity correlation terms and a comparison among them. To answer the third question, one needs to compare the local concentration probability density function with that arising from a purely random process. The radial distribution function also provides a statistical measure of droplet preferential concentration. The last two questions are very important in order to understand the scale by scale variation of the turbulence modulation and may play a significant role in assisting Large Eddy Simulation (LES) sub-grid scale modelling. None of the previous experimental work has addressed these issues. In order to answer those questions, at first, we need to extract the flow structures from the carrier phase velocity data. For this purpose, Proper Orthogonal Decomposition or POD (Lumley, 1967) is applied to the gas velocity data. POD provides an optimum and unbiased

method to extract the structures in a turbulent flow (Holmes *et al.*, 1996). The droplet-gas and gas velocity correlations can be calculated for each structure of the gas velocity field determined by POD one at a time. Comparison of the correlation terms for different length scales of the flow will elucidate the turbulence-droplet interactions at those length scales of the flow.

For the measurement of the evaporative spray, the first aim is to develop an experimental technique by combining ILIDS for measurement droplet properties with PLIF for measurement of the vapour concentration distribution around individual droplets. Compared to the combined ILIDS and PIV technique, the major difference is that instead of the glare points, the liquid fluorescence signal will be obtained in the PLIF image. In literature only the work of Kurosawa *et al.* (2002) is available that provides similar measurements. However, they did not take into account the discrepancy in the identified droplet centre between focused and defocused images which is inevitable in the combined out-of-focus (ILIDS) and in-focus (PLIF) techniques. This would lead to incorrect pairing of the droplet size/velocity and the surrounding vapour distribution. In order to demonstrate the capability of the combined technique, it will be applied first to a mono-sized droplet stream of acetone. Two different droplet sizes (and inter-droplet distance) will be considered. Next, the technique will be applied to an evaporating acetone spray. Acetone was the ideal choice as the working fluid because of reasons mentioned earlier. Eliminating contributions of the droplet florescence is a crucial step in the PLIF image processing and this will be considered in detail. The simultaneous measurements of droplet size and velocity and vapour concentration will be used to evaluate the instantaneous group evaporation number and the correlation between droplet size/velocity with the surrounding vapour concentration.

1.5 Outline of the thesis

The general lay-out of the thesis is as follows: Chapter 2 provides a brief overview of the ILIDS and PIV techniques with particular emphasis on the image processing

algorithms. Then the principle of the combined technique is explained followed by a description of the experimental set-up. Considerable attention is paid to predict and quantify the "droplet centre discrepancy" between focused and defocused images by a theoretical analysis based on geometrical optics and measurements with a mono-sized droplet stream respectively. The potential of the technique for two-phase spray measurements is demonstrated. Chapter 3 reports the results obtained by applying the combined ILIDS/PIV technique to a water spray in a spray-dryer rig. The spatial correlation coefficients of droplet-gas velocity fluctuations are reported for different droplet size classes. Various other statistical quantities are presented to assist the understanding of the interaction mechanism between the two phases. The results are presented at various measurement locations in the spray. The selective influence of the large scale eddy structures of the gas phase flow on the droplet-gas flow interaction is examined in Chapter 4. The gas flow eddy structures are extracted by applying Proper orthogonal decomposition (POD) on the instantaneous gas velocity data. An attempt is made to explain the turbulence modulation at different length scales of the flow. Chapter 5 describes the combined ILIDS and PLIF technique for planar characterization of droplet size, velocity and vapour concentration in an evaporative spray. The experimental set-up and the image processing details are described. The combined ILIDS/PLIF technique is evaluated by measuring in a mono-sized acetone droplet stream. Then it is applied to an acetone polydispersed spray and measurements of the droplet characteristics and vapour phase are presented. Finally, Chapter 6 summarizes the main conclusions of the present thesis, and provides recommendations for future research.

Chapter 2

Combined ILIDS and PIV Technique

In the first chapter, the motivation behind combining ILIDS with PIV was established and the novel aspect of detailed characterization of both dispersed and continuous phases and their interaction in a spray was demonstrated. This chapter describes the principle of the combined technique and, the associated experimental arrangement and image processing. Combination of the defocused (ILIDS) and focused (PIV) optical arrangement led to an unexpected problem of discrepancy in the position of the centre of the same droplet when imaged through both techniques. This issue, termed as "Droplet centre discrepancy", will be addressed and discussed in detail. A method will be proposed to minimize the error in the droplet position. Finally, the potential of the combined technique for two phase planar measurements of the spray will be demonstrated. However, before proceeding to the combined technique, which is a novel achievement, it is essential to present an overview of the instrumentation and image processing involved in each of the individual techniques. Hence the chapter begins with a concise description of the ILIDS and PIV techniques, respectively. [1]

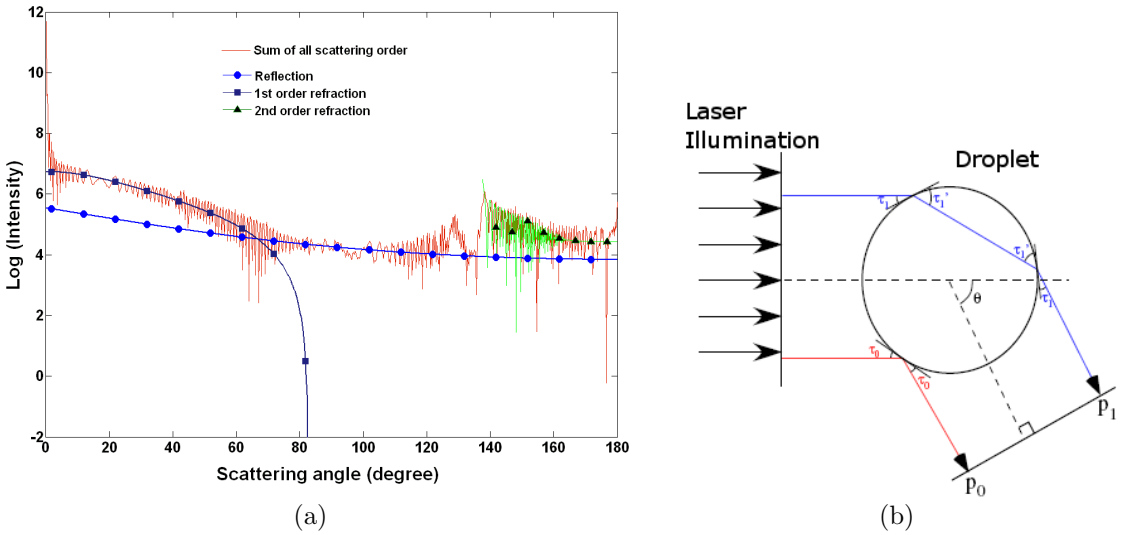
[1]The combined ILIDS and PIV technique including issue of the droplet centre discrepancy has been published in Hardalupas *et al.* (2010)

2.1 Interferometric Laser Imaging for Droplet Sizing (ILIDS)

2.1.1 Background

Considering the importance of experimental characterization of sprays, a wide range of optical techniques have been developed over the years. These techniques broadly fall under the category of line-of-sight measurements *e.g.* Malvern particle-sizer (Dodge, 1984; Hirleman, 1986), single point techniques *e.g.* Phase Doppler Velocimetry or PDA (Bachalo and Houser, 1984; Saffman *et al.*, 1984; Bauckhage *et al.*, 1987) and direct imaging *e.g.* (Dombrowski and Fraser, 1954; Chigier, 1976). However, none of the techniques is completely satisfactory. Malvern particle-sizer lacks the desired spatial resolution. PDA can provide good spatial resolution, but it requires large number of individual point measurements to determine spatial variations in the flow. Also, both of these techniques can not provide instantaneous spatial distribution of droplet size/velocity, which is essential for the measurement of the droplet-gas velocity correlation terms as discussed in the previous chapter. The direct imaging techniques suffer from the requirement for high magnification to resolve small droplets, which results in a restricted field of view. Thus, ILIDS was developed to meet the requirement of instantaneous droplet measurements over a wider field of view.

The fundamental principle of ILIDS is based on Mie scattering theory and was developed by considering the interference of scattered light from a single transparent droplet, when illuminated by a coherent laser source. Figure 2.1(a) shows the scattered light intensity from a single $100\mu m$ droplet expressed as a function of scattering angle, calculated with Mie scattering theory for vertical polarization of light (van de Hulst, 1957). Regular oscillating intensity lobes can be observed in the wide-angle forward scatter region (30° to 70°). Glantschnig and Chen (1981) showed that the oscillations in the scattering diagram in the forward scattering region primarily arise because of the interference between the reflected ray (p_0) and the first order refracted ray (p_1). This is because the contributions from the higher orders are



(a) (b)

Figure 2.1: (a) Intensity of scattered light around a single droplet ($D = 100\mu m$) as a function of scattering angle and contribution from the first three scattering orders for an incident plane wave ($\lambda = 532\ nm$) for vertically polarized light (b) Schematic of the optical paths of external reflection and first order refraction through the transparent spherical droplet.

negligible in the forward scattering region, for instance, the contribution from the second order refracted ray, p_2, is negligible in the range $30° < \theta < 70°$ as evident from Figure 2.1(a). Based on geometrical optics calculations, by considering only p_0 and p_1 as shown in Figure 2.1(b), they concluded that the angular frequency of the fringes is directly proportional to droplet diameter and hence, can provide accurate measurement of the droplet size. However, the applicability of geometrical optics is subjected to the condition that the size parameter $\pi D/\lambda \geq 5$ where, D and λ are the droplet diameter and wavelength of light, respectively.

ILIDS has its origin in Konig *et al.* (1986), who focused a laser beam on a mono-sized droplet stream, and measured the size of the droplets by recording the fringe patterns on a linear array detector. By using the geometric analysis they could predict the angular fringe spacing. Recognizing the potential for highly accurate size measurement with the technique they also suggested its usefulness for a spray. Similarly, Ragucci *et al.* (1990) also reported an optical technique for droplet sizing based on out-of-focus imaging of light at side scatter direction of 90°. However, since in this region the geometric analysis approach is not valid, they calculated calibration

curves for angular fringe spacing versus droplet diameter with the Lorentz-Mie theory. Glover *et al.* (1995) combined the approach of Konig *et al.* (forward scattering angle and geometrical analysis) with Ragucci *et al.* (out-of-focus imaging) and used a wider field of view to record the fringes from many droplets in a spray simultaneously. They named the technique Interferometric Laser Imaging for Droplet sizing or ILIDS.

2.1.2 Principle

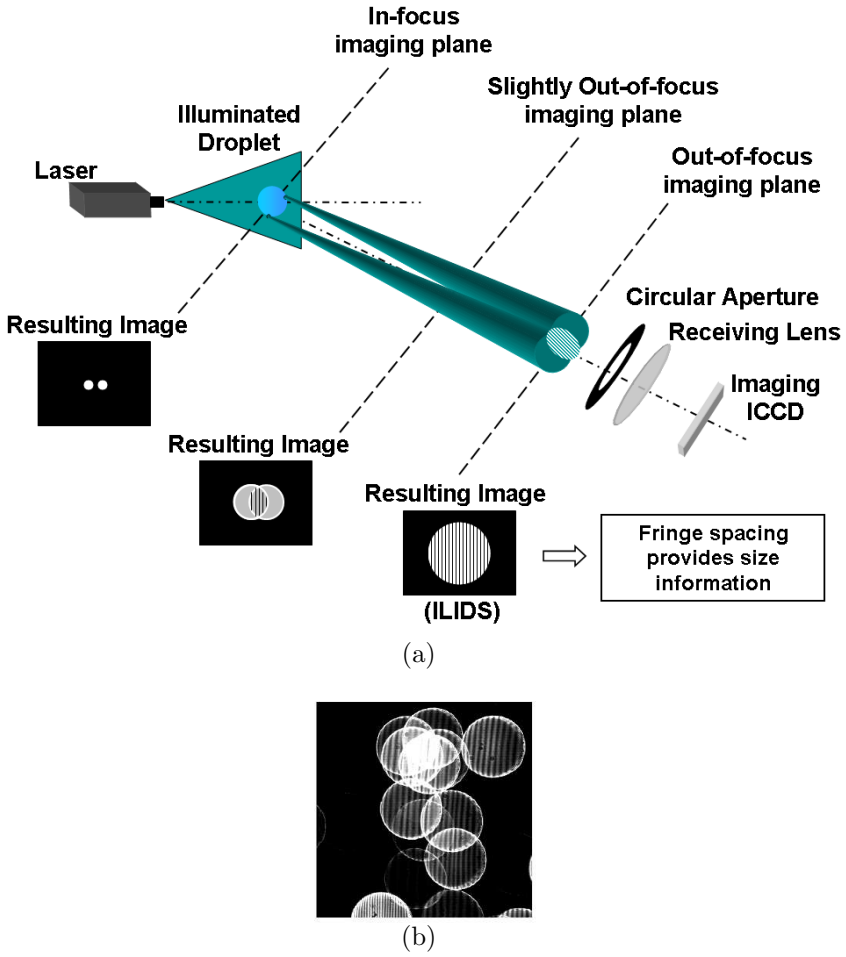


Figure 2.2: (a) Principle of the interferometric laser imaging technique (b) A typical ILIDS image using the conventional technique.

Figure 2.2(a) shows the basic optical arrangement of the interferometric sizing technique. When a transparent spherical droplet is illuminated by a coherent laser source, two glare points are observed on the focal image plane corresponding to

reflection and first order refraction. Given, the relative refractive index of the droplet (droplet to surrounding medium), m and the observation angle (scattering angle, θ), the droplet size can, in principle, be obtained from the separation between the glare points (van de Hulst and Wang, 1991). However, it is hard to determine the separation between the glare points, especially for small droplets, because of the lack of spatial resolution and necessity of magnification of the glare points. This approach provides no distinct advantage over direct imaging. Outside the focal plane, as the degree of defocus increases and spatial resolution of the optical system decreases, the reflection and refraction spots become larger and interference is observed in their overlapping region. The shape of the defocused image depends only on the shape of the aperture while the size of the defocused image depends on the degree of defocusing. For small droplets, this technique can image droplets over a large observation area with relatively low image resolution and, thus, overcome the limitations of direct imaging (Damaschke *et al.*, 2002). The remaining dislocation of the two defocused images can only be detected if the magnification and resolution of the CCD camera is high enough, but is generally disregarded.

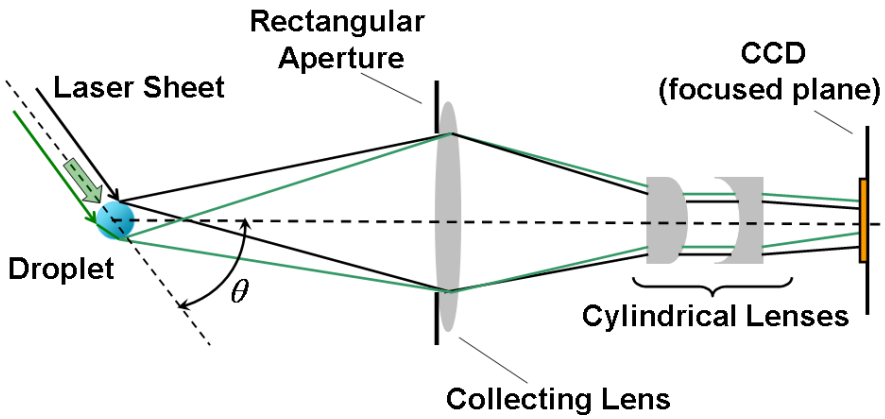
Considering the pair of scattered rays, external reflection, p_0, and first order refraction, p_1, under spatially homogeneous illumination, and using geometrical optics analysis, the relationship between the droplet diameter (D) and the number of fringes (N) can be derived (Golombok *et al.*, 1998) and is presented below,

$$D = N\left(\frac{2\lambda}{\alpha}\frac{1}{\cos(\theta/2) + \frac{m\sin(\theta/2)}{\sqrt{m^2-2m\cos(\theta/2)+1}}}\right) \tag{2.1}$$

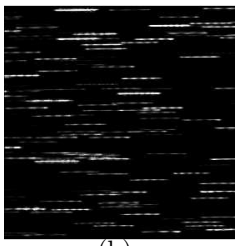
$$= N\kappa \tag{2.2}$$

where θ is the scattering angle or the angle of the observation and α is the collecting angle of the receiver equivalent to the angular inter fringe spacing ($\delta\theta$) multiplied with the fringe count (N). κ is the bracketed term and can be defined as the diameter per fringe. For given λ, θ, α and m, the value of κ remains constant and

so, the droplet diameter is proportional to the number of fringes. α is determined from the effective diameter of the objective lens and the object distance, *i.e* distance between the droplet and the objective lens. From Figure 2.1(a), for water droplets, the intensity ratio between the reflection and refraction is equal to 'one' around $\theta = 69°$ for perpendicularly polarized light. Thus, for maximum amplitude of the interference signal or better fringe visibility, this particular scattering angle is chosen.



(a)



(b)

Figure 2.3: (a) Schematic of the optical configuration of ILIDS including the optical compression unit introduced by Maeda *et al.*, 2000 (b) A typical compressed ILIDS image.

The conventional ILIDS technique, as described by Glover *et al.* (1995), often encounters serious problems of overlapping of circular interferrograms in high particle concentration regions. This can be well observed from the ILIDS image as shown in Figure 2.2(b). The difficulty arises because of the laborious image processing

required to correctly identify the fringe pattern from each droplet and extract the droplet properties. Thus, the application of the technique is restricted to very dilute regions in the spray. To overcome this limitation, Maeda *et al.* (2000, 2002) came up with a unique approach of introducing an optical compression unit in the receiving optics. Figure 2.3(a) illustrates the simplified optical configuration consisting of a rectangular aperture, circular objective lens, a pair of cylindrical lenses and a CCD camera (which is at the focused image plane). Figure 2.3(b) shows one of the ILIDS images captured with the modified technique. The circular fringe patterns are now compressed vertically, thus increasing the number of droplets being imaged without overlapping regions. The pair of cylindrical lenses, introduced between the objective and the CCD camera, serves two purposes simultaneously. First, to optically compress the circular fringe pattern *only* in the vertical direction and secondly, to generate the out-of-focus image on the focal plane. The roles of the rectangular aperture in front of the objective lens are to adjust the collecting angle and to enhance the depth of focus. The width of the rectangular slit is decided on the basis of the range of diameter to be measured, and, for its given value, the degree of defocus is regulated by adjusting the separation between the two cylindrical lenses. The larger the separation between the lenses, the greater the degree of defocus or the wider the width of the rectangular fringe patterns. When the separation is zero, the effect of the compression unit is virtually nullified, *i.e* the glare points are observed on the CCD camera. It should be noted that the droplet size (or the number of fringes) is independent of width of the fringe patterns and depends only on the angular fringe spacing ($\delta\theta$). Comparison of Figure 2.2(b) with Figure 2.3(b) demonstrates the following advantages of the method of Maeda *et al.* (2000)'s using the optical compression unit.

(a) The number of observed droplets drastically increases. As mentioned in Maeda *et al.* (2000, 2002), for the same viewing area, about 100 particles could be identified with the optical compression technique as compared to about 15 particles (at best) using the conventional approach. Though the effect of overlapping of rectangular fringe patterns still exists, it is significantly smaller and so, allows imaging denser regions of the spray.

(b) The technique improves the optical signal to noise ratio by vertically integrating the circular image with fringes.

(c) Distorted and/or irregular fringes can be easily validated automatically.

As a logical extension of the above technique, the droplet velocity can be obtained by using a double-pulsed laser source and performing droplet tracking between successive images. The velocity u_d of individual droplets are obtained by the displacement ΔS of the interferogram between two images with the time interval Δt, $u_d = \Delta S/\Delta t$. The displacement of the interferogram is estimated by finding the location of the 'peak' of the cross-correlation spectrum of the image, similar to PIV, and will be explained in the following section.

2.1.3 Image Processing

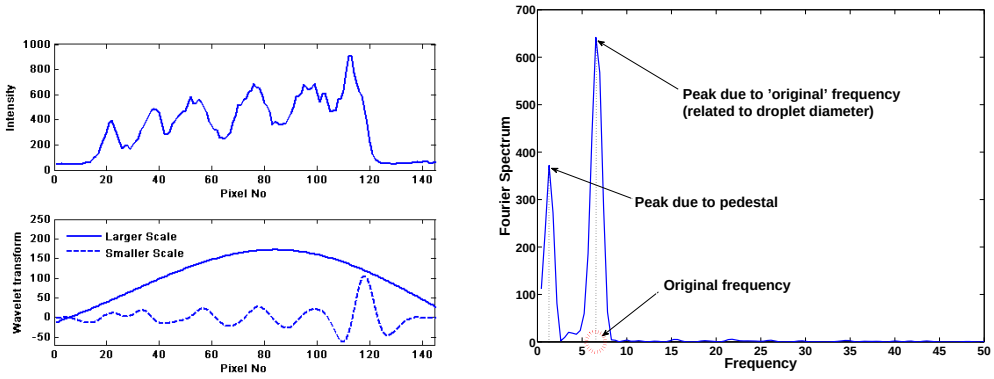
Image processing plays a significant role on the performance of the ILIDS technique. The task of extracting the information on the droplet size/velocity from the individual fringe patterns necessitates development of an automatic image processing software, which is often challenging. The challenge comes from the difficulty in accurately identifying the individual fringe patterns in the compressed ILIDS image. The width of each interferogram must be determined appropriately in order to avoid both aliasing errors caused by discrete sampling and overlapping with the neighbouring interferogram by an adjacent droplet (Maeda *et al.*, 2000). Also, multiple scattering, as a result of higher droplet density, often tend to lower the signal to noise ratio (SNR) making the fringe counting tedious. To determine the angular frequency of the interference fringes, and hence the droplet size, there are two approaches: to estimate the spatial frequency of the fringes and to simply count the number of fringes in the defocused image. However, the former approach is more robust at lower SNR and hence followed here. It should be mentioned here that, for the droplet velocity estimation through particle tracking, it is essential to locate the *image* of the centre of the droplet in the fringe pattern. But, since the image in ILIDS is always defocused, it is not possible to locate the 'actual' droplet centre in the fringe pattern. Hence

the geometric centre of the fringe pattern (mid-way between the beginning and end pixels) is assumed to be the image of the droplet centre.

The present work uses the algorithm based on Continuous Wavelet Transform (CWT), developed by Zarogoulidis (2011), for the droplet size and velocity estimation. Certain modifications were essential to the existing software to improve the accuracy in locating the droplet centre, estimating the length of the fringe patterns, and evaluating the droplet velocity. The CWT, unlike Fourier Transform (FT), is suitable for analysing non-stationary signals with high frequency components for short duration and low frequency component for longer duration. It provides good time/space resolution at higher frequency, *i.e.* it can suitably tell us, when or where the high frequency components exist. Since the intensity distribution of ILIDS images resembles closely such a signal, the CWT was chosen. The transformation is obtained as the convolution of the discrete signal with the scaled and translated version of the mother wavelet (Torrence and Compo, 1998). The peak values of the wavelet transform spectrum indicate the position in the image where the particular frequency (corresponding to the scale of the wavelet) exists. The droplet size was measured by applying the Fast Fourier Transform (FFT) along a horizontal line of the fringe pattern to identify the fringe spacing from the power spectrum. Particle tracking velocimetry between two images, obtained at consecutive times, quantified the droplet velocity from the corresponding droplet displacement. The details of the CWT and its use in the present algorithm can be found in Zarogoulidis (2011). A brief summary of the modified algorithm is presented here.

Algorithm

(i) Detection of the length of the fringe pattern is one of the crucial step in the ILIDS image processing since it directly influences the accuracy in drop size estimation and locating the droplet centre. For this purpose, the CWT was applied along each horizontal line of the image for two different scales of the mother wavelet or wavelet basis. The Mexican Hat wavelet was chosen for



(a) (b)

Figure 2.4: (a) top: Intensity variation for a fringe pattern in the ILIDS image of a droplet and bottom: its corresponding continuous wavelet transform spectrum at two different scales (b) Fourier spectrum of the fringe pattern.

this purpose due to its strong localization properties. Figure 2.4(a) shows the intensity profile of a fringe pattern and the corresponding wavelet transforms at different scales. The transformation at larger scale (approximately equal to the fringe pattern length) resulted in a wavelet transform spectrum with the maximum almost at the geometric centre of each fringe pattern, while the transformation at the smallest scale yielded maxima corresponding to each intensity modulation of the individual fringes.

(ii) The fringe pattern length was found by considering the approximate centre identified by the large scale transform and maxima yielded from the transformation at smaller scale and by using a suitable, but arbitrary, intensity threshold based on the mean intensity of the fringe. Thus, the 'droplet centre' is located at the geometrical centre of the fringe pattern.

(iii) The fringe frequency (N) is obtained by taking FFT of the signal (individual fringe pattern). A Hanning window was used to minimize the spectral leakage *i.e.* to suppress the high side-lobes in the FFT spectrum. The frequency corresponding to the 'highest peak' in the FFT spectrum is expected to provide the droplet diameter. However, as observed in Figure 2.4(a), each signal has two frequency components: one is the high frequency component related to the

droplet diameter and the other is the pedestal component related to the droplet location (Maeda *et al.*, 2000). Figure 2.4(b) shows the Fourier spectrum of the fringe pattern shown in Figure 2.4(a). It can be observed that the peak due to the pedestal remains dominant in the low frequency regime, which may cause bias in deciding the actual frequency when fewer number of fringes are present in the fringe pattern. Since fewer number of fringes corresponds to droplets with smaller sizes for a given optical setting, this "pedestal effect" sets up a constraint in the minimum measurable droplet diameter by ILIDS. Thus, a minimum threshold for the frequency needs to be chosen, and the frequency corresponding to the highest peak in the power spectrum is searched only above that limit. In the present case, the minimum threshold was decided on trial and error basis and chosen as '3'. Once the dominant frequency is determined, the droplet diameter can be obtained via Equation (2.2).

(iv) In order to ensure, detection of fringes instead of background noise, a threshold was chosen for the SNR of the fringe pattern (expressed using the logarithmic decibel scale). Only those droplets are detected, for which the corresponding SNR of the fringe pattern is higher than the threshold. The fringe patterns out of which the diameter were obtained are termed as 'detected droplets'.

(v) The next task is to determine the velocity of the 'detected droplets' from the defocused ILIDS image pairs captured at a definite time interval, Δt. Figure 2.5 schematically shows the method followed. At first, each of the images is processed to obtain the location and size of the droplets. To determine the droplet velocity, it is required to track the same droplets in both images. To accomplice this, for any given detected droplet in the first image, an 'interrogation window' is centred around the corresponding fringe pattern. In Figure 2.5, the detected fringe pattern is denoted as F_I with size D_i, as an example. Then, the algorithm looks for any droplets, if present, within the corresponding area in the second image, termed as 'search window'. In the present example, four fringe patterns F_{S1}, F_{S2}, F_{S3} and F_{S4} were found in the

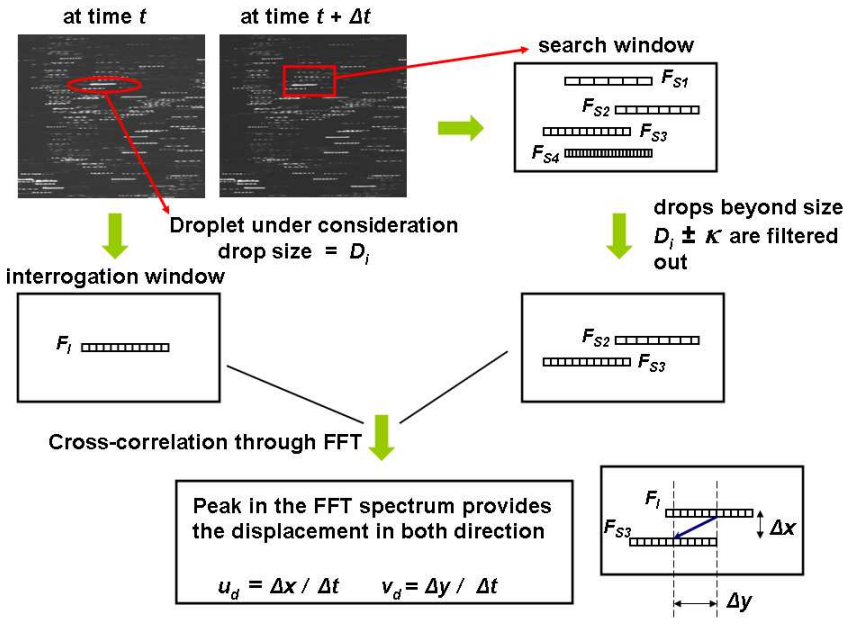


Figure 2.5: Demonstation of droplet velocity estimation in ILIDS processing

search window. Out of those droplets, the droplets with size equal to $D_i \pm \kappa$, are sorted out. Thus, the search window now contains the fringe patterns of the *validated* droplet/droplets (F_{S2} and F_{S3}), based on their diameter.

(vi) The droplet displacement is found by cross-correlating the interrogation window with the search window. Normally the correlation can be obtained either through direct computation or via FFT. However, both approaches have their own advantage and limitation. While the direct computation of the correlation is more accurate, the processing time is high. The FFT based computation is faster but less accurate. Thus, a modified algorithm was used (Ronneberger *et al.*, 1998) which relies on evaluating the correlation similar to the approach of the direct computation but through FFT. The new method is as accurate as the direct computation of the correlation, while being much faster and will be described in detail later in the section on 'image processing in PIV'. The 'peak' in the cross-correlation spectrum is accurately located by sub-pixel interpolation based on Gaussian curve fitting. The new algorithm was also found to reduce the 'peak-locking effect' in velocity estimation which

was otherwise significantly prominent in case of the FFT based computation of correlation. Because of peak locking (Raffel *et al.*, 1998), the signal peak location is biased towards the nearest pixel while using the curve-fit to locate the 'peak' with sub-pixel accuracy, eventually resulting in erroneous estimation of the turbulence fluctuations in velocity especially for smaller displacements.

Ideally, the peak in the correlation spectrum is expected to be situated closer to the centre of that fringe pattern in the search window for which maximum correlation was observed (in the present example shown in Figure 2.5, let's say it is F_{S3}). However, this may not always occur due to the inaccuracy in fringe pattern length detection. In order to ensure both (centre of the fringe pattern and correlation peak) are closer, a cut-off distance was chosen and, only those droplets are considered for which the distance between the peak and the centre of fringe pattern (termed as 'peak distance') is less than this threshold distance. Once the droplet satisfies this criterion, the droplet velocity is determined by the horizontal and vertical displacement of the peak from the centre of the interrogation window, as shown in Figure 2.5. The droplets in the first image for which the velocity could be obtained are termed as 'validated droplets'. Thus, out of the total number of droplets present in a given instantaneous ILIDS image, the 'detected droplets' have only the size information while the 'validated droplets' have both size and velocity. The ratio of the total number of detected to validated droplets is defined as *validation ratio*. In the present work the validation ratio for two phase measurements with the spray was of the order of 50%.

The cut-off threshold for the image intensity, minimum number of fringes, SNR and, peak distance are decided on the basis of the signal quality, which in turn depends on various factors such as the range of droplet size under consideration, the droplet number density and laser power. For instance, the SNR is usually high in the case of mono-sized droplet stream because of the absence of multiple scattering and so, a higher value of the SNR threshold can be chosen. However, for a poly-dispersed spray

it needs to be lowered. Zarogoulidis (2011) provides the details about the selection of the cut-off thresholds.

2.1.4 Important notes for the application of ILIDS

There are few important issues in ILIDS which needs to be discussed. These are explained below.

1. A small viewing area (of the order of $10 \times 10\ mm^2$) is always preferred in ILIDS operation. For a specific objective lens, a larger viewing area results in lower magnification or larger object distance. This results in lower collecting angle, α. From Equation (2.1), this implies higher value of diameter per fringe, κ which in turn results in increasing the lower limit of droplet size that can be measured. Thus, the compromise is between the smallest measurable diameter and the field of view. Though, α can be increased by using an objective lens with larger diameter, its cost, availability and physical constraints in the experimental set-up often prohibit this option. In addition, with a smaller viewing area, any distortion of the fringe patterns due to lens aberration (especially towards the boundary of the image) can be avoided.

2. In order to map the position and velocity of the droplets from the image plane (CCD array) to the plane of the laser sheet (real position in space), the camera needs to be calibrated using a calibration plate having some predefined 'marks' positioned at specific distances. Ideally, the calibration should be performed under the defocus setting of the camera. However, there are two limitations in this approach. First, this makes the detection of the 'defocused marks' difficult. Second, this necessitates the degree of defocus (or separation between the cylindrical lenses) to be known beforehand. Thus, in the present work, the camera calibration was done under the 'focused' condition. This permits changing the degree of defocus, as required, during the experiment. The change in the viewing area while performing the defocusing is inherently assumed to be negligible.

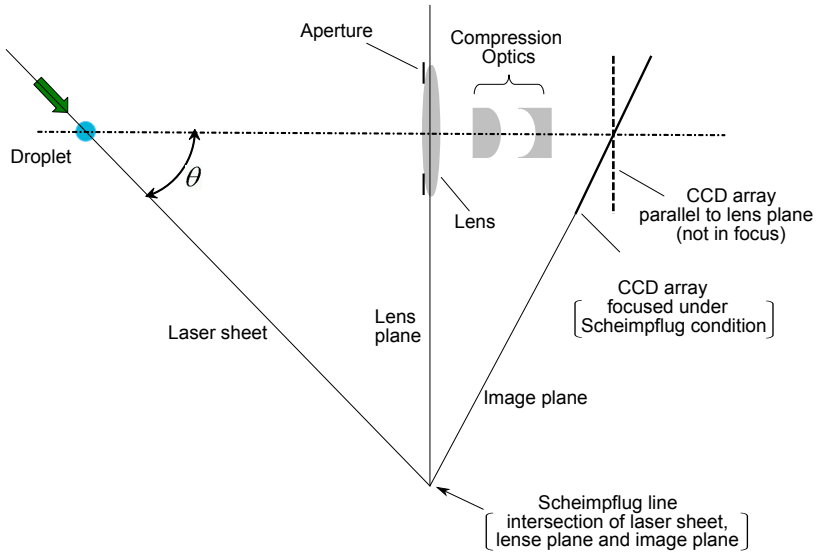


Figure 2.6: Location of the image plane with Scheimpflug condition.

3. It can be observed from Figure 2.3(a) that the field of view is not parallel to the CCD array of the camera due to the requirement of imaging at the scattering angle θ, which is different than 90°. This results in varying degree of defocus across the image plane. The length of the fringe patterns, being proportional to the degree of defocus, also varies. So, Scheimpflug condition (Prasad and Jensen, 1995) was introduced, as depicted in Figure 2.6. In such case, the CCD array, initially parallel to the lens plane (shown as dotted line), was tilted such that the object plane, the principal plane of the lens and the image plane, all intersected at a common line. Hence, the same degree of defocus (or in turn fringe pattern length) could be retained in the image plane. Though the Scheimpflug condition is not essential for ILIDS, its use is certainly advantageous. The uniform length of the droplet fringe patterns makes the length detection (using CWT) more convenient, which is a crucial step in the image processing of ILIDS images. As a consequence of the Scheimpflug condition, the magnification varies across the image plane. However, because of relatively smaller viewing area, the change is always negligible.

4. It is essential to realize the limits of the measurable droplet size range of ILIDS for a given optical configuration. The lower limit of droplet size is determined

by three criteria. The first one is the limit of applicability of the geometrical optics (*i.e.* intersection of reflected and the first order refracted rays only in the forward scattering region). This is possible only when the size parameter, $\pi D/\lambda > 5$. Considering λ=532 nm, this sets up the lower limit of droplet size to approximately $0.85\mu m$. The second criterion is the adequate collecting angle (α) to allow collecting sufficient number of fringes to measure the droplet size. Since the droplet should display at least two fringes, the smallest measurable particle is equal to $2 \times \kappa$ through Equation (2.2). In the present work the maximum value of κ (diameter per fringe) was about $7\mu m$ (for the lowest value of α), which leads to the minimum droplet size to about $14\mu m$. The third and the most important criteria originates from the existence of the pedestal in the FFT spectrum of the fringe pattern (see Figure 2.4(b)), as mentioned before. Though the first two criteria have been mentioned before in the literature, the third criterion adds a higher size limit, which has gone unnoticed. The pedestal appearing in the fringe pattern results in an 'extra' peak in the FFT power spectrum in the lower frequency regime. For unbiased estimation of the dominant frequency, a threshold for the minimum number of fringes needs to be chosen. Since in the present case, it is equal to 3: the minimum measurable diameter, D_{min} was equivalent to $3 \times \kappa \approx 20\mu m$.

5. The maximum measurable diameter depends on the use of FFT for determination of the fringe frequency. According to Nyquist criterion, the sampling frequency should be at least twice that of the fringe frequency. Since at least two pixels are required to represent one fringe, thus minimum four pixels are necessary to resolve one fringe through FFT. Hence, the maximum number of fringes in a fringe pattern is given by $N_{max} = L/4$, where L is the length of the fringe pattern in pixels. In the present work, $L \approx 180$ *pixels* and $\kappa_{max} \approx 7$, which leads to $N_{max} \approx 45 \implies D_{max} \approx 315\mu m$. The length of the fringe pattern (L) is proportional to the degree of defocus. A higher degree of defocus leads to larger L, thus increasing the upper limit of measurable diameter

(D_{max}), but it simultaneously increases the fringe overlapping probability. On the other hand, for smaller L, the image is not a true far-field image, and so, the overlapping area of the light from the glare points reduces leading to undesirable fringe pattern (the sharp pedestal becomes smooth at the edges and the fringes exhibit distortion causing bias in detection of the dominant fringe frequency). Hence a compromise needs to be struck. Thus, with the present optical set-up for ILIDS, the measurable droplet diameter range was between $20\mu m$ and $300\mu m$. A further consideration is the thickness of the laser sheet itself. Droplets with size, larger than the thickness of the laser sheet can not be measured. In the current set-up the thickness of the laser sheet was about 1 mm, which is larger than the maximum droplet size of 300 μm.

2.2 Particle Image Velocimetry (PIV)

Particle Image Velocimetry, popularly known as PIV, retains a special status in Fluid Mechanics because of its ability to make global velocity measurements. PIV can provide instantaneous velocity measurements over global ($2D$ or $3D$) domains with high accuracy and can be considered as a logical extension—from qualitative to quantitative—of the classical flow-visualization techniques that have been practised for decades. The basic idea of PIV is imaging the displacement of tracer particles at two instances in time and the subsequent processing of these images into fluid velocities. More background and a large number of applications can be found in the references by Raffel *et al.* (1998), Prasad (2000) and Westerweel (1997). Since the principle of the technique has already been described by many authors in the past, only a brief overview will be presented here. Particular emphasis will be given on the image processing algorithm used in this work for the measurements of both phases in sprays.

PIV requires four basic components (as shown in Figure 2.7) which includes:

1. A light source (laser) to illuminate the region of interest. Lasers are capable of emitting monochromatic light with a high intensity, so that any chromatic

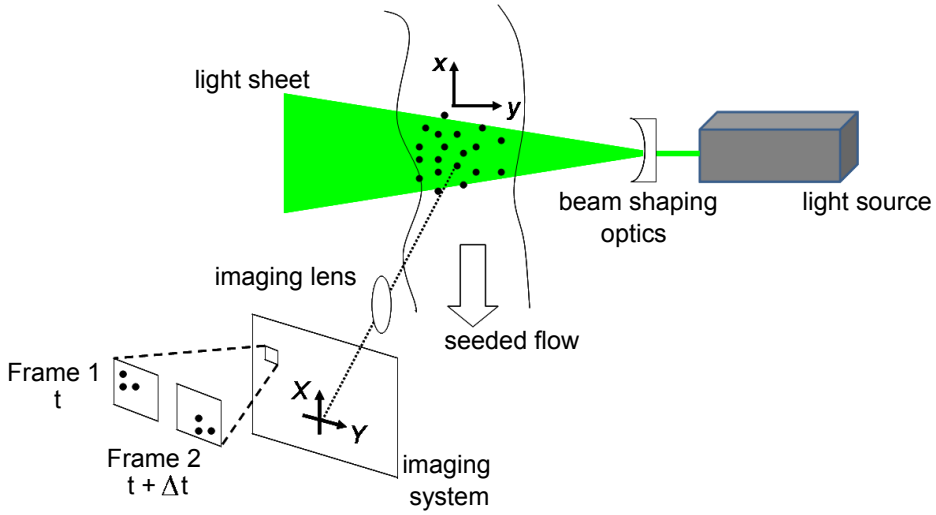


Figure 2.7: Schematic of the Particle Image Velocimetry technique.

aberrations in the imaging are avoided (Raffel *et al.*, 1998). Since most PIV systems record a pair of images (Frames 1 and 2 in Figure 2.7) with a very short interval time (Δt), "double pulsed" lasers are used. The laser beam is transformed in to a thin light sheet which serves as the measurement volume.

2. An optically transparent test-section containing the flow seeded with tracer particles. The tracer particles should have a response time that is very small compared to the time scales of the fluid motion so that those can follow the smallest fluid fluctuations of velocity. On the other hand, they should be large enough to scatter a sufficient amount of laser light.

3. Recording hardware consisting of a CCD camera to image the flow. Since the interval time between the images should be relatively small (at maximum a few milliseconds), this would require a camera with high frame rate. Suitable lenses (with adjustable aperture) are used to collect the scattered light from the seeding particles.

4. Suitable computer software to process the recorded images and extract the velocity information from the tracer particle positions. The two successive images are correlated to extract the velocity data. The computer system also acts as 'master' system, sending electronic trigger signals to all the components.

It serves as a way to control the laser and camera settings (exposure times, laser power, repetition rate etc.).

2.2.1 Image Processing

The translation of image data into fluid velocity estimation can be done using several methods, though, is broadly classified in two categories, namely particle tracking velocimetry (PTV) and correlation based PIV.

In case of PTV, the particles are detected individually in each of the frames and a matching algorithm identifies corresponding particles in both images. The local fluid velocity is calculated from the displacement of each particle. Usually, this method is used in low image density images, since otherwise the matching becomes impossible. The implication is that the data density is somewhat lower. Difficulties arise due to overlapping or fragmented particle images, or if the second image of an image-pair is lost when the particle exits the light sheet between exposures due to out-of-plane motion. While PTV has the advantage of not being affected by the "averaging effects" similar to correlation based PIV, the drawback is that the velocity vectors are located randomly in the region of interest, as it is impossible to control particle positions in the flow field. Consequently, it is necessary to resort to interpolation to obtain vectors on a uniform grid in order to calculate vorticity and other such information.

In contrast to PTV, the correlation-based PIV determines the average motion of small groups of particles contained within small regions known as interrogation windows (shown in Figure 2.8). The overall frame (Frame 1) is divided into regular interrogation windows, and the correlation function is computed by cross-correlating each interrogation window with a "search window" defined in Frame 2 captured after time Δt. This is done sequentially over all windows providing one displacement vector per window. Typically, interrogation windows are rectangular/square shaped and therefore, the velocity map obtained from PIV presents vectors arranged on a uniform grid. More importantly, the process of averaging over multiple particle pairs within an interrogation window makes the technique remarkably noise-tolerant and robust in comparison to PTV. The determination of the average particle displacement

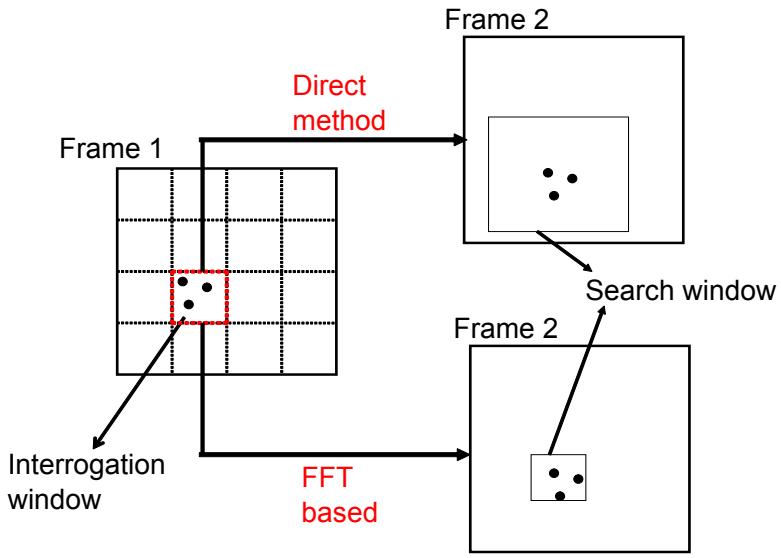


Figure 2.8: Correlation based PIV and the two approaches for evaluating the correlation.

is accomplished by computing the spatial cross-correlation of the particle images.

The estimate of the cross correlation is the central point of the PIV image processing. Two approaches have been reported in the literature for this purpose (a) Discrete cross-correlation and (b) FFT based cross-correlation. Both are schematically depicted in Figure 2.8. In the former case, the correlation is obtained by searching for the best match between the interrogation window and various parts of the search window (the size of which is larger than the interrogation window). Denoting the pixel intensity values of the two windows as 'I_1' and 'I_2', the correlation coefficient can be written as:

$$R_{x,y} = \frac{\sum_{i,j}(I_1(i,j) - \bar{\mu_1}) \cdot (I_2(i+x, j+y) - \bar{\mu_2})}{\sum_{i,j}(I_1(i,j) - \bar{\mu_1})^2 \cdot \sum_{i,j}(I_2(i+x, j+y) - \bar{\mu_2})^2} \tag{2.3}$$

where $\bar{\mu_1}$ and $\bar{\mu_2}$ are the mean intensities of the interrogation window and the section of the search window which is being correlated, and the denominator represents the respective rms values. However, a direct computation of the correlation by evaluating Equation (2.3) is prohibitively expensive. This is because of the quadratic increase in multiplications with sample size, which imposes a substantial computational effort (Raffel *et al.*, 1998). The alternative to calculating the direct correlation is to take the advantage of Fourier transform, which reduces the tedious processing time of

Equation (2.3) by computing two two-dimensional fast Fourier Transforms (FFT) on equal sized samples of the image followed by a complex conjugate multiplication of the resulting Fourier coefficients. These are then inversely Fourier transformed to produce the actual cross correlation plane of the same spatial dimensions as the two input samples. Thus, the correlation coefficient becomes

$$R = \frac{FFT^{-1}(FFT(I_1 - \bar{\mu_1}) \cdot FFT(I_2 - \bar{\mu_2})^*)}{\sum(I_1 - \bar{\mu_1})^2 \cdot \sum(I_2 - \bar{\mu_2})^2} \tag{2.4}$$

where the superscript '*' denotes the complex conjugate. However, there are two effects which limit the accuracy of the FFT based correlation calculation. The first one is the constraint of fixed sample size, *i.e.* the size of the interrogation and search windows needs to be same and also, should have a base-2 dimension (16×16, 32×32, 64×64 etc.). Since the search window (in Frame 2) is taken at the same position as the interrogation window (in Frame 1), all of the particle images of the shifted particle pattern could not be captured resulting in "in plane loss of pairs". The second reason is the inherent assumption of periodicity of the data while applying the Fourier transform. In FFT, the integrals are computed over finite domains which is justified by assuming the data to be periodic. This means that the image sample continuously repeats itself in all directions and the pixels leaving the image during the shift are wrapped around. Another important aspect to be considered while using FFT is the presence of aliasing. However, the aliasing effect was not present in the present applications since the maximum spatial frequencies of the images were lower than the Nyquist frequency (in other words since the seeding particles occupied more than two pixels in the PIV image, any undersampling was avoided).

Thus, following either of the above methods for estimation of the cross-correlation leads to a compromise between processing time and accuracy. The optimal accuracy is reached only when a larger size of the search window is used within which the best match of the interrogation area is searched for. This requires evaluating Equation (2.3). In order to overcome the limitation of enormous computational effort required by discrete correlation approach, Ronneberger *et al.* (1998) recommended evaluating

the same equation with some simple mathematical transform using FFT. Following their approach, the numerator of Equation (2.3) can be written as:

$$r_{x,y} = \sum_{i,j} I_1(i,j) \cdot I_2(i+x, j+y) - \frac{1}{N^2} \sum_{i,j} I_1(i,j) \sum_{i,j} I_2(i+x, j+y) \tag{2.5}$$

where N^2 is the number of pixels in the interrogation window. The denominator is treated in the same way as before. To use the FFT, we have to pad zeros around partial image I_1 to enlarge it to a 'power of 2' size. This has the additional advantage of removing the square shape of the window. This cutting and padding can be taken into account by multiplying with a mask 'm', so that Equation (2.5) becomes:

$$r_{x,y} = \sum_{i=1}^{N} \sum_{j=1}^{N} m_{i,j} I_1(i,j) \cdot I_2(i+x, j+y) - \frac{1}{\sum_{ij} m} \sum_{i=1}^{N} \sum_{j=1}^{N} m_{i,j} I_1(i,j) \sum_{i=1}^{N} \sum_{j=1}^{N} m_{i,j} I_2(i+x, j+y) \tag{2.6}$$

With normalized mask $\sum_{ij} m = 1$, the above equation can be rewritten as:

$$r = FFT^{-1}\left(FFT^*(mI_1) \cdot FFT(I_2)\right) - \sum mI_1 \cdot FFT^{-1}\left(FFT^*(m) \cdot FFT(I_2)\right) \tag{2.7}$$

where mI_1 denotes the element by element multiplication of two images: $(mI_1)_{ij} = m_{ij} \cdot I_{1_{ij}}$. With the definition of a cross correlation operator $\otimes$ as

$$a \otimes b = FFT^{-1}\left(FFT^*(a) \cdot FFT(b)\right) \tag{2.8}$$

Now the correlation coefficient can be written as:

$$R = \frac{mI_1 \otimes I_2 - \sum mI_1 \cdot m \otimes I_2}{\sqrt{\left(\sum mI_1^2 - \left(\sum mI_1\right)^2\right) \cdot \left(m \otimes I_2^2 - (m \otimes I_2)^2\right)}} \tag{2.9}$$

In the standard cross correlation one has to compute three Fourier transforms. The FFT-based free shape correlation needs six Fourier transforms (the Fourier transform of the mask can be calculated once before the whole evaluation). So

the computing time can be expected to be only twice compared to the traditional evaluation. That is much faster than doing a direct correlation with the additional advantage of flexibility in the shape of the window. The present work uses this modified correlation estimation method using FFT, which would be still considerably faster than the direct correlation method, while retaining nearly the same accuracy in velocity estimation. In order to locate the highest peak in the correlation plane, sub-pixel interpolation was performed using Gaussian fit in both direction (Raffel *et al.*, 1998).

Application to simulated PIV images

In order to evaluate its accuracy and advantages with respect to the direct and FFT based computations of the cross-correlation, the modified correlation algorithm is applied to the simulated PIV images created by Okamoto *et al.* (2000). Based on Large Eddy Simulation (LES) calculations of a transient jet shear flow, these authors created PIV images of the flow using Monte Carlo simulation to generate random particles which followed the fluid. They produced many series of seeding particle images of the calculations based on number of particles and particle size. The present algorithm is tested against the series named "301" which has the following characteristics as mentioned below:

Number of Particles per Image: 4000
Maximum Particle Displacement: 10 Pixel/Interval
Particle Diameter: About 5 pixel
Number of Images: 145

The vertical and horizontal directions are denoted as x and y respectively. The standard images had a 8 bit grey scale and a resolution of 256×256 $pixels^2$. The simulated images were processed using all the three algorithms described before, namely direct estimation, FFT based estimation and modified direct estimation using FFT. Since the maximum instantaneous displacement was of the order of 10 pixels,

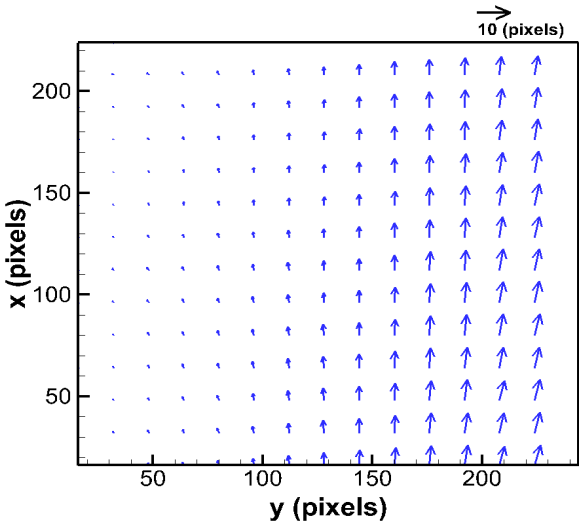


Figure 2.9: Mean velocity plot of the flow field corresponding to the Okamoto *et al.* (2000)'s images processed using the modified direct method using FFT.

Algorithm	% Error in mean in x-dir	% Error in mean in y-dir	% Error in rms in x-dir	% Error in rms in y-dir
$Direct$	1.87	11.20	6.05	1.85
$FFTbased$	6.04	25.53	32.13	11.42
$Modified\ direct$	1.87	11.20	6.05	1.85

Table 2.1: Error in mean velocity and rms velocity for both velocity components for the three PIV algorithms with respect to the LES calculations. The error is spatially averaged over the viewing area. The interrogation window size was $32 \times 32\ pixel^2$.

the interrogation window size was chosen to be 32×32 $pixel^2$ for all the three cases. Figure 2.9 shows the mean flow field which indicates larger vertical component of velocity as compared to the horizontal component. The modified algorithm resulted in almost the same velocity field as the direct correlation for the interrogation window size considered here. The average error in mean and standard deviations of the instantaneous vertical velocities (averaged over all the velocity locations) with respect to the LES calculations are compared for the three algorithms in Table 2.1. As can be noted, large error resulted with the conventional FFT based algorithm in both x and y directions. The error in the mean and standard deviation of the velocity obtained by the direct method was the same as that of the modified algorithm in both directions. Compared to the FFT based approach, for the other two algorithms, the error in mean was reduced by about 3 and 5 times in x and y directions respectively and, this indicates significant increase in accuracy. Smaller displacement in the horizontal direction resulted in higher error. As far as processing time per image is concerned, the modified algorithm was about 5 times faster than the direct method and 3 times slower than the conventional FFT based method.

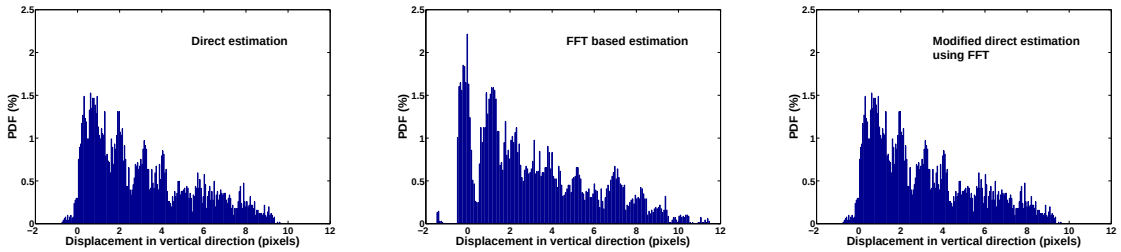


Figure 2.10: Probability density functions of PIV displacement data in vertical direction obtained by processing the full sequence of the Okamoto images using various algorithms for computing the cross-correlation: (a) Direct estimation, (b) FFT based estimation and (c) Modified direct method using FFT.

Another advantage of the modified algorithm was observed in terms of reduction in the bias errors in velocity estimation resulting from a phenomenon called "pixel-locking" or "peak locking" (Raffel *et al.*, 1998). Because of peak locking, the signal peak location is biased towards the nearest pixel while using the curve-fit to locate the discretized signal with sub-pixel accuracy. Peak-locking becomes more prominent

when the particle image size decreases below 2 pixels and, it also depends on the curve-fitting used for sub-pixel interpolation, the employed cross-correlation algorithm was also found to be an influencing factor. Figure 2.10 shows the probability density functions of the displacement data in vertical direction obtained from all the sequence of the images by using the three methods of evaluating the cross-correlation. For the FFT based approach, the displacements can be observed to be locked towards the integer values, which would result in erroneous estimation of the turbulence fluctuations in velocity, especially for smaller displacements. This effect was found to be considerably reduced with the modified algorithm.

PIV for two phase measurements

Application of PIV in two phase flows has always been a challenge. This is because the corresponding PIV image contains the images of both dispersed and continuous phases. The PIV processing aims in obtaining the velocity distribution of the continuous phase, which is seeded with micron sized particles following the fluid. However, it is essential to eliminate the contributions from the dispersed phase (droplets or particles), which would otherwise create bias in the fluid velocity estimation which is also known as "$cross - talk$" between the two phases.

In the present work, the aim is to obtain simultaneous measurement of velocity of both droplets and the surrounding gas in a spray. As will be discussed in the next section, this is achieved by seeding the gas with micron sized particles and imaging the flow field through the combined ILIDS and PIV technique. While ILIDS intends to obtain the droplet velocity, PIV is employed for the gas velocity estimation. However, since both phases are imaged, the PIV images contain individual images of both droplets and seeding particles. There are two difficulties to be dealt with. The first one is to discriminate images of droplets from those of seeding particles and, second, to process those PIV images, which are now devoid of eliminated images of the droplets. The method of detecting the droplets in the PIV image and subsequent filtering from the images will be elaborated in detail in the next section. Because of the droplet removal, the intensity values of the pixels occupying the droplet position

are now zero. Thus, the images have discontinuities in the intensity distribution which is far from ideal.

As verified before, the modified direct correlation algorithm using FFT is optimum in the sense of both processing time and accuracy. However, direct application of the algorithm to the droplet filtered PIV images may result in erroneous estimation of the fluid velocity. This is because the effect of the areas in the image where the pixel intensity is already zero would also contribute to the correlation calculation. In order to deal with such problems, the present work intends to adopt an approach similar to Gui *et al.* (2003), who described an application of the "digital mask technique" for a phase-separated evaluation of PIV recordings of two-phase flow based on FFT approach. The digital mask technique will be applied in conjunction with the modified PIV algorithm described before. The essence of the masking technique lies in the fact that *only* the pixels with non-zero intensity values are considered for evaluation of the correlation coefficient (or to be more precise, the mean and standard deviation values required at each point in the correlation plane).

The image area of the droplet filtered PIV recording can be divided into two regions: region D covering the images of the droplet phase and region G containing the seeding particle images to be processed. In order to separate the information of the two regions a mask $\Delta(i,\, j)$ is defined such that,

$$\Delta(i,j) = \begin{cases} 0 & \text{if pixel } (i,\, j) \text{ belongs to region } D \\ 1 & \text{if pixel } (i,\, j) \text{ belongs to region } G \end{cases} \tag{2.10}$$

Mask function $\Delta(i,\, j)$ can be considered as a binary image. Since the position of the same droplets may vary between the two images in a pair of PIV recording, the mask function is separately defined for each one of the PIV images and will be denoted as Δ_1 and Δ_2 respectively. Now the numerator of Equation (2.3), which represents the coefficient discrete cross correlation can be written as,

$$r_{x,y} = \sum_{i=1}^{N}\sum_{j=1}^{N}(\Delta_1 I_1)\cdot(\Delta_2 I_2) - \frac{1}{\sum_{ij}(\Delta_1\Delta_2)}\sum_{i=1}^{N}\sum_{j=1}^{N}(\Delta_1 I_1)\sum_{i=1}^{N}\sum_{j=1}^{N}(\Delta_2 I_2) \tag{2.11}$$

where the operation (ab) denotes the element by element multiplication of a and b *i.e.* ab=$(a_{ij} \cdot b_{ij})$.

Following Equation (2.9), the above equation can be evaluated using FFT and the correlation coefficient can be written as:

$$R = \frac{(\Delta_1 I_1) \otimes (\Delta_2 I_2) - \sum(\Delta_1 I_1) \cdot \Delta_1 \otimes (\Delta_2 I_2)}{\sqrt{\left(\sum(\Delta_1 I_1^2) - (\sum(\Delta_1 I_1))^2\right) \cdot \left(\Delta_1 \otimes (\Delta_2 I_2)^2 - (\Delta_1 \otimes (\Delta_2 I_2))^2\right)}} \tag{2.12}$$

where the operator $\otimes$ denotes $a \otimes b = FFT^{-1}(FFT^*(a) \cdot FFT(b)$.

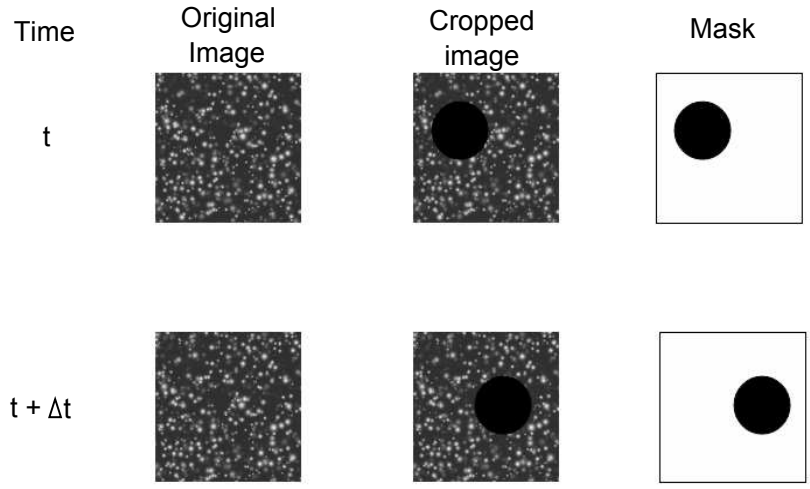


Figure 2.11: A pair of simulated PIV images: Original, Cropped and the corresponding Mask.

In order to simulate the droplet filtered PIV images in the two phase measurements in the spray, the above algorithm was validated against the simulated PIV images of Okamoto *et al.* (2000) (as mentioned before) with certain areas randomly cropped off. This means that the values of the pixel intensity at those regions were made equal to zero. Each of the cropped areas were circular in order to replicate the droplet removal. The diameter of the removed circular areas and their positions were decided based on a random function. However, the positions of the cropped areas in the second pair of the PIV image were kept at a definite distance with respect to the first image. Figure 2.11 shows an example of a pair of PIV images, the same images after a circular area was cropped off and the corresponding masks.

The whole sequence of the PIV images were processed in this way both with

and without consideration of the masking technique corresponding to Equation (2.9) and (2.12), respectively. Subsequently, the mean and standard deviations of the instantaneous velocities were obtained. The interrogation window size was same as before *i.e.* 32×32 $pixel^2$. The number of removed circular areas were 20 with their diameter ranging in between 16 to 32 $pixels$ which was about 12% of the total area. Two test cases are reported. The first one having the cropped positions same in both images and in the second one a shift of 6 pixels were introduced for any given cropped part between the pair of PIV images. This was done in order to verify the influence of this crop shift on accuracy.

Algorithm	crop shift ($pixels$)	% Error in mean in x-dir	% Error in rms in y-dir	% Error in mean in x-dir	% Error in rms in y-dir
$Modified\ direct$	0	4.57	19.44	10.39	3.52
$Modified\ direct + Mask$	0	2.85	13.26	5.99	2.86
$Modified\ direct$	6	4.89	152.29	38.60	29.97
$Modified\ direct\ +Masking$	6	3.14	42.69	26.90	15.81

Table 2.2: Error in mean velocity and rms velocity for both velocity components with respect to the LES calculations for the 12% cropped simulated PIV images for the modified PIV algorithm both with and without consideration of the masking technique. The error is spatially averaged over the viewing area. The interrogation window size was 32 × 32 $pixel^2$.

Table 2.2 shows the corresponding errors in the mean and standard deviation of the vertical component of velocity with respect to the LES calculations. Comparison of the results indicates that using the masking technique along with the PIV algorithm results in higher accuracy. Again, the higher relative error in y direction is due to the smaller magnitude of displacement in that direction. The crop shift between the removed circular areas (6 pixels in this case) resulted in increasing the error especially in the rms velocity though not significantly. Comparing Table 2.2 and Table 2.1 (with no cropping), an order of magnitude increase in the error can be observed for the given percentage of cropping (12%) in the simulated PIV images. Also, the error was found

to be higher when the crop diameter exceeded the interrogation window size. This has the important implication that the size of the interrogation window should be judiciously decided while processing the droplet filtered PIV images in case of the two phase experiments, and this determines the spatial resolution of the velocity vectors.

2.3 Combining ILIDS with PIV

Although the application of either ILIDS or PIV is not new, their combination offers a unique way for simultaneous and planar (or whole field) characterization of both phases in a spray. The combined technique utilizes ILIDS for measurement of size and velocity of individual droplets in a two-dimensional area and PIV for gas phase velocity measurement surrounding each droplet. Apart from the above, the ILIDS and PIV techniques provide the instantaneous droplet concentration (*i.e. droplet number/mm*^{3}).

2.3.1 Principle

The fundamental principle of ILIDS for droplet size/velocity measurement was explained before by considering geometrical optics. A similar approach is followed here for the combined technique. For the purpose of simultaneously characterizing the velocity of the air flow in the proximity of individual droplets, the air surrounding the spray is seeded with micron-sized particles and the viewing area is imaged for PIV measurements. The basic principle behind the technique lies in the fact that the position of droplets in a spray, obtained by ILIDS beforehand, helps to identify the images of the same droplets in the focused PIV image. This makes it possible to assign the droplet properties to the glare points of the focused droplet images, and thus correlate the droplet size and velocity with the velocity of gas flow.

Figure 2.12 shows the flow field, consisting of a water droplet surrounded with seeding particles, illuminated by a coherent laser source. Both droplet and seeding particles scatter light at all directions. However, as mentioned before, the reflected and first order refracted light from the droplet dominate in the forward scatter region,

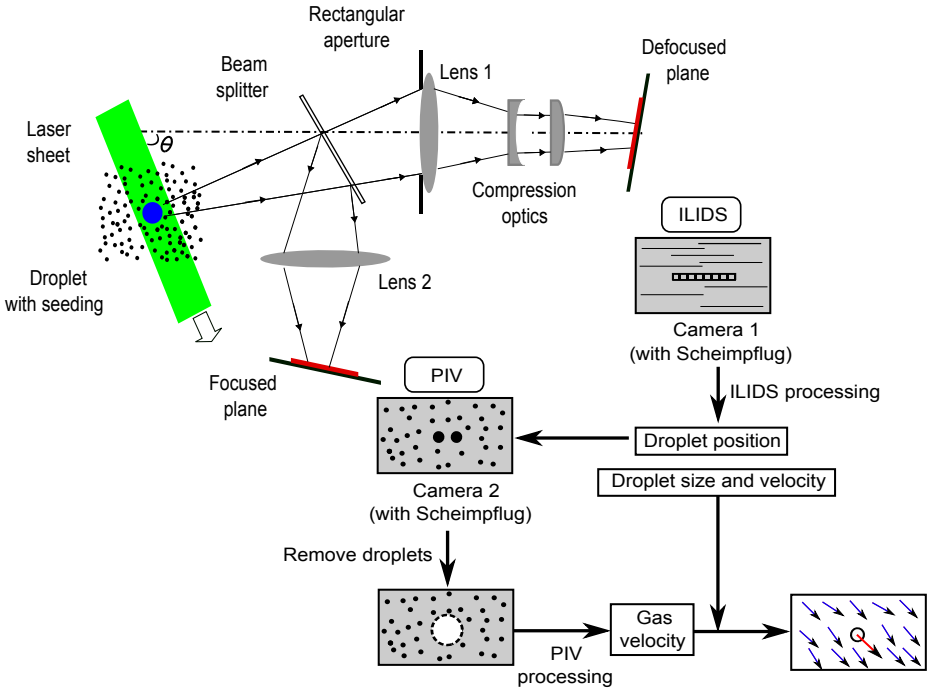


Figure 2.12: Principle of the combined ILIDS and PIV technique.

which interfere on a defocused plane to produce parallel fringes. The characteristic interferogram is observed at the defocused plane with a far field arrangement of receiving optics through camera 1 (Figure 2.12). The defocusing is achieved and controlled by using a pair of cylindrical lenses placed in between the collecting lens (lens 1) and camera 1. For simultaneous PIV operation, part of the incoming scattered light is split using a beam splitter and collected through a second camera, camera 2 as shown in Figure 2.12. With this optical system, bright spots called glare points, corresponding to focused reflected and refracted rays, appear in camera 2 along with the seeding. Hence, the same droplet is imaged as a rectangular region with a superimposed fringe pattern on the defocused (ILIDS) image and as distribution of two glare points on the focused (PIV) image. The defocused seeding particles also appear in the ILIDS image, but without producing any superimposed fringes. This is because, micron-sized solid and non-transparent particles are chosen to seed the air instead of liquid droplets, which may result in their own fringe pattern. From Figure 2.12 it can be observed that both cameras are aligned under the Scheimpflug condition. As mentioned before, this results in uniform length of the fringe patterns

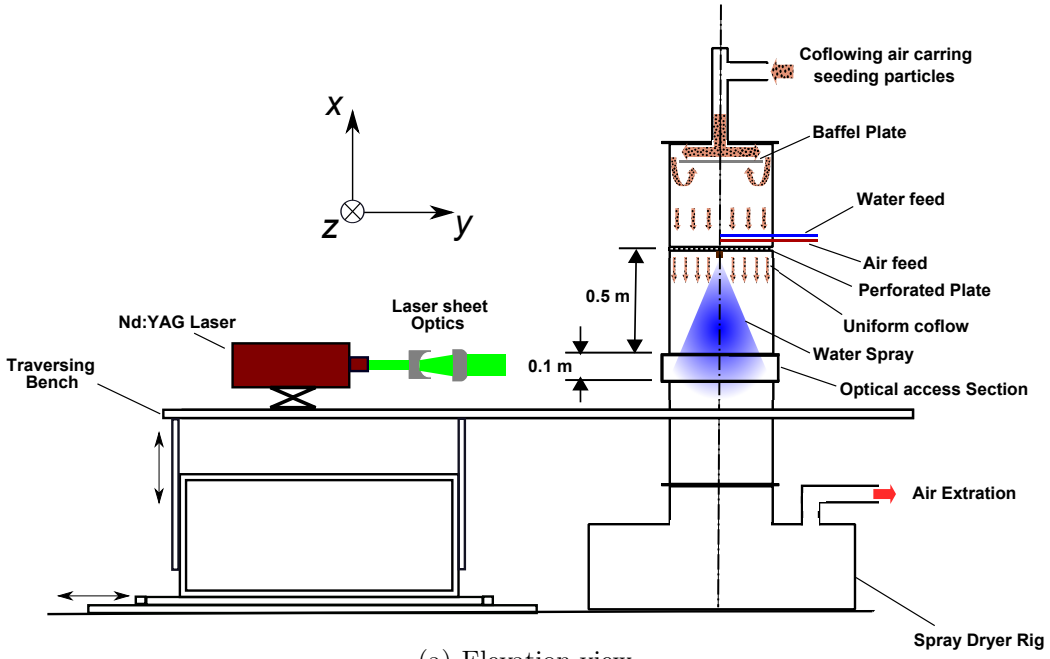
in the ILIDS image. Though the use of the Scheimpflug condition is not critical for ILIDS, it is essential for PIV, since the image plane has to be under in-focus condition.

It is important to note that a droplet on the ILIDS and PIV images is identified by the position of the centre of fringe pattern and glare points respectively. So, locating the droplet centre plays a vital role in identifying the same droplet in both images. In case of either of the techniques, the geometric centre of the droplet image (fringe pattern in ILIDS or glare points in PIV) is assumed to be the centre of the droplet. However, a closer observation at Figure 2.1(b) reveals that the glare points due to the reflected and refracted rays may not be symmetrically located about the droplet centre. Hence the geometric centre need not be the same as the actual droplet centre. A discussion on the validity of this assumption will appear later in this chapter. Once the droplet centre of the fringe pattern is located in the ILIDS image, the corresponding glare points in the PIV image can be tracked and the droplet size/velocity (obtained from ILIDS) is assigned to it. Then the glare points are filtered out to retain only the seeding particles in the PIV image (Figure 2.12) which can be subsequently processed to obtain the gas velocity. In this way, the instantaneous droplet size and velocity, and the gas velocity surrounding the droplet are determined by the combined technique.

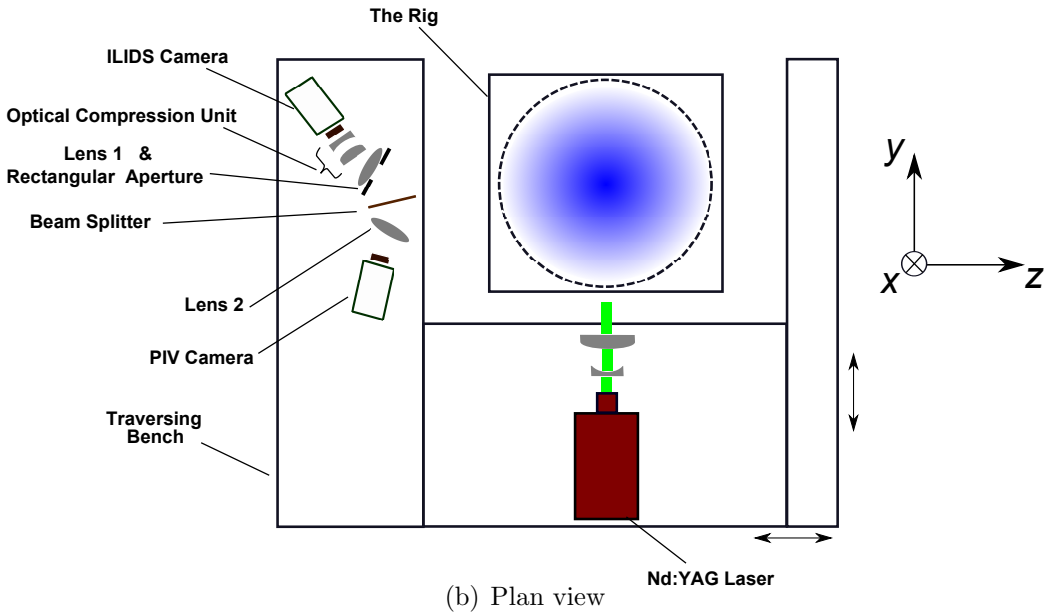
2.3.2 Experimental Set–up

Flow arrangement

An overview of the experimental rig is shown in Figure 2.13. The present work employed a model spray dryer rig for two-phase measurements, the details of which can be found in Kavounides (2006). The use of the spray dryer rig was advantageous in many ways. Specifically, its provision for the coflowing air around the spray was ideal for the kind of two phase measurements, the present research was aiming at. The rig consists of a tower constructed of four separate and nominally identical stainless steel cylinders with height and diameter of 0.5 m. The coflowing air was allowed to enter the tower from the top and was seeded with aluminium oxide particles (diameter range $1 - 5\ \mu m$) before entering the rig using a custom-made seeder (which also controlled



(a) Elevation view



(b) Plan view

Figure 2.13: Schematic of the Experimental Rig (a) Elevation view and (b)Plan view.

the seeding density). The flow rate of air was measured and controlled through a rotameter before the air was seeded. The coflowing air flow must not influence the flow field generated by the spray. Any kind of velocity gradient or turbulence in the flow was undesirable. A baffle plate at the top cylindrical chamber and a perforated plate (with circular holes of 5 mm diameter and with an open area ratio of 0.5) in between the first two chambers ensured flat profile of the radial velocity of air. The coflowing air flow rate, carrying the seeding particles, was set at 4×10^{-3} kg/s, resulting in area-averaged air velocity 3.4×10^{-2} m/s around the spray. Such a low velocity of air (corresponding Reynolds number, $Re_{coflow} \approx 11$) confirmed the absence of any turbulence in the coflow.

The atomizer was a custom-built air-assisted nozzle placed on the centreline of the cylindrical chamber right below the perforated plate. It produced a solid cone spray with a Sauter Mean Diameter (SMD) of the order of $150 - 200$ μm at liquid feed rates of the order of 1.5×10^{-3} kg/s and air feed rate of the order of 0.12×10^{-3} kg/s. Since the purpose of the study was to understand the mechanism of interaction between the spray and the entrained air, measurements should be conducted relatively downstream the nozzle, where such interactions were more expected. The optical access section (Figure 2.13), situated at 500 mm down the nozzle, was suitable for this purpose. This section was isolated from the surrounding using perspex sheets. This not only prevented the inside flow being affected by the external drafts but also the cameras and optics from the seeding particles. The whole optical assembly including the laser, laser sheet optics, cameras, lenses and the beam-splitter were mounted on a table (a large iron frame mechanism) capable of linearly traversing in all three Cartesian directions. As shown in the figure, the table was mechanically isolated from the tower. Hence, once the optical system (laser, cameras etc.) were aligned to take the measurements over a particular field of view, the whole assembly could be traversed to any desired position, and the measurements corresponding to various locations inside the spray were possible. The droplets along with the seeding particles were extracted from the bottom of the rig using an air-extraction equipment.

In order to assess the ability of the combined technique for the two-phase

measurement, especially to identify the same droplet in both ILIDS and PIV images, it was decided to first perform the experiments with a mono-sized droplet stream instead of the spray. For this purpose, a custom-built ultrasonic droplet generator (Pergamalis, 2002), capable of producing a single stream of equally spaced mono-sized droplets, was used. In this way the complexities of the spray, because of the presence of distribution of droplet sizes and multiple scattering could be avoided. The droplet generator was supported inside the rig and seeded air was allowed to flow around it. The pinhole size at the exit of the mono-dispersed droplet generator was 100 μm. The injection pressure was set at 1.0 bar, while the water flow rate was 6.0 cm^3/min. The resonance frequency of the piezoelectric elements of the generator was set to 20 kHz. Under this condition, the diameter of the droplets was approximately 212 μm with an accuracy of 97% (Pergamalis, 2002).

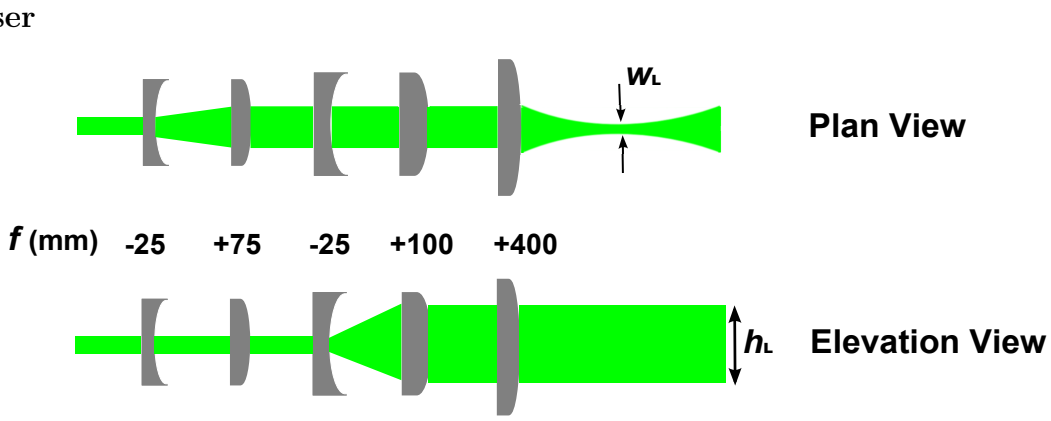


Figure 2.14: Generation of the laser sheet using series of lenses.

A frequency-doubled, double pulse Nd:YAG laser (120 $mJ/pulse$ at 532 nm; beam diameter 5 mm; New Wave Research) was used to illuminate the flow. The laser was vertically polarized. As shown in Figure 2.14, using a series of lenses, the cylindrical laser beam is expanded into a light sheet with a rectangular cross section (with height, h_L). The final lens in the series focuses the expanded light sheet across its width causing it to be minimum (w_L) at the focal distance, where the measurement area is located. In the present work, two different sets of laser sheet optics were employed for experiments with the droplet generator and the spray, respectively. Figure 2.14

depicts the optical arrangement for the case of the spray. For measurements with the droplet stream, the laser sheet was generated using a cylindrical lens ($f = -50\ mm$) and a spherical lens ($f = +200\ mm$) resulting in the laser sheet dimensions to be about $h_L = 20\ mm$ and $w_L = 1.5\ mm$, at the measurement location. The focal length of the final lens, in this case, was too short to be suitable for imaging in the central area of the spray. However, the use of longer focal length necessitates using larger beam width in order to achieve similar width of the laser sheet waist (w_L). Hence, for measurements with the spray, five cylindrical lenses were employed expanding the beam in to both directions. At first, the required beam width was acquired by the first pair of lenses ($f = -25\ mm$ and $+75\ mm$). The next pair of lenses ($f = -25$ mm and $+100\ mm$) vertically expanded the beam to obtain the appropriate height. At last, the final lens (with focal length, $f = +400\ mm$) focused the laser sheet to produce the waist. The dimensions of the laser sheet, at the measurement location, was approximately $h_L = 20\ mm$ and $w_L = 1\ mm$, respectively.

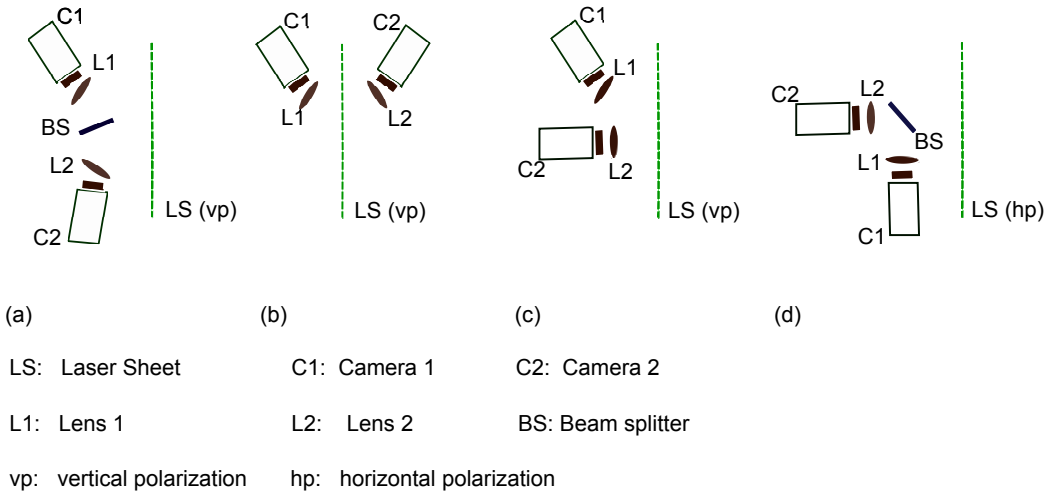


Figure 2.15: Possible optical arrangements for the combined ILIDS and PIV measurements.

Cameras

Two identical cameras were used (PCO; Sensicam QE, 12 bit, 1040 $\times$ 1376 $pixels^2$) along with two lenses (135-mm $f/2.8$ Nikon lens for ILIDS and 135-mm $f/8$ Nikon lens for PIV) to collect the scattered light from the droplets. The ideal observation angle for the ILIDS camera is $\theta = 69°$, which is the optimum scattering

angle for refractive index of 1.33 (water in air) for interference with best contrast between the refracted and reflected rays with a vertically polarized laser sheet. Though, ideally no such restrictions exists for the PIV camera, the observation angle other than 90° necessitates the use of Scheimpflug condition (see page–62 for the discussion on Scheimpflug condition). Thus, the selection of appropriate position of the cameras relative to each other and also with respect to the laser sheet needed careful judgement. There were four possible optical arrangements as illustrated in Figure 2.15 and described below.

(a) Placing the cameras on the same side of the laser sheet: This arrangement is certainly advantageous because by using a beam splitter, the incoming scattered light can be split in two parts and this allows both cameras to view the same region in the flow field. Also the arrangement needs minimum optical access to the flow facility. However, Scheimpflug condition is necessary in this case because of the non-90° orientation of the cameras.

(b) Placing the cameras, one at each side of the laser sheet: The disadvantage with this approach is that identifying a given droplet in both images can be ambiguous because of the droplet movement perpendicular to the laser sheet. Moreover, since obtaining the droplet velocity in the third dimension (normal to laser sheet) was not the aim, this arrangement was not beneficial.

(c) Same as in (a) but the PIV camera at $\theta = 90°$: With this arrangement, both cameras can have the same field of view without the use of the beam splitter. Also no Scheimpflug condition is required for the PIV camera. However, referring back to Figure 2.1(a), it can be observed that, at $\theta = 90°$ for vertically polarized light, the contribution from the first order refracted ray is almost zero. The scattered light remains dominated by the reflected ray with little contribution from the second order refracted rays. Thus no glare points, as before, can be observed. Since this would make detection of the centre of the focused droplet images ambiguous, hence this option was avoided.

(d) Using horizontally polarised light: The use of horizontally polarized light

gives the highest visibility at a scattering angle of 90° and so no Scheimpflug condition is required. But it should be noted that the scattered intensity is smaller by about $10 - 100$ times than for the forward scatter configuration (Damaschke *et al.*, 2005). This means accordingly the laser power must be higher. Hence, this option is not always convenient. Other scattering angles with interference between higher orders can also be used, but the relation between fringe spacing and particle diameter is no longer analytically solvable and the glare point separations are more dependent on small disturbances of the sphericity and homogeneity.

Considering all of the above options, the first one was found to be the most advantageous. Thus the cameras were positioned on the *same* side of the laser sheet at $\theta = 69°$. In order to avoid varying degree of focus/defocus across the CCD array, both the cameras were aligned under the Scheimpflug condition (similar to Sugimoto *et al.* 2006), with the aid of special Scheimpflug mounts (Zarogoulidis, 2011), attached on top of the camera mount. During alignment, at first, both lens and cameras were set at the forward scattering angle θ with respect to the laser sheet and then, *only* the cameras were rotated (relative to the lens) till uniform degree of focus was achieved across the image. The defocusing of the image in camera 1 was achieved, as mentioned before, by the pair of cylindrical lenses ($+50\ mm$ and $-50\ mm$ focal length). The scattered light from droplets was divided into two parts by using a pellicle beam splitter of thickness of $2\ \mu m$ to avoid the formation of ghost images. The light refracted through the pellicle beam splitter was directed at the defocused plane for measurements with ILIDS, while the reflected light was used for PIV measurements. Though this choice was not critical, the purpose behind this configuration is that the reflected light from the beam splitter is more sensitive to the alignment of the beam splitter than the refracted one. Since the ILIDS camera is usually operated with maximum aperture, the problem of image distortion would have been more pronounced if the reflected light was used. The rectangular aperture ($4 \times 30\ mm^2$) was placed right in front of the collecting lens for camera 1. The collecting angle (α) was 6.35° for an object distance of 300 mm, resulting in a resolution, $\kappa = 5.28$

$\mu m/fringe$ for the ILIDS system. Since the objective lens consists of a set of lenses with variable dimensions, it should be carefully checked if the width of the rectangular aperture is smaller than any of these lens dimensions and also the lens aperture. Otherwise, the value of α would be incorrect.

The field of view for both cameras must be the same. As mentioned before, in ILIDS operation, the choice of the field of view is a compromise between the area of observation and the smallest measurable droplet diameter. Thus, in order to be able to measure *at least* 20 μm droplets, both cameras were adjusted to provide a field of view of approximately $10 \times 12\ mm^2$, which is comparatively small with respect to that of usual PIV system operation. The resolution was approximately 9 $\mu m/pixel$ in both directions, and the magnification was about 0.70, for both cameras. Because of the relatively smaller viewing area, negligible variation in magnification (0.69−0.72) was observed across the image. This minimizes the limitations of the Scheimpflug condition. Throughout the text, the term "focused plane" refers to the PIV image (which would not be true without application of the Scheimpflug criterion), while the "defocused plane" refers to the ILIDS image.

Using the magnification, the diffraction limited image diameter can be calculated as (Raffel *et al.*, 1998),

$$d_{diff} = 2.44 f_{\#}(M+1)\lambda \tag{2.13}$$

In this equation, $f_{\#}$ is the aperture number of the lens, M the magnification and λ the wavelength of light equal to 532 nm. This yields a minimum particle image of 17.8 μm for aperture of $f_{\#} = 8$. With a pixel size of $9\mu m$, this means that the only partial diffraction limited imaging is expected. The expected image of a particle with diameter, d_p can be calculated as:

$$d_\tau = \sqrt{(M d_p)^2 + d_{diff}^2} \tag{2.14}$$

Thus, a tracer with d_p = 5-10 micron will yield an image of approximately 2 pixels. The reason to calculate the expected tracer image size is to avoid so-called 'peak-

locking' (as was mentioned before also). This effect, which refers to a bias of the displacement to integer pixel values, occurs when the tracer images are of the order of 1 pixel. In the present case, with a tracer particle image of 2 pixels, some mild peak-locking is expected.

It is worth mentioning here about another optical parameter, the depth of field (δ_z), estimated using the following formula (Raffel *et al.*, 1998):

$$\delta_z = 2f_{\#}d_{diff}(M+1)/M^2 \tag{2.15}$$

Using the same magnification and aperture as in experiment, the depth of field was found to be about 0.9 mm. Since the laser sheet thickness at the measurement location was about 1 mm, it implies that the out-of-focus effect was negligible.

Camera calibration

The camera calibration is a crucial factor for the accuracy of the proposed optical arrangement. It should be noted that the calibration was performed with both cameras in focus. The calibration provides a mapping between the two-dimensional object plane (laser sheet) and each two-dimensional image planes. To ensure both cameras imaged the same area, a calibration plate with equally spaced "crosses" was used. The choice of the 'crosses' was to ensure better accuracy in locating its centre. The total number of crosses (n), observed by each image, were equal to 24 (4 in vertical and 6 in horizontal directions). The spacing being 2 mm and assuming the bottom left 'cross' to be at coordinate (0, 0), the real coordinates of all crosses were determined. The location of the centres of the crosses in the calibration images were determined by cross-correlating the images with a template image (containing a 'single cross') with sub-pixel accuracy and, mapped to the respective pixels by fitting a mapping function. To account for non-uniform magnification and other non-linearities, a cubic polynomial was chosen for third order mapping. Defining the real coordinates (in mm) and image plane coordinates (in $pixels$) as (x, y) and (X, Y),

respectively, the mapping function is given as:

$$x = a_0X^3 + a_1Y^3 + a_2X^2Y + a_3XY^2 + a_4X^2 + a_5Y^2 + a_6XY + a_7X + a_8Y + a_9 \tag{2.16}$$

$$y = b_0X^3 + b_1Y^3 + b_2X^2Y + b_3XY^2 + b_4X^2 + b_5Y^2 + b_6XY + b_7X + b_8Y + b_9 \tag{2.17}$$

The coefficients $a_0, a_1, a_2 \cdots a_9$ and $b_0, b_1, b_2 \cdots b_9$ can be determined by solving the following equations using a least square solution:

$$A \begin{bmatrix} a_1 \\ a_2 \\ a_3 \\ \vdots \\ a_9 \end{bmatrix} = \begin{bmatrix} x_1 \\ x_2 \\ \vdots \\ x_n \end{bmatrix} \qquad and, \qquad B \begin{bmatrix} b_1 \\ b_2 \\ b_3 \\ \vdots \\ b_9 \end{bmatrix} = \begin{bmatrix} y_1 \\ y_2 \\ \vdots \\ y_n \end{bmatrix}$$

where,

$$A = B = \begin{bmatrix} X_1^3 & Y_1^3 & X_1^2Y_1 & X_1Y_1^2 & X_1^2 & Y_1^2 & X_1Y_1 & X_1 & Y_1 & 1 \\ X_2^3 & Y_2^3 & X_2^2Y_2 & X_2Y_1^2 & X_2^2 & Y_2^2 & X_2Y_2 & X_2 & Y_2 & 1 \\ \vdots & \vdots & \vdots & \vdots & \vdots & \vdots & \vdots & \vdots & \vdots & \vdots \\ X_n^3 & Y_n^3 & X_n^2Y_n & X_nY_n^2 & X_n^2 & Y_n^2 & X_nY_n & X_n & Y_n & 1 \end{bmatrix}$$

The accuracy in calibration was $\pm 15\ \mu m$ and $\pm 4\ \mu m$ in horizontal (y) and vertical (x) directions respectively. Note that the effect of the non-90° observation angle and the Scheimpflug condition is occurring in yz-plane only, which justifies the lower accuracy in the horizontal direction. Thus, given a droplet location on the image (centre of the fringe patterns in the ILIDS image or glare points in the PIV image), the real position in space could be obtained.

2.4 Droplet Centre Discrepancy

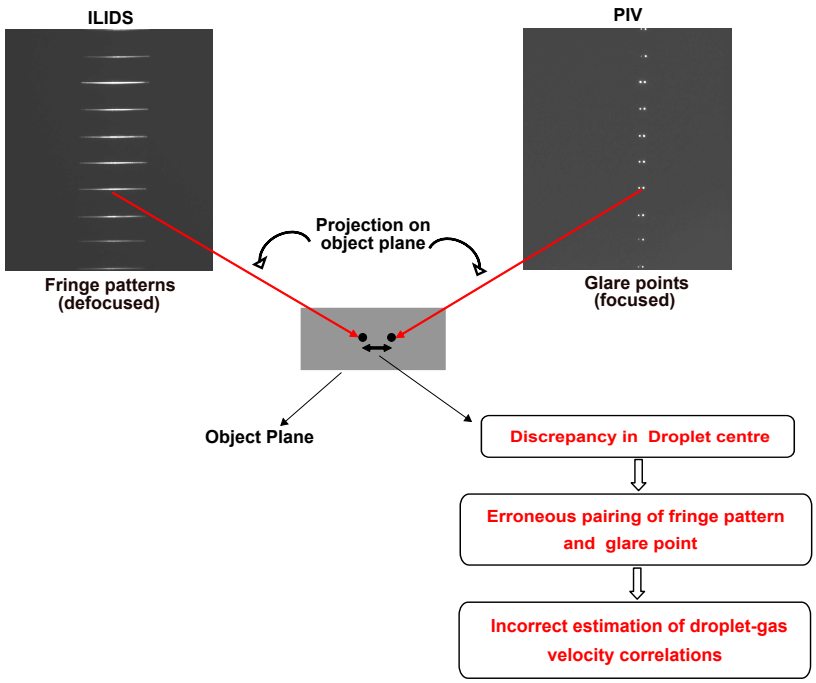


Figure 2.16: Depiction of the discrepancy in droplet centre.

Although the principle of combining ILIDS with PIV as described previously is intuitively convincing, its application is not straight forward. ILIDS, being an out-of-focus technique, when combined with PIV, results in discrepancy in the location of the centre of the same droplet when imaged through both techniques. Figure 2.16 shows a pair of instantaneous ILIDS and PIV images corresponding to a stream of mono-sized water droplets issuing from the droplet generator *without* the coflowing air. The images were captured simultaneously with the optical set-up described in the previous section. Each droplet can be observed in Figure 2.16 as a set of horizontal stripes of light in the ILIDS image (left) and as a pair of glare points in the PIV image (right). The details of image processing to locate the geometric centres of the fringe pattern and glare points will be explained later. The droplet diameter (D) estimated by ILIDS was 228 μm, which is within 7.5% of the theoretically calculated value for the operation of the mono-dispersed droplet generator.

Using the mapping functions (Equations (2.16) and (2.17)), the coordinates of the centre of the fringe patterns (X_f, Y_f) and glare points (X_g, Y_g) were projected to the

plane of laser sheets to obtain their respective real coordinates (x_f, y_f) and (x_g, y_g). The one-to-one correspondence between the fringe patterns and their respective glare points could be reliably obtained by calculating the distance between the projected centres, r, such that $r = \sqrt{(x_f - x_g)^2 + (y_f - y_g)^2}$. The correct pair of fringe pattern and glare points should have the minimum value of r. Note that, this approach of identifying the correct pairs is possible only in the case of the mono-dispersed droplet stream. For a spray, the same approach would lead to ambiguity because of higher droplet number density. Once the correct pairs were found, the error in the droplet centre was calculated in both directions, namely $err_x = (x_f - x_g)$ and $err_y = (y_f - y_g)$. There were two possibilities regarding the magnitude of the errors:

(i) As far as the error due to calibration is concerned, it was expected to be negligible because the inaccuracies in calibration in both directions were much less than the droplet diameter.

(ii) Somewhat higher error in y-direction. Because of the non-symmetric distribution of the glare points about the droplet centre, the geometric centre of the droplet image (which was assumed to be the actual centre) might cause a discrepancy in the position of the droplet centre when projected to the object plane. However, since this discrepancy can never be more than a droplet diameter, so this error (err_y) was believed to be with in one droplet diameter.

However, err_y was not only much larger ($>> D$) but also found to vary with the position of the droplet stream in the image. This discrepancy in the droplet position has the serious consequence of erroneous pairing up of the fringe patterns and glare points which would eventually lead to incorrect estimation of the droplet-gas velocity correlations. In order to conceive the origin of the discrepancy in the droplet centre, the problem was theoretically approached through geometric optics.

2.4.1 Theoretical prediction of the centre discrepancy

Figure 2.17(a) shows a simplified ray diagram of the combined focused and defocused optical configuration. The direction of the light sheet is shown by an arrow. The

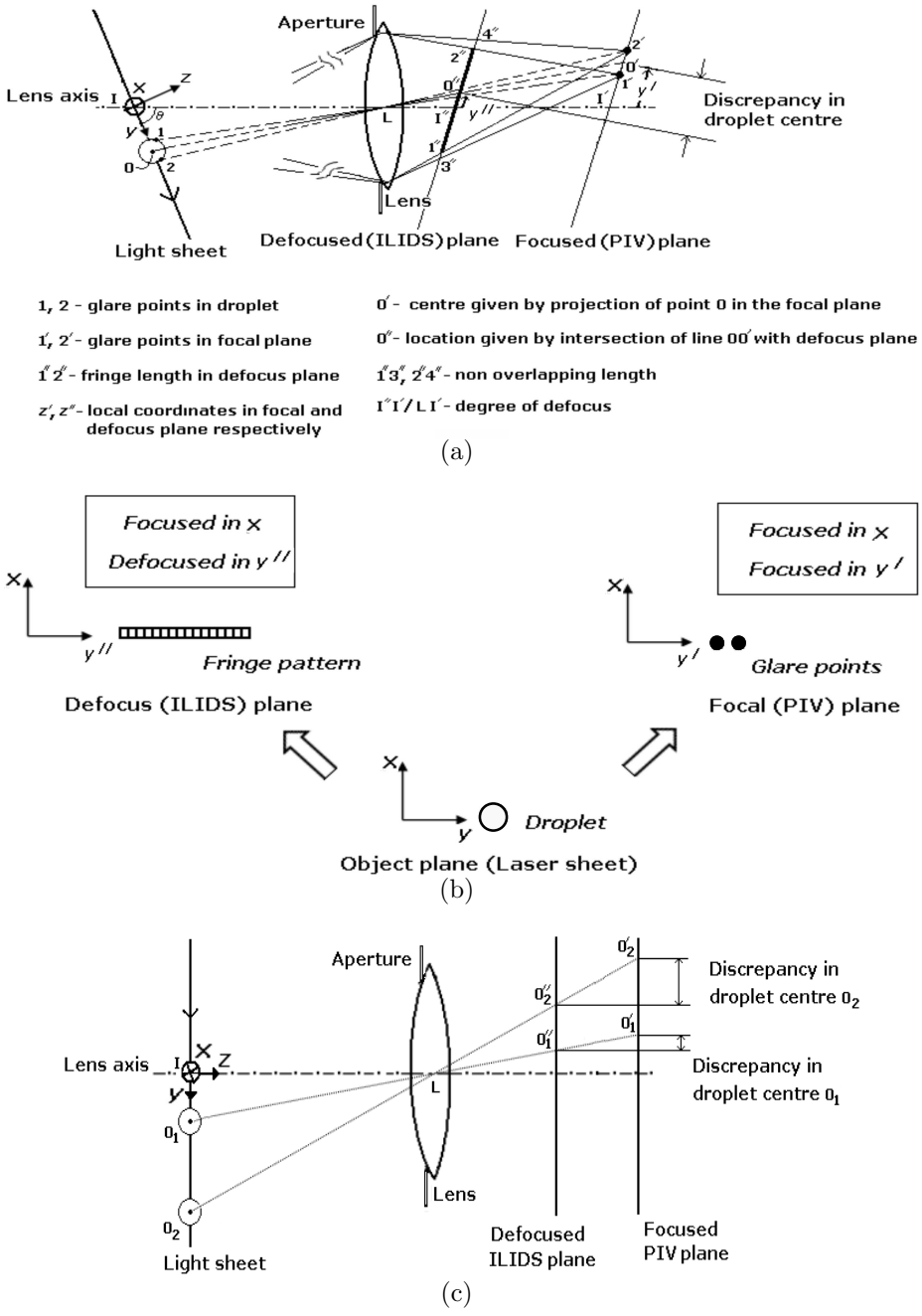


Figure 2.17: (a) Schematic of the optical system for theoretical prediction of discrepancy in droplet centres between the focused and defocused planes (b) Images along the axis of the lens of a droplet in the focussed and defocused planes and the corresponding coordinate systems (c) A simplified schematic of the same optical system shown in Figure 2.17(a) (but with the laser sheet, focused plane and defocused plane normal to the lens axis) in order to depict the dependency of the centre discrepancy on the droplet position.

lens is positioned at forward scattering angle θ with respect to the laser sheet. The origin of the co-ordinate system is located at the point where the lens axis intersects the laser sheet. The position of any droplet, situated within the laser sheet, is given by the coordinates of its centre $0(x,\ y,\ z)$ where x and y refer to the vertical and horizontal position with in the plane of observation (xy-plane), and z corresponds to the droplet position normal to the laser sheet. As shown in Figure 2.17(a), a droplet of diameter D is considered to be situated in plane $z = 0$ at a distance y from the origin. The droplet is imaged on the ILIDS and PIV CCD arrays, both maintained under the Scheimpflug condition. The theoretical analysis was performed under certain assumptions, as mentioned below:

(i) The analysis does not consider the droplet position normal to the yz plane, i.e. along the x direction. We expect this limitation to have minor influence over the result. Thus, the position of the centre of the droplet (point '0') under consideration can be denoted as $(0,\ y,\ 0)$.

(ii) For simplicity, the images on the ILIDS and PIV CCD arrays are represented as being formed by a single lens instead of, as in the experiment, by two independent lenses (Figure 2.12). This is because the process of defocusing—by using compression optics–is equivalent to translating the ILIDS image plane along the axis of the imaging lens, while keeping the ILIDS array parallel to the PIV array. Though translation of the image plane does not allow image compression, it is assumed that, in the ILIDS plane, the defocused image is compressed in x direction (*i.e.* normal to the plane of the paper) and defocusing is done only in the y direction (Figure 2.17(b)).

(iii) The droplet centre ('0') is co-linear with the glare points '1' and '2' corresponding to reflection and first order refraction, respectively. The positions of '1' and '2' are given by their projection on plane $z = 0$. The relative distances of the glare points with respect to the centre can be calculated from a geometrical optics light scattering model similar to Golombok *et al.* (1998).

In the in-focus (PIV) plane, the glare points are imaged to points $1^{'}$ and $2^{'}$ with the centre of the droplet imaged to $0^{'}$, which will be called as the 'derived centre': the geometrical centre of the image, in contrast, is midway between $1^{'}$ and $2^{'}$. The calibration of the ILIDS and the PIV CCD arrays is carried out with the ILIDS optics adjusted to be in focus, so the coordinate systems fixed to the focused ILIDS and PIV CCD arrays, $y^{'}$ and $y^{''}$, respectively, both have their origin on the axis of the lens. After calibration, the ILIDS image is defocused by shifting the image plane towards the lens, the degree of defocus[2] being the ratio of the distance between the centres of defocus plane to in-focus plane ($I^{''}I^{'}$) to that of centre of lens to in-focus plane $LI^{'}$. The geometrical centre of the ILIDS image is the mid-point of the fringe pattern $1^{''}2^{''}$. The point of intersection of the ray $00^{'}$ with the defocused ILIDS plane is $0^{''}$ (which is generally not coincident with the geometric centre of the ILIDS fringe pattern) and is the "derived centre" of the fringe pattern. Figure 2.17(a) shows that location $0^{''}$ is offset, in $y^{''}$ coordinates, from $0^{'}$.

The following terminologies are defined as: 'centre deviation' is the difference in location of the geometric centre from the derived centres of a given droplets image, in either the in-focus or the defocus planes, and is a signed quantity. Similarly, the 'centre discrepancy' is the difference in either the derived or the geometric centres between in-focus and defocus plane and is also a signed quantity. The centre deviation and discrepancy are qualitatively demonstrated by the schematics inset to Figures 2.18(a) and 2.18(b), respectively. Unless otherwise mentioned, the term 'centre discrepancy' will refer to the geometrical centres of the fringe pattern and glare points—the geometrical centres being the only experimentally accessible aspect of the above images.

The input parameters for the analysis, as for the experiment, were: $\theta = 69°$, $D = 0.2\ mm$, object distance = $360\ mm$, focal length of the lens = $135\ mm$, image distance = $216\ mm$ and aperture size = $40\ mm$. In order to satisfy the condition

[2]Note that quantifying the degree of defocus in a given experiment is not straight forward since it is difficult to determine the distances $I^{''}I^{'}$ and $LI^{'}$ exactly.

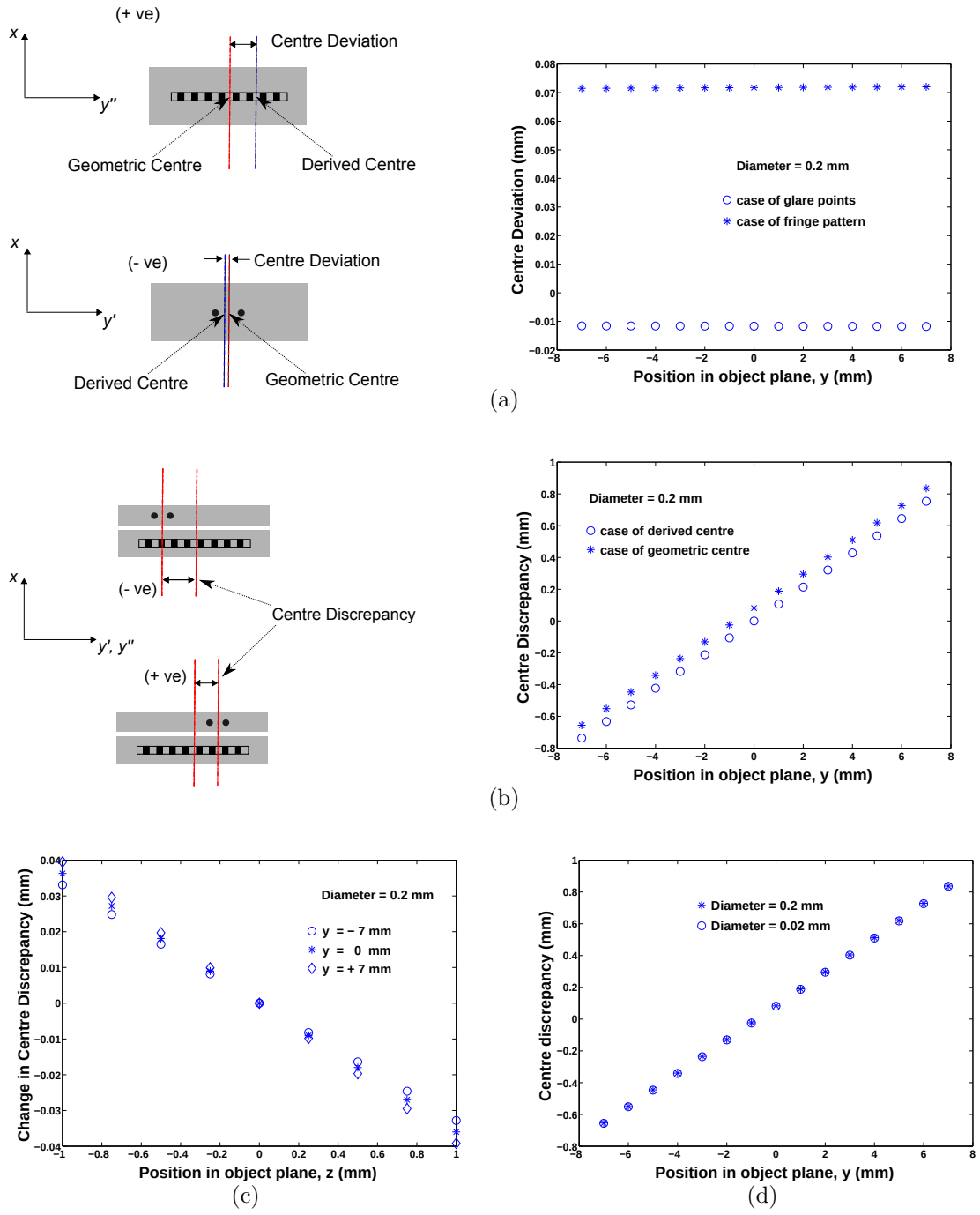


Figure 2.18: (a) Deviation of the geometric centre from the derived centre of the droplet image as a function of z position in the object plane (b) Discrepancy in derived centre and geometrical centre between in-focus and defocus planes as a function of z position in the object plane (c) Relative change in centre discrepancy as a function of position x in the object plane for a droplet situated at three positions z = -7, 0 and 7 mm, respectively (d) Comparison of the centre discrepancy for two droplet sizes of 200 and 20 μm as a function of position y. Focal length was 135 mm, magnification was 0.6 and aperture size was 40 mm.

of far field optics for ILIDS, the defocus distance ($I''I'$) was chosen [3] to be 40 mm: the corresponding non-overlapping length was 0.2% of the fringe pattern length and the degree of defocus was 0.19. The following conclusions were derived from the analysis and are valid for all far field defocused planes where the 'non-overlapped length' outside the fringe is negligible ($\sim$1%) compared to the fringe pattern length.

1. In the PIV plane, the "centre deviation", shown as open circles in Figure 2.18(a), is of the order of 0.01 mm—a small fraction of the droplet diameter which is almost independent of the position (y) of the droplet in the object plane but decreases proportionally with droplet size. Thus the mid-point of the glare points corresponds closely to the location of the centre of the droplet, with an error of only $0.1D$.

2. In the ILIDS plane, the "centre deviation", shown as asterisks in Figure 2.18(a), is of the order of 0.07 mm and is proportional to the degree of defocus. Its magnitude is about one-third of the droplet diameter, and so it cannot be considered negligible. The "centre deviation" does not, however, depend strongly on either the droplet size or position in the object plane. Hence, when the experimental results from ILIDS and PIV were finally combined, the positions of the droplets were found from the centre of glare points.

3. The "centre discrepancy" between the centres of the glare points and the fringe pattern, in the in-focus and defocus planes, respectively, was determined for both the derived (the distance $1'2''$ in Figure 2.17(a)) and geometrical centres. For both cases, the discrepancy is, as expected, proportional to the degree of defocus and dependent on the droplets y position. Figure 2.18(b) shows that the centre discrepancy (for either derived or geometric centre) varies almost linearly across the image plane, from being negative on one side of the image plane to positive on the other side. For the particular parameters considered

[3]Note that, this is an arbitrarily selected value and the corresponding distance in the experiment presented later is different.

here, the maximum discrepancy[4] is towards the edge of the CCD array and can be of the order of 1 mm, or five times greater than even the relatively large droplet diameter considered here. The dependency of the centre discrepancy over the droplet position is schematically shown in Figure 2.17(c) for two different positions of the droplet in the object plane. To avoid complexity in the ray diagram, the laser sheet and, hence, the defocused/focused plane were kept normal to the lens axis. Larger discrepancy for the droplet position away from the lens axis can be observed.

4. The dependence of centre discrepancy (with respect to the original position) across the thickness of the laser sheet is plotted, in Figure 2.18(c), as a function of position z (see Figure 2.17(a)) for three y positions of the droplet. The thickness of the laser sheet was taken as 2 mm. The maximum change in discrepancy is about ± 0.04 mm, corresponding to about a fifth of the diameter, D, as the droplet moves within the thickness of the laser sheet, for z equal to -1 mm to $+1$ mm.

5. The magnitude of 'centre discrepancy' was almost independent of droplet size. For example, the difference in discrepancy between a droplet of 200 and 20 μm diameter droplet in Figure 2.18(d) is only 2 μm. The origin of the observed small dependence of centre discrepancy on droplet size is the non-symmetric position of the glare points around the droplet centre in the image plane, which varies with droplet size.

6. Though not presented here, calculation without the Scheimpflug condition in the defocus (ILIDS) plane showed that the magnitude of the discrepancy remained almost unaltered (but, as expected, it reduced the magnitude of centre deviation in the defocused plane by a factor of 10).

The theoretical results presented above are limited by the simplification in the calculations used to avoid making the analysis cumbersome. Also, the theory does

[4]This discrepancy, here related to the use of the geometric centre, arises even if we were able to use the 'derived centre' of the glare points/fringe pattern.

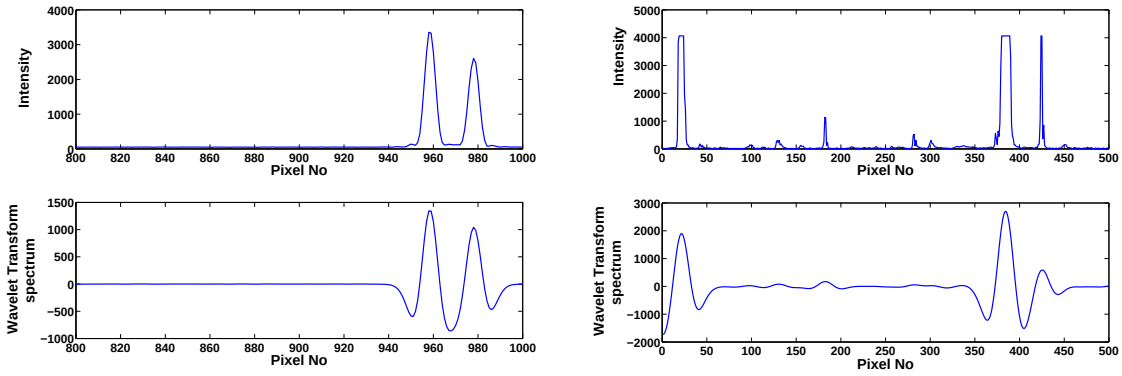
not take into account the position of the droplets in x direction (perpendicular to the plane of paper). Hence, in order to quantify the droplet centre discrepancy in a practical arrangement, particularly under the defocus setting of the compression optics in the ILIDS arrangement, experiments are required.

2.4.2 Quantification of droplet centre discrepancy

Detection of droplet centre

Since identification of the location of droplet centres plays a vital role in subsequent image processing, the first step is to describe the method of detection of the geometric centre of the fringe patterns in the ILIDS image, and of the glare points in the PIV image. The method of detection of the centre of the fringe patterns has been described previously using the continuous wavelet transform (CWT). Two scales of the mother wavelet (Mexican hat) were used for this purpose: larger one approximately equal to the fringe pattern length and the other one equal to the smallest scale (2 pixels in the present case). The precision in locating the centre of the fringe patterns in the ILIDS image, for the case of spray, was estimated as being ± 20 pixels in horizontal direction and ± 1 pixels in vertical direction. In the case of the droplet generator, the precision in centre location was better (± 6 and ± 1 pixels in horizontal and vertical directions respectively) because of higher signal to noise ratio of the fringe patterns since multiple scattering was absent, in contrast to spray.

The glare points of each droplet in the PIV image (for example in Figure 2.16) were detected by applying the wavelet transform with a small scale along each line of the image using the same mother wavelet as before. As shown in Figure 2.19(a), for every droplet, each maximum obtained from the wavelet transform spectrum corresponds to the location of a glare point. The geometrical centre between the two adjacent maxima (glare points) was assumed to be the actual centre of the droplet. From geometrical optics, it can be shown that for each droplet, the distance between the two glare points is proportional to the droplet size (the droplet diameter is about 1.4 times this distance) and thus can be a measure of droplet diameter. However, the determination



(a) (b)

Figure 2.19: (a) Intensity distribution of the glare points in the PIV image of the mono-sized droplet stream and its corresponding wavelet transform spectrum (b) Intensity distribution and wavelet transform spectrum of the glare points and seeding particles corresponding to the polydisperse spray.

of droplet diameter through this approach is not reliable. This is because it is not always possible to resolve the distance between the glare point pairs, even for relatively large droplets, due to restrictions in CCD array resolution. The demand of higher spatial resolution and the necessity for magnification by the receiving optics causes the method to have no distinct advantages over direct imaging. Diffraction limited imaging also imposes a restriction on the minimum measurable droplet size. Finally, the theoretical model (Section 2.4.1) shows that the relative distance between the two glare points of a given droplet can vary across the CCD as the droplet changes its position in the object plane. The minimum measurable droplet diameter, through glare points, was of the order of 100 μm for our experimental conditions. Hence, in this work, the glare points were used only to detect the location of droplets on the PIV image. The corresponding droplet glare points at the later time of a pair of PIV images were found through particle tracking velocimetry, similar to the approach used for ILIDS.

Note that in Figure 2.19(a), which corresponds to the large droplets issuing from the droplet generator, the intensity profile can provide the glare point centre directly without using the CWT. However, the same approach leads to ambiguity in the polydisperse spray. Shown in Figure 2.19(b) is the intensity profile and the CWT

spectrum of some of the glare points identified in the PIV image of the spray with the coflowing air containing the seeding particles. Unlike Figure 2.19(a), the two intensity maxima for each pair of glare points are no longer resolved because of the smaller droplet size. Since the size of the seeding particles was orders of magnitude smaller than the droplets, the measurements were performed with higher laser power in order to achieve good SNR in the PIV image. This resulted in the intensity of the glare points saturating the camera. So, the detection of centre of glare points based only on intensity can be ambiguous. In contrast, the peak in the CWT spectrum provides a good approximation in this regard. The precision of locating the centre of glare points in PIV image was estimated as ± 2 pixels in both horizontal and vertical directions.

Use of CWT also has the additional advantage of discriminating the glare points from the seeding particles in the PIV image. By selecting an appropriate scale of the wavelet, it is possible to suppress the peaks produced by the seeding particles in the CWT spectrum and then, by selecting a suitable threshold, glare points only are identified, thereby eliminating signals from seeding particles. For example, though the peak of the intensity profile at the extreme right of Figure 2.19(b) has amplitude similar to the other two peaks, its corresponding CWT spectrum has lower amplitude and is eliminated as a seeding particle. The thresholds for intensity and wavelet transform, and the suitable scale of the wavelet were decided on the basis of PIV images captured for *only* the spray (without seeding particles around) and also *only* seeding particles (without the spray).

Quantification of the centre discrepancy by droplet generator

Once the droplets are detected in both ILIDS and PIV images, the next task is to identify the glare points in the PIV image corresponding to the appropriate fringe pattern in the ILIDS image. However, the discrepancy in identifying the location of the droplet centre between the two images reduces the probability of identifying the correct glare points, especially for the case of a spray. It is essential to quantify the magnitude of the discrepancy and eliminate it. Hence, experiments were performed

with the droplet generator at five different positions along the 'y' dimension as shown in Figure 2.13. The degree of defocus was kept the same for all cases by maintaining the same position of the cylindrical lenses in the optical compression unit.

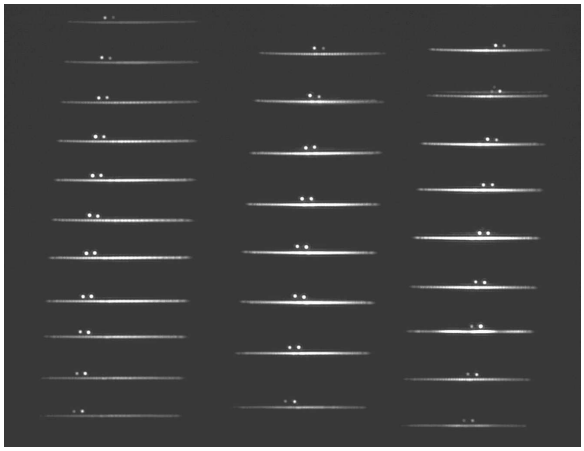
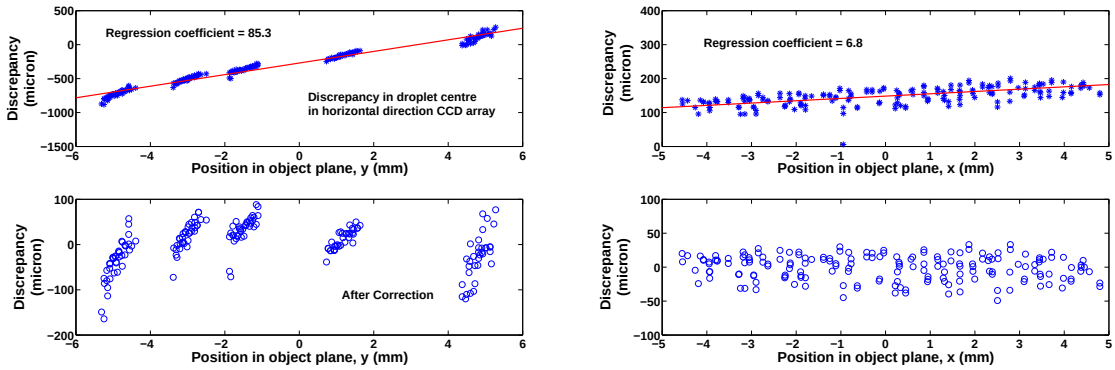


Figure 2.20: Fringe patterns and corresponding glare points for a stream of mono-dispersed droplets without gas phase seeding at three different positions in the object plane, $y = -5.0$, $+1.0$ and $+5.0$ mm, respectively. The ILIDS images are superimposed on the PIV image. Note that the origin of the coordinate system ($x = 0$ and $y = 0$) lies in the centre of the CCD array, which coincides with the centre of the image of the figure.

The corresponding images are shown in Figure 2.20 for three different positions in the object plane. In order to demonstrate the variation of droplet centre position, the focused and defocused images have been superimposed. The glare points seem to be moving from left to right with respect to the fringe centre with increasing y location. Two sets of images were processed for each position. At first, the locations of the droplet geometrical centres in ILIDS and PIV images were obtained by processing these separately. Then, these were projected to the object plane using calibration coefficients[5], as depicted in Figure 2.16. A fringe pattern was associated with a pair of glare points if the difference in their resulting image centres in the object plane was

[5]Another way of dealing with the problem of droplet centre discrepancy would be to have the ILIDS camera defocused during calibration: but then the detection of the "defocused crosses (calibration marks)" is more difficult. Also, this approach is based on an assumption that if the droplet centre and the centre of the "mark" coincide in the object plane initially, than after defocusing, the geometric centre of the "defocused mark" coincides with the geometric centre of the defocused droplet image as well. However this may or may not be true, because of the fact that the glare points are not symmetrically spaced around the droplet centre. Nevertheless the resulting error is likely to be small. Hence the approach of calibration before defocusing was preferred in this work which has the additional advantage of permitting the change of the degree of defocus, if required, during an experiment.

minimum in both horizontal (y) and vertical (x) directions. Since, in this case, the droplet number density was low and there was no seeding in the air, the probability of correctly identifying the corresponding glare points with a fringe pattern was almost 100%.



(a) (b)

Figure 2.21: (a) top: Centre discrepancy between ILIDS and PIV images in the horizontal (y) direction as a function of y position in the object plane. The straight line is a linear fit to the original data. bottom: The remaining droplet centre discrepancy after subtracting the estimated error. (b) top: Centre discrepancy in the vertical (x) direction as a function of x position in the object plane and the estimated error. The straight line is a linear fit to the original data. bottom: The remaining droplet centre discrepancy after subtracting the estimated error.

The droplet centre discrepancy as a function of horizontal, y, position in the object plane is shown in Figure 2.21(a), and the discrepancy can be as large as 1,000 μm, which is about 5 times the droplet diameter in the present case. The droplet stream was found to have been inadvertently inclined (by about 5.5°) relative to the vertical (x) direction of the image (xy plane) during experiment. So, for each (nominal) position in the y direction, a spread in the measured error can be observed. The variation of the discrepancy with y is close to linear, and the magnitude is greater than the droplet size (towards the edge of the CCD array). Although it is hard to make direct comparison with the theory of Section 2.4.1 (because it is difficult to quantify the defocus distance experimentally), the magnitude of the centre discrepancy (i.e. the vertical scale) in Figure 2.21(a) is comparable to that expected from the analysis, as shown in Figure 2.18(b). The overall trend of the error can be described empirically

through a linear fitting and ultimately can be virtually eliminated from the original values. The residual error is plotted in Figure 2.21(a) and was less than a droplet diameter (maximum of about half of the droplet size) in this case.

This remaining error can be due, in principle, to various sources such as additional inclination relative to the vertical in the xz plane, i.e. normal to the plane of the laser sheet (which leads to variation in object distance of the droplets), inaccuracy in camera calibration and the error involved in detection of fringe centre and glare point centre in ILIDS and PIV processing respectively. However, according to the theoretical analysis (Figure 2.18(c)), the error due to out-of-plane movement of the droplets within the laser sheet for the current experiments is only of the order of 20 μm. The inaccuracy in camera calibration is only of the order of 15 μm, and the precision in the detection of centre of the glare points and the centre of the fringe pattern are of the order of 20 and 100 μm, respectively. We conclude from comparison of the above cases that the cause of the residual error can be attributed primarily to the inaccuracy of detection of the fringe centre. It should be noted that the experimental measurements of Figure 2.21 are not directly comparable to the theoretical analysis of Figure 2.18(b). This is due to, as explained earlier, the unknown defocus distance of the lens in the experiment, which is different from the indicative 40 mm distance used in the theoretical section. As a consequence, the location of the minimum centre discrepancy occurs at different location along the CCD array and is not the same as indicated in 2.18(b).

In the vertical (x) direction, the trend of the discrepancy Figure 2.21(b) was found to slightly increase from the top to the bottom of the CCD array with magnitude between 100 and 200 μm, which is much smaller than the error obtained in the y direction and can be considered to be constant. Since no defocusing was performed in the x direction, ideally the discrepancy should be zero in this case. Thus, its appearance can be thought of being related to the systematic error in the calibration of the optical arrangement with both cameras and also to the inaccuracy in droplet centre location during image processing. Similar to the case of the discrepancy in the y direction, the error was represented through a linear fit and subtracted from the

original values, which resulted in a final remaining error of the order of 40 μm.

2.4.3 Application to a polydisperse spray with no gas phase seeding

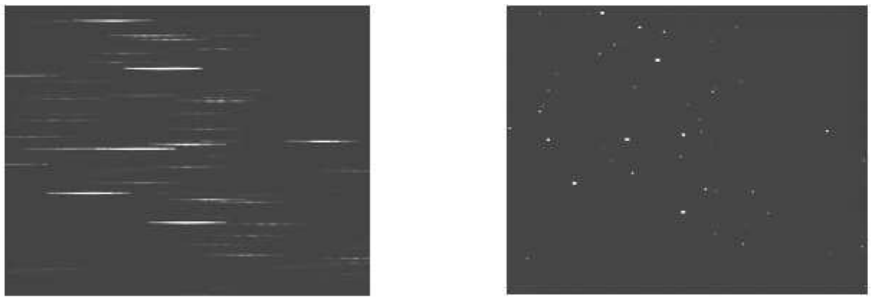


Figure 2.22: Simultaneous ILIDS (left) and PIV (right) images of droplets in a polydisperse spray without seeding particles.

The matching of a fringe pattern with a pair of corresponding glare points becomes more challenging for a spray, relative to the case of monodispersed droplets, because the droplet number density is much higher and the inter-droplet distance is random. The measurements in a spray were taken for a relatively dilute region at 500 mm below the nozzle centre and 20 mm away from the nozzle axis. The injection pressure was 1 bar, and volume flow rate of water was 10.83×10^{-4} kg/s. The Sauter mean diameter (SMD) was 68 μm as estimated from ILIDS. The droplet number density was about 25 droplets/image when compared to 10 droplets/image for the case of the droplet generator. The corresponding ILIDS and PIV images are shown in Figure 2.22.

In total, 10 pairs of image pairs were processed to obtain droplet centres. In the focused image, detection of the pairs of glare points was more difficult (when compared to the case of the droplet generator with much larger droplet size) because these tended to overlap for the smaller droplet sizes and could appear as a single bright spot instead of two. In such cases, only one peak was obtained in the wavelet transform (refer to Figure 2.19(a)), the position of which was then assumed to be the droplet centre. According to the analysis, the discrepancy between droplet centres

from focused to defocused images is almost independent of droplet size. Therefore, the estimated error in centre discrepancy in both x and y directions, obtained for the mono-dispersed droplets (by linear fitting of the measured discrepancies), should be the same for a spray with a distribution of droplet sizes, since the degree of defocus of the ILIDS optics was not changed. The respective estimated errors, depending on the y position in the object plane, were subtracted from the position of the centre of each fringe pattern in the ILIDS images. For each of the fringe patterns, the corresponding pair of glare points was sought within a search window, defined in the object plane. The size of the search window was set by the remaining discrepancy in both directions obtained in the previous section (Figures 2.21(b) and 2.21(a)) using the mono-dispersed droplet stream. In the present case, it was set to 100 μm in both directions. A smaller size of search window would result in higher accuracy in finding correct pairs of glare points and fringe pattern but could simultaneously decrease the probable validated pairs, and hence a compromise had to be made. If more than one candidate was present, the one with minimum error in both x and y directions was chosen.

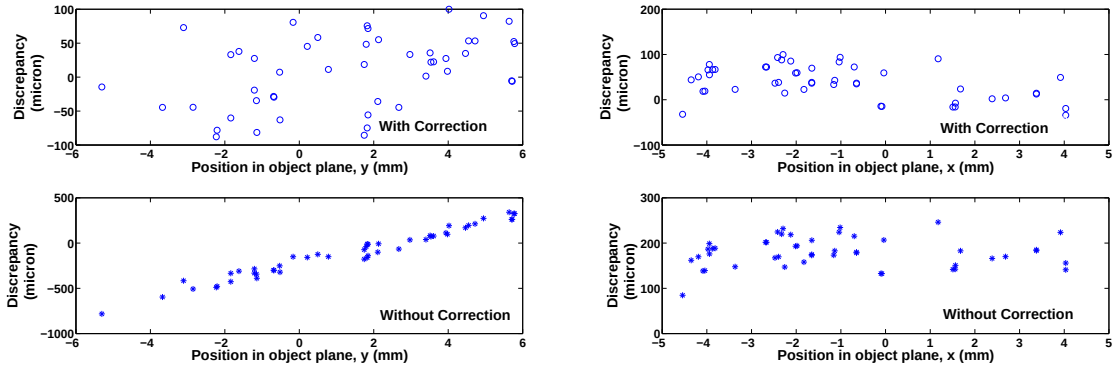
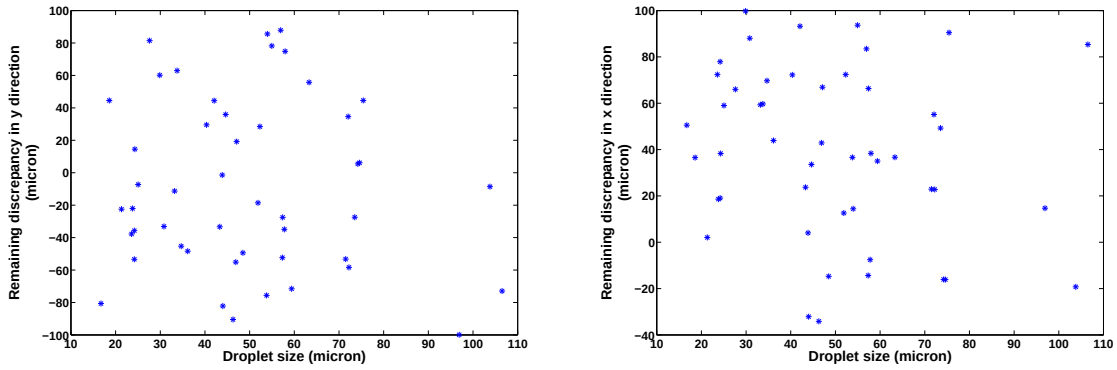


Figure 2.23: (a) top: Centre discrepancy between ILIDS and PIV images in the horizontal (y) direction as a function of y position in the object plane for the spray. The discrepancy was obtained after subtracting the estimated error (resulting from linear fit of the measured discrepancy for the mono-disperse droplet stream) from droplet centres in the ILIDS image. bottom: The same information without correction. (b) top: Centre discrepancy in the vertical (x) direction as a function of x position in the object plane. The discrepancy was obtained after subtracting the estimated error from droplet centres in the ILIDS image. bottom: The same information without correction.

In total, 68 droplets were detected on the ILIDS images, of which 50 had their corresponding glare points identified immediately. Since the defocusing inevitably caused a small increase in the viewing area with respect to the focused image due to the way in which defocusing was performed in our case, there is a possibility that the droplets near the edges of the defocused ILIDS images did not appear in the corresponding PIV images. In such cases, a fringe pattern in the ILIDS image may not have any corresponding glare points on the PIV image. The final discrepancies of the droplet centres in y and x directions are plotted in the top part of Figure 2.23(a) and Figure 2.23(b), respectively. In order to demonstrate the advantage of the present approach, the corresponding discrepancy without correction is also calculated and shown in the bottom part of Figure 2.23(a), 2.23(b). The droplet centre discrepancy along the y direction, with correction, reduced from about 1,000 μm to less than 100 μm. In terms of pixels, this will be a reduction from about 100 pixels to below 10 pixels. Considering the SMD, the final discrepancy now becomes of the order of a droplet diameter. Similarly, in the x direction, the error reduced to the same order which otherwise would have been about 200 μm without correction. Without applying the correction to the location of the droplet centre, it is not possible to find the correct pairs of fringe pattern and glare point.



(a) (b)

Figure 2.24: (a) Remaining droplet centre discrepancy in horizontal direction (y) as a function of droplet size. (b) Remaining droplet centre discrepancy in vertical direction (x) as a function of droplet sizes.

Figures 2.24(a) and 2.24(b) show the variation of the residual discrepancies with

respect to droplet size, in both x and y directions, respectively, which can be observed to be completely random in both cases. This is because the discrepancy has negligible correlation with droplet size, as shown in Figure 2.18(d). It should be mentioned here that the average inter droplet distance, for the above case, was of the order of 50 times the SMD of the droplets. Thus, it is much larger than the dimensions of the search window, which was about twice the SMD. For a dense spray, if the inter-droplet distance reduces to about the size of the search window, then the task of finding the corresponding pair of fringe pattern and glare points can become inaccurate. Hence, the present approach becomes increasingly reliable in identifying matching fringe patterns and pairs of glare points as the spray density reduces.

2.5 Combined ILIDS and PIV measurements

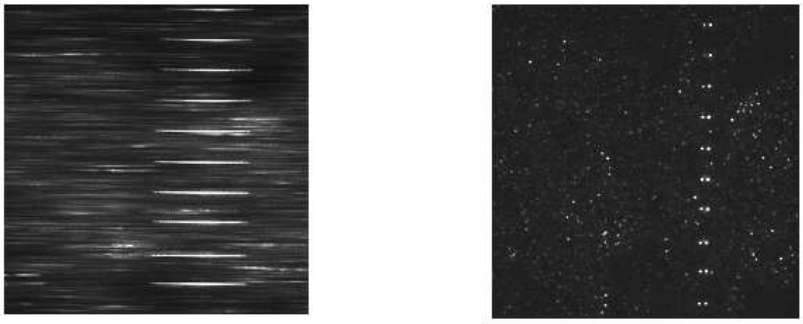


Figure 2.25: Simultaneous ILIDS (left) and PIV (right) images corresponding to the monodispersed droplet stream surrounded by co flowing air seeded with aluminium oxide particles.

In order to measure the gas velocity in the vicinity of droplets by PIV, air, seeded with aluminium oxide particles, was allowed to flow around the mono-dispersed droplet stream. The seeding particles were added to the coflowing air before it entered the spray rig. In this section, the data processing algorithm and the corresponding results are presented for one set of experimental images obtained from the combined measurements. The same operating condition of the droplet generator was maintained as in the absence of seeding. Sequential images were collected with a time interval of 40 μs. Both "seeding" particles and droplets were contained in the focused PIV

images, in which the glare points had to be identified and removed so that the resulting images would be processed to obtain the gas velocity. Figure 2.25 shows simultaneous ILIDS and PIV images for the case of a mono-dispersed droplet stream. The overall effect of the presence of seeding particles was to decrease the signal to noise ratio, making the detection of droplets more difficult. In the ILIDS image, the "seeding" particles were also defocused and so the image looked similar to that of a dense spray. For the same droplet number density, this results in validating lesser number of droplets as compared to the case without the seeding particles. But the defocused seeding particles did not produce regular fringe patterns and so were not detected while processing the ILIDS images. In PIV processing, the scattering intensity from a "seeding" particle sometimes exceeded the intensity threshold imposed by the algorithm to discriminate between seeding particles and droplets.

2.5.1 Droplet filtering from PIV images

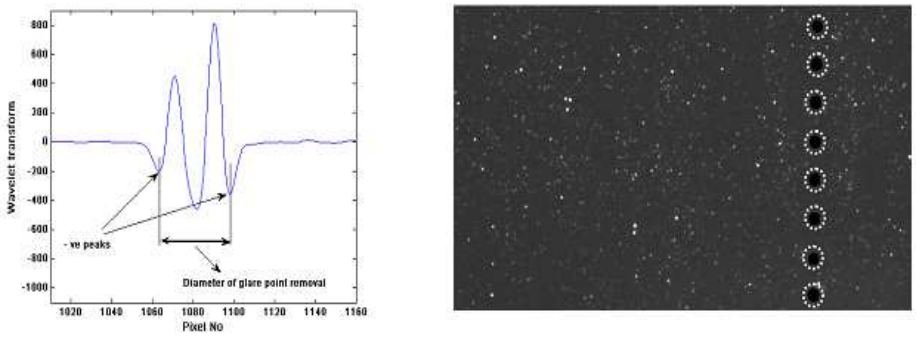


Figure 2.26: (Left) Demonstration of identification of glare points in PIV image using the wavelet transform. (Right) The PIV image after removal of the glare points (the boundaries associated with the removed glare points are shown as dotted circles).

The pair of PIV images was processed to obtain the geometric centres of the glare points and the same glare points at both time instants. The pair of ILIDS images was processed to obtain the geometric centres of the fringe patterns and the size and velocity of the droplets. For each fringe pattern, corresponding glare points were detected in the PIV images, as described in the previous section, after incorporating the correction for droplet centre discrepancy. The glare points in the PIV images

were required to be removed in order to be able to obtain gas velocity. Thus, in the PIV image, around each centre determined by the glare points, a circular area corresponding to the measured droplet diameter (from ILIDS) was removed. However, this approach has a limitation in the sense that it was not always possible to match all of the glare points in the PIV image with their corresponding fringe patterns in the ILIDS image. Also, the filtering of the glare points depends on the accuracy of diameter determination during processing of ILIDS image. Figure 2.26 shows the method for the removal of glare points followed in this work based on the wavelet transform. As shown in the figure, each pair of glare points resulted in three negative peaks, with the outer ones completely encompassing the positive pair of peaks. A circular region centred on the middle of the glare points, and with diameter equal to the distance between the two extreme negative peaks, can be thought of as being occupied by the droplet. Hence, the pixel intensity values corresponding to this region were set to zero intensity. For overlapping glare points, the transform resulted in two negative peaks only, instead of three, and pixel intensity values were set to zero based on those peaks only.

The glare points, removed from the PIV image, were those that had corresponding fringe patterns in the ILIDS image. However, under the present experimental conditions, for any given pair of instantaneous images, the number of fringe patterns detected in the ILIDS image was only about 30% of the number of glare points detected in the PIV image. In other words it was not possible to detect all of the fringe patterns in the ILIDS image, particularly when the droplet number density was too high or the signal to noise ratio was poor. This would eventually result in the corresponding glare points remaining undetected in the PIV image as well. In such cases, the undetected glare points (especially from relatively larger droplets) could produce bias in the PIV correlation. Hence, it was decided to remove all of the detected glare points in the PIV image. Thus, not all of the glare points in the PIV image could be validated against the fringe patterns from ILIDS. For such glare points, there was no matching—or, at least, none detected—fringe patterns in the ILIDS image and thus the droplet size/velocity information corresponding to those

droplets was not available. Figure 2.26 shows the same PIV image from Figure 2.25 after removal of glare points.

2.5.2 Calculation of the gas velocity through PIV and integration of the result with ILIDS

The focused PIV images, filtered to retain only seeding particles, were now processed to obtain gas velocity. Use of a conventional PIV algorithm for this purpose is not advisable, because of the resulting non-uniform seeding particle concentration due to droplet removal. Hence, as described in Section 2.2, the modified PIV algorithm (Ronneberger *et al.*, 1998) was used in conjunction with the "masking technique". The digital mask was created with pixel intensity values of "zero" for the pixels corresponding to the circular region from where the glare points had been removed. A pixel intensity value of "one" was assigned for the remaining pixels, which corresponded to the gas phase. Application of the modified algorithm over the simulated PIV images (Section 2.2) confirmed that when the size of the removed area in the PIV image became similar to that of the interrogation window, the error in the resulting displacement increased. This error was even greater when the displacement was of the order of one pixel or less. Since the diameter of the area of the removed glare points was about 30 pixels in case of the droplet generator, the interrogation window area was hence chosen to be 64×64 $pixel^2$. Thus, there is a trade-off between accuracy in velocity and spatial resolution. The seeding density was 15 particles within the interrogation window. In the case of the droplet generator considered here, the seeding density could have been made higher since the larger droplet size (relative to spray) resulted in a large contrast in light intensity between the droplets and seeding particles. But, for the spray, a higher seeding density was not used as this would have adversely affected the detection of droplets and so would have resulted in a loss of validated pairs of fringe pattern and glare points.

After calculating the gas velocity, the result was integrated with that of ILIDS. This is necessary in order to assign the droplet velocity and size at the appropriate

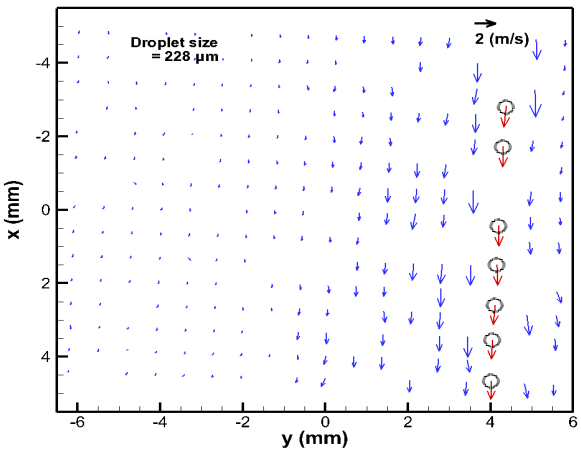


Figure 2.27: Simultaneous droplet and gas velocity vector plots for the case of the mono-sized droplet stream surrounded with seeding particles at a given instant. Bold vectors represent droplet velocity, which is scaled down by a factor of 5.

locations of the PIV images, which correspond to the location of the removed glare points. Though droplet velocity can be obtained both through ILIDS and PIV processing, the former includes diameter validation for the corresponding droplet at the two subsequent time instances. Since this is not always possible for the case of glare points in PIV, ILIDS image processing is more likely to be the more reliable method. However, there is one additional reason behind finding the corresponding glare points in the images at both time instances through particle tracking. Droplet size and velocity from ILIDS are assigned only to those glare points that have corresponding fringe patterns in the images at both time instances. The centre of a given droplet in the object plane was decided based on the centre of the glare points. Figure 2.27 shows the simultaneous velocity vectors for gas and droplets at a given instant. As expected, the gas velocity is almost negligible away from the droplet stream but increases gradually close to it. The average droplet size estimated from ILIDS was 228 μm. The velocity of the droplets was of the order of 10 m/s while that of gas in the vicinity of droplets was of the order of 1 m/s. The minimum distance between the droplet centres and gas velocity vectors was about 0.5 mm, which is expected because of the spatial resolution ($\approx$0.6 mm), obtained from the gas velocity in the PIV image.

2.5.3 Application to a Spray

Application of the combined technique to a polydisperse spray (with seeded surrounding air) is more challenging as compared to the case of droplet stream. The combined effects of increase in droplet number density and the presence of seeding particles tend to reduce not only the number of validated fringe patterns in the ILIDS images but also the corresponding glare points in PIV image. Before performing the combined ILIDS and PIV experiments with spray, it is essential to quantify the discrepancy in the droplet centre for the particular optical setting (especially the degree of defocus). For this purpose, as explained before, one has to follow the laborious task of positioning the droplet generator at different locations to image the droplet stream at various positions in the CCD array under the same optical settings. In order to avoid this inconvenience, accounting for the fact that the discrepancy in droplet centre is independent of the droplet size, the combined ILIDS and PIV images were captured corresponding to any dilute regions in the spray (where, inter-droplet distance $\gg$ droplet size) without seeding for the gas. Thus the one-to-one correspondence between the fringe patterns and glare points could be established and the correlation between the discrepancy and droplet position could be established.

Application of the present approach−including the method for eliminating the discrepancy between droplet centres on focused and defocused images, removal of glare points from the PIV image and subsequent processing of the filtered PIV images−is briefly demonstrated in Figure 2.28 for a polydisperse spray with gas phase seeding. In order to quantify the discrepancy in droplet centre between ILIDS and PIV images, 50 simultaneous images were captured through both the ILIDS and PIV cameras, in a dilute region of the spray without seeding particles in the surrounding air flow. The discrepancy between the droplet centres in the object plane, for both the horizontal and vertical directions, was found and then represented by a linear fit (shown at the top part of Figure 2.28). The pair of ILIDS and PIV images of the spray with seeding particles, the PIV image after filtering out the glare points (the removed glare points shown as the dotted circles) and the simultaneous droplet and gas velocities, obtained

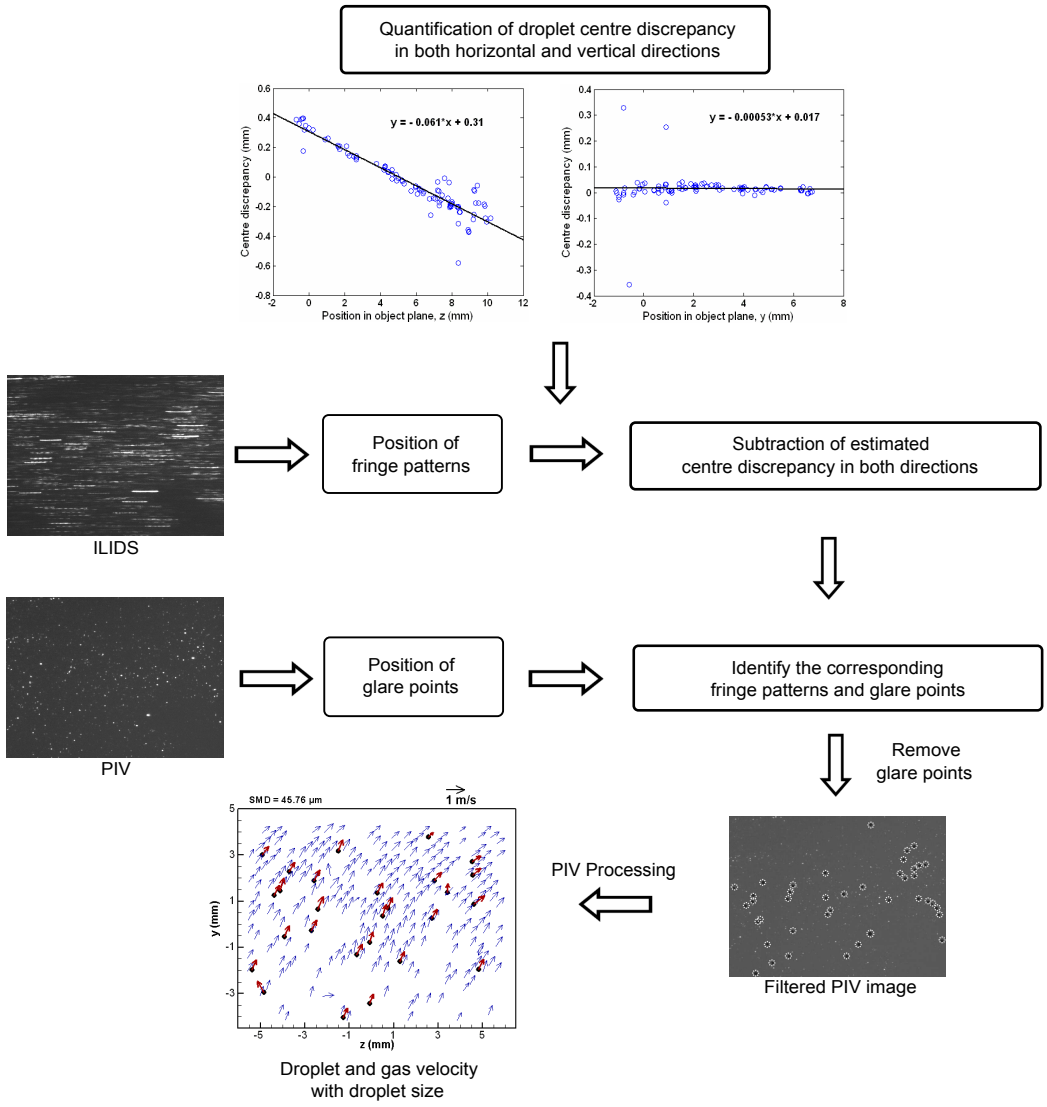


Figure 2.28: Illustration of the image processing details of the combined ILIDS and PIV technique. Boundaries of the removed glare points from the PIV image are shown as dotted circles. In the plot of simultaneous droplet and gas velocities, the blocked disks represent droplets and the associated bold vectors represent droplet velocity.

after processing PIV images, are also shown in the same figure.

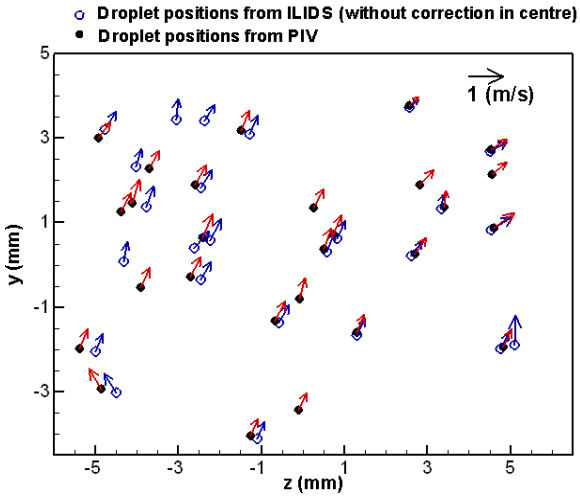


Figure 2.29: Droplet positions and velocities from ILIDS (open circles) and PIV (blocked circles). Droplet positions from ILIDS are plotted without correction for centre discrepancy.

Figure 2.29 shows the positions of the droplets, corresponding to the image pairs of Figure 2.28, obtained simultaneously from ILIDS and PIV (shown as open and blocked circles respectively). The droplet positions from ILIDS do not include the corrections for the centre discrepancy. The droplet positions from PIV are equivalent to the positions obtained from ILIDS after subtraction of corrections for centre discrepancy. As can be observed, the position of a given droplet when obtained through ILIDS differs from that obtained through PIV and the difference can be as large as 1 mm (1,000 μm) towards the left side of the figure and it decreases towards right side. This shows that straightforward use of droplet positions obtained from ILIDS can certainly lead to erroneous estimation of the droplet-gas velocity spatial correlation, i.e. when calculated as a function of the distance between position of the droplet and its surrounding gas velocity vectors.

2.6 Summary

This chapter describes a new approach towards simultaneous two-phase measurements in sprays by combining the out-of-focus imaging ILIDS technique with the in-focus imaging PIV technique. ILIDS provides planar droplet size and velocity, while the

gas velocity in the vicinity of individual droplets is obtained by PIV. The advantage of the approach lies in its capability of identifying the same droplets in both images, thus making it possible to associate the droplet size/velocity obtained from the ILIDS image to the glare-points in the PIV image. The glare-points from the PIV image are removed retaining only seeding particles, which follow the gas phase flow. The PIV images are then processed to obtain the gas velocity in the vicinity of each droplet. The details of the ILIDS and PIV image processing algorithms are described.

Experiments with a stream of monosized droplets revealed that the defocusing of the ILIDS technique leads to a discrepancy between the centre location of the given droplet on the defocused and focused images. An analysis was performed by considering a simple optical configuration. Both the theory and measurements show that the discrepancy varies almost linearly with the position in object plane for a given degree of defocus and can be as large as 1,000 μm. The estimated discrepancy, obtained from experiments with a droplet generator, can be subtracted from the centre of fringe patterns in the ILIDS images, from a polydisperse spray. This approach was shown to reduce the discrepancy from about 1,000 to about 100 μm and thus significantly enhance the probability of correctly identifying corresponding pairs of fringe patterns and glare points in a polydisperse spray, without seeding. The remaining discrepancy was found to be mostly due to inaccuracy in locating the centre of the fringe pattern during ILIDS processing.

Simultaneous ILIDS and PIV measurements are reported for a monodispersed droplet stream with air, 'seeded' with particles, flowing around it. Finally, application to a polydispersed spray 'with seeding' particles in air is presented to demonstrate the applicability of the technique. Also, the position and velocity plots of 'only' droplets from a spray, obtained simultaneously through ILIDS and PIV, are shown, demonstrating the importance of corrections for centre discrepancy. It is concluded that after elimination of the droplet centre discrepancy, the combined ILIDSPIV technique can be applied in a polydispersed spray for simultaneous two-phase measurements.

Chapter 3

Two phase interaction in an isothermal spray

The present chapter aims at investigating the interaction of a polydisperse spray with the entrained air flow field in the model spray dryer rig of Figure 2.13, as described in Chapter 2. The degree of interaction between the two phases can be quantified by measuring the spatial correlations of droplet-gas velocity fluctuations *conditional* on droplet size. However, such measurements necessitate the challenging task of simultaneous planar measurements of properties of both phases in the spray and so, have been rarely reported in the literature. Combined ILIDS and PIV technique, as described in the previous chapter, provides an unique way to measure not only the planar velocity of both phases but also the droplet size and droplet concentration in a spray. The combined technique was applied to the polydisperse water spray with seeded coflowing air in the spray dryer rig and the raw images were processed using the image processing algorithms described before. Attention is paid to both uncertainty and consistency of the turbulence data. The spatial droplet-droplet and gas correlations are obtained and compared with the droplet-gas correlations in order to understand the mechanism of momentum transfer between the two phases. The instantaneous droplet concentration is also measured to examine the influence of the entrained flow field on the droplet number density fluctuations, which may be associated to droplet clustering.

3.1 Measurement location

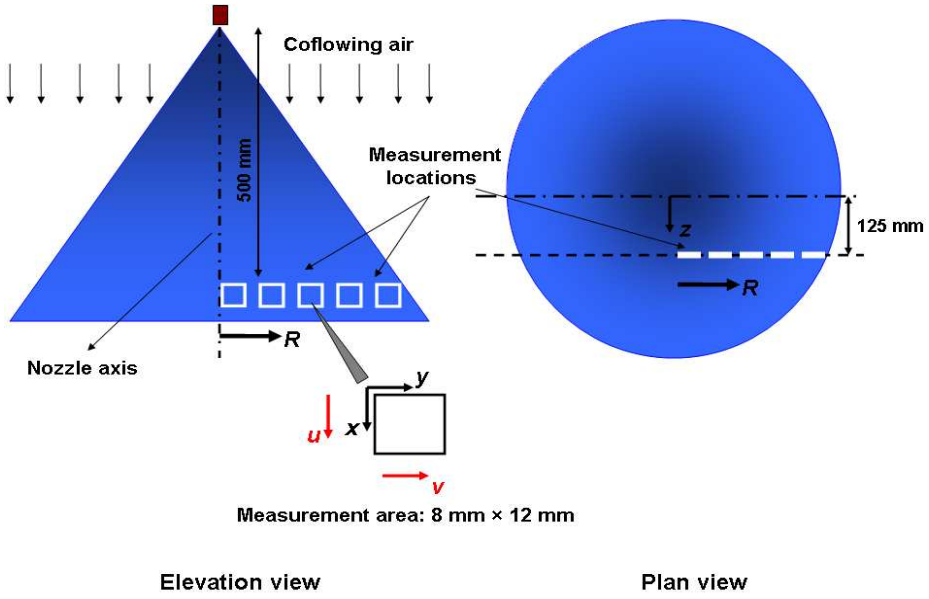


Figure 3.1: Measurement locations in the spray and the coordinate system.

The combined ILIDS and PIV technique, as described in Chapter 2, was applied to a solid cone water spray in the model spray dryer rig. The flow arrangement and the experimental set-up were depicted in Figure 2.13. The spray was surrounded by co-flowing air, seeded with micron-sized particles. The water and air feed rates to the nozzle were of the orders of 1.5×10^{-3} kg/s and 0.12×10^{-3} kg/s respectively. The flow field was illuminated by a double pulse Nd:Yag laser (λ=532 nm) and the scattered light from the droplets and seeding particles (at scattering angle, $\theta = 69°$) were captured by two cameras, one for the defocused imaging (ILIDS) and the other for the focused imaging (PIV). Both cameras were aligned to view the same area within the spray. Each droplet was imaged as a fringe pattern and a pair of glare-points in the ILIDS and PIV cameras respectively. The defocused images of seeding particles also appeared in the ILIDS image but without any fringe patterns. The triggering of the laser and the cameras were synchronised so that the first and the second frame of each ILIDS and PIV image pairs were captured corresponding to the respective laser pulses.

Since the interaction of the entrained flow field and the spray is expected to be

stronger downstream of the nozzle, the combined ILIDS and PIV measurements are reported for five different cross-stream locations, 500 mm below the nozzle exit, as presented in Figure 3.1. At any given measurement location, the notations 'x' and 'y' refer to the local axial and cross-stream directions respectively, both lying on the plane of the laser sheet. The corresponding instantaneous velocities are denoted by 'U' and 'V' and, velocity fluctuations by 'u' and 'v' respectively. Throughout the text, the subscript 'd' and 'g' denote droplet and gas respectively. Similarly 'overbar' over any quantity indicates time-averaging and the subscript 'r' denote root mean square (rms) of that quantity. The notation 'z' refers to the direction perpendicular to the laser sheet and is measured from the nozzle axis, and 'R' refers to the distance from the nozzle axis till the beginning of the measurement area at any cross-stream location. Since the measurement locations were situated far downstream of the nozzle, the mean droplet and gas flow velocity in the vertical (x) direction is expected to be dominant (as verified to be true later in the vector plots of the mean velocity of both phases). Hence the effect of the velocity component perpendicular to the laser sheet (in z-direction), causing out of plane motion of the droplets and the seeding particles, can be considered negligible in the present case.

Because of the experimental constraints in the set-up, measurements were performed at an off-axial position of 125 mm along the z direction (Figure 3.1), in order to maintain the required object distance between the viewing area and the collecting lenses in ILIDS. Measurements at nozzle axis required the object distance to be larger, resulting in very low collecting angle for the given aperture size of the collecting lens, thus limiting the minimum measurable diameter of the ILIDS technique. Thus the phrase "cross-stream" is used instead of "radial" throughout the text. Each measurement area was approximately 8×12 mm^2 and the cross-stream measurement locations were located at $R = 0$, 50, 100, 150 and 185 mm respectively from the nozzle axis. Again, limitations in the experimental set-up did not allow measurements beyond $R = 185$ mm.

The mass loading (ϕ_m) is defined as the ratio of the mass of the droplets within the measurement volume to the total mass of the gas in the same volume and was obtained

by considering the average number of droplets detected in the PIV image. For the present experimental locations within the spray, ϕ_m was about 5%. The corresponding volume load (ϕ_v) was about 0.006%. Since this is much below 3%, the droplet-droplet interaction was considered negligible (Hardalupas *et al.*, 1989). Elghobashi (1994) has pointed out that for a volume load between 0.0001% and 0.1%, turbulence modification may occur. Since the volume load in the present study is within this regime, the momentum exchange between the two phases can be expected.

For each measurement location, 1700 image pairs were captured through each of the cameras. Since the validation rate[1] in the two phase measurements was low (about 30%), this large number of images was required to reduce the statistical uncertainty of the measured quantities. The time scale of the air flow turbulence was approximately 0.1 *sec* (Kavounides, 2006), signifying that the flow is relatively 'lazy' as compared to other laboratory scale turbulent flows. Hence, the repetition rate of the laser was set to 1 Hz, so that the acquired samples remained statistically independent.

3.2 Drop size distribution

The probability of the measured droplet size distribution (from ILIDS) is shown in Figure 3.2 for all of the five the measurement locations. Considering the accuracy of the droplet size measurement for the present case ($\pm$ 3.25μm), the size distributions can be considered to be independent of the measurement locations. The Arithmetic Mean Diameter (AMD) and Sauter Mean Diameter (SMD) of the drop size distribution at any measurement location were of the order of 35μm and 45μm respectively. The minimum measurable droplet size was 20μm. The size distribution shows that most droplets are in the range of 20–40 μm causing the distribution to be skewed towards left. The calculated statistical characteristics of the spray, include mean droplet velocity, rms of droplet velocity fluctuations and the spatial correlations of velocity fluctuations for three droplet size classes (denoted by notation

[1]Here the validation rate is defined as the ratio of the number of glare points in the PIV image for which the corresponding fringe patterns in the ILIDS image could be found for both image pairs to the total number of the glare points detected in the PIV image.

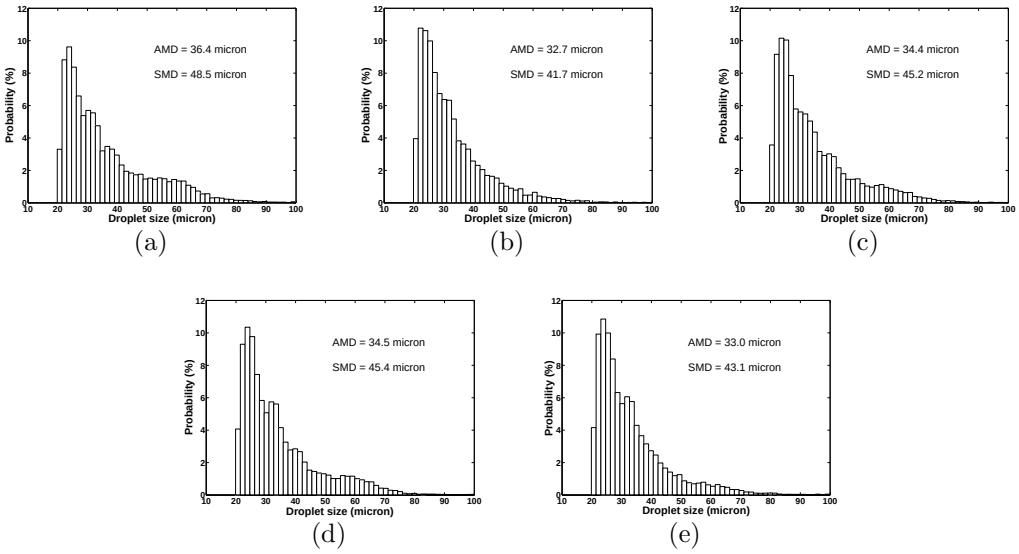


Figure 3.2: Probability of droplet size in the measurement region at the cross-stream location, (a) $R = 0\ mm$, (b)$R = 50\ mm$, (c)$R = 100\ mm$, (d)$R = 150\ mm$ and (e)$R = 185\ mm$.

'D') with overall size range (ΔD) of 15 μm. Higher size classes were 20–35μm, 35–50μm and 50–65μm respectively. Still higher size classes were not considered to avoid higher statistical uncertainty. The range of the droplet size classes was decided as a compromise between higher statistical uncertainty (with smaller ΔD) and obtaining size averaged information (with larger ΔD).

The Stokes number (St) of a droplet size class is defined as the ratio of the droplet aerodynamic time constant (τ_p) over an appropriate turbulent time scale of the flow (τ_f). τ_p or the 'particle relaxation time' is given by, $\tau_p = \rho_p d_p^2/18\mu$, where ρ_p and d_p are the particle density and diameter respectively and μ is the viscosity of the fluid. The Reynolds number of the droplets being very small in the present case (≈ 0.1 based on mean slip velocity), the assumption of Stokes flow around the droplet remains satisfied. The characteristic time of the spray (τ_f) at the present measurement locations is chosen as the ratio of a large eddy length scale ($\approx 100\ mm$) to the axial rms velocity of the air flow on the spray axis (at $R = 0\ mm$). Thus, the values of St for the three droplet size classes were found to be of the order of 0.005, 0.015 and 0.025 respectively. These values suggest good response of the droplets to

the corresponding large scale fluid motion.

At $R = 0\ mm$, assuming isotropic turbulent flow, the Taylor time scale (τ_λ) and Kolmogorov time scale (τ_η) were estimated. The Taylor microscale (λ) was obtained through the dissipation rate (ϵ), which, in turn, was calculated from the spatial gradient of the turbulent fluctuations of axial component of the gas velocity in axial direction. The Kolmogorov scale (η) was estimated again from the dissipation rate. The above mentioned length scales were obtained according to the following equations (Tennekes and Lumley, 1972):

$$\epsilon = 15\nu\overline{\left(\frac{\partial u}{\partial x}\right)^2} \tag{3.1}$$

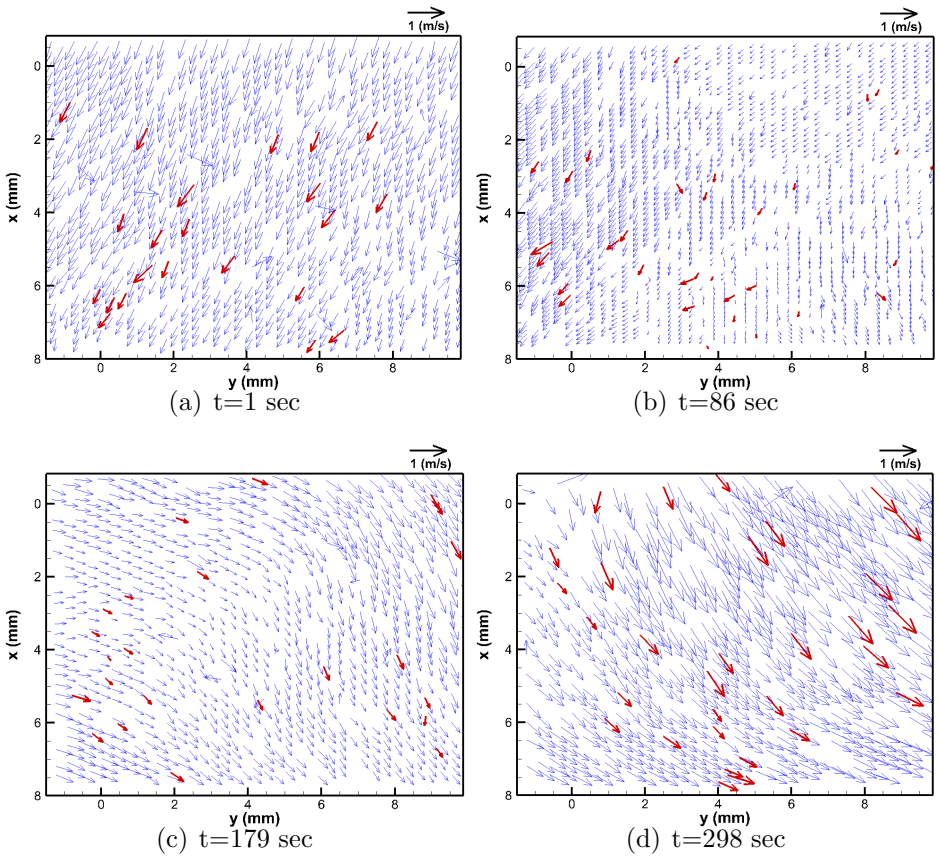
$$\lambda = \left(15\nu\frac{u_r^2}{\epsilon}\right)^{0.5} \tag{3.2}$$

$$\eta = \left(\frac{\nu^3}{\epsilon}\right)^{0.25} \tag{3.3}$$

where ν is the kinematic viscosity of the carrier phase. The Kolmogorov scale and the Taylor micro scale were estimated to be of the order of 0.55 mm and 0.085 mm respectively. Thus, the size of all of the considered droplets was less than the Kolmogorov length scale of the flow. The Stokes numbers for the 20–35μm, 35–50μm and 50–65μm droplet size classes were of the order of 4.32, 10.7 and 19.6 respectively, based on the Kolmogorov scale, and 1.12, 2.78 and 5.09 respectively, when based on the Taylor scale. This signifies partial response of the smaller droplets to the flow at these length scales, while the largest size has limited response.

In order to evaluate the gravitational effect on droplets, the terminal velocity of the droplets (u_t) was determined according to $u_t = \tau_p g$, where g is the acceleration due to gravity. The terminal velocity is the maximum velocity of a body falling through a viscous fluid, when the dragging force of the medium is equal in magnitude and opposite in direction to the force of gravity. In the present study, the terminal velocities for the 20–35μm, 35–50μm and 50–65μm droplet size classes were of the order of 0.02 m/s, 0.05 m/s and 0.09 m/s respectively.

3.3 Droplet/gas instantaneous, mean and turbulent velocity



(a) t=1 sec (b) t=86 sec

(c) t=179 sec (d) t=298 sec

Figure 3.3: Instantaneous velocity plot of simultaneously measured droplet and gas velocities at the cross-stream measurement location, $R = 0\ mm$. The bold vectors in red represent droplet velocity.

The instantaneous velocity plots of droplets and gas velocities (for four different arbitrarily chosen time instants) at the measurement location, $R = 0\ mm$ are shown in Figure 3.3. As can be observed from the velocity plots, the droplet-gas relative velocity is small and–in this case–the droplets and the gas velocity vectors are reasonably aligned.

Since ILIDS uses Particle Tracking Velocimetry (PTV) for calculation of the droplet velocity, the droplet position inside the measurement area was always random. So, unlike PIV, no regular grid could be associated with the instantaneous droplet

velocities. Thus, for calculation of the mean velocity, the observed experimental area was divided into regular and rectangular sub-areas or windows. The droplet velocities within each of these windows were averaged over all samples and the spatially-averaged velocity was associated with each particular window at its centre. If the size of these sub-areas were chosen to be too small, the number of samples would be low and hence the statistical uncertainty would become too large, while conversely if the sub-area were chosen to be too large, the spatial resolution would be reduced. Since the number of detected droplets within a given window depends on the droplet size class, the window size was varied for different droplet size classes to ensure accurate statistics. Also, while deciding the size of the window, the local gradient of the mean droplet velocity should be taken into account: a large gradient would require smaller window size. But, since this is not known apriori in the present case, the size of the sub-areas (for a given size class) was selected on a trial and error basis and the final compromise for the spatial resolution of the mean droplet velocity was about 2×2 mm^2 for droplet size class $20-35\mu m$ and 3×3 mm^2 for droplet size classes $35-50\mu m$ and $50-65\mu m$. Since PIV processing results in gas velocities associated with a regular, structured grid, the spatially-averaged mean could be calculated for each position on the grid, where the gas velocity could be defined. The spatial resolution for the mean gas velocity was about 0.15×0.15 mm^2, same as that of instantaneous velocity. It was about an order of magnitude greater than the largest droplet size considered here and only two orders of magnitude greater than the Kolmogorov length scale.

Figure 3.4 shows vector plots of the droplet mean velocity for droplet size classes of 20-35μm, 35-50μm and 50-65μm, and for the gas flow at various cross stream measurement locations (R) starting from the spray axis and moving towards the outer spray region. The mean velocity of droplets of a given size class and the mean gas velocity, at any measurement location, for both axial and cross-stream velocity components, could be observed to be quasi-uniform across the measuring area. Thus, the choice of window size was not extremely critical in the present case. The corresponding root mean square (rms) of velocity fluctuations was also found to show similar trend. Both mean and rms velocity for droplets and gas was found

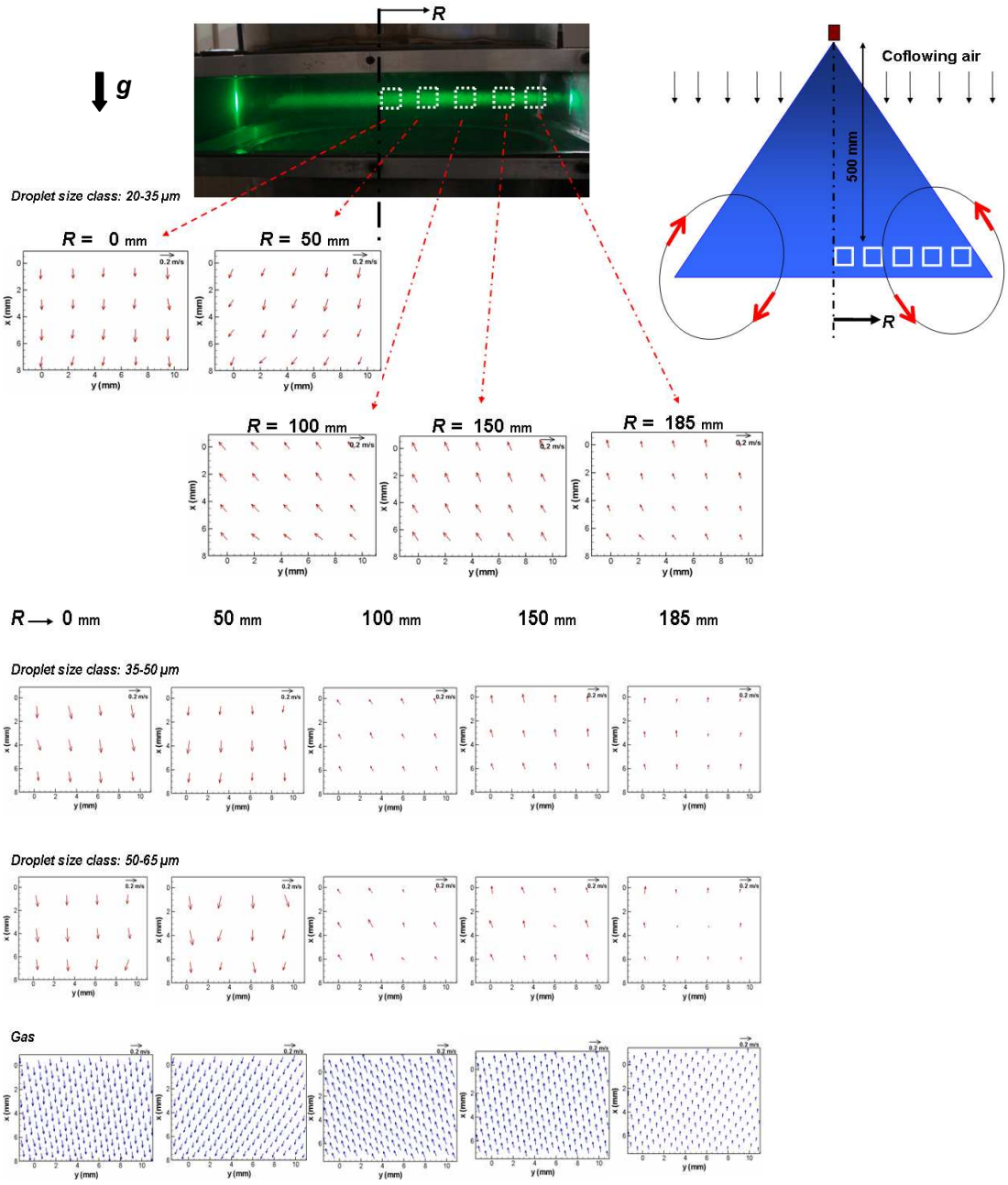


Figure 3.4: Mean velocity for droplet size classes of 20-35μm, 35-50μm, and 50-65μm and for the gas flow for various cross-stream measurement locations, R.

to vary within $\pm 20-30\%$ across the measuring area at any given location. This is possibly because of the smaller size of the viewing area (8×12 mm^2 in the present case) as compared to the length scales of the large eddies of the flow, which was about 100 mm (as explained below). The length scale of the energy containing eddies was assumed to be 1/5 of the jet width (Tennekes and Lumley, 1972). The top of Figure 3.4, shows that the spray flow field, illuminated by the laser sheet, spans the whole width of the rig, and so the gas flow width can be considered the same as the rig diameter, i.e 500 mm.

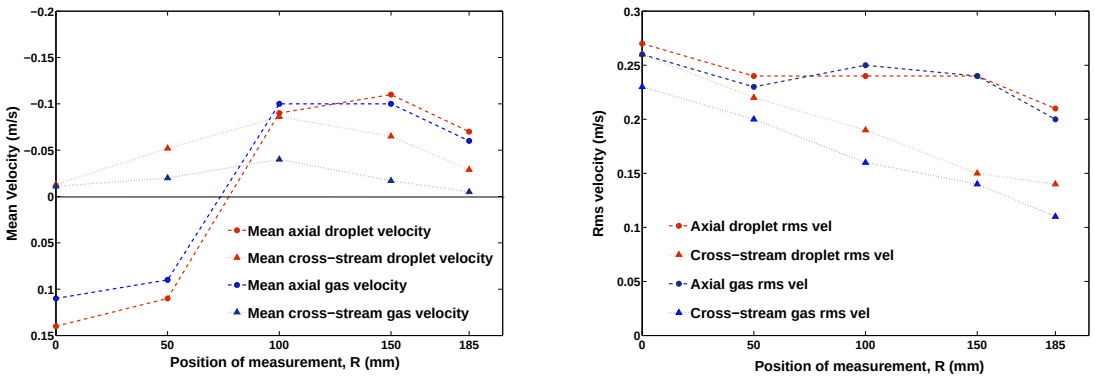
Phase	Axial mean vel. $\overline{U}(m/s)$	Cross-stream mean vel. $\overline{V}(m/s)$	Axial rms vel. $u_r(m/s)$	Cross-stream rms vel. $v_r(m/s)$
D: 20–35μm	0.140±0.025	0.013±0.023	0.279	0.261
D: 35–50μm	0.178±0.033	0.031±0.029	0.295	0.265
D: 50–65μm	0.178±0.041	0.022±0.037	0.277	0.255
Gas	0.113±0.019	0.011±0.022	0.268	0.232

Table 3.1: Area-averaged statistics of velocity of various droplet size classes and gas flow for the first cross-stream measurement location, $R = 0$ mm. The viewing area was 8×12 mm^2.

Considering the case of 1st measurement location, at $R = 0\ mm$, Table 3.1 presents the magnitude of the area-averaged mean velocity with the values of the error bar for a 95% confidence interval and the rms velocity. The statistical uncertainty of any measurement depends on the rms of the fluctuations of the variable and the number of samples. In the present case, the statistical uncertainty increased for higher droplet size class due to reduction of the number of samples, as evident from the probability distribution of droplet sizes in Figure 3.2. Typical uncertainty of both axial and cross-stream mean velocities was of the order of $\pm 0.03\ m/s$. In the cross-stream direction, since the magnitude of the mean velocity is quite low ($\sim 0.02\ m/s$), the uncertainty was of a similar order. At this measurement location ($R = 0$ mm), being close to the spray axis, the axial component was dominant as compared to the cross stream component and so, on average all the droplets move downward in the same direction. The average droplet velocity ($\sim 0.15\ m/s$) was always slightly higher than the average gas velocity ($\sim 0.10\ m/s$) and the droplet velocity of size class of $50-65\mu m$ was about

20% higher than that of size class $20-35\mu m$. Thus, no significant difference is present in the mean velocity between the droplet size classes and between the two phases.

The instantaneous fluctuating velocities (u and v) were calculated by subtracting the respective mean values ($\overline{U}$ and $\overline{V}$) from the instantaneous velocities. The root mean square of the velocity fluctuations (u_r and v_r) were calculated and found to be of the order of $0.2 \sim 0.3\ m/s$ for both droplets of the selected size classes and gas flow, as shown in Table 3.1. It should be noted that the rms velocity in the axial direction was about two orders of magnitude greater than the mean velocity and of the same order as the rms velocity in cross-stream direction. The anisotropy (u_r/v_r), being close to 'one' and almost spatially invariant, indicates that the flow field (within the viewing area considered here) to be nearly homogeneous and isotropic close to the spray axis. Also, the rms velocity of droplets were similar for both velocity components and independent of droplet sizes.



(a) (b)

Figure 3.5: Area-averaged (a) mean and (b) rms velocity, for droplet (size class 20–$35\mu m$) and gas flow for various cross-stream measurement locations, R.

The mean velocity of the droplets and gas flow, for all measurement locations (different R) can be compared in Figure 3.4. Figures 3.5(a) and 3.5(b) show the variation of area averaged mean and rms velocity in both axial and cross-stream direction for droplet size class of 20–$35\mu m$ and gas flow for various measurement positions, R. The droplets, away from centre of the spray, tend to move upwards, i.e "towards the top of the tower". This can be interpreted by the motion of the

air surrounding the spray being entrained into the spray in a recirculating pattern similar to the schematic shown in the top of Figure 3.4. Towards the outer spray, the droplets are prevented from drifting downward under the action of gravity, as might be expected, by the upward component of the gas velocity.

The statistical uncertainty of the velocity estimation at all locations was of similar order as for the case of $R = 0\ mm$. The mean and rms velocity of droplets at any given location were more or less independent of droplet size. Though a small increase or decrease (about 20%) in mean axial velocity of larger droplets (50–65 μm) was observed, as compared to the smaller droplet size class 20–35μm, depending on whether the droplets move downward closer to the spray centre or upward against gravity towards the outer regime of the spray. The velocity of droplets with higher size class was found to be relatively smaller towards outer spray: for instance, the axial mean velocity for 50–65μm droplet size class at $R = 185\ mm$ was of the order of 0.06 m/s, one third of the axial velocity at $R = 0\ mm$. At any measurement location, the axial rms velocity of the droplets (all size classes) and the gas were of the similar order, while in cross-stream direction, the rms velocity of the gas was about 10–20 % lesser than that of the droplets. The fluctuating velocities of both droplets and gas decreased away from the spray axis implying reduction of the turbulent kinetic energy in the outer spray region. In cross-stream direction, considerable reduction in the rms velocity (about 50%) was observed from $R = 0$ to 185 mm, while in axial direction the rms velocity decreased by about 20%. Hence, the anisotropy (u_r/v_r) in both droplet and gas velocity was about 1.1 at $R = 0\ mm$, which increased upto about 1.5 and 1.9 for droplets and gas velocity respectively, at $R = 185\ mm$.

Figure 3.6 presents the scatter plot of fluctuating axial and cross-stream components of droplet velocity ($u_d \sim v_d$) for droplet size class of 20–35μm at $R = 0$ mm, which has no preponderant correlation between the two components of velocity. Similar behaviour was observed for droplets of other size classes and also, at other measurement locations. This is expected, because the measurement location in the spray is far from the injector, and also has no strong normalized Reynolds shear stress, $\sum u_g v_g \ / \ u_{gr} v_{gr} < 0.2$, as shown in Figure 3.7. The shear stress was normalized with

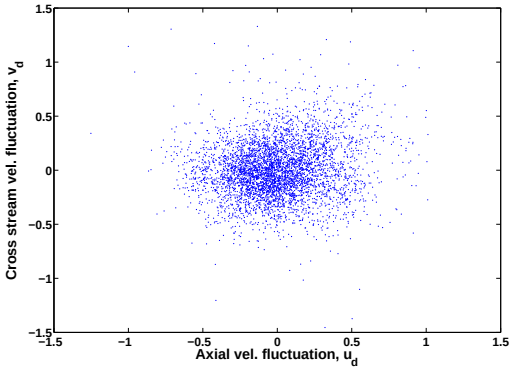


Figure 3.6: Scatter plot of instantaneous fluctuating droplet velocity, $u_d \sim v_d$, for droplet size class 20–35μm at $R = 0\ mm$.

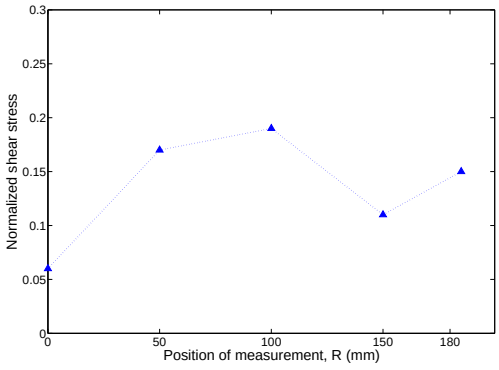


Figure 3.7: Normalized shear stress obtained from the gas velocity for various cross-stream locations, R.

respect to the respective rms velocities and was area averaged. The magnitude of the shear stress was maximum at $R = 100\ mm$.

The trend in the turbulence statistics of the gas flow as described above is similar to the single-phase turbulence measurements of a confined axisymmetrical water jet as reported by Risso and Fabre (1997). At about 400 mm distance from the nozzle (diameter 10 mm), the authors observed very low magnitude of the mean velocity and its gradient in both axial and radial direction, and also very small Reynold's shear stress indicating negligible turbulence production and dominance of diffusion. Also, similar to the present study, the rms velocity in axial direction was about twice that of the mean velocity. The anisotropy at the jet axis was close to 'one', which increased away from the spray axis. These trends are attributed to the lateral confinement which forces the mean flow to vanish far downstream of the nozzle, while leaving the main role to the fluctuating motion. However, unlike the results reported here, Risso and Fabre (1997) found an order of magnitude increase in the axial rms velocity near the wall of the cylindrical confinement compared to that at the jet axis. Though the reason behind such trend was not mentioned in their work.

	Terminal vel/Axial mean vel ($u_t/\overline{U_d}$)		Terminal vel/Axial rms vel (u_t/u_{dr})	
R	0 mm	185 mm	0 mm	185 mm
D: 20–35μm	0.14	0.26	0.07	0.09
D: 35–50μm	0.28	0.69	0.17	0.22
D: 50–65μm	0.50	1.52	0.32	0.40

Table 3.2: Ratio of the terminal velocity to the mean and rms of the droplet velocity for various droplet sizes for the cross-stream measurement locations, $R = 0\ mm$ and 185 mm respectively.

In order to estimate the gravitational effect on the droplet motion, the ratio of the terminal velocity (u_t) to the mean and fluctuations of the droplet velocity were obtained for different size classes. The ratios $u_t/\overline{U_d}$ and u_t/u_{dr} are shown in Table 3.2 for the measurement locations at $R = 0\ mm$ and 185 mm. Both ratios were found to increase for the larger droplet size classes as expected. The magnitude of the ratios clearly indicate that the influence of the gravity on the droplet motion increases away

from the spray axis and so, can not be neglected.

The trends in the mean and rms velocities in the present study can be compared with the two phase measurements in the far field of a polydispersed particle-laden jet by Prevost *et al.* (1996). The measurement locations in their study was 300 mm downstream from the nozzle where the Stokes number of the droplets were in the range 0.03–5 and the mass loading (ϕ_m) was similar to the present experiment. They found a sharp decrease in the axial rms velocity for both droplets and gas in the radially outward direction from the spray axis compared to the radial rms velocity. Also, the radial rms velocity was smaller for larger droplet size classes closer to the jet axis. Higher level of anisotropy ($\approx$ 1.5–4) was observed for the particles on the jet axis which was attributed to the production of particle turbulence by the mean particle velocity gradients. The rms of both velocity components were nearly equal towards the edge of the jet. The present experimental result shows that the gradient in mean droplet or gas velocity was negligible indicating absence of turbulence production. Also, because of very small Stokes number of the droplets ($\approx$ 0.01 based on large eddy length scales of the flow), the droplet mean and rms velocities (both components) were nearly independent of the drop size. This was primarily due to the flow confinement and also, larger axial locations (500 mm) of the measurement areas down the nozzle.

Again in contrast to Prevost *et al.* (1996), in the present case, only a small decrease in the axial rms velocity of both phases was observed away the spray axis (see Figure 3.5(b)), which resulted in increasing the anisotropy towards the spray edge. Similar observation is also reported in the two-phase measurements of a particle-laden flow downstream of a confined bluff-body by Boree *et al.* (2001). Though in their case, strong radial gradients of mean particle/gas velocity was present in both axial and radial directions and gravitational effect was negligible. Thus, the lateral confinement of the flow may be a reason behind the increasing anisotropy away from the spray axis. Though, Risso and Fabre (1997), in their single phase study of a confined water jet, found a sharp increase in the axial rms velocity towards the wall, which is neither observed in the present study nor in the work of Boree *et al.* (2001). Another possible explanation of this issue of increasing anisotropy can be the stretching of

the vortical structures in the carrier phase due to increasing influence of gravity on droplets towards the outer spray (Table 3.2). This causes creation of a local gradient of the drag force, which consequently results in increasing the rms velocity of the gas flow in the gravitational direction as compared to a particle-free case (Ferrante and Elghobashi, 2003; Yang and Shy, 2005).

3.4 Spatial correlation of droplet and gas velocity fluctuations

Measurement of the droplet-gas velocity correlation terms, appearing in the transport equations for kinetic stress tensor of the droplets and turbulent kinetic energy of the gas phase for a droplet-laden gas flow (with negligible volume fraction of droplets), is essential to give further insight into the two-phase flow physics and to validate some new approaches for modelling the droplet/gas fluctuating motion. However, such measurements are rarely reported in the literature, which includes the PDA measurements by Prevost *et al.* (1996), Ferrand *et al.* (2003) and Boree *et al.* (2001), and the PIV measurements by Sakakibara *et al.* (1996). This prime reason behind the scarcity of data on velocity correlation measurements is the difficulty in obtaining simultaneous planar measurements of both phases. The technique of combining ILIDS with PIV offers such an opportunity. The method of calculating the spatial correlations is described below. It should be noted here that the correlation terms appearing in the TKE equation of the carrier phase (Equation (1.2)) corresponds to the correlation evaluated at the droplet position or at the closest proximity to the droplet. However, this is practically impossible since the droplet always occupies certain space and evaluating the gas velocity *right at* the droplet position is not possible. At the same time, evaluation of those terms right at the droplet surface is challenging, since this would necessitate super resolution measurements. Such measurements (see Tanaka and Eaton, 2010) usually necessitates using a very small viewing area. Hence a large number of samples are required to ensure higher statistical

uncertainty and also, most of the flow structures in the carrier phase can not be captured if the integral length scale is orders of magnitude greater than the viewing area. Therefore, the actual distance from the droplet surface where the correlation terms should be evaluated is an open question. Hence, in the present work, the correlation terms were evaluated as a function of distance from the droplets. This would illustrate the influence of the gas motion away from the droplets on the droplet motion—an aspect that the models depicting the two-way coupling should take into account.

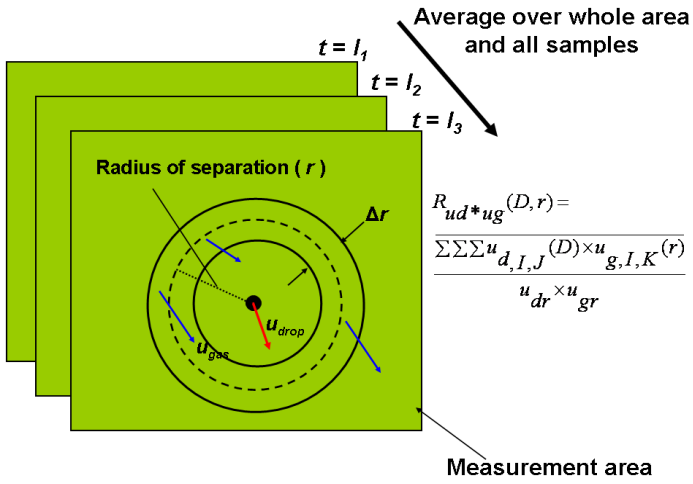


Figure 3.8: The method of calculation of the spatial correlation of the velocity fluctuations. The formula corresponds to the droplet-gas velocity correlation in axial direction, as an example.

3.4.1 Method of calculation of spatial correlations

The velocity correlation terms were calculated over the whole viewing area for each measurement location, R. Since no strong spatial gradients of mean and rms velocity in either axial or cross-stream direction were found within the viewing area, such averaging was expected to have no influence on the magnitude of the correlations. The process of calculating the spatial correlation coefficient of droplet-gas velocity fluctuations, $R_{dg}(D,\ r)$, as a function of droplet size class, D, and distance 'r' is depicted in Figure 3.8.

For every instantaneous image, I, around each droplet position, J, a circle with

a given radius, named 'radius of separation', r, was defined. For each droplet the correlation between the fluctuating droplet velocity and all the fluctuating gas velocities, index K, which have been measured inside an annular ring (defined within $r \pm \Delta r/2$), was calculated. This is done for all droplets belonging to the size class D in that instantaneous image, and then repeated for all image samples, N. Then, the average of all calculated correlations was obtained and normalized with the product of the respective rms of fluctuations of droplet and gas velocity to obtain the final correlation coefficient, R_{dg}, for the size class D and for the radius of separation r. It should be mentioned here that the mean velocity of droplets and gas used to calculate the fluctuating velocity and, the respective rms velocity (used for normalization) were the area-averaged values. Then R_{dg} is calculated for different values of 'r' and for all of the droplet size classes present. Also, the correlations were calculated for several combinations of the different velocity components of the droplet and gas flows and each of the correlations was conditional on different droplet size classes. For example, the following figure shows the correlation coefficient between the axial components of droplet and gas velocities as a function of separation distance, which can be represented as $R_{u_d * u_g}(D,\, r)$ and is given as:

$$R_{u_d * u_g}(D, r) = \frac{\overline{\sum_I \sum_J \sum_K u_{d,I,J}(D) \times u_{g,I,K}(r)}}{u_{dr} \times u_{gr}} \tag{3.4}$$

Where u_{dr} and u_{gr} are the rms of the fluctuating component of velocity of droplet (with size class D) and gas in axial direction and, u_d and u_g are the respective fluctuating components of velocity.

It is worth mentioning that the present approach of calculating the instantaneous spatial correlations of velocity fluctuations at any given radius of separation r from a given droplet inherently assumes directional independency of the correlation around the droplet. The assumption was verified by calculating the normalized spatial correlation (R_{gg}) of the gas flow along both axial (x) and cross-stream (y) directions separately. This is shown in Figure 3.9 for the case of $R = 0\ mm$. The gas correlation

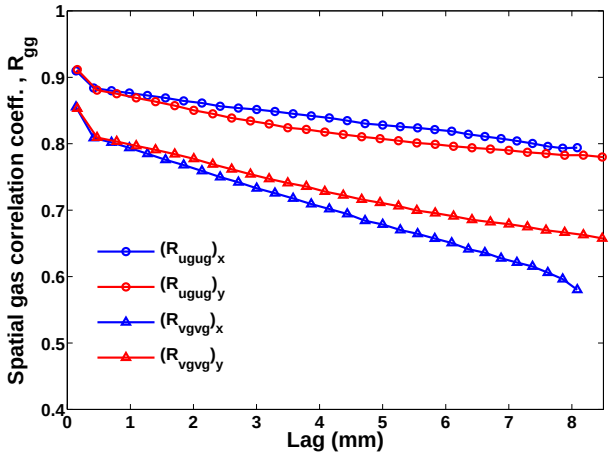


Figure 3.9: Spatial correlation coefficent of gas velocity fluctuations of axial and cross-stream velocity components along both directions at the measurement location, $R = 0$ mm.

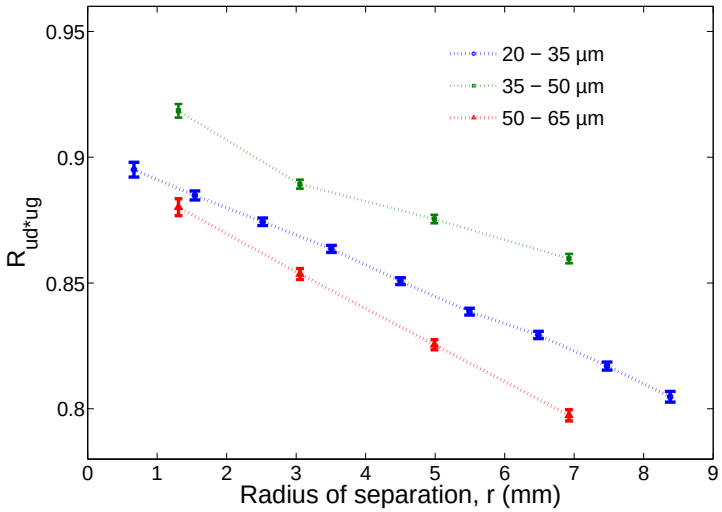
coefficient for axial velocity component along x-direction, as expected, was found to be slightly higher than that along y-direction *i.e.* $(R_{ug*ug})_x > (R_{ug*ug})_y$. The difference was of the order of less than 0.02 at any separation distance. This also indicates the higher accuracy of gas velocity measurement. In the cross-stream direction, the correlation coefficient, R_{vg*vg}, again as expected, was higher along y-direction than the x-direction and the difference was increasing with respect to the separation distance. However, the difference remains less than 0.1 within the separation distance considered here. So the assumption of directional independency of the correlation around the droplet is justified. Similar results were observed for other measurement locations.

The discrete values of the radius of separation, r, and the width of the annular ring, Δr, were chosen as a trade-off between statistical accuracy and spatial resolution of the correlation coefficient. Though one would always prefer to obtain the correlation coefficient as close to the droplets as possible (*i.e.* smaller r), but it should be noted that the number of instantaneous individual correlations that can be obtained, between a given droplet and the surrounding gas velocities, is proportional to both r and Δr. Very small values of r and Δr would decrease the sample space of the instantaneous correlations (for a given number of images), causing higher uncertainty

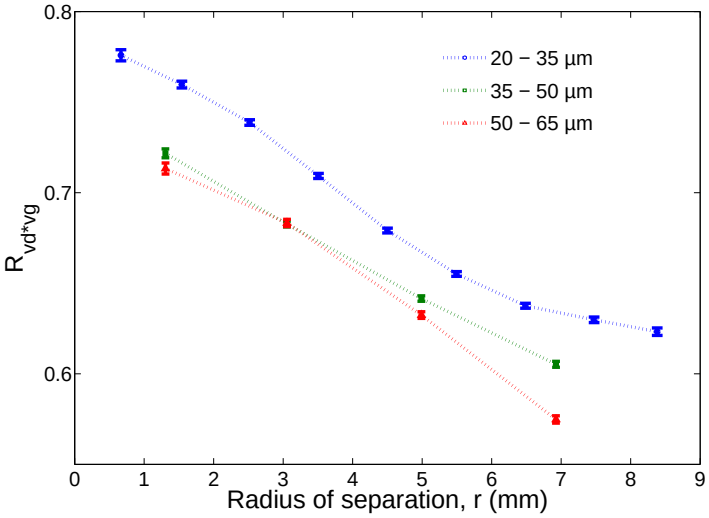
while, the higher values would result in decreasing the spatial resolution of the calculated correlation coefficients. In the present case, the increment of r and the value of Δr were chosen to be 0.5 mm and 1 mm respectively for droplet size class 20–35μm and 1.5 mm and 3 mm for the other two larger size classes resulting in lower spatial resolution of R_{dg} for the larger size classes owing to their lower probability of occurrence. The resolution of the gas velocity vectors from PIV measurements decides the closest possible distance from a given droplet, where the correlation can be calculated. In our case this distance, equal to half of the spatial resolution, is about 0.07 mm same order as the Kolmogorov length scale of the flow. Thus in the present case, the value of R_{dg}, at minimum radius of separation, $r = 0.5$ mm, represents the spatially averaged value of the correlation calculated between $r = 0.07$ mm to 1 mm.

3.4.2 Droplet-Gas velocity correlation

The plots of droplet-gas velocity correlations for axial and cross-stream velocity components, represented as R_{ud*ug} and R_{vd*vg} respectively as a function of radius of separation, r, are shown in Figure 3.10(a) and Figure 3.10(b) respectively for different droplet size classes, at $R = 0$ mm. The statistical uncertainty of the correlation coefficient for 95% confidence interval is also shown. The uncertainty of the correlation coefficients was low and of the order of ± 0.002 for all droplet size classes. Figure 3.10(a) shows that the spatial correlation in the axial direction for droplets of all size classes with the gas flow is quite high and decreases with distance away from the droplets though the change is quite low ($\sim 10\%$). This was somewhat expected. Since the particle stokes number (based on large eddy length scale of the flow) was very small ($St \ll 1$), the droplets of all three size classes are expected to closely follow the large scale gas motion. Also, comparing the value of R_{ud*ug} for the three size classes, no significant difference (< 0.1) in the correlation coefficient could be observed at any r. Thus, R_{ud*ug} can be considered to be independent of droplet size. However, in the cross-stream direction, the magnitude of the droplet-gas velocity spatial correlation (R_{vd*vg}) decreased more sharply away from the droplets, as shown in Figure 3.10(b). Also, the magnitude of the correlation was higher for the smallest



(a)



(b)

Figure 3.10: Spatial correlation coefficients of droplet-gas velocity fluctuations for various droplet size classes for (a) axial component of velocity and (b) cross-stream component of velocity , at $R = 0\ mm$. Error bars indicate the statistical uncertainty of the correlation coefficient for 95% confidence interval.

droplet size class.

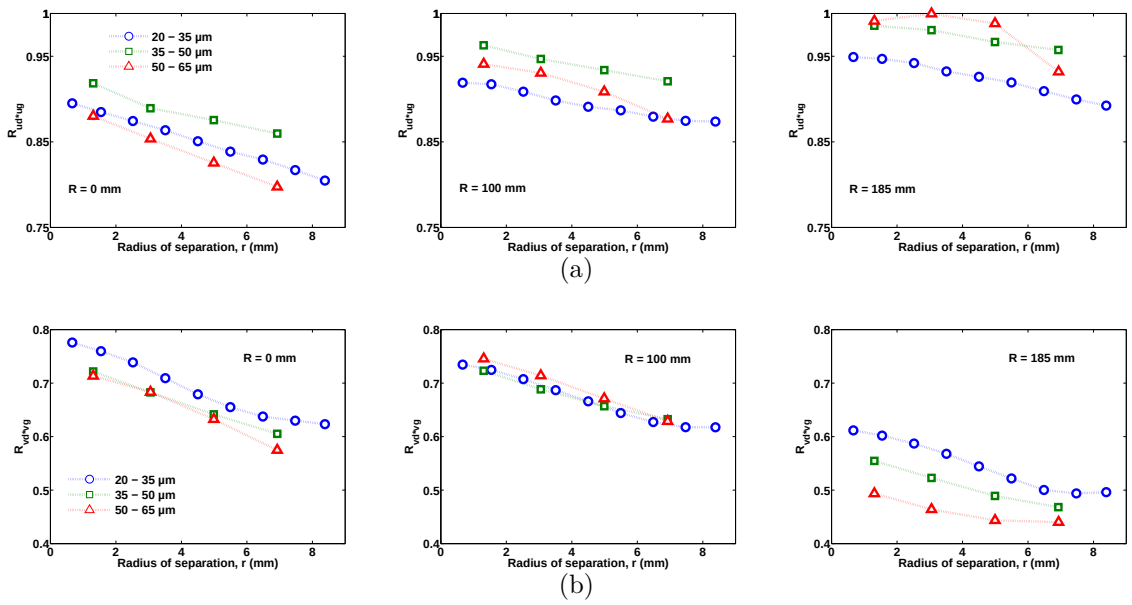


Figure 3.11: Comparison of spatial correlation coefficients of droplet-gas velocity fluctuations in (a) axial direction, R_{ud*ug} and (b) cross-stream direction, R_{vd*vg} for the three droplet size classes for the cross-stream measurement locations $R = 0$, 100 and 185 mm, respectively.

Figures 3.11(a) and 3.11(b) show the comparison among the droplet-gas velocity correlations for the measurement locations, $R = 0$, 100 and 185 mm in axial and cross-stream directions respectively. Away from the spray axis, the correlation coefficient between the two phases in the axial direction was found to increase though by a small value (~ 0.05). The correlation at any measurement location was nearly independent of the droplet size classes. In the cross-stream direction, the correlation coefficient decreased slightly up to $R = 100$ mm, but, towards the outer spray regions ($R = 185$ mm), it reduced to low values (~ 0.5). The droplet-gas velocity correlation is always higher in the axial direction than in the cross-stream direction ($R_{ud*ug} > R_{vd*vg}$) indicating better correlation in the mean flow direction. This result is in good agreement with previous studies on particle-laden jets (Prevost *et al.* (1996) and Ferrand *et al.* (2003)). The separation between R_{ud*ug} and R_{vd*vg}, at any radius of separation (r) from droplets, becomes wider for measurement locations away from the spray axis. This can be explained on the basis of anisotropy in the droplet and

gas motion. Higher anisotropy leads to larger difference between the droplet-gas velocity correlation term in axial and cross-stream direction and vice-versa. In the above mentioned studies on particle-laden jets, the anisotropy was higher closer to the spray axis and so, $R_{ud*ug} > R_{vd*vg}$. Towards the edge of the jet, the difference in the two terms reduced since the ratio of rms velocity in both directions were of similar order.

It should be recalled here from Figure 3.5(b) that, both droplets and gas flows have axial rms velocity almost invariant with respect to the measurement location R, while the rms velocity in cross-stream direction decreases (between $R = 0\ mm$ and $R = 185\ mm$) by about 50%. Thus in the outer spray regime, gravity, acting opposite to the flow direction (see Figure 3.4) increases the dragging on droplets reducing the fluctuations in droplet velocity especially in the cross-stream direction. This results in lowering the correlation between droplets and surrounding gas in the cross-stream direction and such effect is expected to be more pronounced for larger droplets. Hence, the R_{vd*vg} term can be observed to decrease from $R = 0\ mm$ to 185 mm for droplets of all size classes and also, a steady decrease in that term occurred for larger droplet size classes at $R = 185\ mm$.

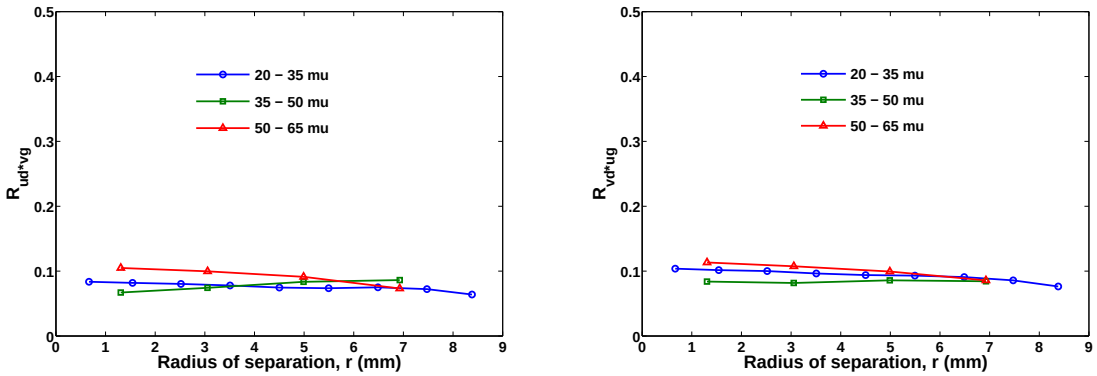


Figure 3.12: Spatial correlation coefficients of droplet-gas velocity fluctuations for (a) droplet axial velocity with gas cross-stream velocity and (b) droplet cross-stream velocity with gas axial velocity, for different droplet size classes, at $R = 0\ mm$.

The correlation coefficient of droplet axial velocity with gas cross-stream velocity and vice-verse (R_{ud*vg} and R_{vd*ug}) were also obtained for all size classes as shown in

Figure 3.12(a) and 3.12(b) respectively at $R = 0\ mm$. These correlations were found to be of the order of 0.1 and almost independent of droplet size. This is expected in the present flow, which has very small shear stress in the gaseous phase (the normalized shear stress was also of the similar order as shown in Figure 3.7). Similar results were obtained for other measurement locations. However, a slight increase in these correlations was observed at $R = 100\ mm$.

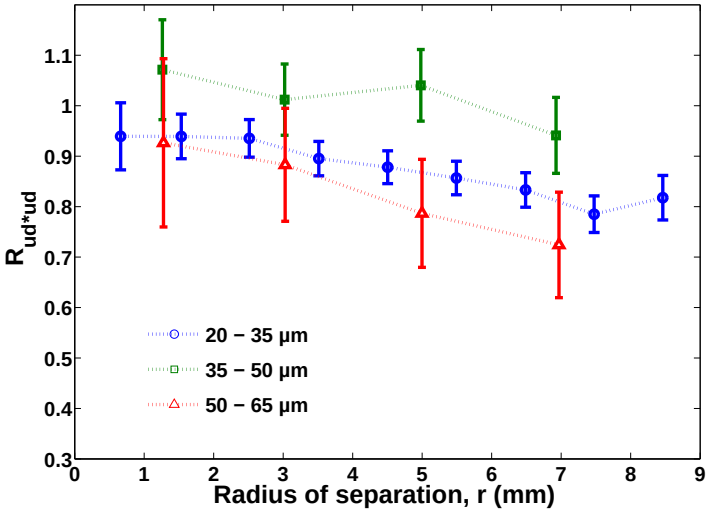
3.4.3 Droplet-Droplet velocity correlation

The spatial droplet-droplet velocity correlation, R_{dd}, was calculated in a similar way as R_{dg}. However, in this case, for a given droplet in every image sample, another droplet velocity (instead of gas velocity) was searched in the annular area defined within $r \pm \Delta r/2$. The same value of increments for r and Δr were used as before, thus maintaining the same resolution for R_{dd} as for R_{dg}, for a given droplet size class. Again, similar to R_{dg}, R_{dd} was calculated for several combinations of droplet velocity components conditional on different droplet size classes. For example, the droplet-droplet spatial correlation coefficient for the axial component of droplet velocity for the same size class, represented as $R_{dd}(D, r)$, is given as:

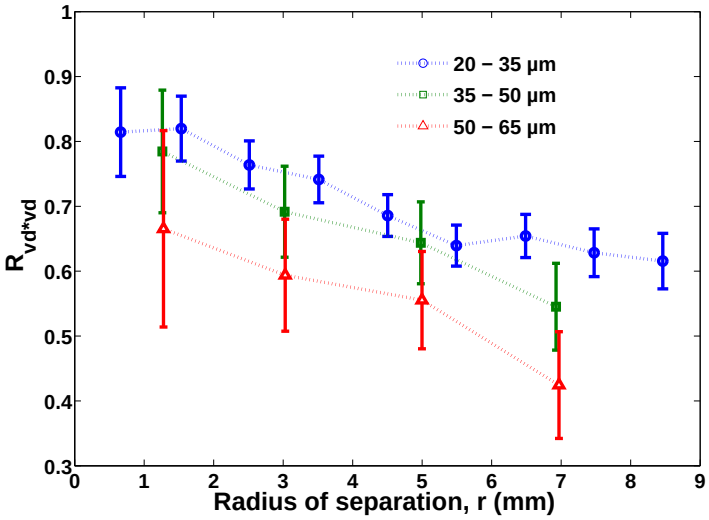
$$R_{u_d * u_d}(D, r) = \frac{\overline{\sum_I \sum_J \sum_K u_{d,I,J}(D) \times u_{d,I,K}(r)}}{u_{dr} \times u_{dr}} \tag{3.5}$$

Here, the notation K refers to the droplet velocity found in the annular ring defined for a given radius of separation r.

Figures 3.13(a) and 3.13(b) present the droplet-droplet velocity spatial correlations for axial and cross-stream velocity components, represented as R_{ud*ud} and R_{vd*vd} respectively, as a function of radius of separation, r, for various droplet size classes along with the statistical uncertainty (for 95% confidence interval) for the cross-stream location, at $R = 0\ mm$. In this case, the statistical uncertainty was higher, about ± 0.05, ± 0.1 and ± 0.15 for the three droplet size classes, the largest value corresponding to the higher size class. In comparison to the droplet-gas velocity spatial correlation, the uncertainty was higher here. This is primarily due to the



(a)



(b)

Figure 3.13: Spatial correlation coefficients of droplet-droplet velocity fluctuations for various droplet size classes for (a) axial component of velocity and (b) cross-stream component velocity, at $R = 0\ mm$. Error bars indicate the statistical uncertainty of the correlation coefficient for 95% confidence interval.

decrease in sample record size because the number of validated droplet velocity in any image was much less than the number of validated gas velocity vectors (the ratio being 10:5000 in any image). Again, the greater statistical uncertainty with larger droplet-size class is evident from the probability of drop size distribution in Figure 3.2, which shows significant reduction in the probability of the presence of higher droplet size classes. Also, because of smaller sample size, the statistical uncertainty was large for smaller radius of separation for any droplet size class.

In Figure 3.13(a), the value of the correlation coefficient along axial direction (R_{ud*ud}) for size class of 35–50 μm and 50–65 μm, for small separation r, was found to slightly overshoot 'one'. Considering the statistical uncertainty involved, the droplet-droplet velocity correlation for all size classes can be considered to be high (> 0.9) and of the same order for a given r. Though, larger droplets are expected to have higher correlation, at least for small value of r, because of higher inertia. Along cross-stream direction (Figure 3.13(b)), the spatial correlation coefficient was lower than the axial direction and found to decrease with droplet size class. Similar trend has been reported Prevost *et al.* (1996) and Ferrand *et al.* (2003). Thus, larger the droplet size, the lower the correlation with their motion in cross-stream direction. For other measurement locations, R_{ud*ud} and R_{vd*vd} followed the trend similar to the respective droplet-gas correlation coefficients as shown in Figures 3.11(a) and 3.11(b) respectively. The correlation between the axial and cross-stream velocity components (R_{ud*vd} or R_{vd*ud}) were found to be very small and of the order similar to the normalized shear stress in the gas flow and are not presented here.

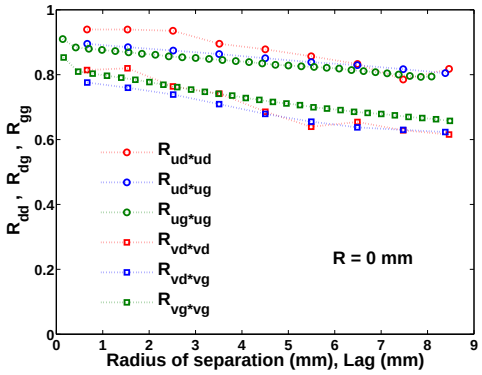
3.4.4 Comparison of Droplet-Gas, Droplet-Droplet and Gas correlation

Referring back to the TKE equation for the carrier phase (Equation (1.2)), it can be observed that the modification of the turbulence of the gas flow due to presence of particles is primarily governed by the second term on the right hand side which involves spatial droplet-gas and gas velocity correlation terms and represents the

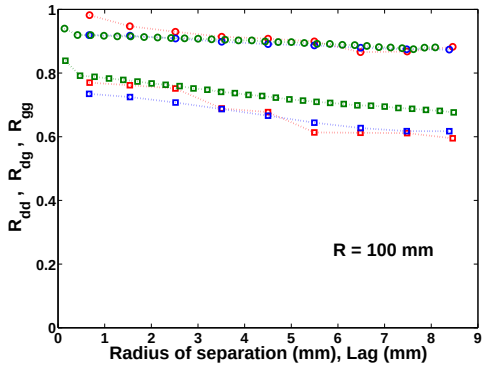
energy rate of change due to particle drag force. The other terms involving the fluctuations of droplet concentration can be considered negligible in the present flow conditions, as will be explained later. Thus the modification of the TKE (denoted here as 'e_p') is now proportional to the difference in the correlation terms ($\overline{u_{ig}u_{ig}} - \overline{u_{id}u_{ig}}$), where u_i represents either of the velocity components. Depending on if the sign of e_p is positive or negative, the droplets can either attenuate or augment turbulence in the carrier phase. However, the magnitude of e_p is also proportional to the mean droplet concentration ($\overline{C}$) and inverse of the droplet relaxation time (τ_p). Thus, to further elucidate on the momentum transfer between the two phases, the normalized spatial correlation of droplet-gas velocity fluctuations (R_{dg}) needs to be compared with the spatial gas velocity correlation (R_{gg}) and also, spatial droplet-droplet velocity correlation (R_{dd}). For gas, the spatial correlation of the axial velocity component along the axial direction (R_{ug*ug}) and of cross-stream velocity component in cross-stream direction (R_{vg*vg}) were obtained.

Figure 3.14(a), 3.14(b) and 3.14(c) show the comparison of the correlations for both velocity components for droplet size class 20–35 μm, at the three measurement locations, $R = 0$, 100 and 185 mm respectively. It should be noted, however, that the relevant values for the terms in Equation (1.2) are those at zero separation distance. The following observations are made from Figure 3.14.

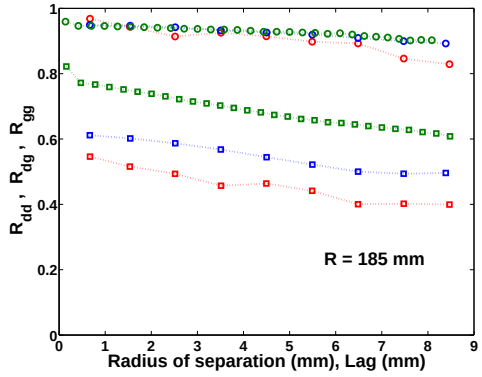
1. The droplet-droplet velocity correlation in axial direction, closer to the droplets (smaller r), was slightly higher than the gas correlation. This indicates that the droplets retain their kinetic energy longer than the surrounding gas in axial direction and, is because of the higher inertia of droplets as compared to gas elements. The droplet-gas and gas velocity correlation coefficients are of same order ($R_{ud*ug} \approx R_{ug*ug}$) at any radius of separation, r. Also, similar behaviour is more or less observed at all measurement locations. Hence, $e_p \approx 0$ and the momentum transfer between the droplet and gas phases can be considered to be negligible in the axial direction for the droplet size class of 20–35 μm droplets. Since the droplet-droplet and the droplet-gas velocity correlation were almost independent of the droplet size (Figures 3.11(a) and 3.13(a)), the same trend is



(a)



(b)



(c)

Figure 3.14: Comparison of spatial correlation coefficients of droplet-droplet (R_{dd}) and droplet-gas (R_{dg}) velocity fluctuations for droplet size class 20–35μm and gas velocity correlation (R_{gg}) for both axial and cross-stream velocity components at the cross-stream measurement locations (a) $R = 0\ mm$, (b) $R = 100\ mm$ and (c) $R = 185\ mm$, respectively.

expected for droplets of other size classes. This is in contrast to Prevost *et al.* (1996) and Ferrand *et al.* (2003) who found $\overline{u_d u_d} > \overline{u_d u_g}$. This was primarily due to the strong gradient in the mean particle velocity in the radial direction resulting in production of particle turbulence and considerable particle shear stress ($\overline{u_d v_d}$) in the measurement location, both negligible in the present work.

2. In cross-stream direction, the correlation of droplet motion with the surrounding gas tends to decrease at larger distances R from the central region of the spray. However, the gas remains well correlated with itself at any measurement location with a slight decrease in R_{gg} at $R = 185\ mm$. Thus for any measurement location and at any r, along the cross-stream direction, $R_{gg} > R_{dd}$ and R_{dg}. It can be observed that, at $R = 0\ mm$ both dispersed and continuous phases are well correlated with each other and also with themselves. As one moves away from the spray axis towards the outer spray, R_{gg} tends to be more dominant as compared to R_{dg}. Though, because the rms velocity in the cross-stream direction for droplets was somewhat higher than that for the gas flow ($v_{dr}/v_{gr} \approx 1.2$), $\overline{v_d v_g} \approx \overline{v_g v_g}$ for the size class of 20–35 μm at any measurement location R. However, the behaviour is different for the larger size classes. As can be observed in Figure 3.11(b), at $R = 185\ mm$, for larger droplet sizes, the R_{vd*vg} term reduces to about 0.5 causing $\overline{v_g v_g} > \overline{v_d v_g}$. Thus $e_p > 0$ and momentum transfer can be expected from the carrier fluid to the droplets resulting in turbulence attenuation. Since R_{vd*vg} was lower for the 50-65 μm size class compared to the size class of 35-50 μm, the term ($\overline{v_g v_g} - \overline{v_d v_g}$) increases further. This explains the increased influence of the drag and gravity, especially on the larger droplets, towards the spray edge. The droplet-droplet velocity correlation in cross-stream direction, at any r, decreased considerably compared to the gas correlation away from the spray axis. This is due to the reduction in the particle kinetic stress again because of the increased drag and gravity, and so a reduction in the droplet rms velocity was observed (Figure 3.5(b)). The above result is again in contrast to Prevost *et al.* (1996) and Ferrand *et al.* (2003) who found

the particle kinetic stress in radial direction to be approximately equal to the particle-fluid velocity correlation ($\overline{v_d v_d} \approx \overline{v_d v_g}$) and argued it on the basis of the quasi-uniform statistics of the radial droplet velocity through out the jet.

3. Comparison of the experimental findings with the explanations from numerical study of the dispersed two-phase flow is important since both approaches complement each other and it can provide further insight in to the physics of the problem. For this purpose, the DNS results of Ferrante and Elghobashi (2003) is considered who reported the modification of the isotropic turbulence in the carrier fluid by the dispersed particles for various particle Stokes numbers. The authors explained the energy rate of change due to the particles drag force on the basis the comparison of the corresponding velocity correlation terms for each cases. The trajectories of the micro-particles ($St_k \ll 1$) are always aligned with that of the fluid elements and the kinetic energy of those particles remains larger than the fluid due to their finite inertia. Hence the velocity autocorrelation of the particles ($\overline{u_d u_d}$) is higher than the fluid velocity autocorrelation ($\overline{u_g u_g}$) and the particle-fluid velocity correlation ($\overline{u_d u_g}$) remains in between. The larger particles ($St_k \gg 1$) do not respond to the velocity fluctuations of the surrounding fluid as quickly as microparticles do, but rather escape from their initial surrounding fluid. Large particles retain their kinetic energy longer than the surrounding fluid and thus $\overline{u_d u_d} > \overline{u_d u_g}$. However, because of the "crossing trajectories" effect, the fluid velocity autocorrelation is larger than the correlation between the particle velocity and the fluid velocity *i.e.* $\overline{u_g u_g} > \overline{u_d u_g}$, causing a transfer of energy from the fluid to the particles. It should be noted that these velocity correlations are the temporal correlations and have been calculated under the 'point particle' assumption, so the fluid velocity could be estimated *at* the particle position.

   It should be emphasized here that unlike Ferrante and Elghobashi (2003), a wide variation in the response of the droplets to the gas flow was observed in the present experimental condition. This is evident from the range of the

Stokes numbers, the droplets of a given size class could attain depending on the size of the eddies they interact with. For instance, for the 20–35 μm droplets, the Stokes numbers based on the large eddy length scale and the Kolmogorov length scale were of the order of 0.005 and 4.3 respectively. Thus, the droplets with a given size (or size class) are expected to either augment or attenuate the turbulent kinetic energy of the carrier fluid depending on the length scales of the fluid flow. Though, the magnitude of the turbulence modification at a given length scale of the flow depends also on two parameters namely (a) the mass loading of that droplet size (or size class) and (b) the ratio of the kinetic energy associated with a given length scale of the flow to the total turbulent kinetic energy. Hence, the velocity correlation terms presented in Figure 3.14 can be considered to be the result of the integrated effect of the turbulence modulation at various length scales by droplets. In order to study the momentum transfer between the two phases at specific length scales of the flow, it is essential to extract the associated flow structures and evaluate the corresponding correlation terms. This important issue will be discussed in Chapter 4.

Comparison of the experimental results with the simulations of particle-laden isotropic flow by Ferrante and Elghobashi (2003) indicates that even a slight anisotropy in the flow can cause considerable difference in the behaviour of the particle-fluid correlated motion. At $R = 0\ mm$, the droplet and gas flow were nearly isotropic ($u_r/v_r \approx 1.1$). In axial direction, for droplets of any size class, $\overline{u_d u_d} > \overline{u_d u_g} > \overline{u_g u_g}$, which is in agreement with Ferrante and Elghobashi (2003). Though a similar trend was obtained in the cross-stream direction, a slight decrease in the $\overline{u_d u_d}$ and $\overline{u_d u_g}$ terms were observed with larger droplet size classes. As the flow becomes more anisotropic towards the outer spray region, greater deviation from the numerical results are observed. The droplet response to the fluid motion becomes different for the different velocity components. Compared to axial direction, the larger droplets poorly respond to the fluid motion in the cross-stream direction. Also, in the cross-stream direction, the droplet kinetic stress ($\overline{u_d u_d}$) tend to be smaller than the droplet-gas velocity

correlation ($\overline{u_d u_g}$).

4. From the central spray region towards the edge, the gas correlation coefficient in axial direction (R_{ug*ug}) slightly increases implying elongation of the large eddies in the gas flow in axial direction. R_{ug*ug} remains high for all measurement locations and this is in agreement with the large value of the estimated length scale of the gas flow, $O(100\ mm)$. Away from the spray axis, the gas correlation coefficient in cross-stream direction (R_{vg*vg}) tends to decrease and at any 'r', the separation between the two correlation coefficients becomes wider. This implies stretching of the large scale structures of the gas flow in the axial direction in the outer region of the spray. Also, at $R = 185\ mm$, the increasing trend of R_{ud*ug} (Figure 3.13(a)) and the decreasing trend of R_{vd*ug} (Figure 3.13(b)) for larger droplet size classes clearly shows the influence of gravity altering the effective length scales of the droplet-gas correlated motion. This observation is *atleast qualitatively* supported by the DNS results of Ferrante and Elghobashi (2003), who have also reported stretching of the vortical structures in the gravitational direction due to accumulation of particles via *preferential sweeping*.

5. In the cross-stream direction, $R_{ug*ug} > R_{ud*ug}$ and $R_{ud*ug} > R_{ud*ud}$. Hence, the effective length scales of the droplet-droplet correlated motion was always smaller than the length scales of the eddy structures in the carrier phase.

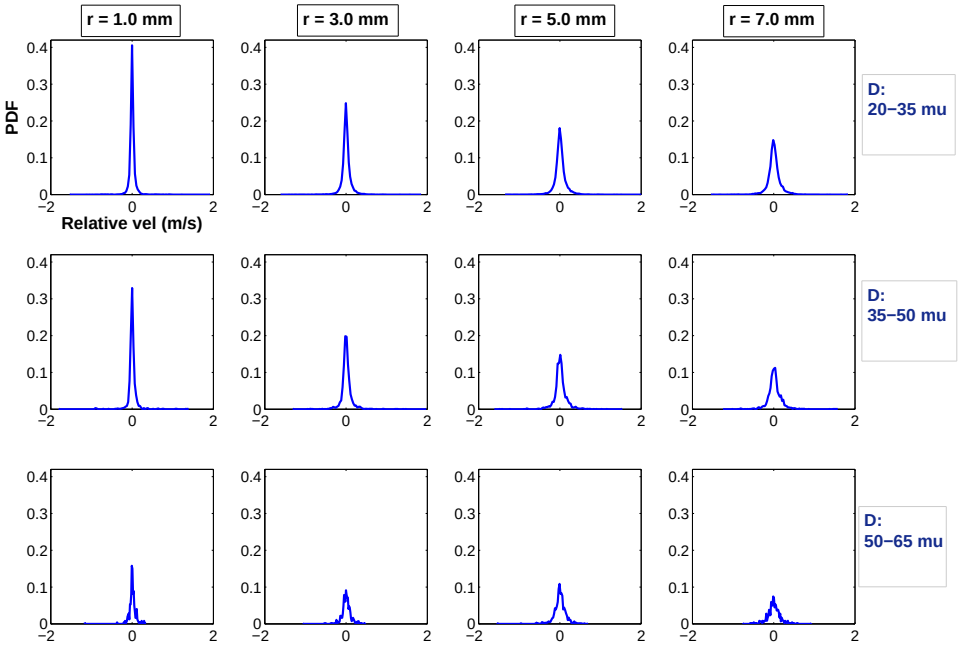
3.5 PDF of droplet-gas relative velocity

The planar measurement of both droplet and gas velocities provided by the combined ILIDS and PIV technique also facilitates estimating the probability density functions (PDF) of relative fluctuating velocities between the two phases. The PDF is obtained as a function of radius of separation, r and for various droplet size classes similar to the spatial velocity correlation described earlier. The PDF of droplet-droplet relative velocity was also obtained in a similar way. These PDFs will further exemplify on the physics of the interaction mechanism between the two phases by indicating if a local

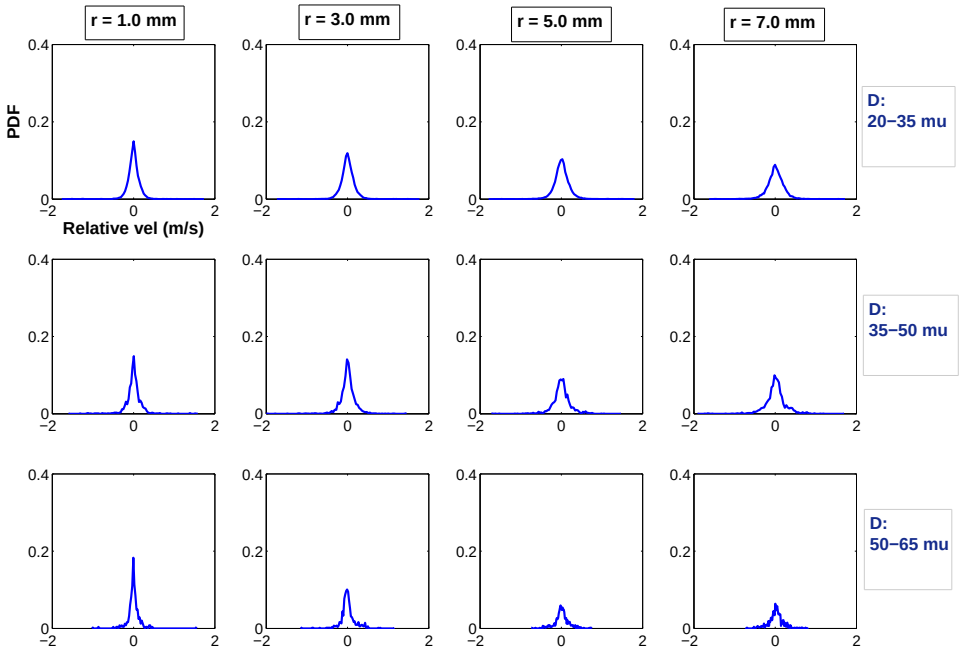
fluctuation in velocity of a droplet is linked to *larger* or *smaller* velocity fluctuations in either the gas phase surrounding that droplet or the other droplets near by. The increment of r and, the value of Δr were chosen to be 1.0 mm and 2 mm respectively for the droplets of all size classes.

The PDF of droplet-droplet relative velocity is shown in Figure 3.15 for both axial and cross-stream components at $R = 0\, mm$. The mean (μ_{re}), standard deviation (σ_{re}), skewness (γ_{1re}) and kurtosis (γ_{2re}) of the PDFs for axial velocity are plotted in Figure 3.16. The mean and standard deviation are normalised with the respective droplet mean and droplet rms velocities. Many interesting trends can be observed. At any r, the probability of zero relative velocity was found to decrease for droplets of larger size classes. This can be attributed to relatively poor response of the larger droplets to the velocity fluctuations of other droplets (of same size) near by. For any droplet size class, the mean relative velocity (μ_{re}) was found to increase slightly away from the droplets while the standard deviation of the PDF (σ_{re}) increases more rapidly. The relative velocity in axial direction is maximum around zero closer to the droplets (very high value of γ_{2re}), which decreases rapidly away from the droplets indicating reduced influence of one droplet over other. The asymmetry in the distribution, given by γ_{1re}, was found to lie closer to zero for the smallest droplets while it was negative for the droplets of largest size class (50–65 μm). The PDF of relative velocity tends to follow a gaussian distribution away from the droplets. In cross-stream direction Figure 3.15(b), the probability of zero relative velocity is reduced by about 50%. Also, it was found not to be a strong function of droplet size.

Similar trends were observed in case of the probability density functions of droplet-gas relative velocity, Figure 3.17. The slight reduction in the probability of zero mean velocity between the two phases, closer to the droplets, indicates better correlation of the velocity of the dispersed phase with itself than the carrier phase. The PDFs of both velocity components in this case were almost independent of the droplet size. Figure 3.18 shows various statistics of the PDFs plotted in Figure 3.17. Comparison of Figure 3.18 with Figure 3.16 shows that the normalized mean droplet-gas relative velocity (μ_{re}) for any size class is almost independent of the distance from the



(a)



(b)

Figure 3.15: Probability density functions of droplet-droplet relative fluctuation of (a) axial component of velocity and (b) cross-stream components of velocity for various radius of separation, r and three droplet size classes at $R = 0\ mm$.

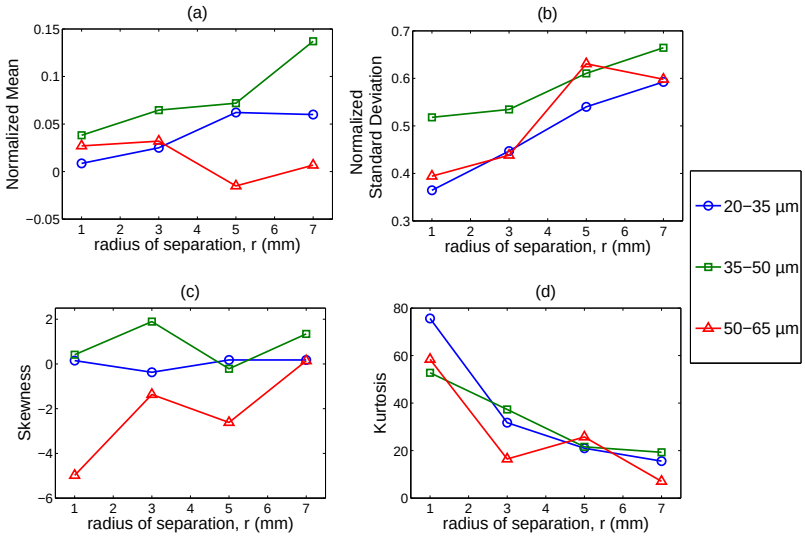
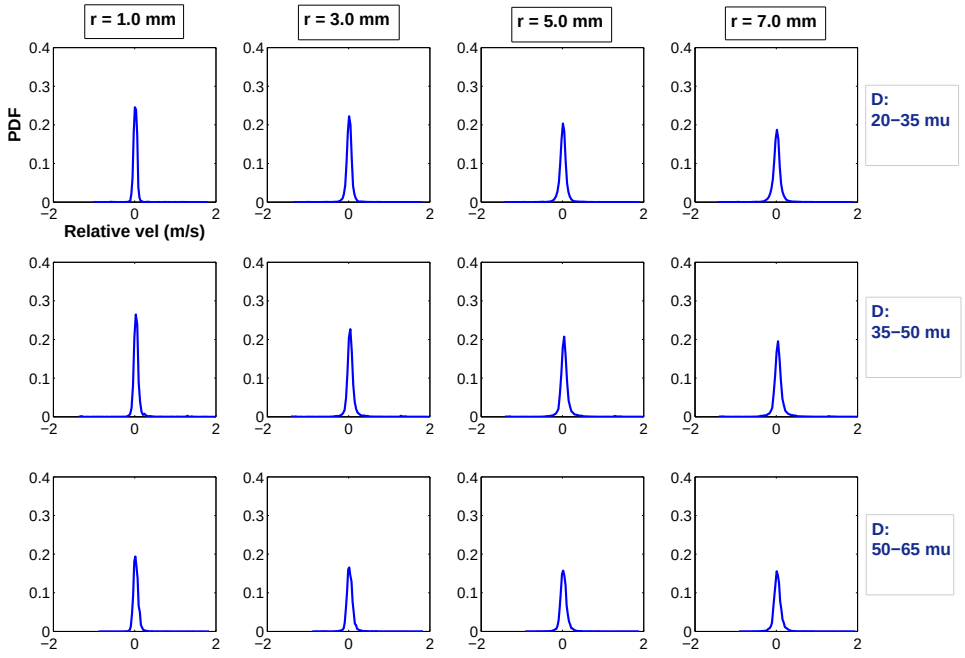


Figure 3.16: Various statistics of the PDFs of the relative axial component of velocity of droplets corresponding to Figure 3.15. a) Mean, (b) Standard deviation, (c) Skewness and (d) Kurtosis.

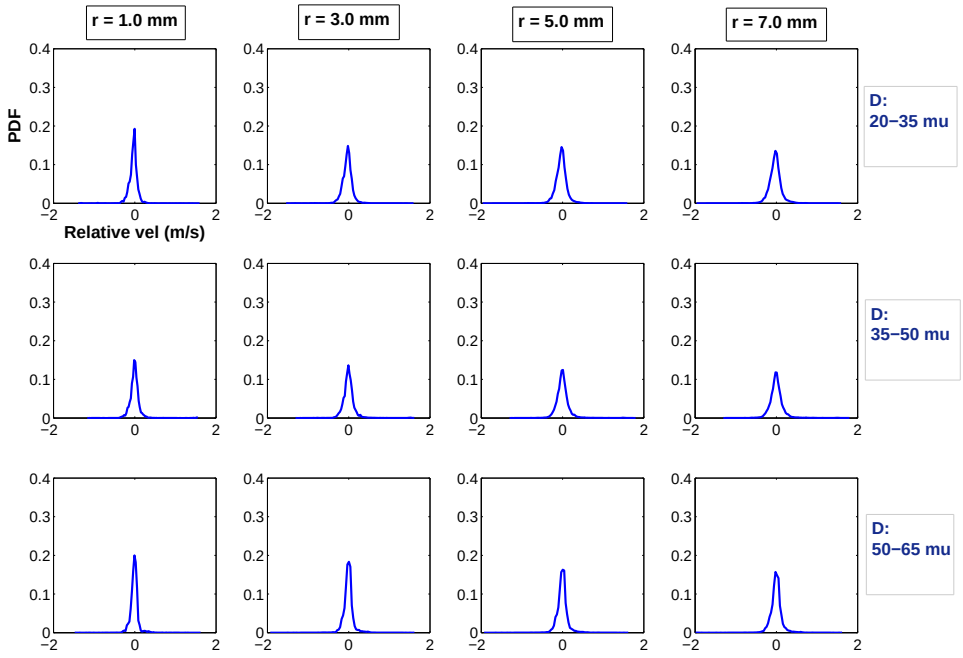
droplets and is higher than than the mean droplet-droplet relative velocity. Similar trends in the normalized standard deviation and kurtosis are observed in both cases. However, closer to the droplets, the skewness was negative for the droplet-droplet relative velocity in contrast to the positive values for the droplet-gas relative velocity. This signifies that closer to the droplets, the local fluctuation in droplet velocity is accompanied with a larger fluctuations in velocity of droplets near by and smaller fluctuations in the surrounding gas velocity. Similar results were found for the other measurement locations apart from the location at $R = 185\ mm$ where a reduction in the probabilities of droplet-gas relative velocity in cross-stream direction was observed with larger droplet size classes.

3.6 Effect of the flow field on the droplet concentration

It has been known for a long time that in a particle-laden flow, the semi-organized or coherent structures in turbulence may move the particles in an organized manner and



(a)



(b)

Figure 3.17: Probability density functions of droplet-gas relative velocity for (a) axial component of velocity and (b) cross-stream component of velocity for various radius of separation, r and three droplet size classes at $R = 0\ mm$.

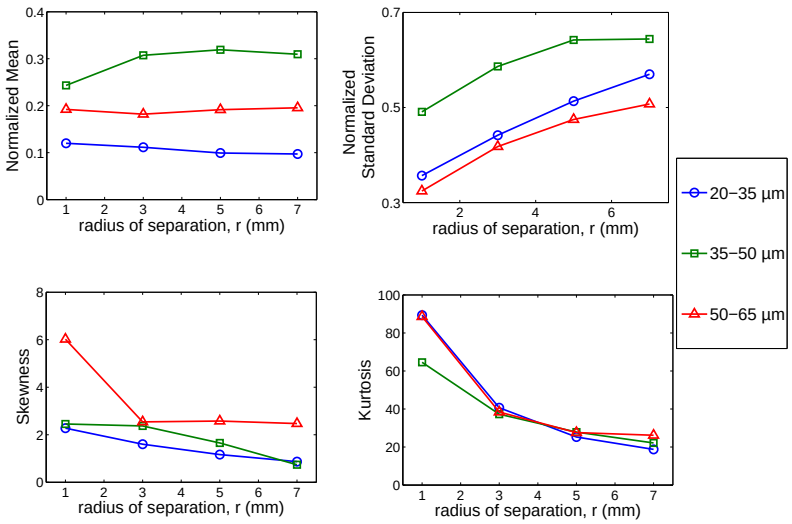


Figure 3.18: Various statistics of the PDFs of the relative axial component of velocity of droplets and gas corresponding to Figure 3.17. a) Mean, (b) Standard deviation, (c) Skewness and (d) Kurtosis.

are likely to produce instantaneous concentration fluctuations even if the particles are initially uniformly distributed (Fessler *et al.*, 1994). The degree to which turbulent eddies can modify the instantaneous concentration field depends on the Stokes number (St, as defined before) of the particles. Particles with St on the order of one, tend to flung away from the vortex cores and in many cases collect in rings surrounding the vortices. This phenomenon of preferential concentration is also called inertial clustering because it is caused by the difference in inertia between a particle and the fluid. Hence it is essential to measure the instantaneous droplet concentration in a spray in order to examine the presence of the droplet clustering caused by interaction of the entrained flow field with the spray.

The combined ILIDS and PIV technique, along with providing the planar measurements of droplet size, velocity and gas velocity, also has the potential of measuring the instantaneous droplet concentration. This is achieved by detecting the droplet glare points in the PIV image (using wavelet transform) as described in the previous chapter. Since all of the glare points may not find their corresponding fringe patterns in the ILIDS image, so the droplet number density measurement was performed independent of the droplet size. However, ILIDS was used to measure the

Radial Distribution Function (RDF) which is another way of evaluating the droplet clustering effect.

3.6.1 Scale of droplet clustering

In order to obtain the characteristic dimensions of the clusters in the flow, the local concentration probability density function are compared with that arising from a purely random process, (Aliseda *et al.*, 2002). For this purpose, at first, the instantaneous droplet number density was obtained from the two-dimensional cross-cut PIV images of the flow at the different measurement locations. At any given instant, the concentration probability density function (PDF) was obtained by dividing an image into boxes of a certain size and counting the number of droplets inside each box. If N_p is the total number of detected droplets and N_b is the total number of boxes, then the probability of finding n droplets per box is obtained as the ratio of the sum of the number of droplets in the boxes containing 'n' droplets and the total number of droplets in all of the boxes (N_p). The average PDF of all of the images were obtained and compared with the distribution of droplets in boxes for a random process, given by a binomial distribution:

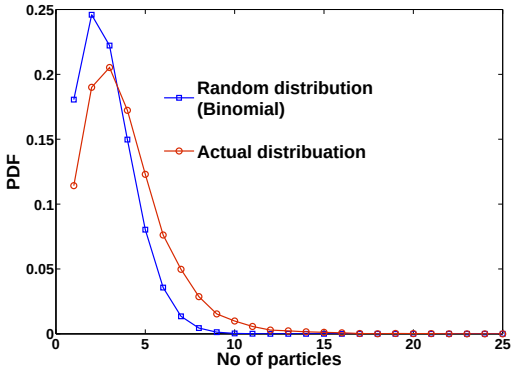
$$P_{binomial}(n) = \binom{\bar{N}_p}{n} \left(\frac{1}{N_b}\right) \left(1 - \frac{1}{N_b}\right)^{N_p - n} \tag{3.6}$$

where, $\bar{N}_p$ is the average number of the detected droplets (averaged over all sample images). The comparison between the PDF found for a given box size and the random process provides an indication of how turbulence affects the particle concentration field. Two parameters were used to compare the measured PDF to the random distribution. The first one, D_1, was introduced by Fessler *et al.* (1994), and is the difference between the standard deviation of the two distributions (σ and $\sigma_{binomial}$):

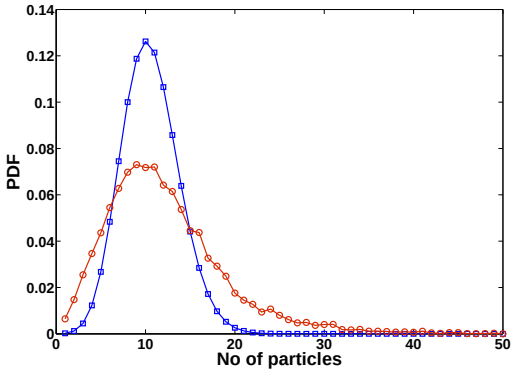
$$D_1 = \frac{\sigma - \sigma_{binomial}}{\lambda} \tag{3.7}$$

where λ is the mean number of particles per box. Positive values of this parameter indicate the presence of concentrated regions, while zero or negative values represent a quasi-uniform concentration field. The second parameter, D_2, was used by Wang and Maxey (1993) which represents the square of the difference of probabilities given by the two distributions, and is always positive or zero:

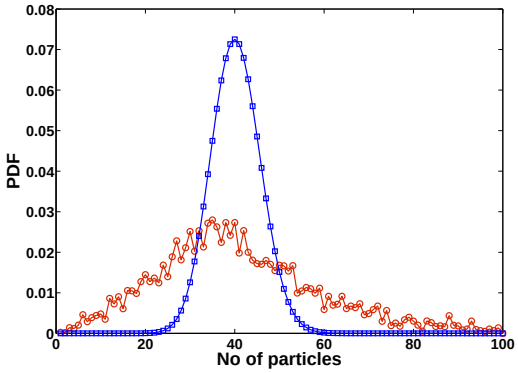
$$D_2 = \sum_{1}^{N_p} (P(n) - P_{binom}(n))^2 \tag{3.8}$$



(a) Box size = $H/8 \times L/10$



(b) Box size = $H/4 \times L/5$



(c) Box size = $H/2 \times L/2$

Figure 3.19: Comparison of PDF of the number of droplets per box with a binomial distribution for the cross-stream measurement location at $R = 0$ mm for three different box sizes with dimensions (a) $H/8 \times L/10$, (b) $H/4 \times L/5$ and (c) $H/2 \times L/2$ where the measurement area is $H \times L$.

The length scale for which preferential concentration is most effective can be identified by computing these statistics for boxes of different sizes. Figure 3.19 shows

$Boxsize$	$D1$	$D2$
$H/8 \times L/10$	0.102	0.014
$H/4 \times L/5$	0.295	0.015
$H/2 \times L/2$	0.375	0.023

Table 3.3: The parameters $D1$ and $D2$ for the different box sizes corresponding to Figure 3.19.

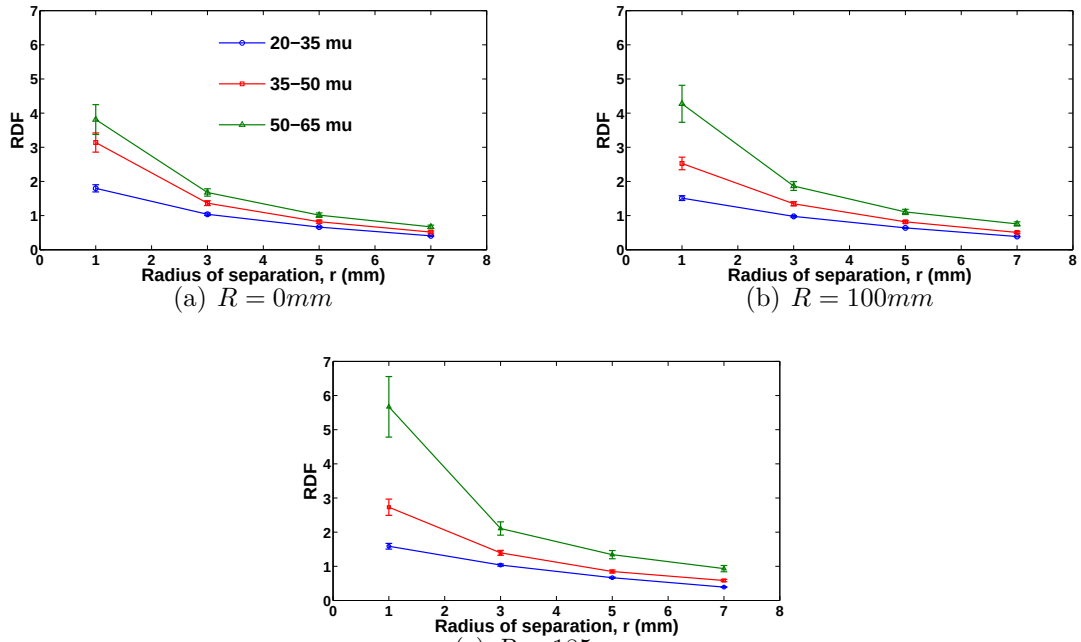
the comparison for three different box sizes. Denoting 'H' and 'L' as the horizontal and vertical dimensions of the measurement area ($= 8mm \times 12mm$), the size of the boxes were chosen to be $H/8 \times L/10$, $H/4 \times L/5$ and $H/2 \times L/2$, respectively. Table 3.3 shows the results of computing the two parameters, D_1 and D_2. It can be seen that the parameters D_1 and D_2 increases consistently with the size of the box size. For box size equal to one-fourth of the measurement area, large deviation from the random behaviour is observed (Figure 3.19(c)). Because of the viewing area of the images, the PDF comparison could not be performed for boxes of still larger sizes. However, comparison of the maximum values of D_1 and D_2 from Fessler *et al.* (1994) and Aliseda *et al.* (2002) (which, though, corresponds to homogeneous isotopic turbulence), suggests that the particle clustering should be more prominent at length scales of the order corresponding to the box size $H/2 \times L/2$. In such case, any larger box size would result in low values of D_1 and D_2. Similar trend in droplet clustering length scales were observed for other measurement locations.

3.6.2 Radial distribution Function (RDF)

The radial distribution function (RDF) is a statistical measure of clustering (Salazar *et al.*, 2008). It is defined as the probability of finding a second particle at a given separation distance from a test particle compared to a case where the particles are homogeneously distributed. The RDF is computed from a field of M particles by binning the particle pairs according to their separation distance, and calculating the function

$$RDF(r_i) = \frac{N_i/\delta V_i}{N/V} \tag{3.9}$$

where N_i is the number of particle pairs separated by a distance $r_i \pm \delta r/2$, δV_i is the volume of the discrete shell located at r_i, $N = M(M-1)/2$ is the total number of pairs and V is the total volume of the system. Since the present experimental technique is restricted to two-dimensions only, so in the above equation the discrete volumetric shell is replaced by an annular area with radius r_i, similar to Figure 3.8. The RDF was calculated using the droplet positions obtained from ILIDS, the advantage being the ability to obtain RDF(r_i) for the different size classes. In the present case the value of r_i and δr were chosen to be 1 mm and 2 mm respectively.



(a) $R = 0mm$ (b) $R = 100mm$ (c) $R = 185mm$

Figure 3.20: Evaluation of RDF for the cross-stream measurement locations at (a) $R = 0$ mm, (b) $R = 100$ mm and (c) $R = 185$ mm respectively.

Figure 3.20 shows the RDF calculated at three different measurement locations $R = 0$, 100 and 185 mm. Effectively, the value of RDF = 1 means that the droplet distribution is random. For values of RDF > 1, this means that clustering occurs. The value of r_i for which RDF(r_i) becomes larger than 1, provides an estimate of the scale of the clusters. Considering the distribution of RDF for $R = 0$ mm in Figure 3.20, it can be observed that this value of r_i is of the order of 4–7 mm for the considered droplet size classes. This agrees well with the box size $H/2 \times L/2$

for which the $D1$ and $D2$ parameters were found to be maximum (Table 3.3) thus indicating the length scale of droplet clustering.

Also, it can be observed that at any measurement location R, for larger droplet size the RDF is larger for any radius of separation r_i. So more clustering is evident for larger sizes of droplets and also, the length scale of the clusters is larger. It can be recalled here that the Stokes numbers based on the Kolmogorov scale (St_k) for the 20–35μm, 35–50μm and 50–65μm droplet size classes were of the order of 4.32, 10.7 and 19.6 respectively. Hence the tendency of the droplets for preferential accumulation is higher for larger Stokes number. However, Wood *et al.* (2005) and Salazar *et al.* (2008) have reported that the largest magnitude of RDF occurs for particles with $St_k \approx 1$. For $St_k < 1$, RDF tend to increase with Stokes number and for $St_k > 1$, RDF rend to decrease with Stokes number. These trend contradicts with the present experimental observation in Figure 3.20. However, it should be mentioned that in the work of Wood *et al.* (2005) and Salazar *et al.* (2008), the terminal velocity of particles was much less than the fluid velocity fluctuations and thus, the effect of gravity on preferential accumulation was negligible. Under the present experimental condition, the gravitational effect on droplets (especially for the two larger size classes) is evident as described before (Table 3.2). Due to gravity, the particles tend to accumulate on the side of vortical structures through the mechanism of preferential sweeping (Ferrante and Elghobashi, 2003; Yang and Shy, 2005). This tendency is expected to be more prominent for larger particles. This explains the increase in RDF for larger St_k. Since the effect of gravity on droplet motion increases from central spray region to the outer edge of the spray (Table 3.2), RDF was found to increase from $R = 0$ mm to 185 mm for the largest droplet size class (50–65 μm).

3.6.3 Correlation between fluctuations in droplet concentration and gas velocity

The equation for modification of TKE of the carrier phase in a two phase flow contains certain terms which includes the correlation of fluctuations of particle concentration

and gas velocity. Hence it is necessary to measure those terms in order to evaluate their contribution on the turbulence modification, which can assist the mathematical models as well. For this purpose, each of the instantaneous image sample was divided into certain number of boxes and the droplet concentration was measured for each of those boxes, as explained earlier. In the present case, the size of the box was chosen to be the one corresponding to the length scale of the flow where maximum preferential concentration is expected. From Figure 3.19(c), this box size is equal to one-fourth of the measurement area, *i.e.* $H/2 \times L/2$. Thus the correlation terms were evaluated for four boxes (each box is denoted by B_i, i being the box number). Denoting 'c' as the deviation of instantaneous droplet number density or concentration from the mean and c with subscript 'r' referring to the standard deviation of the fluctuations, the correlation coefficient between fluctuations of droplet concentration and axial component of gas velocity can be written as:

$$R_{c*u_g}(B_i) = \frac{\overline{\sum_I \sum_J c \times u_g(I,J)}}{c_r \times u_{gr}} \tag{3.10}$$

where I and J represent the coordinates of a gas velocity vector in the box B_i. The normalization was performed with the rms values of the fluctuations of droplet concentration and gas velocity measured over that particular box. In a similar way, the correlation coefficient corresponding to the cross-stream component of velocity was determined.

$R = 0\ mm$		$R = 100\ mm$		$R = 185\ mm$	
0.045	0.017	0.115	0.068	-0.107	-0.102
0.028	0.029	0.042	0.064	-0.141	-0.148

Table 3.4: Spatial correlation coefficients of fluctuations of droplet concentration and axial component of gas velocity evaluated for each of the four boxes (of size $H/2 \times L/2$) for the measurement locations at $R = 0$, 100 and 185 mm.

Tables 3.4 and Table 3.5 present the correlation coefficients of droplet concentration fluctuation with fluctuations in the axial and cross-stream velocity components respectively for the three measurement locations at $R = 0$, 100 and 185 mm. Very low values of the $R_{c*u_g}(B_i)$ ($\approx 0.05 \sim 0.1$) can be seen in all cases signifying

$R = 0\ mm$		$R = 100\ mm$		$R = 185\ mm$	
0.057	0.074	0.079	0.014	0.085	0.069
0.087	0.034	0.070	0.075	0.084	0.058

Table 3.5: Spatial correlation coefficients of fluctuations of droplet concentration and cross-stream component of gas velocity evaluated for each of the four boxes (of size $H/2 \times L/2$) for the measurement locations at $R = 0$, 100 and 185 mm.

that the fluctuations of fluid velocity are only weakly correlated with the droplet concentration field. Similar behaviour can be observed at all three measurement locations. For axial velocity, at $R = 185\ mm$, the correlation was negative indicating that increase in the gas velocity fluctuation is associated with decrease in fluctuations of droplet concentration and vice versa. However, because of the low magnitude of the correlation, this effect is less pronounced. The R_{c*u_g} term was also evaluated for the other two box sizes ($H/8 \times L/10$ and $H/4 \times L/5$) and found to be the order of $\approx 0.05 \sim 0.1$ for both cases. This indicates that R_{c*u_g} is independent of the length scales of the gas flow for the present experimental locations in the spray. Since the droplet and gas motions were well correlated with each other ($R_{u_d*u_g}$ and $R_{v_d*v_g} > 0.6$) at all measurement locations, so the correlation between the fluctuations of droplet concentration and droplet velocity ($R_{c*u_{id}}$) is also expected to be of similar order as $R_{c*u_{ig}}$. Hence, for the present experimental condition, the terms in the right hand side of the TKE equation for the carrier phase (Equation (1.2)) which includes the fluctuations in droplet concentration can be neglected.

3.7 Summary

In this chapter the two-phase measurements at far downstream locations of a confined polydispersed spray were described with an aim to understand the interaction mechanism between the droplets and the entrained gas flow. Simultaneous planar measurements of droplet size, velocity and concentration and gas velocity were achieved by applying the combined ILIDS and PIV techniques. This allowed evaluation of several statistics (first and higher order) vital for understanding the physics of the interaction mechanism. The findings can be summarized as below:

1. At any measurement location, the mean droplet velocity was found to be low and independent of the droplet size. The magnitude of the mean gas flow was similar to that of the mean droplet flow and could be interpreted through the interaction with the recirculating pattern of the entrained air flow into the spray. The rms velocities of both phases were an order of magnitude greater than that of the mean. While the axial rms velocity slightly decreased away from the spray axis, the cross-stream rms velocity decreased by about 50% towards the outer spray.

2. The spatial correlation coefficients of droplet-gas and droplet-droplet velocity fluctuations (R_{dg} and R_{dd}) were obtained as function of the distance from droplets ('r') conditional on droplet size classes, and compared with the spatial correlation of gas velocity fluctuations (R_{gg}). The velocity correlations were always higher in the axial direction than in the cross-stream direction. The corresponding separation was found to be wider towards the outer spray region, where the flow was more anisotropic and gravity dominated.

3. In axial direction, at any measurement location, $R_{dg} \approx R_{gg}$ for any droplet size class, indicating low drag and, therefore, negligible momentum transfer between the two phases. In cross-stream direction, away from the spray axis, R_{gg} decreased only slightly, while R_{dg} and R_{dd} were found to decrease considerably. At the outermost measurement location near the spray edge, especially for the larger sizes, R_{gg} was much larger than R_{dg} signifying increased drag in the cross-stream direction and the possibility of energy transfer from the fluid to the droplets. These results elucidate the effect of gravitational force on the droplets and the anisotropy of the flow, which can cause considerable deviation in the behaviour of droplet-fluid correlated motion relative to an isotropic flow, as described by Ferrante and Elghobashi (2003).

4. The PDFs of relative droplet-droplet and droplet-gas fluctuating velocities were obtained as a function of distance from the droplets ('r') conditional on droplet size class, at $R = 0\ mm$. The probability of zero relative velocity

in both cases was found to be higher in axial direction than in cross-stream direction supporting the similar observations in velocity correlation coefficients. Compared to the droplet-gas case, the probability of droplet-droplet zero relative velocity was found to decrease more sharply with increasing r and also, decrease more rapidly with larger droplet sizes at any given r. Closer to the droplets, the skewness of the PDF was negative for the droplet-droplet relative velocity in contrast to the positive values for the droplet-gas relative velocity. This signifies that closer to the droplets, the local fluctuation in droplet velocity is accompanied with larger fluctuations in velocity of droplets near by and smaller fluctuations in the surrounding gas velocity.

5. In order to obtain the characteristic dimensions of the droplet clusters in the flow, the local droplet concentration probability density function were compared with that arising from a purely random process by dividing an image into boxes of a certain size and counting the number of particles inside each box. At any measurement location, for box size equal to about one-fourth of the measurement area, maximum deviation from randomness was observed indicating particle clustering to be more prominent at this length scale. This was supported by the trend in the radial distribution function (RDF), obtained conditional on droplet size classes. At small radius of separation, droplets of higher size classes had higher values of RDF. So the droplet clustering was more prominent for the larger droplets.

6. At $R = 185\ mm$, the droplet-gas correlation coefficient (R_{dg}) for larger droplet sizes was found to increase in the axial direction and decrease in the cross-stream direction. This signifies an increase in length scales of the effective droplet-gas correlated motion in the gravitational direction and shows similarity with the particle accumulation due to preferential sweeping in finite gravity, as mentioned by Ferrante and Elghobashi (2003). This effect is also supported by the trend of the RDFs, which shows increasing dimension of the droplet clusters for larger sizes.

Chapter 4

Influence of large scale flow structures on two phase interaction

A turbulent flow is characterized by the existence of several length scales, some of which assume very specific roles in the description and analysis of the flow (Tennekes and Lumley, 1972). In the context of droplet-laden two phase flows, it remains important and interesting to study the interaction between the dispersed phase and the large scale motions or flow structures present in the continuous phase (entrained air flow around the droplets in the present case). Specifically, it is essential to evaluate the individual contributions of the flow structures on droplet-gas correlation coefficients and, also, study the momentum transfer mechanism at various length scales, which form the objectives of the present chapter. This provides, not only a deeper understanding of the physics of the droplet-gas interaction in a spray, but also a basis for modelling the coupling between the two phases. However, for this purpose, at first, it is essential to extract the different flow structures present in the carrier phase. Out of the several existing structure eduction methodologies, Proper Orthogonal Decomposition (POD), proposed by Lumley (1967), provides an unbiased method to extract the large scale structures in a turbulent flow, and this chapter begins with a brief description of the mathematical background of POD.

4.1 Proper Orthogonal Decomposition (POD)

Proper Orthogonal Decomposition, or POD, is a powerful and elegant method of data analysis. Based on Karhunen-Loeve procedure of probability theory (Loeve, 1955), POD aims at reducing the dimensionality of a data set, while retaining as much as possible of variations present in it. The method itself is known under a variety of names in different fields: Karhunen-Loeve procedure, Principal Component Analysis (Hotelling, 1933), Singular Value Decomposition (Golub and Van Loan, 1983), Empirical Eigenfunction Decomposition (Sirovich, 1987) and others. The basic idea behind POD is to describe a given statistical ensemble with the minimum number of deterministic modes. Also, because of the fastest convergence property, the number of energetically significant modes is minimum.

The application of POD in a turbulent flow offers a rational method for extraction of a complete set of spatial eigenfunctions or modes (also called 'characteristic eddies of turbulence') from the measured two point velocity cross-correlation matrix. Reviews can be found, for example, in Berkooz *et al.* (1993) and Holmes *et al.* (1996). The shape of the extracted modes depends on the particular flow field and serves as a set of optimal basis functions for expansion of the flow. The velocity field can be represented as a sum of the modes. Among all linear decompositions, POD is the most efficient one because it captures the largest amount of kinetic energy of fluctuations for a given number of modes. It can be considered as a Fourier-like expansion generalized for inhomogeneous directions of a turbulent flow. In fact, in a homogeneous flow direction, the POD 'degenerates' to a Fourier expansion. However, it should be made clear that the POD makes no assumptions about the linearity of the problem to which it is applied. In this respect, it is as blind as Fourier analysis (Berkooz *et al.*, 1993).

From a mathematical point of view, POD decomposes the flow, *i.e.* the instantaneous velocity data $u(x,t)$ (where 'x' and 't' are the two independent variables denoting space and time respectively), into a sum of product of spatial eigen functions

$\phi_n(x)$ and temporal coefficients $a_n(t)$ such that,

$$u(x,t) = \sum_{n=1}^{r_k} a_n(t)\phi_n(x) \tag{4.1}$$

where n represents the number of eigen functions considered and r is the rank of the velocity matrix $[u]_{M\times N}$. Here M is the number of image samples, N is the number of velocity data defined in each sample and the rank $r_k = \min(M,\ N)$. Equation (4.1) shows that both spatial and temporal orthogonal modes are coupled, *i.e.* each space component is associated with a time component partner. The latter is the time evolution of the former and the former is the spatial configuration of the latter, Aubry (1991).

Basic Theory

Lets consider a random generalised function $u(s)$ with s as a parameter (either space or time). In order to get a single deterministic function most similar to all the member of $u(s)$ on average, an averaging operation is required which again can be in either space or time. Mathematically, it corresponds to seeking a function ϕ such that the following function will be maximized,

$$Max\frac{\overline{(u,\phi)^2}}{(\phi,\phi)} = \lambda \tag{4.2}$$

where the overbar denotes averaging and $(,)$ is the scalar product. The classical method of the calculus of variations with a restriction $(\phi,\phi) = 1$ gives a necessary condition for Equation (4.2) to hold, which necessitates ϕ to be an eigen function of $R(s,s^*)$ so that

$$\int R(s,s^*)\phi(s^*)ds^* = \lambda\phi(s) \tag{4.3}$$

where $R(s,s^*) = \langle\ u(s) \times u(s^*)\ \rangle$ is an integrable cross correlation Hermitian tensor between two points s and s^* and '$*$' denotes the complex conjugate. There exists not

only one but an infinity of solutions to the above equation resulting in eigenfunctions ϕ_i and corresponding eigen values λ_i, where i denotes a member of the sequence. Because of symmetry and non-negative definiteness of $R(s, s^*)$, which ensures $\lambda_i \geq 0$, the eigenvalues can be ordered as $\lambda_i \geq \lambda_{i+1}$. Thus, the maximum in Equation (4.2) is achieved and corresponds to the largest eigen value λ_1. For the case when u represents instantaneous velocity fluctuations, the eigenvalues (λ_i) corresponds to the turbulent kinetic energy of the respective eigenfunctions or modes. Now any ensemble of random generalized functions can be represented by a series of orthonormal functions with random coefficients, the coefficients being uncorrelated with one another:

$$u = \sum_{n=1}^{\infty} a_n \phi_n \tag{4.4}$$

where

$$\overline{a_n a_m} = \delta_{mn} \lambda_{mn}$$

The coefficients a_n can be obtained using the orthonormal property of ϕ_n. It is necessary to mention here that the random coefficients are orthonormal if and only if the orthonormal functions (ϕ_n) and the constants (λ_n) are respectively the eigenfunctions and the eigenvalues of the correlation matrix.

Since experimental data are always discritized, a vector form of POD is used. This requires the integrations to be replaced by a finite quadrature form. The signal becomes an ensemble of finite-dimensional vectors $u(x, t)$ with x as spatial and t temporal parameters. If M is the number of flow realizations corresponding to discritized time intervals of t_i, $i = 1, 2, 3 \ldots M$ and if data are available for N spatially located points for each realizations, then $u(x, t)$ can be expressed as a matrix with dimension $M \times N$. The correlation function $R(s, s^*)$ becomes a correlation matrix. Then the two point velocity correlation tensor can be expressed in terms of flow

realizations by averaging in time as:

$$R(s, s^*) = \frac{1}{M} \sum_{i=1}^{M} u(x, t_i) \times u(x^*, t_i) \tag{4.5}$$

In this case POD always yields finite number of modes. The number of modes always equals to rank r of the matrix u and $r_k = \min(M,\ N)$. Thus, Equation (4.4) transforms into Equation (4.1).

The significant property of POD is that it minimizes the mean square error because of finite dimension representation and it is optimum in this regard. So for any, $k \leq r_k$,

$$\left(u - \sum_{n=1}^{k} a_n \phi_n \right)^2 \longrightarrow min \tag{4.6}$$

Hence the original field can be reconstructed by taking into account any number of modes with optimally minimized mean error.

Method of snapshot

Generally the number of data points related to a fluid problem, obtained either through experiments or computations, is very large ($N = 10^3 \sim 10^6$). In order to compute the POD modes, one must compute the $N \times N$ two point cross correlation matrix (Equation (4.5)) and solve the eigenvalue problem of Equation (4.3). A direct solution is computationally expensive or even not feasible. Sirovich (1987, 1991) pointed out that the temporal correlation matrix will yield the same dominant spatial modes, while often giving rise to a much smaller and computationally more tractable eigen problem - the method of snapshots. The method of snapshots dramatically reduces the calculation time of empirical eigenfunctions for the case of $M \ll N$. Instead of finding a spatial correlation matrix of size $N \times N$, one can compute a

temporal correlation matrix of size $M \times M$

$$R_T(t, t^*) = \frac{1}{N} \sum_{j=1}^{N} u(x_j, t) \times u(x_j, t^*) \tag{4.7}$$

The temporal coefficients $a_{n,i}$ can be obtained by solving $R_T\ \lambda = a\ \lambda$. Finally spatial eigenvectors ϕ_n are calculated from $\phi_n(\mathrm{x}) = \sum_{i=1}^{M} a_{n,i}\ u(x, t_i)$. The method of snapshots also overcomes the difficulties associated with the large data sets that accompany more than one dimension.

4.2 Application of POD

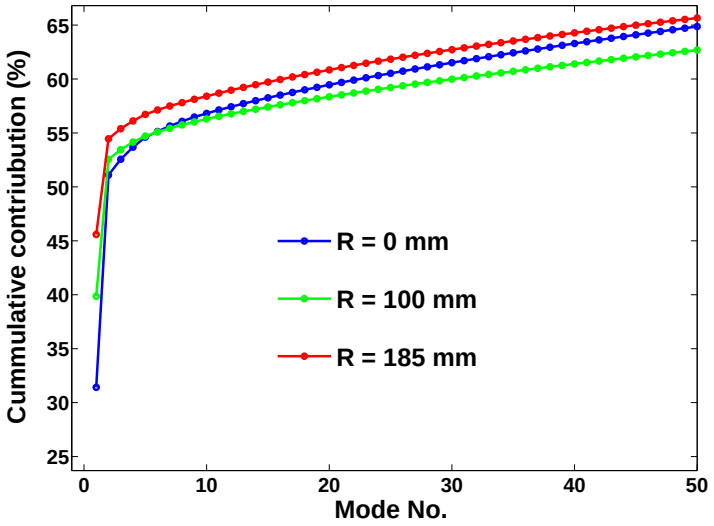


Figure 4.1: Cumulative contributions of the eigen-values of the respective POD modes for the measurement locations at $R = 0\ mm$, 100 mm and 185 mm respectively.

Although POD has been applied to extract flow structures from experimental data by a large number of researchers, its application over a two-phase flow with an aim of studying the interaction between the phases is almost non-existent. The reason being primarily due to the limitation of the techniques for *planar* measurement of velocity of both phases, which is subjugated in the present work due to the combined ILIDS and PIV technique. POD was applied over the instantaneous gas velocity

data (for both axial and cross-stream velocity components) of the two phase spray measurements, after subtracting the mean velocity. The eigen values (λ_n), which corresponds to the TKE content of the corresponding eigen modes, (ϕ_n) are obtained. In order to estimate the individual percentage contributions of the eigen modes towards the total turbulent kinetic energy ($\sum \lambda_i$), the cumulative eigen values of the POD modes ($\lambda_i / \sum \lambda_i$) were determined and plotted as shown in Figure 4.1. The 1st eigen mode contributes about 32%, 40% and 45% of the total turbulent kinetic energy at measurement locations $R = 0$, 100 and 185 mm respectively. Thus, the 1st mode represents the dominant eddy structure present in the carrier phase at various measurement locations considered here. In total about 3 and 500 modes are required to represent 50% and 90% of the total kinetic energy respectively signifying little contributions from the higher modes. The contribution of the 1st eigen-value increases away from the spray axis, which is attributed to the turbulent intensity towards the outer region of the spray [The higher the turbulence level, the higher the contribution from small scale structures].

Figure 4.2 presents the flow structures associated with the 1st, 2nd, 3rd and 4th eigen-modes respectively at the three measurement locations. Comparing the change in the direction of the flow structures corresponding to the 1st mode for all three locations, the 1st mode can be expected to be a part of the largest eddies present in the gas phase flow with length scale of the order of 100 mm (estimated as 1/5 of the spray width, as mentioned in the previous chapter). This is close to the estimated value of the largest length scale of the flow that was described earlier. Since the measurement area at each location (8 $mm \times 12$ mm) was about 10 orders of magnitude smaller than the largest length scale of the flow, the 1st mode could capture only a part of the eddy. The first eigen-mode indicates that the effect of this large scale structure (being mostly axial and upward/downward) is to either increase or decrease the instantaneous axial velocity of the gas flow, since the mean gas velocity is axial and either upwards or downwards (Figure 3.4). Similarly, the flow structure corresponding to the 2nd mode tends to increase/decrease the instantaneous cross-stream velocity towards or away from the spray axis. The 3rd and 4th mode in

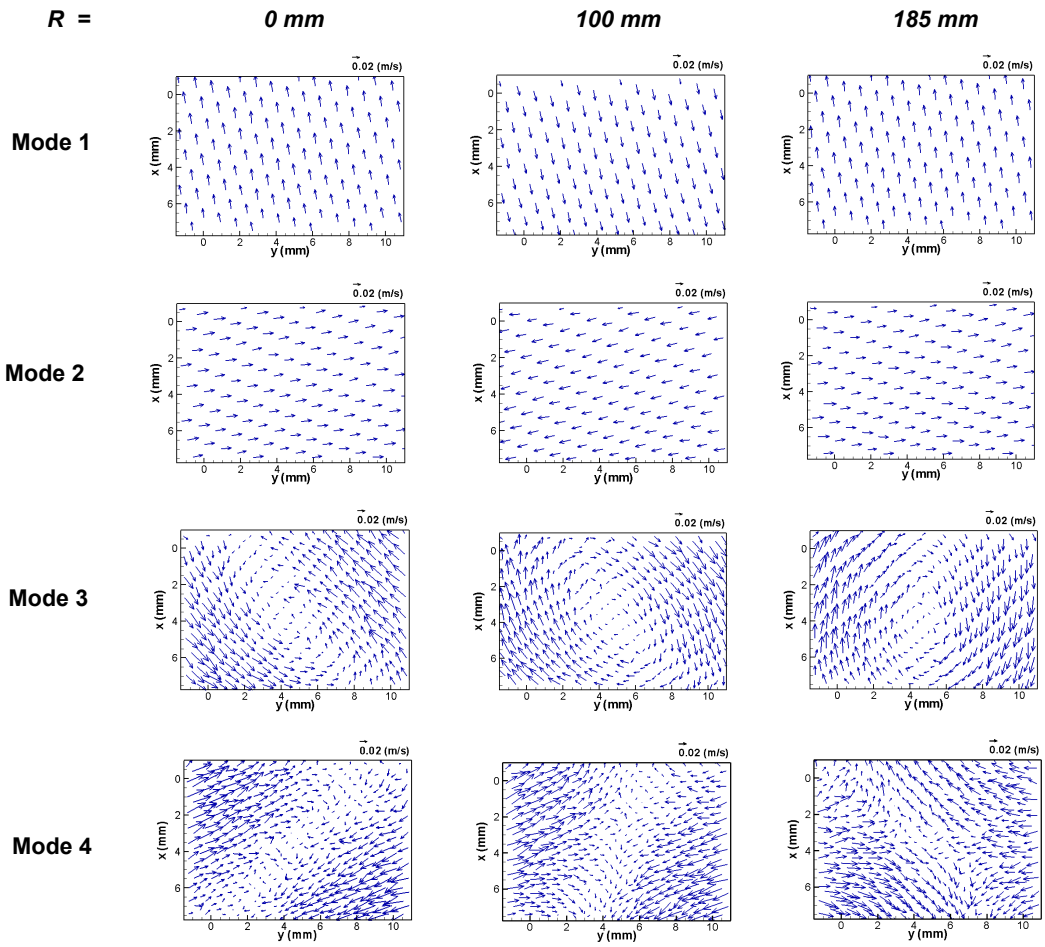


Figure 4.2: Flow structures associated with 1st, 2nd, 3rd and 4th POD modes for the cross-stream measurement locations $R = 0\ mm$, 100 mm and 185 mm respectively.

all cases show the presence of a vortical structure spanning the whole measurement area. Higher modes correspond to low level of turbulent kinetic energy and the corresponding length scales are becoming smaller.

4.2.1 Modal Contributions to droplet-gas velocity correlation

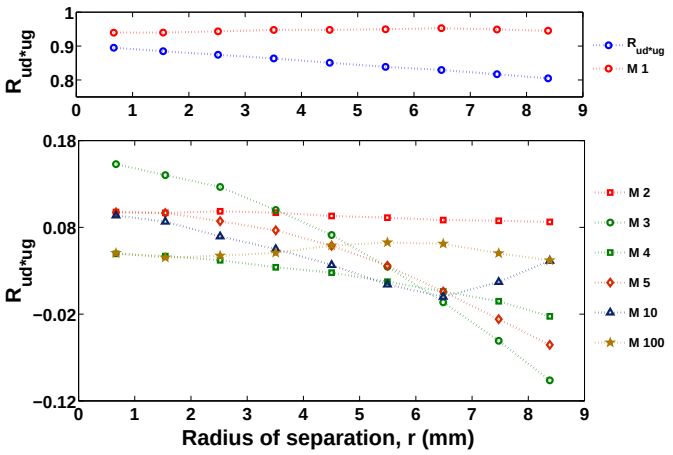
It is important to investigate how each individual flow structure contributes towards the correlation between the dispersed and continuous phases present in the flow. For this purpose, for a given eigen-mode, the instantaneous velocity data were reconstructed by considering that mode only. Thus, for any mode ϕ_i, the instantaneous velocity data (u_i) were obtained using the corresponding coefficient a_i as given below:

$$u_i = a_i \times \phi_i \tag{4.8}$$

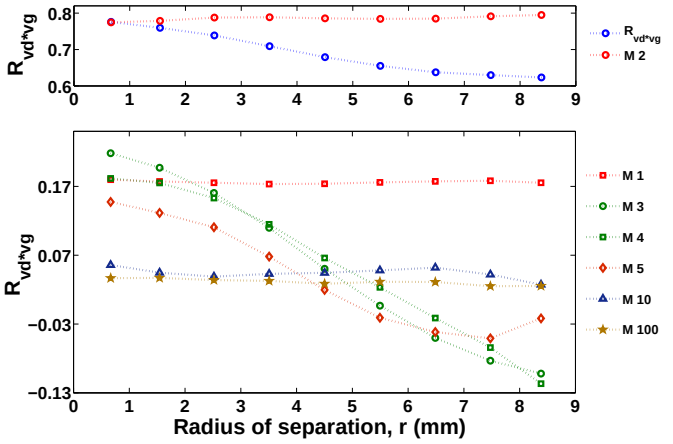
Then, the spatial correlations of droplet-gas velocity fluctuations were calculated following the same procedure, as described in the previous chapter. The droplet-gas velocity correlation can thus be represented as a sum of contributions from each mode. For example, for the axial direction this can be written as follows:

$$\begin{aligned} \overline{u_d u_g} &= \overline{u_d \sum_{i=1}^{r_k} a_i \times \phi_i} \\ &= \overline{u_d \times a_1 \times \phi_1} + \overline{u_d \times a_2 \times \phi_2} + ... + \overline{u_d \times a_{r_k} \times \phi_{r_k}} \end{aligned} \tag{4.9}$$

In Equation (4.9), the first term shows the contribution from the 1st mode and, so on. The correlation coefficient was obtained for each mode conditional on each droplet size classes and for various radius of separation, r. It should be noted here that the rms of velocity fluctuations of the gas flow, used for the purpose of normalization, was recalculated from the instantaneous velocity data. The following analysis will be done for the case of the measurement location at $R = 0$.



(a)



(b)

Figure 4.3: Contributions of various POD modes to the spatial correlation of droplet-gas velocity fluctuations for droplet size class 20-35μm at the measurement location $R = 0\ mm$ for (a) axial velocity component (R_{ud*ug}) and (b) cross-stream velocity component (R_{vd*vg}).

Figures 4.3(a) and 4.3(b) show the modal contributions towards the droplet-gas velocity correlation for droplet size class 20–35 μm for axial and cross-stream velocity components respectively at $R = 0\ mm$. In the axial direction, the flow structure represented by the 1st mode produced maximum correlation value (~ 0.9) and found to be independent of the radius of separation. The 2nd mode showed low correlation, of the order of 0.1, and maintained the same value at any distance from a given droplet. The vortical structure, depicted by the 3rd mode, resulted in a correlation coefficient, which was relatively high and positive closer to any given droplet but was negative away from it. The 4th and 5th modes, containing smaller vortical structures, showed similar behaviour, while, the other higher modes (after 10th mode), which may be characterized as random fluctuating components, showed very low correlation ($\sim$ 0.05). In contrast to the results in the axial direction, for cross-stream direction, the 2nd mode was dominant instead of the 1st mode, Figure 4.3(b). This was somewhat expected. The 2nd mode, being always dominant in cross-stream direction (see Figure 4.2), correlated well with the droplet velocity in the same direction. Other modes produced a correlation, which is similar to the case of axial velocity component. For the larger droplet size classes, the contributions of modes to the droplet-gas velocity correlation, was similar to that of 20–35μm size class.

4.2.2 Modification of turbulent kinetic energy at various length scales

Although comparison of the spatial correlation coefficient (Figure 3.14) provides useful insight into the momentum and energy exchange between the dispersed and carrier phase, it is also important to investigate the physical mechanism of particle-turbulence interaction at various length scales of the flow. It is interesting to see how the interaction of the same size droplets augment turbulence at one length scale of the flow, while attenuate it at others. This is not only important to gain deeper understanding of the physics of the problem, but also, is a prerequisite for the development of mathematical models, for example, subgrid scale modelling in LES.

For this purpose, application of POD over the gas velocity data for extraction of the large scale flow structures was invariably the best option, since it provides a means to study the selective influence of the flow structures on two-phase interaction.

Consider the equation of the modification of TKE of the carrier phase in a droplet-laden gas flow, as mentioned earlier in Chapter 1 before,

$$\frac{dk}{dt} = \left(\frac{dk}{dt}\right)_{sp} - \frac{\overline{C}}{\rho_f \tau_d}\left(\overline{u_{ig}u_{ig}} - \overline{u_{ig}u_{id}}\right) - \frac{1}{\rho_f \tau_d}\left(\overline{cu_{ig}u_{ig}} - \overline{cu_{ig}u_{id}}\right) - \frac{1}{\rho_f \tau_p}\left(\overline{U_{ig}} - \overline{U_{id}}\right)\overline{cu_{ig}} \tag{4.10}$$

Here U and u refers to the instantaneous and fluctuating velocity respectively and the subscript 'i' refers to either of the velocity components. The first term on right comprises the production, dissipation and transport terms in single phase fluid (no droplets/particles). The remaining terms include correlations of the particle concentration fluctuations (c) and velocity fluctuations of the fluid and/or particle-fluid velocity correlations and represents an 'extra' modification of turbulent kinetic energy due to particles. Since the equation is defined for moderate particle mass loading, so particle-particle interactions are assumed not to be present. The feasibility of incorporation of the effect of two-way coupling (*i.e.* modification of turbulence by the particles through interfacial momentum transfer) depends on successful modelling of the cross-correlation terms appearing in the TKE equation.

In the present case, the correlation coefficient between fluctuating fluid velocity and droplet concentration was found to be quite low, *i.e.* $R_{c*u_{ig}} \approx 0.1$, as mentioned in the previous chapter. Also, the triple correlation, $R_{c*ug*ug}$, was low being of the order of 0.2. Since the spatial velocity correlation between the droplets (of all size classes) and gas flow was high ($R_{dg} \geq 0.7$), the triple correlation between the fluctuating droplet and gas velocities and droplet concentration ($R_{c*u_{id}*u_{ig}}$) is expected to be of order of $R_{c*ug*ug}$ as well. Also, the difference in the mean droplet velocity (of all size classes) and the mean gas velocity was negligible ($\overline{U_{ig}} - \overline{U_{id}} \leq 0.05\ m/s$). Hence, the third and fourth terms on the RHS of Equation (4.10) can be considered negligible.

Thus we have,

$$\frac{dk}{dt} = \left(\frac{dk}{dt}\right)_{sp} - e_p \tag{4.11}$$

where,

$$\begin{aligned} e_p &= \frac{\overline{C}}{\rho_f \tau_d} \left(\overline{u_{ig} u_{ig}} - \overline{u_{id} u_{ig}}\right) \\ &= \frac{\overline{C}}{\rho_f \tau_d} u_{igr}^2 \left(R_{gg} - RN_{dg}\right) \end{aligned} \tag{4.12}$$

with,

$$RN_{dg} = R_{dg} \times \frac{u_{idr}}{u_{igr}} \tag{4.13}$$

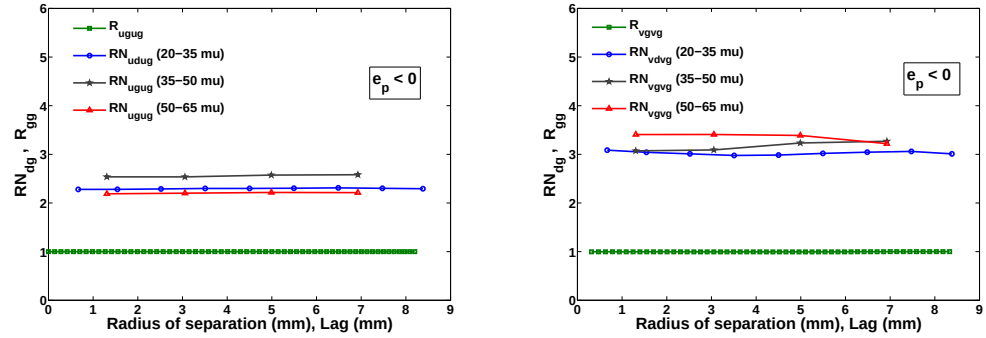
where R_{gg} and R_{dg} are the correlation coefficients defined before. u_{idr} and u_{igr} are the droplet and gas rms velocity respectively. RN_{dg} is the droplet-gas correlation normalized with rms of gas velocity fluctuation. It should be noted that the magnitude of modification of the TKE (the factor e_p) depends not only on the correlation coefficients but is also proportional to the mean droplet concentration ($\overline{C}$) and the inverse of particle time constant (τ_d). In the present experiment, the volume fraction (volume of the average number of droplets to the total measurement volume) was low about 0.005%. Also, as described in the previous chapter, the comparison of the droplet-gas and gas correlation shows the R_{dg} and R_{gg} terms lie close to each other. Thus the energy transfer is expected to be low and the flow can be considered to be one-way coupled *i.e.* the dispersed phase does not affect the turbulence of the carrier phase. However, it does not provide information on the energy transfer mechanism at different length scales of the flow. The two-phases may interact in such a manner that while at one length scale of the flow the turbulence in the carrier phase is attenuated, it is augmented at the other so that the overall energy transfer is negligible (Ferrante and Elghobashi, 2003). Hence, the following analysis

is done in order to discover the 'truth' behind the two-phase interaction. It should be noted here that the comparison of the experimental results with the DNS simulations of Ferrante and Elghobashi (2003) can be qualitative only. Since the droplet mass loading was low in the present case, the magnitude of turbulence modulation in the carrier phase is expected to be low as well.

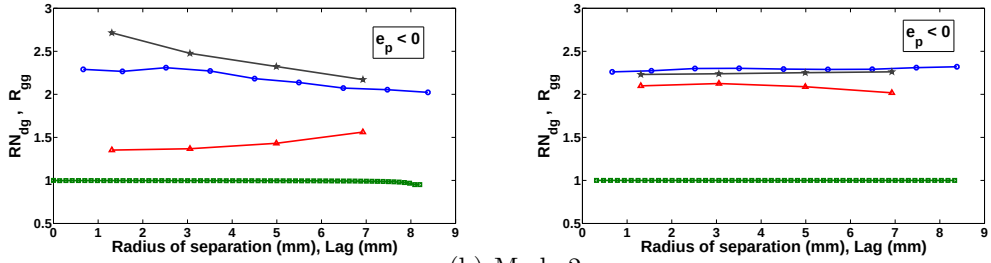
The R_{gg} and RN_{dg} terms were evaluated for different POD modes (flow structures) considering one at a time, for droplets of different size classes. For this purpose, the instantaneous gas velocity field were reconstructed following Equation (4.9). The assumption of neglecting the last two terms on the RHS of Equation (4.10) (*i.e.* correlation between droplet concentration and droplet/gas velocity fluctuations) still holds in this case. The term $R_{c*u_{ig}}$ was found to be very low (≈ 0.1) when evaluated for various modes.

As mentioned before, the correlation terms appearing in Equation (4.10) are defined at the droplet position only. Since this is unrealistic, because the droplets occupy certain volume in space, those terms should be evaluated at a position nearest to the droplet. So, in the present case, the factor e_p is defined only for the minimum value of r. However, the correlation terms (R_{gg} and RN_{dg}) are also evaluated for various radius of separation, r. This would indicate the way the two correlation terms contest with each other away from the droplets. The competition between these two terms can provide the answer to the question, how the droplets are going to modify the TKE of the carrier phase (attenuate or augment the turbulence) at different length scales.

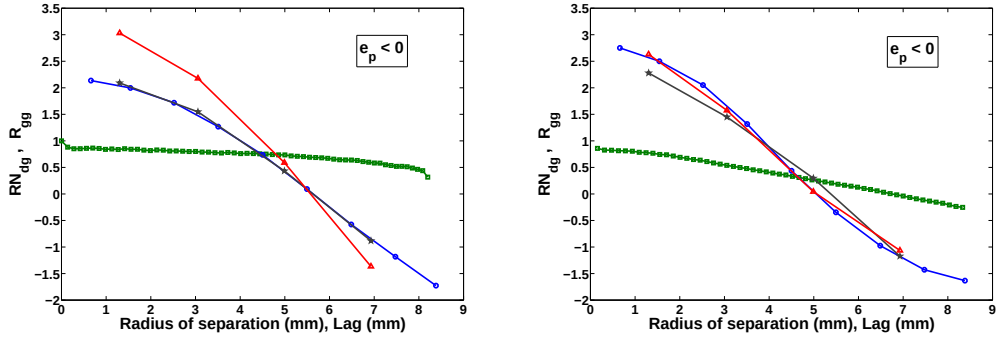
Figure 4.4 shows the comparison between the correlation coefficients R_{gg} and RN_{dg} evaluated for both axial and cross-stream velocities for the first four modes for the measurement locations at $R = 0\ mm$. For the case of the largest flow structure or Mode 1, the modified droplet-gas correlation coefficient RN_{dg} lies well above the gas correlation R_{gg}, as shown in Figure 4.4(a), making the factor e_p in Equation (4.12) negative for both velocity components. This would mean positive contribution to $(dk/dt)_{sp}$ resulting in augmenting turbulence at the corresponding length scale of the flow. The reason behind this can be explained as below. Since the concerned flow



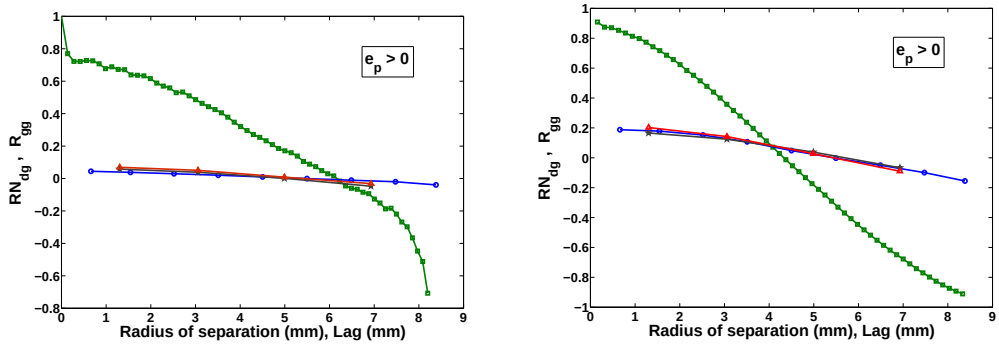
(a) Mode 1



(b) Mode 2



(c) Mode 3



(d) Mode 4

Figure 4.4: Comparison of the spatial gas correlation coefficient R_{gg} and the modified droplet-gas coefficient RN_{gg} for both axial (left) and cross-stream (right) velocity components evaluated for (a) Mode 1, (b) Mode 2, (c) Mode 3 and (d) Mode 4 for the measurement location $R = 0\ mm$.

structure corresponds to the largest length scale of the flow, the associated time scale of the flow (τ_l) is also large which results in smaller Stokes number ($St = \tau_p/\tau_l$) of the droplets of all size classes. This means the droplets tend to behave as 'microparticles' which follow even the small fluid fluctuations. However since the material density of the droplets, ρ_d, is much higher than that of the carrier fluid, ρ_g, they cause the fluid to behave like a 'heavy gas'. Since the 'microparticles' trajectories are almost aligned with fluid points trajectories, and their kinetic energy is larger than that of their surrounding fluid, the correlation $\overline{u_d u_g}$ remains higher than the fluid velocity correlation $\overline{u_g u_g}$. Similar trend in the velocity correlation terms was observed by Ferrante and Elghobashi (2003) for very small Stokes number ($St_k << 1$).

As the droplets (of a given size) interact with smaller flow structures (corresponding to higher POD modes), the Stokes number (St) of the droplets increases since the time scale of the flow structures decreases accordingly: recall that the Stokes number of droplets with size 20–35μm based on integral time scale was 0.005 while its value was 4.32 when based on Kolmogorov time scale. The same droplets (which act as flow tracer in case of the largest flow structure) now behave as larger particles. These particles do not respond to the velocity fluctuations of the surrounding fluid as quickly as 'microparticles' do, but rather tend to 'escape' from their initial surrounding fluid, "crossing" the trajectories of the fluid points. Whereas 'microparticles' remain in the vortical structures of their initial surrounding fluid, large particles are ejected from these structures. Hence, the correlation between the droplet and surrounding gas decreases. However, as can be observed in Figure 4.4(b) in the case of Mode 2, RN_{dg} still remains higher than R_{gg}. Thus, $e_p < 0$ and the turbulence is augmented. Similar trend is observed for Mode 3, though away from the droplet, the droplets and gas velocity fluctuations are negatively correlated.

When the droplets interact with still smaller flow structures (for example, Mode 4), the droplet-gas correlation reduces drastically since the Stokes number of the droplets becomes high. As shown in Figure 4.4(d), the gas correlation becomes dominant or $R_{gg} > RN_{dg}$ causing $e_p > 0$. This results in negative contribution to the term $(dk/dt)_{sp}$ eventually attenuating the turbulence. This is again in

agreement with (Ferrante and Elghobashi, 2003). The same trend is expected for the case of still higher modes or smaller structures. No significant difference in the behaviour of different droplet size classes could be observed. Thus, it can be concluded that the turbulence enhancement by the droplets at the first three length scales of the flow (which contributes about 50% of the total TKE) is compensated by its attenuation at the other small scales so that the gross momentum exchange between the two phases is negligible. This is evident by the similar orders of R_{gg} and R_{dg} for both velocity components as shown in Figure 3.14(a) in the previous chapter. Ferrante and Elghobashi (2003) have previously reported the existence of the dispersed particles with Stokes number (based on Kolmogorov scale), $St \approx 0.25$ (denoted as "ghost particles"), which modify the spectra of the turbulence kinetic energy in such a way that keeps the decay rate of the turbulence energy nearly identical to that of particle-free turbulence. For the present case the Stokes number based on Kolmogorov scale for the three droplet size classes are of the orders of 5, 10 and 20 respectively. For $St = 5$, the DNS simulation showed turbulence attenuation at nearly all length scales of the flow, while the turbulence was augmented at the large length scales of the flow in the present study. The reason behind such discrepancy can be attributed to the range of the eddy sizes present in the carrier flow. While the ratio of the integral length scale to Kolmogorov scale was about 30 in the simulation, it was of the order of 1000 for the present experiment. Thus, the same droplet can show significantly different response to the largest and the smallest eddies in the carrier flow.

4.3 Summary

This chapter continues the discussion on the interaction mechanism between the droplet and gas flow in the polydispersed spray as described in Chapter 3 and attempts to explain the influence of the large scale flow structures in the carrier phase on the droplet-gas correlated motion. The flow structures, at any measurement location, were obtained by applying proper orthogonal decomposition (POD) on the

corresponding instantaneous gas velocity data. Each POD mode corresponds to a flow structure and, is associated with an eigen value, which represents the turbulent kinetic energy content of that flow structure. The first three eigen modes captured about 50% of the total turbulent kinetic energy of the flow signifying the dominance of the large scale flow structures in the gas flow. The flow structures associated with the 1st and 2nd mode, were found to be dominant in axial and cross-stream directions respectively, while the 3rd mode shows the presence of a vortical structure spanning the whole measurement area. Contribution of a given POD mode on the droplet-gas spatial velocity correlation was determined by reconstructing the instantaneous gas velocity data by considering that mode only. For the near axial location at $R = 0$ mm, in axial direction, the 1st mode and in cross-stream direction, the 2nd mode were found to be the dominant contributors.

From Chapter 3 we know that, for the measurement location at $R = 0$ mm, the droplet-gas and gas velocity correlations were close to each other indicating negligible momentum transfer between the two phases. However, this did not provide information on the momentum transfer at different length scales of the flow. In order to understand the turbulence modulation by droplets at different length scales of the flow, the droplet-gas and gas velocity correlations were compared for each flow structures determined by POD analysis. It was found that, in the present case, the droplets tend to augment turbulence in the carrier phase at large length scales of the flow and attenuate it at small length scales so that the total change in the turbulent kinetic energy remains the same. The transition in the manner droplets modify turbulence was observed at Mode 4, where the droplet-gas velocity correlation reduced significantly compared to the gas velocity correlation due to poor response of the droplets to the gas motion. These results provide new insights on the two-phase interaction mechanisms between the dispersed and continuous phases in a spray.

Chapter 5

Combined ILIDS and PLIF technique for evaporative spray measurement

In this chapter, the experimental technique of combining ILIDS and PLIF is described as a novel approach for simultaneous planar measurements of both droplet and vapour phases in an evaporative spray. The principle of the combined technique and the related experimental arrangements and image processing are detailed. Similar to the combined ILIDS and PIV arrangement, the discrepancy in droplet centre also appears in the present technique primarily due to the defocused imaging of ILIDS. This issue is reconsidered with respect to the present optical set up. Two applications of the combined ILIDS and PLIF technique are presented. At first, the combined technique is applied to a stream of mono-sized droplets for two different droplet sizes. Here, the purposes are to demonstrate the potential of the combined technique to identify the same droplet in both defocused and focused images and to study the effect of inter droplet spacing on droplet evaporation rate. The combined technique is then employed for evaporative spray measurement with an aim of evaluating the instantaneous group combustion number and the average vapour concentration fluctuations around individual droplets.

5.1 Combining ILIDS with PLIF

Combining ILIDS with PLIF allows simultaneous planar measurements of droplet and vapour phases in an evaporative spray. For the measurement of droplet size, velocity and inter-droplet distance, the planar sizing technique ILIDS is applied while the vapour concentration distribution in the vicinity of droplets is measured by PLIF. This facilitates unique evaluation of the instantaneous group combustion number and the correlation between vapour concentration around the droplets and droplet properties.

5.1.1 Principle and Experimental Set-up

The principle of combining ILIDS with PLIF is similar to the combined ILIDS and PIV technique as described in Chapter 2. In both cases, the out-of-focus technique (ILIDS) is utilized in conjunction with the in-focus technique (PIV or PLIF). The fundamental difference in the two approaches is in imaging the droplet and vapour fluorescence in PLIF in contrast to imaging the scattered light of droplets (glare points) and seeding particles in PIV. The basis of the combined ILIDS and PLIF technique lies in the fact that the position of droplets in a spray, obtained by ILIDS beforehand, helps in identifying the images of the same droplets (droplet fluorescence) in the PLIF image. This makes it possible to obtain simultaneous planar measurements of the droplet properties along with the vapour concentration around the droplets.

However, the experimental set-up associated with the present method (specifically, the choice of the laser and the fluorescence marker) increases further the complexities of the optical arrangement as compared to the combined ILIDS and PIV technique. The principal requirement of the combined ILIDS and PLIF technique is that the wavelengths of fluorescence for PLIF must be discrete from that of the scattered light for ILIDS. Since intensity of the scattered light of droplets is usually orders of magnitude greater than the corresponding fluorescent intensity, it will be impossible, otherwise, to discriminate between the two. In order to satisfy this criterion, it was

decided to use acetone as the fluorescence marker and employ two laser sources (with different wavelengths, λ) one for each technique. Thus, the green light ($\lambda = 532\ nm$) and the ultra violet (UV) light ($\lambda = 266\ nm$) were selected for ILIDS and PLIF, respectively. Acetone absorbs the UV light at 266 nm and emits fluorescence which has a spectrum in the range 350–550 nm with the peak around 435 nm, while the droplets scatter light at 532 nm without absorbing. The wavelengths of fluorescence and scattered light are almost discrete from each other, so can be separated by using appropriate optical filters. Thus, the camera for PLIF captures only fluorescence from acetone (droplets and vapour), while, the camera for ILIDS captures only the scattered light (from droplets only).

Acetone, as a tracer, has many additional advantages. The high vapour pressure of pure acetone makes it simple to recreate the high evaporation rates of fuel spray without complicated heating arrangements. Also, no separate seeding for the vapour phase is necessary. The florescence from acetone has low dependence on pressure and temperature. This choice of fluorescence marker allows the adaptability to various conditions and helps to avoid the complex correction in the evaluation of the vapour concentration. Moreover, the strong absorption coefficient of acetone at the laser wavelength makes the liquid acetone fluorescence from the large drops limited to a surface contribution while the simultaneous contribution of the gas phase scales as the mass of acetone vapour in the probed volume (Bazile and Stepowski, 1995). This makes it possible to detect and measure the vapour fluorescence on single shot planar images of the spray, while avoiding local saturation of the CCD camera by the drop images.

The experimental arrangement of the combined technique is shown in Figure 5.1. For measurements by ILIDS, the flow field is illuminated by a frequency-doubled, double pulse Nd:YAG laser (120 $mJ/pulse$ at 532 nm; beam diameter 5 mm; 5 ns pulse width; New Wave Research), denoted as Laser 1. For PLIF measurement, acetone droplets and vapour were excited by a fourth harmonic generator, single pulse Nd:YAG Laser (100 $mJ/pulse$ at 266 nm; beam diameter 10 mm; 5 ns pulse width; Continuum), denoted as Laser 2. Since the beams of the two lasers were at

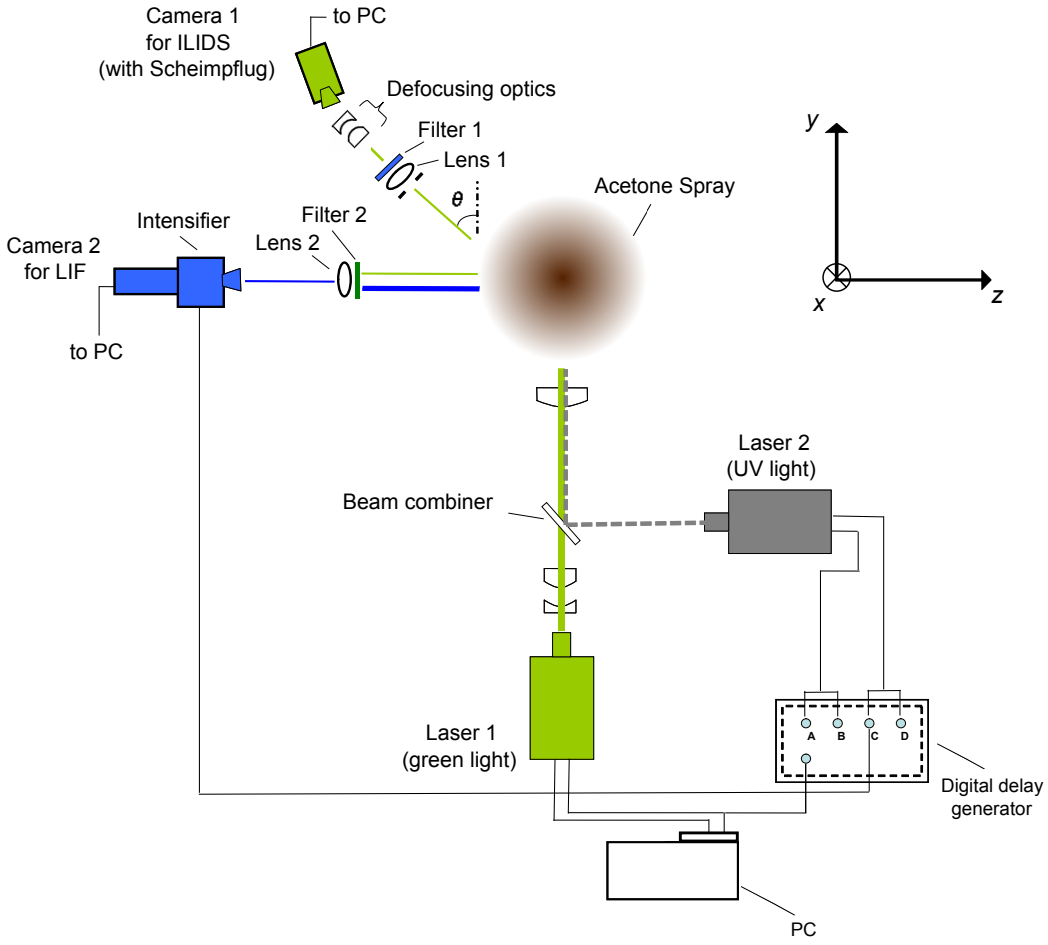


Figure 5.1: Experimental arrangement of the combined ILIDS and PLIF technique.

different heights from the optical bench on which they were mounted, the UV beam was elevated using two prisms to ensure same elevations of both laser beams. Using a pair of concave-convex cylindrical lenses ($f = -25\ mm$ and $+75\ mm$), the green laser beam was expanded to 15 mm in vertical direction. Then, the two beams are combined using a beam combiner (25 $mm \times 36\ mm$; 95% transmittance for green light and 99.9% reflectance for UV). Utmost care was taken to ensure both beam axes were collinear and, parallel to the optical bench. Both laser sheets were focused at the measurement region using a cylindrical convex lens (fused silica; $f = +400\ mm$). The dimensions (height and waist) of the laser sheets, at the measurement location, were approximately 15 mm and 1 mm for the $\lambda = 532\ nm$ beam and, 10 mm and 1 mm for the $\lambda = 266\ nm$ beam, respectively.

The scattered light was collected through Lens 1 (135-mm $f/2.8$ Nikon lens) along with a suitable band pass optical filter (532 nm; 3 nm band width) to restrict the fluorescence signal from the droplets at wavelength around 435 nm. The images were captured through Camera 1 (PCO; Sensicam QE, 12 bit, $1040 \times 1376\ pixels^2$), set at scattering angle $\theta = 70°$, which is the optimum forward scattering angle for acetone droplets for ILIDS droplet sizing with vertically polarized light. The Scheimpflug condition was maintained to ensure uniform defocusing at Camera 1. The defocusing was achieved by a pair of cylindrical lenses ($+50\ mm$ and $-50\ mm$ focal length). The collecting angle (α) was set to 7.15°, resulting in resolution of $\kappa = 5.28\ \mu m/fringe$ for the ILIDS system. The field of view was approximately $9 \times 12\ mm^2$, with magnification of about 0.7 in both horizontal and vertical directions.

The fluorescent intensities were collected through Lens 2 (100-mm $f/4$ Nikon lens) with a suitable band pass filter (260–490 nm) to restrict the scattered light from droplets at 532 nm. The lens, being made of BK7, could absorb the scattered UV light at 266 nm. The fluorescent light was imaged by Camera 2 (PCO; Sensicam QE, 12 bit, $1040 \times 1376\ pixels^2$), coupled to a gated intensifier (IRO image intensifier with PCO; Lavision). The gain of the intensified CCD (ICCD) camera was adjusted to keep the energy recorded by the array detector proportional to the fluorescence signal issued from the liquid and gas phases, which prevents the ICCD camera from local saturation

and blooming induced by the liquid fluorescence. Because of the unavailability of a suitable Scheimpflug mount for Camera 2, the Scheimpflug condition could not be incorporated. So, Camera 2 could not be aligned at the same scattering angle θ similar to Camera 1. Thus, as shown in Figure 5.1, Camera 2 was placed at right angle to the laser sheet, on the same side of the laser sheet as Camera 1. From Chapter 2 (Figure 2.14(c)), it can be recalled that similar configuration was not recommended for the combined ILIDS and PIV arrangement, since this causes negligible contribution from the first order refracted ray making detection of centre of droplet image difficult. It should be noted, however that, in the present case the liquid fluorescence is imaged (instead of the scattered light) which is independent of the direction of imaging. Hence, the 90°–alignment of the PLIF camera with respect to the laser sheet should work well. The field of view was approximately $9 \times 12\ mm^2$, similar to that of ILIDS, with a resolution of about $9\mu m/pixels$ and magnification of 0.7 in both horizontal and vertical directions. The camera calibration was performed with both cameras under in-focus condition. The method is the same as described in Section–2.3.2 for the combined ILIDS and PIV technique in Chapter 2 and hence, not repeated here.

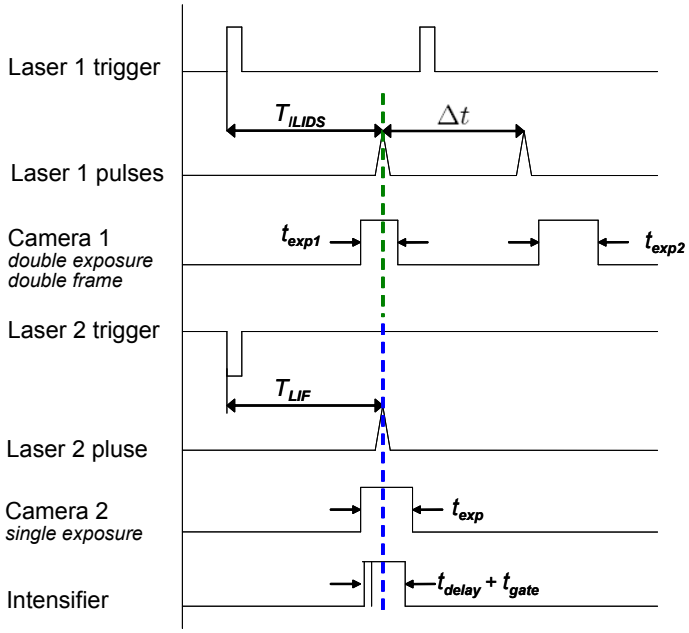


Figure 5.2: Timing diagram of the combined ILIDS and PLIF technique.

Synchronous operation of the lasers, cameras and intensifier is essential for the

combined technique. The corresponding timing diagram is shown in Figure 5.2. Laser 1 was triggered by a computer via LaVision Davis software. At the same time, Laser 2 was triggered by a digital delay generator (DG 535; Stanford Research systems), which is in turn triggered by the computer. The Q-switch delay timing of Laser 2 was controlled by the delay generator in such a way that the corresponding laser pulse (dotted blue line) was synchronous with the 1st pulse of Laser 1 (dotted green line), as shown in Figure 5.2. The exposure times of Camera 1 (for ILIDS) is fixed for the "double pulse double exposure" mode of operation (for droplet velocity estimation), while that for Camera 2 (operating on "single exposure" mode) could be varied by the Davis system. The delay generator also controls the IRO image intensifier through which the delay timing (t_{delay}), the gate exposure time (t_{gate}) and the gain of the intensifier could be adjusted. The triggering and timing of Camera 1 and Camera 2 (via the intensifier) are made synchronous with the respective laser pulses so that, the PLIF image was captured at the same time as the ILIDS image.

The same 3D–traversing frame mechanism (as shown in Figure 2.12 and described in Chapter 2) was used to mount the whole optical assembly including the laser, laser sheet optics, cameras and lenses. This was mechanically isolated from the rig which consists of an aluminium frame containing an air assist nozzle producing a solid cone spray. Measurements at various locations in the spray could be obtained by traversing the iron frame mechanism to the desired places. Liquid acetone, pressurized at 1.2 bar in a pressure vessel, was fed to the nozzle through stainless steel hoses. The flow rates of liquid acetone and air were controlled by the respective rotameters and were set to 0.03 lt/min and 15 lt/min respectively. This resulted in a spray with sauter mean diameter (SMD) of about 45μm at a distance of 350 mm from the nozzle. The acetone droplets and vapour were extracted from the rig using an air extraction system available in the laboratory. In order to examine the potential of the combined technique for droplet/vapour phase measurements, the technique was first applied to a mono-sized droplet stream. For this purpose, the droplet generator was carefully mounted in the same rig.

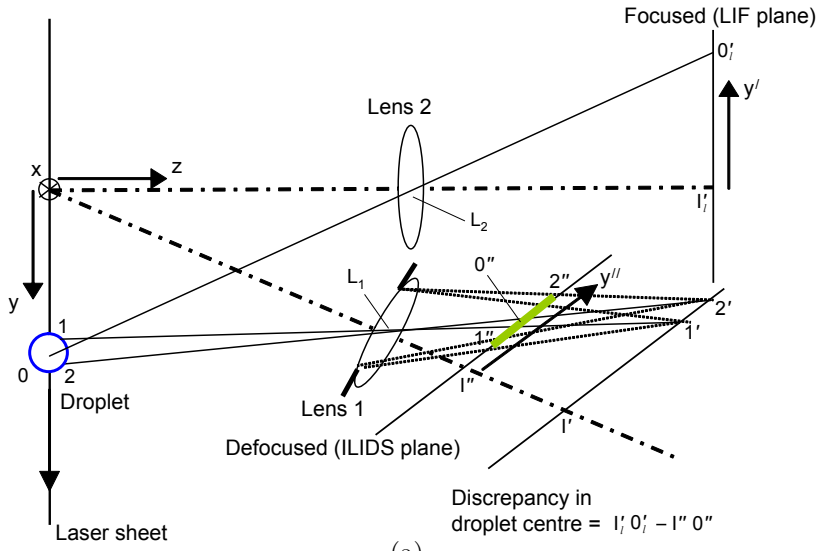
5.1.2 Droplet centre discrepancy

Similar to the combined ILIDS and PIV technique, the out-of-focus imaging of the present combined technique is expected to cause a discrepancy in the centre of the same droplet when imaged through ILIDS and PLIF. This may lead to erroneous pairing up of the droplet properties and vapour concentration distribution in the spray.

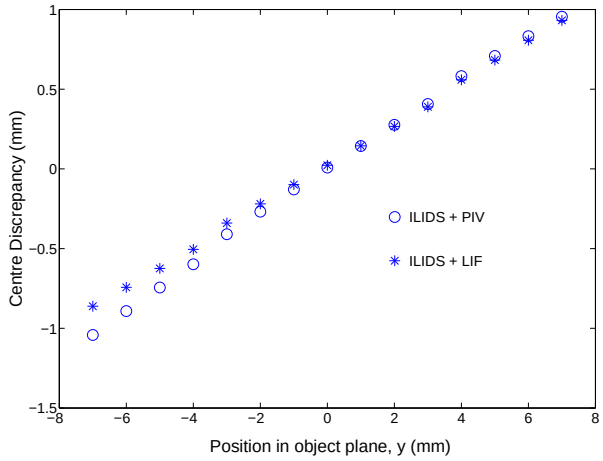
In literature, only Kurosawa *et al.* (2002) have reported combined measurements with ILIDS and PLIF in an evaporative spray. Though they noticed the discrepancy of droplet position in the two images, they attributed the reason behind this occurrence to "the accuracy of position calibration caused by the use of two cameras for each measurement". However, from the theoretical analysis (based on the geometric optics) of the centre discrepancy effect in the combined ILIDS and PIV technique (Chapter 2), we know that the positioning error does not depend on the inaccuracy in camera calibration or locating the droplet centres on the images. Instead it is principally governed by the defocusing of the ILIDS imaging. The magnitude of the discrepancy was found to be a function of position of the droplet image on the CCD array and the degree of defocus, but almost independent of droplet size. Specifically, it varies approximately linearly across the image along the direction of propagation of the laser sheet for a given defocus setting in the ILIDS image.

Following the theoretical analysis of Chapter 2, a similar analysis is briefly presented here which predicts the centre discrepancy for the combined ILIDS/PLIF technique, since the current optical arrangement is different than that of Chapter 2. Figure 5.3(a) shows the simplified ray diagram for a droplet, which is being simultaneously imaged on PLIF and ILIDS CCD arrays. All assumptions of the theoretical analysis of the combined ILIDS and PIV technique remain valid here as well. However, the present analysis differs from the previous case, primarily, in the following two aspects.

(a) Unlike the focal plane in PIV, the focal plane for PLIF is perpendicular to the lens axis. So, the optical configuration includes two lenses and CCD arrays one



(a)



(b)

Figure 5.3: (a) Schematic of the optical system for theoretical prediction of discrepancy in droplet centres between the focused plane in PLIF imaging and defocused plane in ILIDS imaging (b) Discrepancy in geometric centre of the fringe pattern in the ILIDS defocus plane and centre of the droplet image in the PLIF focal plane as a function of the y position in the object plane. The discrepancy for the case of combined ILIDS with PIV arrangement is also plotted for comparison.

for each technique, unlike the previous case where only one common lens was used (Figure 2.17a).

(b) Secondly, the fluorescent intensity signal from a liquid droplet is being imaged on the focal plane instead of glare points.

As shown in Figure 5.3(a), consider a droplet situated on the xy plane, which coincides with the laser sheet. The droplet is in the middle of the laser sheet and on plane at $x = 0$ and a distance y from the origin—the position of the droplet centre is at 0(0, y, 0). The image of the droplet centre on the PLIF focal plane ($0_l^{'}$) can be obtained straight away using lens makers formula unlike in ILIDS/PIV arrangement, where the droplet centre in the focal plane is determined by the middle of the distance between the two glare points ($1^{'}$ and $2^{'}$). The calibration of ILIDS and PLIF CCD arrays is carried out with the ILIDS optics adjusted to be in focus, so the coordinate systems are fixed to the focussed ILIDS and PLIF CCD arrays, both having their origins ($\mathrm{I}^{'}$ and $\mathrm{I}_l^{'}$) on the axis of the lens. After calibration, the ILIDS image is defocused by shifting the image plane towards the lens. The degree of defocus is defined as the ratio of the distance between the centres of defocus plane to in-focus plane ($\mathrm{I}^{''}\mathrm{I}^{'}$) to that of centre of the lens to in-focus plane ($\mathrm{L}_1\mathrm{I}^{'}$). The geometrical centre of the ILIDS image is $0^{''}$, the mid-point of the fringe pattern $1^{''}2^{''}$. Thus, the discrepancy in the centre of the same droplet being imaged in the PLIF and ILIDS CCD arrays is equal to $\mathrm{I}_l^{'}0_l^{'} - \mathrm{I}^{''}0^{''}$. The input parameters for the analysis, similar to the experimental set-up, were: $\theta = 70°$, droplet diameter = 200 μm, focal lengths of Lens 1 (for ILIDS) and Lens 2 (for PLIF) 105 mm and 135 mm respectively, object distances of the corresponding camera lenses 250 mm and 320 mm respectively, and aperture size before Lens 1 = 40 mm. The centre discrepancy is plotted in Figure 5.3(b) for various y locations at the object plane. For comparison purposes, the droplet centre discrepancy for the combined operation of ILIDS and PIV techniques (under the same optical condition) is also plotted.

Figure 5.3(b) shows that the trend of the centre discrepancy in the present case is almost similar to the ILIDS/PIV arrangement, *i.e.* it varies almost linearly across

the image plane, from being negative on one side of the image plane to positive on the other side. For the particular optical parameters considered here, the maximum discrepancy is found towards the edge of the CCD array and can be of the order of 1 mm, or five times greater than even the relatively large droplet diameter considered here. Also, as before, the discrepancy was found to be almost independent of droplet size. The small difference between the trend of the centre discrepancy between ILIDS+PIV and ILIDS+PLIF techniques is due to the non-90° viewing angle of the PIV camera. Experimental quantification of the centre discrepancy, essential to verify the theoretical prediction, will appear in the following section.

5.2 Application of the combined technique to mono-sized droplet stream

In this section, application of the combined ILIDS and PLIF technique is reported for mono-sized acetone droplet streams. There are two objectives. First, in order to examine the ability of the combined technique to locate the same droplet in both images by quantifying the error of the positions of the centre of the droplet images. Secondly, to present measurements of vapour concentration around the mono-dispersed acetone droplet stream and examine the influence of inter-droplet distance on droplet evaporation.

Experiments were performed with a custom-built droplet generator (Pergamalis, 2002), producing a single stream of equally spaced mono-sized droplets. The injection pressure was set at 1.0 bar. Two different droplet sizes were considered. The pinhole sizes at the exit of the mono-dispersed droplet generator were 200μm and 50μm respectively, while the corresponding water flow rates were 7.5 ml/min and 0.8 ml/min. The resonance frequency of the piezoelectric elements of the generator was set to 20 kHz. Under this condition, the diameters of the droplets (theoretical values) were approximately 228 μm and 108 μm respectively with an accuracy of 97% (Pergamalis, 2002). Figure 5.4 shows two pairs of instantaneous ILIDS and

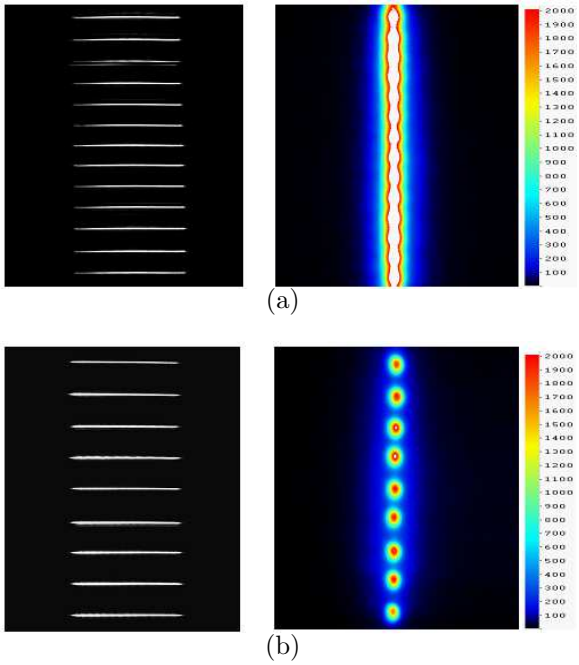
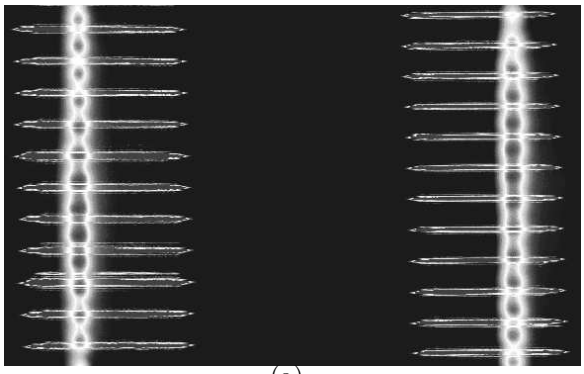


Figure 5.4: Simultaneous ILIDS (left) and PLIF (right) images of the mono-sized droplet stream with size (a) $D_d = 235\mu m$ and (b) $D_d = 122\mu m$ respectively. The color on the right represents the pixel intensity values (linear scale, min = and max =).

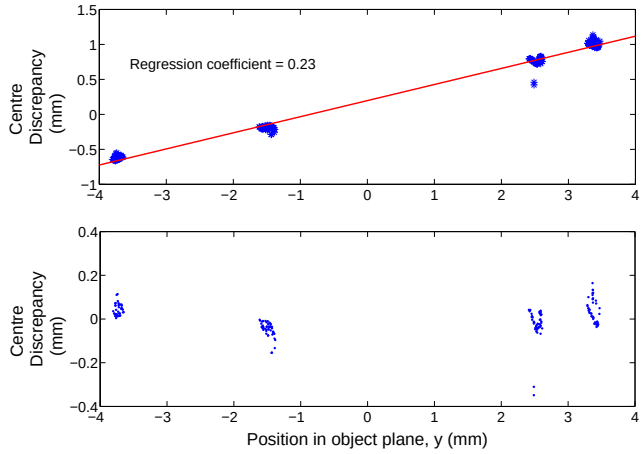
PLIF images of the droplet stream, simultaneously obtained with the optical set-up described in Section 5.1.1 for the two droplet sizes considered here. Each droplet can be observed as a set of horizontal stripes of light on the ILIDS image. The droplet size (D_d), estimated by ILIDS, was $235\mu m$ ($\pm 1\%$) and $122\mu m$ ($\pm 2\%$) respectively. These estimations are within 10% of the theoretically calculated values. Similarly, the estimated droplet velocity were 8.1 m/s and 13.5 m/s (with accuracy of $\pm 5\%$) for the larger and smaller droplets respectively obtained with a delay of $10\mu s$ between the laser pulses.

The fluorescent intensities from both droplets and vapour appear on the PLIF image. As shown in Figure 5.4, the inter-droplet distance was found to increase for the smaller droplet size. Because of the closer spacing between the larger droplets, the vapour distribution was almost surrounding the whole droplet stream. For the droplet stream with smaller droplets, larger inter droplet spacing caused the vapour distribution of any two adjacent droplets to be quite discrete and mainly surrounding individual droplets. This will be discussed further later.

5.2.1 Quantification of the droplet centre discrepancy



(a)



(b)

Figure 5.5: (a) Superimposed ILIDS and PLIF images for a stream of mono-dispersed droplets ($D_d = 235\ \mu m$) at two different positions in the object plane, $y = -3.5$ and $+3.5$ mm, respectively. Note that the origin of the coordinate system ($x = 0$ and $y = 0$) lies in the centre of the CCD array, which coincides with the centre of the image of the figure. (b) top: Centre discrepancy between ILIDS and PLIF images in the horizontal (y) direction as a function of y position in the object plane. The straight line is a linear fit to the original data. bottom: The remaining droplet centre discrepancy after subtracting the estimated error.

The discrepancy of the droplet centre between the ILIDS and PLIF images reduces the probability of identifying the same droplet on both images especially for the case of a polydisperse spray. Hence it is essential to quantify the droplet centre positioning error, which will also verify the prediction of the theoretical analysis described before. This is achieved by performing the experiment with the droplet generator positioned at four different locations along the horizontal (y) dimension of the CCD array. The

droplet stream with droplet size of 235 μm was considered. The degree of defocus in ILIDS camera was kept the same for all cases. In order to demonstrate the variation of the droplet centre position, the focused and defocused images were superimposed and are shown in Figure 5.5(a) for two different y-locations. The liquid fluorescence from the droplet stream can be observed to be moving from left to right with respect to the fringe pattern centre along the CCD array.

Two sets of images were processed at each position. At first, the location of the droplet image centres (geometrical centre) in ILIDS and PLIF images were obtained after processing them separately. The details of the ILIDS image processing for identifying the geometrical centre of the fringe patterns using continuous wavelet transform (CWT) has already been elaborated in Chapter 2 and so, is not repeated here. In the case of PLIF images, the centre of the liquid fluorescence from each droplet was considered to coincide with the centre of the same droplet in the image plane. Identification of this centre was achieved by applying wavelet transform with a suitable scale along each vertical line of the image using the same mother wavelet as in the case of ILIDS, and will be explained later. Once the droplet centres are detected in both ILIDS and PLIF images, they are projected to the object plane using the camera calibration coefficients. A fringe pattern is paired-up with its corresponding droplet fluorescence if the difference in their projected droplet centre in the object plane is minimum in both horizontal and vertical direction. Since, in this case, the droplet number density is low, the probability of identifying the corresponding fluorescent droplet centre to an ILIDS fringe pattern was almost 100%.

The droplet centre discrepancy for various y-locations in the image plane is shown in Figure 5.5(b). The variation of the discrepancy follows a linear trend and the positioning error can be orders of magnitude greater than the droplet size (towards the edge of the CCD array), as predicted by the theoretical analysis (compare with Figure 5.3(b)). The overall trend of the error can be estimated through a linear fitting and finally can be eliminated from the original values. The remaining error is also plotted in the bottom of Figure 5.5(b) and was found to be less than a droplet diameter in this case. The reason behind this remaining error can be attributed to

the error involved in processing the images, especially while detecting fringe pattern length in ILIDS. Improper alignment of the droplet stream causing droplet velocity in the third dimension (normal to the laser sheet) can also be a reason behind this remaining error. In the vertical direction, the trend of the discrepancy was found to slightly increase from the top to the bottom of the CCD array with magnitude between $0.5D_d$ and $1.0D_d$, which is relatively smaller than the former case and can be considered to remain constant. Since no defocusing occurs in this direction, this is attributed to a systematic error in the calibration of the optical arrangement with both cameras.

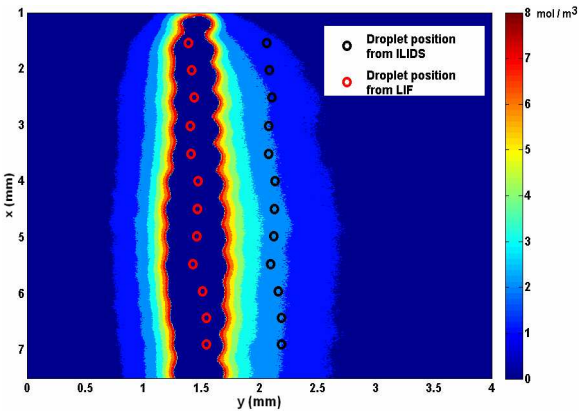


Figure 5.6: Depiction of error in droplet position due to centre discrepancy. Instantaneous contour plot of vapour concentration around a monodispersed droplet stream with droplet size of $235\mu m$ is shown along with the droplet positions obtained from both ILIDS and PLIF images.

The PLIF images were processed to obtain the acetone vapour concentration. The method will be detailed in the following section. Figure 5.6 shows the contour plot of vapour concentration for the droplet stream with droplet size $235\mu m$ corresponding to an instantaneous single shot image. The droplet centres, obtained from PLIF and ILIDS (without any correction), are shown on the image. Large discrepancy between the droplet centres (about $800\mu m$) can be observed, which signifies that the error in droplet position has to be taken into consideration in order to correctly assign the properties of a given droplet to its corresponding vapour distribution.

5.2.2 Vapour phase measurement around the droplet stream

For quantitative evaluation of vapour concentration in PLIF, the raw fluorescence images need to be corrected for background luminosity, non-uniformities in collection optics, and variations in the laser sheet profile. Finally, the corrected fluorescence image is converted into fuel vapour concentration using a calibration with a well known acetone vapour concentration. Hence, at first, a background image was acquired with the laser sheet present but without any droplet stream. The background luminosity and laser scattering could be accounted for by subtracting this image from the fluorescence image. For calibration, liquid acetone was partially filled in a cuvette with its lid securely fixed at the top. Acetone vaporises inside the cuvette and, equilibrium is reached between the two phases. Under such condition, the acetone vapour is always saturated and, for a given room temperature ($T_{ambient}$), the saturated vapour concentration can be obtained from the ideal gas law, $P_{sat} = C_{sat}RT_{ambient}$. Here, R is the universal gas constant and P_{sat} is the saturated vapour pressure of acetone given by the Clausius-Clapeyron formula.

The saturated vapour field was illuminated by the UV laser and the corresponding PLIF image was captured. Care was taken to ensure that the cuvette wall was perpendicular to the laser sheet in order to minimize the loss of energy due to scattering and/or reflection from the wall. The laser energy and the gate exposure time and gain in the intensifier were kept exactly the same as in the experiment with the droplet stream. The variation in fluorescent intensity with respect to the laser sheet height was obtained from the image. Division by this suitably background subtracted image corrected for optical non-uniformities and laser sheet variation. Finally, the vapour concentration (C) around the droplet stream could be obtained from the fluorescence signal (S) using the following equation:

$$C = C_{ref}\frac{S - S_{back}}{S_{ref} - S_{back}} \tag{5.1}$$

where the subscript 'ref' denotes the reference condition which corresponds to the "saturated vapour concentration" in the present case and S_{back} is the background

image. During experiment, the ambient temperature was $T_{ambient} = 15°c$ at which the saturated vapour pressure was evaluated to be $P_{sat} = 0.2\ bar$. Thus, the saturated vapour concentration at the given temperature was 8.15 mol/m^3. A suitable cut-off intensity threshold is essential to discriminate the fluorescence signal of the vapour from that of the liquid. In this way, the contributions from the liquid phase can be filtered out and the images can be processed to obtain the vapour concentration only. For the present case, the threshold was set equal to the saturated vapour concentration of acetone.

It should be noted that the laser beam can also be attenuated along its propagation path due to the presence of acetone vapour. Since fluorescent intensity is proportional to the local power of the laser beam, local fluorescent intensity from any point in the scalar field does not only depend on the local acetone vapour concentration but also on the integrated attenuation of the laser beam up to that point according to Beer's law,

$$I(y) = I_{ref} e^{-\sigma \int_0^y C(y)dy} \tag{5.2}$$

where $I(y)$ is the laser energy at a distance y from the input of laser energy, I_{ref} is the level of input laser energy and σ is the absorption cross-section of acetone vapour. The fluorescence yield of acetone, S, can be related to the laser energy as,

$$S(y) = \chi I(y) C(y) \sigma \tag{5.3}$$

where χ is the overall efficiency of the imaging system. For the saturated condition in the cuvette and for a given input laser energy, $S \propto I$. Hence Equation (5.2) can be written as,

$$S(y) = S_{sat} e^{-\sigma C_{sat} y} \tag{5.4}$$

The above equation was evaluated using the PLIF image of the saturated acetone vapour and the absorption cross-section, σ, was measured to be $3.75 \times 10^{-18}\ mm^2$

at the given ambient temperature. Now the amount of absorption of laser energy can be obtained using Equation (5.2) for various degrees of saturation. Since in the present experiments, the width of the measurement area (y_{max}) was about 12 mm, the total amount of absorption of laser energy by the saturated acetone vapour was found to be about 12% only. Since for the case of the droplet stream, the saturated condition is expected to prevail only in a small vicinity around a droplet, the absorption of laser energy is minimal, and hence, the corresponding corrections in the vapour concentration estimation was not taken into account.

Another important issue that needs discussion is the "halation" effect. The large difference in molecular density between the liquid and vapour phases of acetone causes the fluorescence signal from droplets to be significantly higher than that of its vapour producing a well known "halation" on the recorded image of the ICCD camera. Halation occurs due to increased interference signal near the droplet surface, which overlaps the fluorescence emitted by the acetone vapour phase resulting in an apparent droplet size larger than the real one. This phenomenon has been identified as a possible bias for measurement of fuel-vapour concentration close to droplets because of the difficulty in discriminating the signals of the two phases (Connon *et al.*, 1997) and so, the vapour measurements were possible only at least one droplet diameter away from the droplet surface.

Spatial distribution of vapour around the droplet stream

Measurements were performed with the droplet stream for droplet sizes of $235\mu m$ and $122\mu m$ respectively. In total 50 images were captured at a laser repetition rate of $5Hz$. Figure 5.7 shows contour plots of instantaneous vapour concentration around the droplet stream for both droplet sizes. The color bar identifies quantitative values of vapour concentration. The pure dark blue denotes the lowest range of acetone vapour concentration, beginning at 0%, as well as the liquid acetone and the halation zones, where information about vapour concentration is not available. In the following, the term 'radial profile' refers to the profile measured perpendicular to the axis of the droplet stream and 'r' denotes distance from the droplet centre.

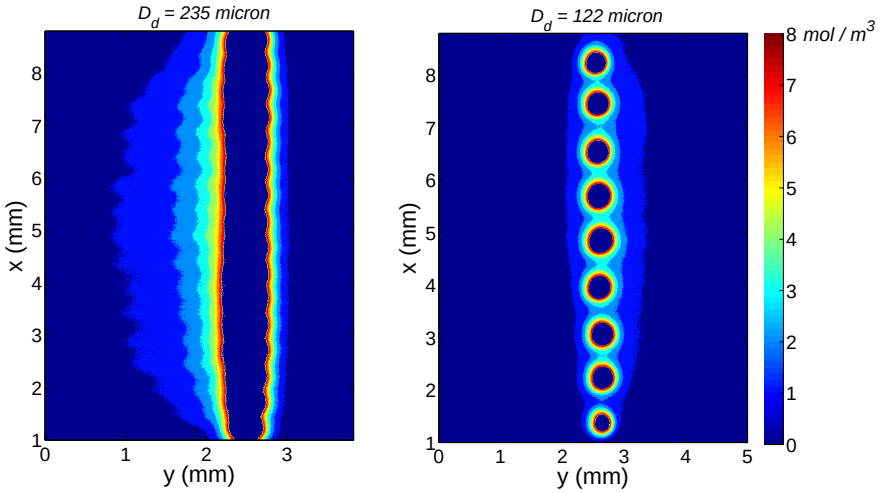
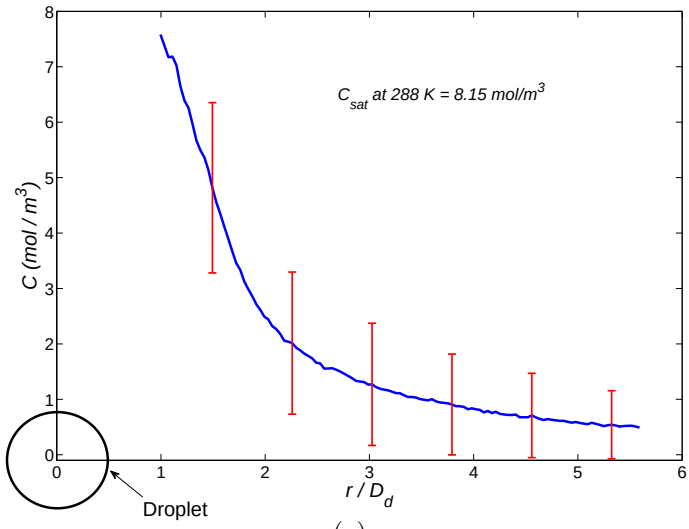


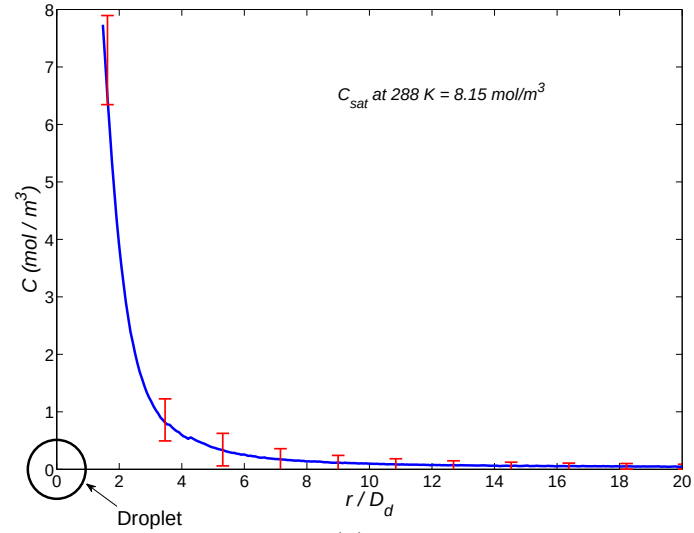
Figure 5.7: Contour plots of instantaneous vapour concentration corresponding to evaporating monodispersed droplet streams of size $235\mu m$ (left) and $122\mu m$ (right) respectively.

The inter droplet distance (l_d) was about $2.1D_d$ for the droplet size of 235 μm and about $7.2D_d$ for droplet size of 122 μm. The smaller droplet spacing for the larger droplets caused the halation effect to be significantly prominent in the region between any two adjacent droplets. This leads to an overestimation of the vapour fraction exceeding the saturated value at the given ambient temperature (Orain *et al.*, 2006). Thus, for this case, vapour concentration measurement was not possible at the region between droplets. Also, because of the same reason, the measurements of vapour concentration are reported only about one droplet diameter away from the droplet stream axis for both drop sizes. As the laser beam travels through the droplets, a considerable absorption of the laser beam occurs. This is due to large fluorescent emission inside droplets inducing self absorption of the laser beam. Therefore, the averaged radial profiles of vapour concentration, obtained from the ensemble of the instantaneous images, are presented only for the right hand side of the droplet stream (the side of laser entry) and are shown in Figure 5.8 for both drop sizes. The error bars in Figure 5.8 represent the root mean square of acetone vapour concentration fluctuations. As observed, the fluctuations in vapour concentration was higher closer to the droplets and, its magnitude was relatively larger for the larger droplet size.

For both cases, the vapour concentration at about one droplet diameter from the



(a)



(b)

Figure 5.8: Radial profiles of acetone vapour concentration around droplets in the mono-sized droplet stream for droplet size (a) $D_d = 235\mu m$ and (b) $D_d = 122\mu m$ respectively, averaged over 50 instantaneous images. The error bars indicate the root mean square of vapour concentration fluctuations.

droplet centre was 7.5 mol/m^3, close to saturation value of 8.15 mol/m^3 at $288K$. Away from the droplet, the concentration of vapour decreases down to approximately 0.5 mol/m^3 at about five droplet diameters for both droplet sizes, Figures 5.8(a) and 5.8(b). Thus, at any given r, the vapour concentration is higher for the larger droplet size indicating the presence of a wider vapour cloud. This can be explained in the following way. For the large droplet size, the spacing between the droplets is smaller and, as a consequence, the vapour surrounds the whole droplet stream rather than individual droplets. Therefore, the contours are aligned with the direction of the droplet stream closer to the droplets as evident from the instantaneous plot in Figure 5.7. Interaction with the ambient air is restricted and axial transportation becomes less important. Hence the vapour is only transported radially due to diffusion. For the smaller droplet sizes, the spacing between droplets is larger and the vapour distribution is present around individual droplets. Along with the radial diffusion, the axial downstream transportation of the vapour becomes prominent because of forced convection existing around the droplet stream due to droplet motion relative to the ambient.

The time scale of the flow (obtained as the ratio of inter droplet distance to droplet velocity) was of the order of 60 μs for the cases of both droplet sizes. The characteristic length scale of diffusion corresponding to this time scale is of the order of 25 μm (diffusivity of acetone vapour = $0.1cm^2/s$), which is much less than the droplet sizes considered here. Hence the vapour transport is expected to be dominated by the axial convection and remain independent of the droplet size. However, the opposite trend was observed. The inter droplet distance act as a deciding factor in determining the droplet evaporation rate. Smaller separation distances leads to droplet-droplet interaction, significantly modifying the evaporation process. This supports the presence of droplet group evaporation rather than single droplet evaporation, Chiu and Kim (1983).

Figure 5.9 shows the averaged radial profile of vapour concentration between any two consecutive droplets in the droplet stream with $D_d = 122$ μm. Unlike the case of larger droplet size, such measurement was possible in this case because of larger

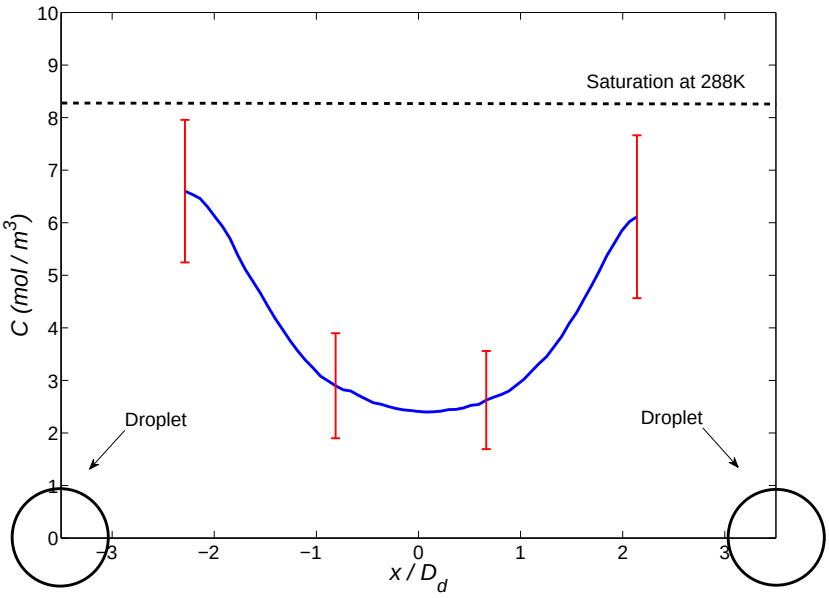


Figure 5.9: Axial profile of acetone vapour concentration around droplets in the mono-sized stream of droplets with size $D_d = 122\mu m$ averaged over 50 instantaneous images. The error bars indicate root mean square of vapour concentration fluctuations.

separation distance between the droplets. The error bar indicates rms of fluctuations in vapour concentration. Similar to the radial profile, in this case also, the rms of concentration fluctuations were higher closer to the droplets. At the mid-point between adjacent droplets, about $3.5D_d$ away from the droplet centres, higher value of vapour concentration (about 3 times) can be observed in comparison to that at an equal distance radially away from the droplet centres (Figure 5.8(b)). This signifies uneven distribution of vapour concentration around a droplet.

5.3 Application of the combined technique to a polydispersed spray

This section is dedicated to application of the combined ILIDS and PLIF technique for two phase characterization of an evaporative spray. In comparison to the mono-sized droplet stream, experiment with the spray is far more complex and demanding mainly because of the challenges encountered in vapour phase measurement. The

difficulties appear in discriminating the droplet and vapour phases and accounting for the progressive absorption of the laser energy by the droplets.

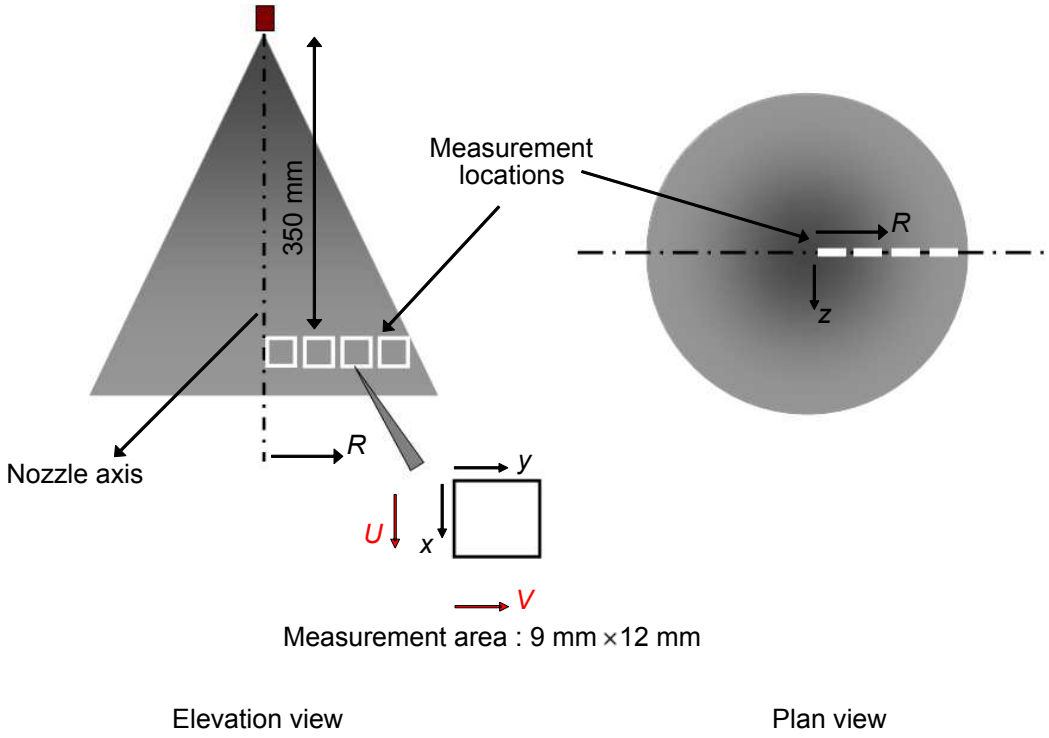


Figure 5.10: Measurement locations in the evaporative spray and the coordinate system.

The combined ILIDS and PLIF technique, as described in Section 5.1.1, was applied to an acetone spray issuing from an air-assist nozzle. The experimental set-up was depicted in Figure 5.1. Liquid acetone, pressurized at 1.2 bar in a pressure vessel, was fed to the nozzle through stainless steel hoses. The flow rates of liquid acetone and air were controlled by the respective rotameters and were set to 0.03 lt/min and 15 lt/min respectively. Experiments were performed 350 mm downstream of the nozzle exit where the vapour-air mixing is expected to be higher. The corresponding width of the spray was about 100 mm. Measurements are reported for four radial measurement locations beginning from the nozzle axis towards the outer spray as shown in Figure 5.10. At any given measurement location, the notations 'x' and 'y' refer to the local axial and radial directions respectively, both lying in the plane of the laser sheet. The instantaneous axial and radial components of velocities are denoted by capital letters 'U' and 'V', while 'u' and 'v' represent their corresponding

fluctuations respectively. Similarly, 'C' and 'c' denote the instantaneous value and the deviation from the vapour concentration. The subscript 'd' denotes droplet. The 'overbar' over any quantity indicates time-averaging and the subscript 'r' denote root mean square (rms) of that quantity. 'R' refers to the beginning of the measurement area, at any radial location, measured from the nozzle axis.

The measurement area was approximately $9 \times 12\ mm^2$ and the radial measurement locations were at $R = 0$, 15, 30 and 45 mm respectively from the nozzle axis. The dispersed phase measurement by ILIDS is reported for all radial measurement locations. However, the combined ILIDS and PLIF measurement is presented only for the outermost radial location at $R = 45\ mm$. This is due to the difficulty in accounting for the laser energy absorption by droplets while evaluating instantaneous vapour concentration from the vapour fluorescence signal in the PLIF images corresponding to inner regions of the spray. Thus, depending on the measurement location, in total 1500 images were captured either only with ILIDS camera only or simultaneously from both ILIDS and PILF cameras. Since the validation rate in the two phase measurements was low, this large number of images was required to achieve low statistical uncertainty in the measured quantities. The time scale of the turbulent flow (τ_f) was estimated as the ratio of a large eddy length scale of the flow and the axial component of the rms velocity of the smallest droplet size class. The dimension of the large eddy was assumed to be 1/5 of the spray width (Tennekes and Lumley, 1972). The width of the spray was about 100 mm at the axial location 350 mm from the nozzle. Thus, τ_f was estimated to be approximately 0.03 sec and hence, the repetition rate of the laser was set to 5 Hz, so that the acquired samples remained statistically independent. The delay time between the laser pulses for ILIDS was $80\mu s$. In the ICCD camera, the delay timing and gate exposure were set to 5 ns and 10 μs respectively and the gain was adjusted to 90%.

5.3.1 Image processing

The ILIDS and PLIF images were subsequently processed to obtain the properties of both phases. Figure 5.11 shows the flow chart of the image processing steps. A pair

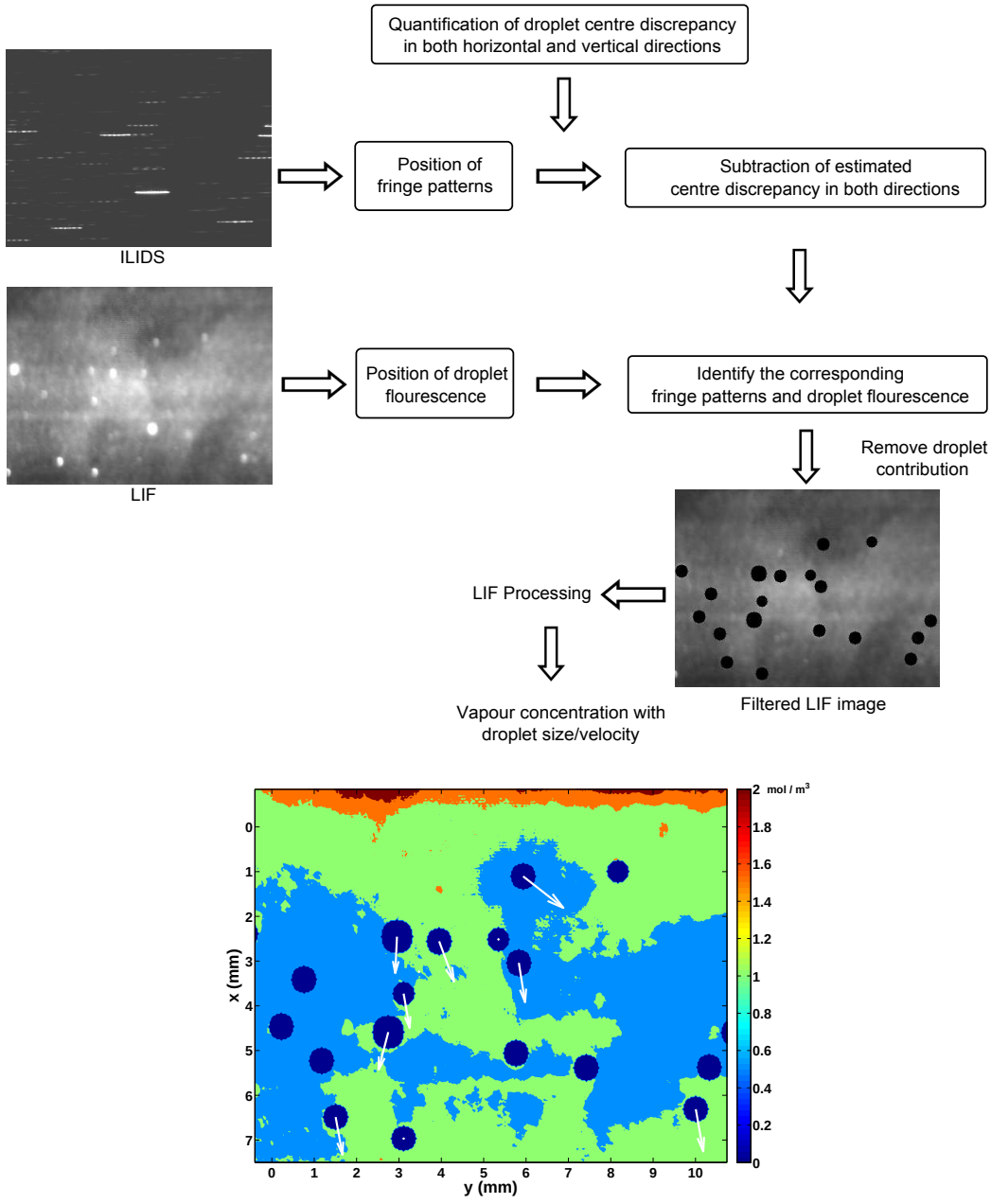


Figure 5.11: Illustration of the image processing details of the combined ILIDS and PLIF technique. A pair of typical instantaneous ILIDS and PLIF images are shown along with the droplet filtered PLIF image. In the plot of simultaneous vapour concentration and droplet velocities, the dark blue regions are the removed droplet positions and the bold vectors in white represent the droplet velocity.

of instantaneous ILIDS and PLIF images, simultaneously obtained by the combined technique, appears at the left side of the same figure. The ILIDS image processing method for locating the droplet centre and estimation of droplet size and velocity were elaborated in Chapter 2 and so, is not repeated here.

Both droplet and vapour fluorescence appear in the PLIF image. Because of the "halation effect", as mentioned earlier, the droplet size appeared to be bigger than it should be. In order to suppress the high frequency signal (noise), the intensity values were binned with a bin size of $4\times4\ pixel^2$, thus resulting in a spatial resolution of $36\mu m/pixel$. As mentioned before, several corrections were necessary to obtain vapour concentration from the fluorescent intensity in the PLIF image. First, the background image was subtracted to account for background luminosity and CCD noise. Then, the intensity non-uniformity of the laser sheet was corrected. Finally, the vapour concentration was quantified accurately by Equation (5.1). Saturated acetone vapour corresponding to a partially filled liquid acetone in the cuvette was considered as the reference condition required in the same equation.

Since the PLIF image contains fluorescence from the droplets as well, the contributions from the liquid phase must be eliminated at first to obtain the vapour concentration only. Several authors have focused on this issue and most have used a cut-off threshold based on intensity to distinguish the two phases, for instance, Bazile and Stepowski (1995) and Kurosawa *et al.* (2002). However, the same approach was not suitable at the present work. Due to the presence of the droplet size distribution dominated by smaller droplets (20–$40\mu m$), the intensity distributions from droplets and vapour phase overlapped to a greater extent. So, it was not possible to set a cut-off intensity to separate the signals. Also, for successful application of the combined technique, it is essential to locate the droplet centre in the PLIF image so that the size and velocity of the same droplet obtained from ILIDS image can be associated with the surrounding vapour. Hence in this work, it was preferred to identify individual droplets in the PLIF image and subsequently filter them out.

The droplet centres were identified in the PLIF image by applying continuous

wavelet transformation or CWT (Torrence and Compo, 1998) similar to identifying glare points in the PIV image as mentioned in Chapter 2. However, because of strong absorption of the UV light within a droplet (optical depth of liquid acetone is about $18\mu m$), the liquid beyond a distance of the order of the optical depth do not contribute to the fluorescence signal. This is because the laser intensity becomes negligible in that region inside the droplet. Applying CWT in horizontal direction (direction of laser sheet) would result in bias in estimation of the droplet centre. Hence unlike glare points, in the present case CWT was applied to each vertical column of the PLIF image and the positions of the positive peaks in the transform (exceeding a cut-off threshold) were considered to be the droplet centre. This is—if not the best—a better alternative to the approach of setting an intensity threshold for droplet removal from the vapour image for the present case. The "Mexican Hat" wavelet was chosen as the mother wavelet for this purpose due to its strong localization properties. The scale of the mother wavelet used for this purpose was approximately equal to the average diameter of the droplet image. The precision in locating the droplet centres on the PLIF image for the polydisperse spray was estimated as being ± 5 pixels in both horizontal and vertical directions.

Once the droplet centres are detected on both images, the next task is to identify the corresponding droplets on both images. As was mentioned before, this is not always possible because of the "discrepancy" in droplet centre due to defocusing of ILIDS images. Similar to the combined ILIDS and PIV technique, here also the centre discrepancy was quantified by capturing the ILIDS and PLIF images in a dilute region of the spray so that the probability of finding the correct pairs of fringe pattern and droplet fluorescence was 100%. The method is identical to that described in Chapter 2 and hence is not described here in great detail. The error in droplet position was estimated by fitting a linear curve on the measured discrepancy in droplet centre and then subtracted from the centre of the fringe patterns in ILIDS images. This approach reduced the droplet centre discrepancy by about 90%. The droplet size/velocity obtained from the ILIDS image are associated to the corresponding droplet positions in the PLIF images. Again, similar to the removal of glare points from the PIV image

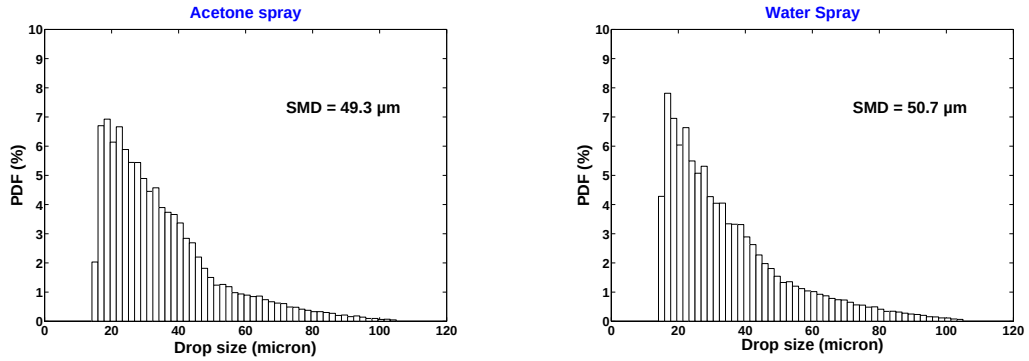
(Figure 2.25), the two negative peaks in CWT around the droplet centre decided the diameter of the circular region where the pixel intensity values were made zero on the vapour concentration image. The PLIF images, after the droplet elimination, were processed to obtain the vapour concentration distribution around droplets.

5.3.2 Dispersed phase measurement

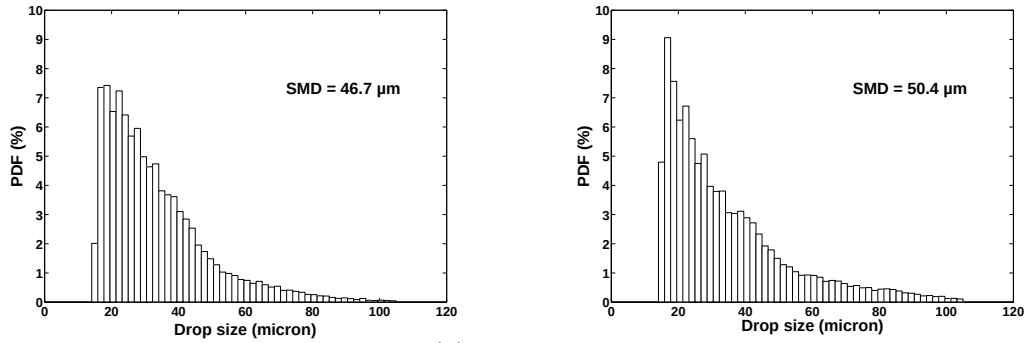
Droplet size

The probability density function (PDF) of the distribution of droplet sizes (obtained from ILIDS) for various measurement locations in the acetone spray is shown in Figure 5.12. The PDFs are averaged over the ILIDS imaging area at each radial measurement location R. The minimum measurable droplet size was $15\mu m$. The sauter mean diameter (SMD) can be observed to decrease from about $50\mu m$ at $R = 0\ mm$ to about $43\mu m$ at $R = 45\ mm$. In order to examine the effect of evaporation on droplet size, comparison with a non-evaporative spray was essential. Hence, experiments were performed with a water spray under same operating conditions of the liquid and air flow rates as for the acetone spray. Although at the ambient temperature of $15^{\circ}c$, the surface tension in water ($7.35\times10^{-2}\ N/m$) is about three times greater than that of acetone ($2.50\times10^{-2}\ N/m$), for the considered experimental regime in the spray, the droplet size can be considered to be independent of the surface tension due to high value of Weber number at the nozzle exit[1]. The probability of droplet size distributions for the water spray are shown in Figure 5.12 for the different radial measurement locations. Accounting for accuracy in drop size measurement ($\pm$ 2.6 μm) for the present ILIDS optical set-up, the SMD at all of the radial measurement locations in the water spray can be considered to be consistent and about $51\mu m$. Comparison of the SMD of the acetone and water spray reveals that closer to the nozzle axis the droplet size is the same for both cases while there is a reduction in SMD towards the outer region of the acetone spray. The decrease in droplet size is

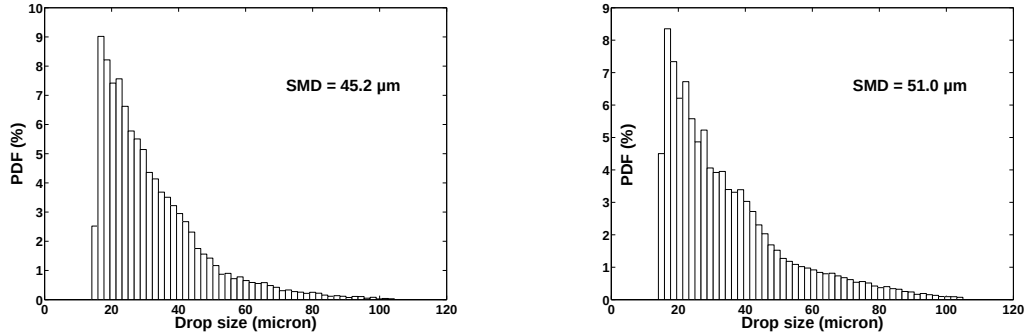
[1]Weber number is defined as $\rho d_{noz} U^2/\sigma$, where d_{noz} is the diameter of nozzle at the exit, ρ and σ are the density and surface tension of the liquid respectively. High value of Weber number indicates negligible surface tension effect.



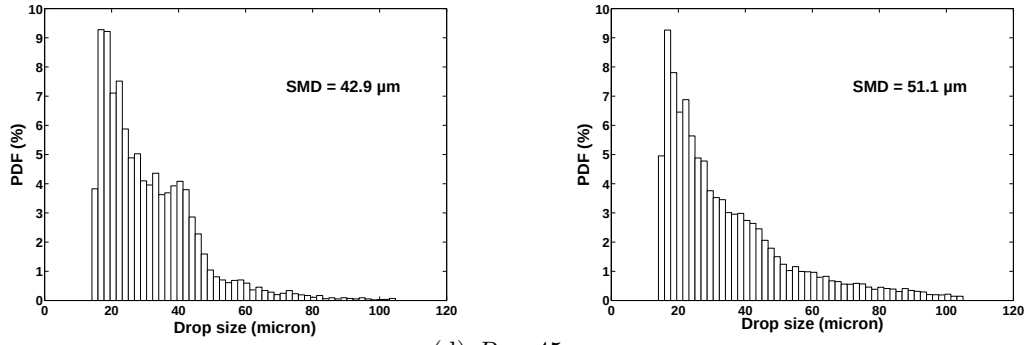
(a) $R = 0\ mm$



(b) $R = 15\ mm$



(c) $R = 30\ mm$



(d) $R = 45\ mm$

Figure 5.12: Probability of droplet size distribution for the acetone spray (left) and water spray (right) for the radial measurement locations (a) $R = 0\ mm$, (b) $R = 15\ mm$, (c) $R = 30\ mm$ and (d) $R = 45\ mm$.

attributed to the evaporation of the droplets, an effect which is more prominent away from the spray axis. A close comparison of the size distribution of acetone and water spray at $R = 45\ mm$ (Figure 5.12(d)) indicates a secondary 'peak' around droplet size of $40\mu m$ and also, reduction in the probability of larger droplet sizes. This suggests the decrease in SMD is due to evaporation especially from larger droplets.

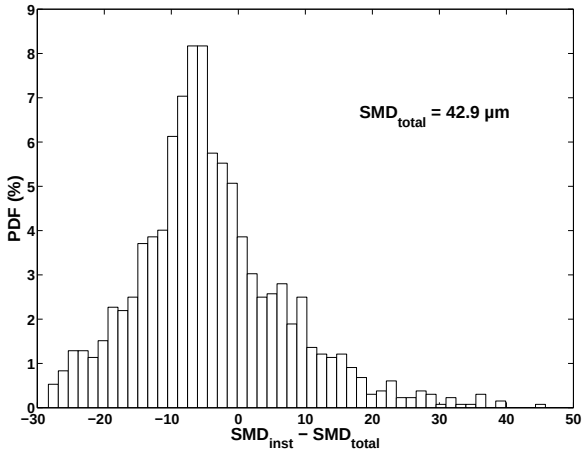


Figure 5.13: probability of variation in instantaneous and total SMD for the radial measurement location at $R = 45\ mm$.

The SMD of droplets in sprays is evaluated by considering the total number of samples, each corresponding at different time instants. It is assumed that the average value of SMD obtained in this way (denoted as "SMD$_{total}$") is a representative of the droplet size for each instantaneous sample. However, the instantaneous SMD for a given sample ("SMD$_{inst}$") can be significantly different from SMD$_{total}$. Figure 5.13 shows the probability of the difference between instantaneous and total SMD at R = 45 mm. The figure illustrates that the instantaneous SMD can have significant positive or negative deviations with respect to the average SMD. The percentage deviation can even reach up to 50% of SMD$_{total}$, implying large fluctuations in the instantaneous droplet size distribution, which directly influences the evaporation rate at that instant.

Three droplet size classes (denoted by 'D' and range 'ΔD') were considered, namely 15-30μm, 30-45μm and 45-60μm respectively. Higher size classes were not considered to avoid high statistical uncertainty due to small number of samples. The

range ΔD of the droplet size classes was decided as a compromise between higher statistical uncertainty (with small ΔD) and obtaining size averaged information (with larger ΔD).

Droplet mean/rms velocity

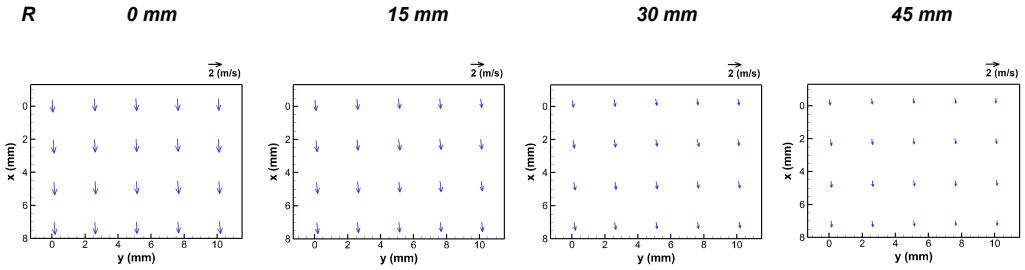
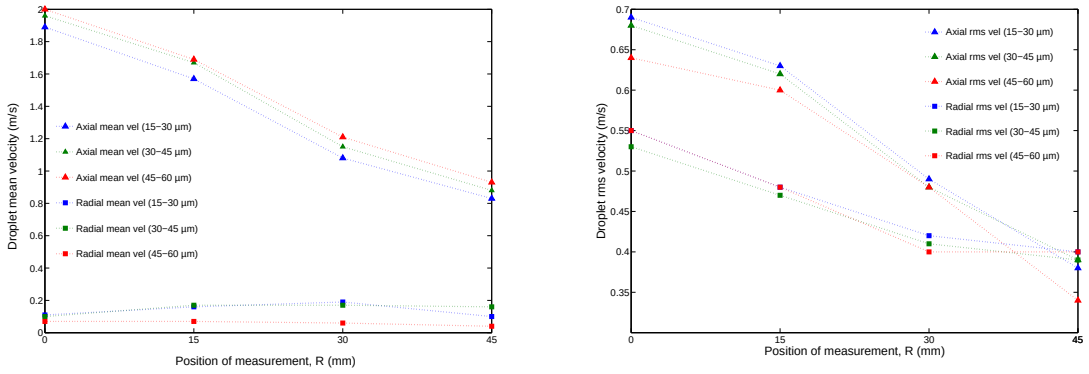


Figure 5.14: Mean velocity for droplet size class of 15–30μm for various radial measurement locations, R.

The droplet mean and rms of velocity fluctuations were measured in specific number of windows of the ILIDS imaging area. For each window, the average velocity of all measured droplets in a droplet size class was obtained. This approach was already described in Chapter 3 and, is not repeated here. The spatial resolution of the mean droplet velocity was about 2.4 $\times$ 2.4 mm^2. The vector plots of mean droplet velocity for droplet size class of 15–30μm is presented in Figure 5.14 for the four measurement locations. The mean velocity of droplets was mostly axial and away from the nozzle at all measurement location and, decreases with the radial direction away from the spray axis. The trend of the mean velocity of the higher size classes was similar, though a small increase (about 4%$\sim$10%) in the magnitude of drop velocity was observed with respect to the 15–30μm size class.

Both mean and rms of the droplet velocity fluctuations were found to be almost spatially invariant across the measurement area at every R. The area averaged mean and rms of droplet velocity are shown in Figure 5.15(a) and 5.15(b) respectively for the three droplet size classes and for various radial measurement locations. In the axial direction, small increases in the mean velocity and decrease in the rms velocity for larger droplet size classes can be observed. At $R = 45\ mm$, the mean velocity of



(a) (b)

Figure 5.15: Area-averaged (a) mean and (b) rms velocity, for droplet size classes of 15–30μm, 30–45μm and 45–60μm for various radial measurement locations, R.

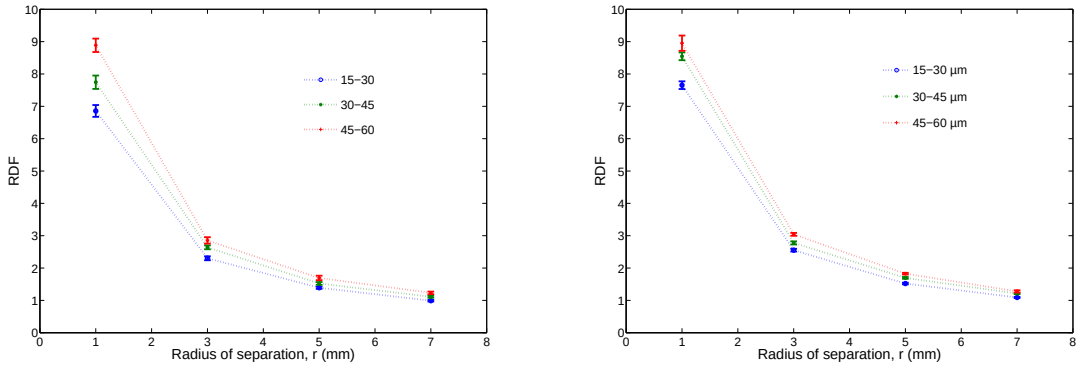
the droplets reduced to about 50% of the velocity near the spray axis at $R = 0\ mm$. At any radial location, the droplet axial rms velocity was about 40% of the mean. In the radial direction, the mean velocity was close to zero for any droplet size classes. Near the nozzle axis, the ratio of the rms of axial to radial velocity fluctuations was 1.25, while it was nearly equal to 'one' at the outer spray region at $R = 45\ mm$. However, at $R = 45\ mm$, for the 50–65μm droplets, the rms velocity in the radial direction was slightly higher than in the axial direction. The Reynolds number of droplets based on both mean slip velocity and turbulent rms velocity were found to quite low, of the order of 0.3 and 2.0 respectively.

As mentioned before, the characteristic time scale of the spray (τ_f) at the present measurement locations is chosen as the ratio of a large eddy length scale (order of 20 mm) to the axial rms velocity of droplets of the smallest size class on the spray axis (at $R = 0\ mm$) which is closet to the gas phase flow. Thus, the values of the Stokes number[2] (St) for the three droplet size classes were evaluated to be of the order of 0.03, 0.1 and 0.21 respectively. These values indicate that the droplets follow partially the large scales of the flow and this justifies the observed droplet velocity behaviour. The terminal velocity of the droplets (u_t) for the three droplet size classes were 0.01 m/s, 0.03 m/s and 0.06 m/s respectively. Since at any radial measurement

[2]Stokes number = τ_p/τ_f, where τ_p is the droplet aerodynamic time constant

location, the ratio u_t/u_{dr} for the three size classes was small (≈ 0.1), the influence of the gravity on droplets can be considered negligible.

Scale of droplet clustering



(a) (b)

Figure 5.16: Radial distribution function (RDF) for the three droplet size classes for the radial measurement locations, at (a) $R = 0$ mm and (b) $R = 45$ mm.

As described in Chapter 3, the radial distribution function (RDF) provides a statistical measure of characteristic dimension of particle clustering. RDF is defined as the probability of finding a second particle at a given separation distance from a test particle compared to a case where the particles are homogeneously distributed (Salazar *et al.*, 2008), and is computed by binning the particle pairs according to their separation distance. Figure 5.16(a) and 5.16(b) shows the RDF calculated for various radius of separation (or distance from droplets), r, and different size classes at the measurement locations $R = 0$ and 45 mm respectively.

By its definition, RDF > 1 implies non-random distribution of droplets indicating clustering. The value of r for which RDF(r) becomes larger than 1, provides an estimate of the scale of the clusters. From the distribution of RDFs in Figure 5.16, it can be observed that this value of r is of the order of 7 mm for the smallest droplet size class. For the higher size classes, the scale of the clustering is expected to be somewhat larger due to slightly higher value of RDF at $r = 7$ mm. Hence the characteristic dimension of the droplet clusters can be considered to be of the order

of the smaller dimension of the measurement area ($9 \times 12\ mm^2$).

Group combustion number

The planar measurement of droplet position and size through ILIDS facilitates the measurement of the instantaneous group combustion number (G) in a spray. As described in Chapter 1, when inter-droplet spacing in a cloud of droplets is sufficiently small, interaction between droplets set, which prevents penetration of the oxidizer in the innermost region of the spray. Thus, a fuel-rich, non-flammable mixture is formed, in which droplets do not burn individually, but rather as a group surrounded by a diffusion flame. The magnitude of the value of G characterizes if individual or group evaporation is going to prevail (Chiu and Kim, 1983). For the case of a mono-disperse cloud, G can be expressed as:

$$G = 3(1 + 0.276Re^{0.5}Sc^{0.33})LeN^{2/3}\frac{D_d}{l_d} \tag{5.5}$$

where Re is the droplet Reynolds number, Sc and Le are the gas Schmidt number and the Lewis number respectively, N is the total number of droplets in the cloud, l_d is the mean inter-droplet spacing, and D_d is the droplet diameter. For low Re of droplets, such as in the present flow conditions (since Stokes number of droplets is low and droplets follow fairly well the gas flow), and assuming $Le \approx 1$, the above equation can be written as,

$$G = 3N^{2/3}\frac{D_d}{l_d} \tag{5.6}$$

In the literature, mostly single point techniques (mainly PDA) have been used for dispersed phase characterization. PDA, being a point measurement instrument, can not accurately quantify the variation of inter-droplet distance within a cloud of droplets. So, G is evaluated under the assumption of uniform inter droplet distance

within the droplet cloud. The above equation thus further simplifies to:

$$G = 2\pi n D_d R_c^2 \tag{5.7}$$

where n is the droplet number density and R_c is the droplet cloud radius.

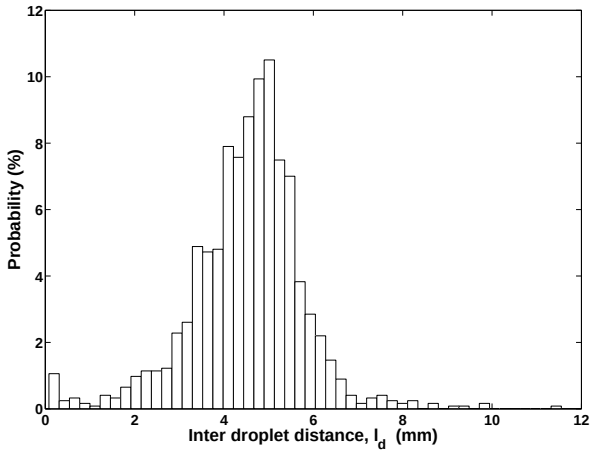


Figure 5.17: Probability of variation in average inter droplet distance for the radial measurement location at $R = 45\ mm$.

However, for a practical spray, the inter droplet spacing and the droplet size can have significant variation from one time instant to other. The instantaneous variation in SMD with respect to the average SMD has already been shown in Figure 5.13. The probability of the average inter droplet distance (obtained from the instantaneous image samples and, independent of droplet size) is shown in Figure 5.17 for the measurement location at $R = 45mm$. The figure clearly shows the presence of large variation in the average inter droplet distance within the spray. Hence, it is important to evaluate the instantaneous group combustion number, which can elucidate on the dominant mode of evaporation for a given location in the spray.

The group combustion number G was evaluated for each time instant following both Equation (5.6) and Equation (5.7), and is denoted by G_1 and G_2 respectively. To obtain the instantaneous G_1, at any given time instant, the average droplet diameter and average inter droplet spacing (corresponding to that time instant) were considered. For obtaining G_2, the droplet cloud diameter was assumed to

R	0 mm	15 mm	30 mm	45 mm
$\overline{G_1}$	0.15	0.13	0.10	0.11
G_{1r}	0.06	0.07	0.18	0.20
$\overline{G_2}$	1.40	1.30	0.75	0.68
G_{2r}	0.82	0.77	0.55	0.49

Table 5.1: The mean and rms of the group combustion number for the different measurement locations, R. G_1 is according to Equation (5.6) and G_2 is according to Equation (5.7).

be equal to the smaller dimension of the measurement area (as estimated by trend of RDFs in Figure 5.16). Table 5.1 shows the mean and rms of both G_1 and G_2 for the four measurement locations. At any measurement location the uncertainty in the statistical mean calculation for $G1$ and $G2$ were of the orders of ± 0.002 and ± 0.02 respectively. Comparison of the magnitude of $\overline{G_1}$ and $\overline{G_2}$ in both cases clearly indicates the overestimation of the mean group combustion number following Equation (5.7) by several orders of magnitude. This resulted from the assumption of uniform droplet spacing in the cloud. Also, the rms of the fluctuations of G_1 (G_{1r}) were overestimated in case of G_2. For the considered experimental regime in the spray, 350 mm downstream of nozzle, the mean group combustion number, $\overline{G_1}$, was found to slightly increase towards the spray axis. Though the fluctuations of G_1 (G_{1r}) were found to reduce from $R = 45\ mm$ to $R = 0\ mm$. The magnitude of G_1 (< 1) suggests that the mode of evaporation falls in the regime between individual evaporation to inter group evaporation (Sirignano, 1999). Thus, a first ring of individual evaporating droplets is expected to be centred on a core of droplets. Also, the tendency of the droplets to evaporate as a group becomes higher closer to the spray axis. If the approach of G_2 was used ($G_2 \approx 1$), the evaporation regime would be 'external group evaporation'(Sirignano, 1999) especially closer to the spray axis. This implies an increased size of the core with its boundary enveloping all the droplets and the individual droplet evaporation seizes to exist. However, this mode of evaporation is less probable to occur at the measurement locations considered in this study. The following discussion on vapour concentration measurement provides further evidence on this argument.

5.3.3 Vapour phase measurement

The "laser shadow" behind acetone droplets (due to strong absorption of the laser energy within droplets) prevents the measurement of vapour concentration in the central area of the spray. This effect progressively minimizes the possibility of reliable measurement of instantaneous vapour concentration for the inner measurement locations around the spray axis. Hence, measurement of the acetone vapour concentration is reported only for the outermost radial location in the spray at $R = 45\ mm$, where the laser absorption due to droplets could be neglected. The intensity of laser light $I(\lambda)$ transmitted through a cloud of droplets is related to the intensity of the incident light $I_0(\lambda)$ by Bouguer-Lambert-Beer's law as follows:

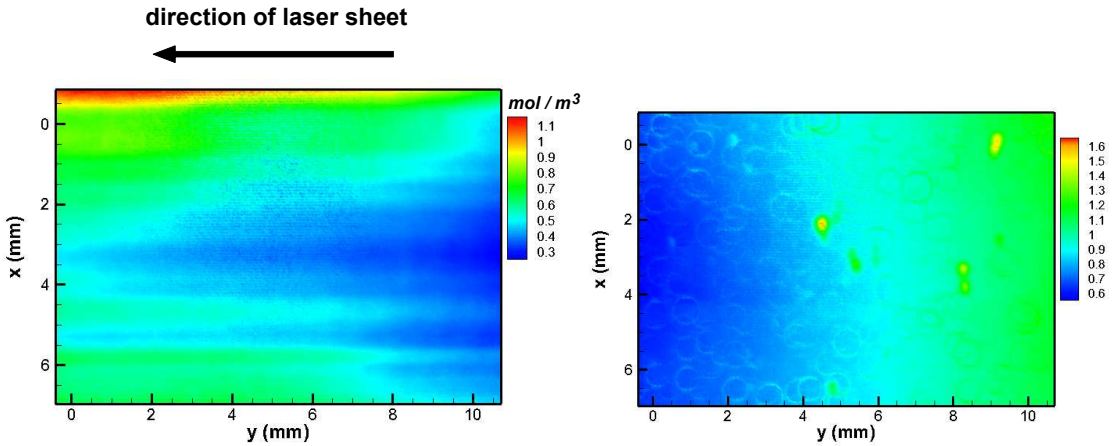
$$\left(\frac{I}{I_0}\right) = e^{\int_0^{y_{max}} K_{ext}(\lambda)dy} \tag{5.8}$$

where y_{max} is the horizontal dimension of the measurement area and K_{ext} is the extinction coefficient for a cloud of droplets and is given by,

$$K_{ext}(\lambda) = -\frac{\pi}{4}\int_0^{\infty} Q_{ext}(\lambda)N(D)D^2dD \tag{5.9}$$

where Q_{ext} is extinction efficiency of the droplet cloud, N is the droplet number density distribution and D is the droplet diameter. Equation (5.8) was evaluated via Equation (5.9) by considering the fact that the extinction efficiency approaches a constant of '2' for droplets much larger than the wavelength of light $\lambda(= 266nm$ here). The percentage of laser energy absorption was estimated for each instantaneous image samples at the radial location $R = 45\ mm$. The mean absorption was found to be about 0.16%, while the maximum was about 1.5% of the incident laser energy. Since these values are very small, the assumption of neglecting the laser energy absorption by the droplets for evaluation of vapour concentration is valid. Similarly, as mentioned before, the maximum absorption of laser energy in presence of saturated vapour all along the laser path (within the measurement area) can be expected to be about 12%. However, at the considered measurement locations far downstream of the nozzle exit,

the concentration is expected to be below the saturation level due to mixing with entrained air. So the correction for laser energy absorption due to vapour was not considered in the quantitative evaluation of concentration of acetone vapour. In their PLIF measurement of burning spray jet of acetone, Bazile and Stepowski (1995) found the correction for laser absorption was significant (= 20%) only for the radial locations within a distance about one-fifth of the spray width from the nozzle axis.



(a) (b)

Figure 5.18: Contour plots of (a) mean vapour concentration and (b) ratio of rms of fluctuations to the local mean value for the radial measurement locations at $R = 45\ mm$.

The contour plot of mean vapour concentration field ($\overline{C}$) at $R = 45\ mm$ is presented in Figure 5.18(a). The instantaneous concentration values were defined on a regular structured grid corresponding to the array of pixels in the binned PLIF image. It must be noted that 'zero' values of vapour concentration in instantaneous samples represent the filtered droplet fluorescence signal at the location of the eliminated droplets (Figure 5.11). The mean values were evaluated at each pixel in the grid by averaging the *non-zero* instantaneous concentration values at that pixel over all samples. The statistical uncertainty of the mean values at each pixel was about ±5% with 95% confidence interval. Figure 5.18(a) shows that, as compared to the saturated condition at the ambient temperature of $288°K$ ($8.15\ mol/m^3$), the mean vapour concentration was very low through out the measurement area. The low vapour mass fraction (about 2%) suggests considerable mixing of the acetone vapour with the surrounding air because the measurement area corresponds to the outermost location

in the spray. This is supported by the low mean velocity of droplets at $R = 45\ mm$ (Figure 5.14), which is expected to be similar to the entrained air flow. This agrees well with the mode of droplet evaporation, as predicted by the G_1, to be between individual evaporation to inter group evaporation. Since the order of G_1 is nearly the same in all radial locations, similar mode of evaporation is expected to prevail at those locations as well. Also, the occurrence of external group evaporation as indicated by the value of G_2 implying restricted oxygen penetration in to the droplet cloud is not expected. This justifies the overestimation of the group evaporation number when calculated following Equation (5.7).

A progressive increase of the mean vapour concentration ($\overline{C}$) can be observed along the radial direction towards the spray axis. In the axial direction, the mean vapour concentration slightly decreases for the larger axial distances (bottom of the measurement area). The root mean square (rms) of the vapour concentration fluctuations (c_r) was also obtained at each pixel, where the mean value was defined and the contour plot of the ratio of rms to the local mean value ($c_r/\overline{C}$) is shown in Figure 5.18(b). An interesting trend can be observed. At the right hand side of the plot, the fluctuations of vapour concentration exceeded the mean by about 50% while the ratio gradually decreased towards the left hand side. At the extreme left of the plot, the rms value can be observed to be 50% of the mean. However, no preferential change in the ratio could be observed in axial (x) direction. This signifies that the fluctuations of vapour concentration relative to the mean are higher at the outer spray region, where more mixing with the intermittent air flow is expected, and decreases as one moves towards the spray axis. Similar observation can also be found in the work of Bazile and Stepowski (1995). The increasing trend of $\overline{C}$ in the radially inward direction is in agreement with the far field mean concentration profile in a single-phase turbulent jet reported by (Webster *et al.*, 2001). However, the rms of fluctuations in vapour concentration in the turbulent jet increases towards the spray axis, in contrast to the observations in the present study. This can be explained on the basis of the continuous vapour generation due to droplet evaporation at the outer spray region, which is evident from the reduction in SMD of the acetone droplets at

the $R = 185\ mm$ as compared to the water spray.

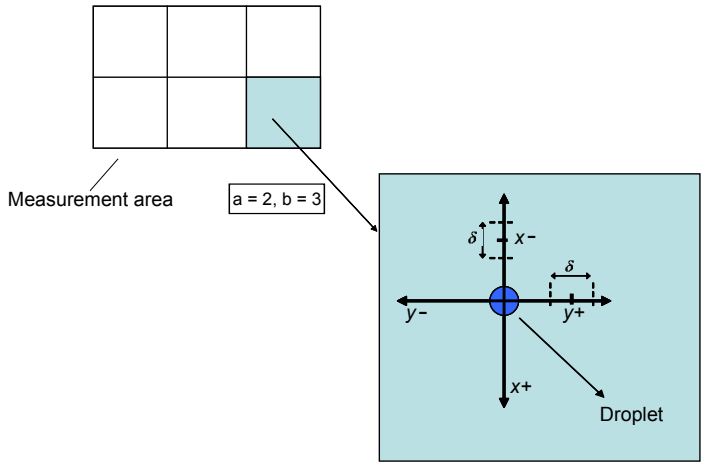


Figure 5.19: Local coordinate system for evaluation of distribution of the mean and the fluctuations of vapour concentration around a droplet.

In order to understand the influence of air-vapour mixing on the evaporation rate of droplets, it is important to evaluate the distribution of the mean and the fluctuations of vapour concentration around individual droplets in the spray. For this purpose, considering the preferential variation of the rms of vapour concentration in the measurement area especially in the radial direction (Figure 5.18(b)), the viewing area was divided into finite number of rectangular windows, each denoted by index (a, b) as shown in Figure 5.19. Here a and b represent the row and column numbers for a particular window. A local coordinate system was defined around each droplet as shown in the same figure. The horizontal directions to the left and right of any droplet position are denoted by y^- and y^+ respectively. Similarly, x^- and x^+ denote the vertical directions above and below the droplet. The mean and the fluctuations were obtained around droplets for all four directions considering each separately. For every instantaneous sample, I, inside a given window (a, b), for any given location (say y^+) from a droplet, the instantaneous vapour concentrations were averaged over a distance of $y^+ + \delta/2$ to $y^+ - \delta/2$ (Figure 5.19). This is done for all droplets belonging to the same droplet size class residing in that window and then, repeated for all instantaneous samples. The average of the instantaneous concentration, $R_{\overline{C}}$, was obtained for various locations along the four directions and also, for different size

classes. For example, $R_{\overline{C}}$ in y^+ direction can be written as:

$$R_{\overline{C}}(D,a,b,y^+) = \overline{\sum_I \sum_J \sum_{y^+-\delta/2}^{y^++\delta/2} C_{I,J,y^+}(D)} \tag{5.10}$$

Similarly, the variation of fluctuations of vapour concentration, R_c, was obtained. For example, R_c in y^+ direction can be written as:

$$R_c(D,a,b,y^+) = \overline{\sum_I \sum_J \sum_{y^+-\delta/2}^{y^++\delta/2} c_{I,J,y^+}(D)} \tag{5.11}$$

The size of the windows was decided considering the gradient in mean and rms of vapour concentration (larger gradient requires smaller window size) and consistency in statistical average (very small window size increases uncertainty). Hence, a compromise had to be made. In the present case, in total 6 windows (2 rows and 3 columns) were considered each with size about $3.6mm \times 4.0mm$. The increment in any direction and magnitude of δ were both $500\mu m$.

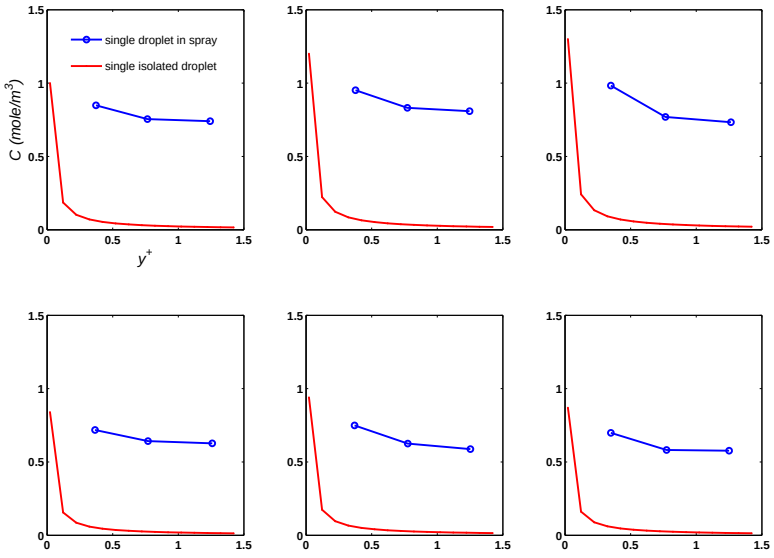


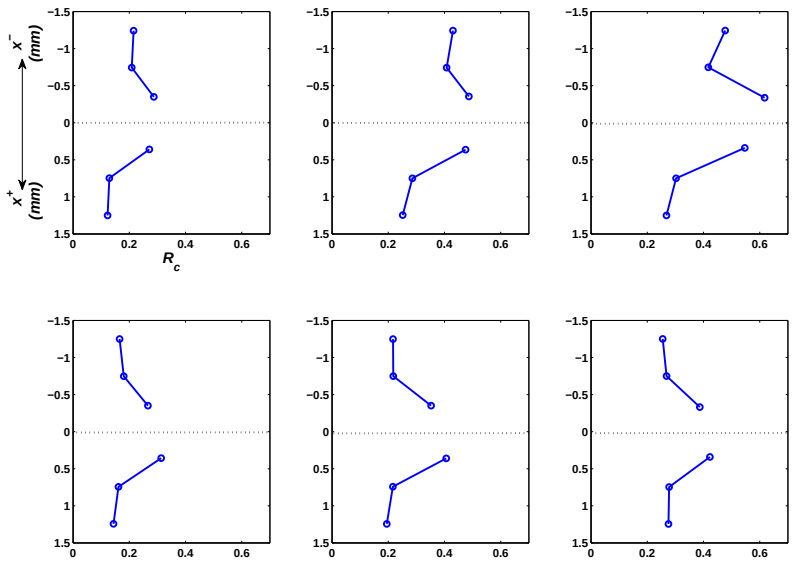
Figure 5.20: Comparison of mean vapour concentration distribution in y^+ direction with the theoretically predicted trend in case of an isolated droplet as described by the d^2-law (Spalding, 1951).

For studying the group evaporation phenomenon, it is important to recognize the influence of the presence of clouds of droplets on the droplet evaporating rate. For this purpose, the mean vapour concentration ($\overline{C}$) around a droplet obtained from the present experiment was compared to the theoretically predicted trend in case of an isolated droplet as described by the d^2-law (Spalding, 1951) assuming quasi-steady evaporation, which is given in terms of mass fraction:

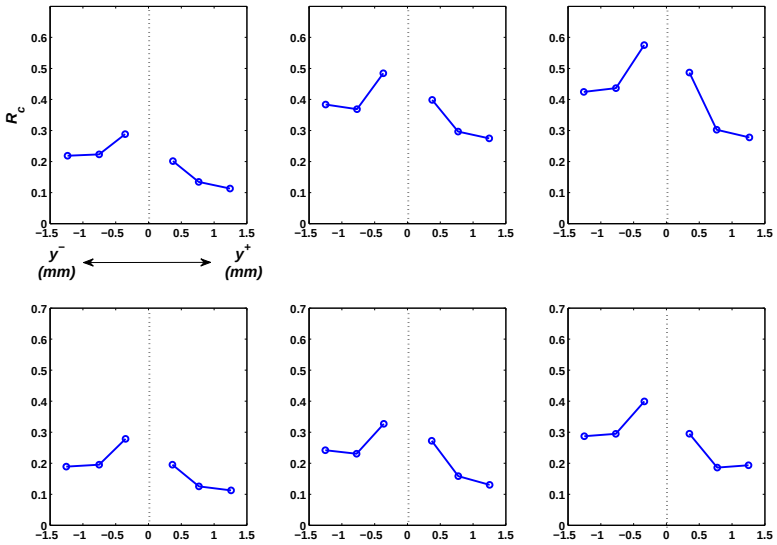
$$\left(\frac{1-m}{1-m_{\text{inf}}}\right) = \left(\frac{1-m_o}{1-m_{\text{inf}}}\right)^{r_o/r} \tag{5.12}$$

where m is the mass fraction of the acetone vapour and $\overline{C} = m(P/RT)(M_{ac}/M_{air})$. Here, P and T are the ambient temperature and pressure and, M_{ac} and M_{air} are molecular mass of acetone and air respectively. m_o and m_{inf} are the mass fraction of acetone vapour on the droplet surface and at a large distance away from the droplet respectively. r_o is the droplet radius. Figure 5.20 shows the comparison in y^+ direction for different windows within the measurement area. For the theoretical calculation, a droplet size of diameter $22.5\mu m$ (median of the droplet size class 15-35 μm) was considered. The vapour concentration at the droplet surface, required for the theoretical prediction, was obtained by fitting an appropriate curve to the experimental data. Similarly, the vapour concentration at infinity was assumed to be 'zero'. As can be observed from Figure 5.20, the gradient of vapour concentration closer to the droplet was much higher in case of an isolated droplet as compared to a spray and also, at any given y^+, the mean vapour concentration was orders of magnitude greater than that of an isolated droplet. Similar observations were found for the other three directions. Thus, the presence of simultaneously evaporating droplets in the vicinity of any droplet drastically reduces the evaporation rate of droplets.

The distribution of fluctuations of vapour concentration around a droplet has direct influence on the evaporation rate of the droplet. Large fluctuations in the vapour concentration can significantly alter the droplet evaporation rate especially when the mean value is closer to the saturated condition (Chen *et al.*, 2006).



(a)



(b)

Figure 5.21: Variation in fluctuations of vapour concentration (R_c) for the droplet size class of 15–30 μm in (a) x^- and x^+, and (b) y^- and y^+ directions respectively, at the radial measurement location $R = 45\ mm$. R_c is shown for various windows with in the measurement area. The dashed line represents the position of the droplet centre.

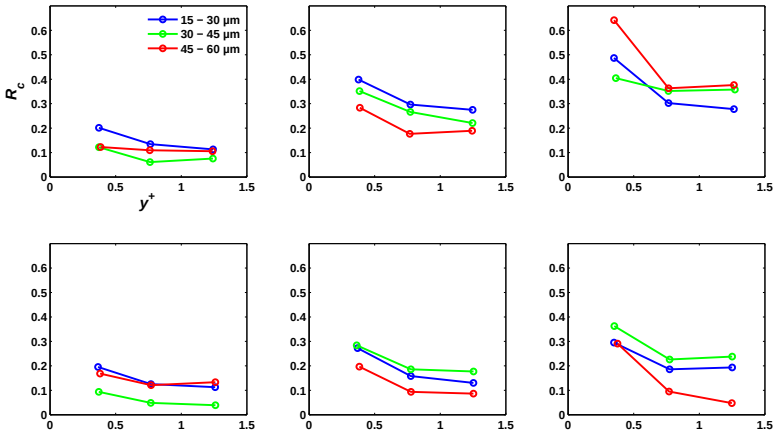


Figure 5.22: Variation in fluctuations of vapour concentration (R_c) in y^+ direction for the three droplet size classes and for various windows with in the measurement area, at the radial measurement location $R = 45\ mm$.

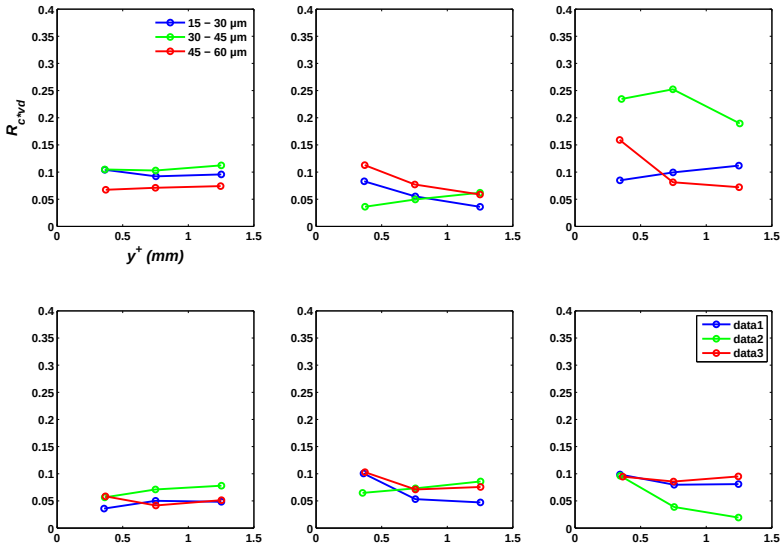
Figure 5.21(a) and 5.21(b) show the fluctuation of vapour concentration in the local coordinate directions around droplets of size class 15–30μm. The statistical uncertainty in R_c was higher closer to the droplets and its maximum value was of the order of ± 0.06 in all four directions. It can be observed that for any window within the measurement location, the fluctuations of vapour concentration is higher closer to the droplets and decreases away from it. Similar trend was also observed in case of the mono-sized droplet stream (Figure 5.8). This can be attributed to the velocity of vapour surrounding the droplets. Closer to the droplets, higher vapour velocity causes larger fluctuations of vapour concentration. Thus the rms of fluctuations of vapour concentration was higher for the larger droplet size (235μm) than the smaller droplets (122μm). The smaller fluctuations of vapour concentration in the considered experimental location in the spray is due to small magnitude of the mean velocity of droplets ($\approx 0.8\ m/s$). The smaller values of R_c indicates little effect of local fluctuations of vapour concentration on the droplet evaporation. The distribution of R_c around a droplet is not completely symmetric. Somewhat higher fluctuations of vapour concentration can be noted in y^- and x^- towards left and top of any droplet respectively and this tendency is more pronounced for smaller axial distances from the nozzle (in top row). Also, the magnitude of R_c in all four directions decreases

towards the spray axis in accordance to the ratio of rms to mean values of vapour concentration as shown in Figure 5.18(b). Figure 5.22 shows R_c along y^+ direction for the three droplet size classes for different windows within the measurement area. Similar trend is observed for droplets of different size classes. This is due to very small difference in the droplet mean velocity ($< 0.1\ m/s$) between different drop size classes.

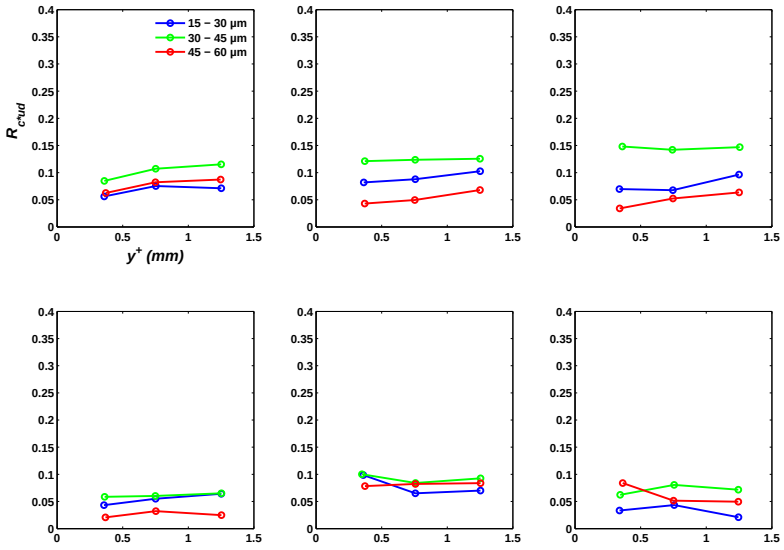
The correlation coefficients between fluctuations in droplet velocity and vapour concentration (R_{c*u_d} or R_{c*v_d}) were obtained in the four local directions around the droplets for various droplet size classes. Figures 5.23(a) and 5.23(b) show the correlation coefficients for both axial and radial components of velocities in y^+ direction. Both R_{c*u_d} and R_{c*v_d} were found to be quite low (≈ 0.2), almost independent of droplet size and invariant across the measurement area. Similar results were found in other directions and so, not shown here.

5.4 Summary

This chapter describes a novel approach for measurement of two phases in an evaporative spray which combines ILIDS for droplet size and velocity measurement with LIF for simultaneous measurement of vapour concentration. Similar to the combined ILIDS and PIV technique of Chapter 2, here also, the discrepancy in droplet centre was noticed. The discrepancy in droplet centre was theoretically evaluated for different positions of the droplet in the CCD array for the considered optical arrangement. The theoretical prediction agreed well with the experimentally observed trend for a mono-sized droplet stream. Subtraction of the estimated error from the experiment resulted in reducing the positioning error by about 90% and thus, increased the probability of locating the same droplets in both images. The combined ILIDS and LIF technique was first applied to a stream of mono-dispersed droplets for two droplet sizes of $235\mu m$ and $122\mu m$ to examine the influence of inter-droplet distance on droplet evaporation. Then, the application of the technique was reported for an evaporative acetone spray with the objective of studying the group evaporation



(a)



(b)

Figure 5.23: Spatially averaged correlation coefficients between fluctuations in droplet velocity and vapour concentration (R_{c*u_d} or R_{c*v_d}) for the three droplet size classes for (a) axial and (b) radial directions respectively, at the radial measurement location $R = 45$ mm.

of droplets. Measurements were performed for four different radial locations, R, at 0, 15, 30 and 45 mm respectively from the spray axis situated at 350 mm downstream from the atomiser. The findings can be summarized as below.

1. For the mono-sized droplet stream, the smaller inter droplet spacing of the larger droplet sizes causes the vapour to surround the droplet stream and cause group evaporation. For smaller droplet sizes, the large droplet spacing allowed interaction of the vapour field with the surrounding air modifying the vapour distribution. Thus, the inter droplet distance act as a deciding factor in determining the droplet evaporation rate.

2. Comparison of the droplet size distribution in the radial measurement locations for the evaporative acetone polydispersed spray and a non-evaporating water spray indicated the effect of evaporation to be more prominent towards the edge of the spray. The evaporation occurred primarily from larger droplets ($>$ 40 μm). Large variation in the instantaneous sauter mean diameter (SMD) with respect to the total SMD (obtained by considering all instantaneous droplet sizes) signified considerable fluctuations in the instantaneous droplet evaporation rate.

3. The mean velocity of droplets was mostly axial and downward at any measurement location and decreases in the radial outward direction away from the spray axis. At $R = 45$ mm, the mean velocity of droplets reduced to about 50% of the velocity near the nozzle axis at $R = 0$ mm. Near the nozzle axis, the ratio of axial to radial rms velocity was 1.25, while it was nearly equal to 'one' at the outer spray region at $R = 45$ mm indicating the flow to be nearly isotropic.

4. The instantaneous group evaporation number (G) was evaluated following two approaches. First, by considering the mean droplet size and inter droplet distance at the considered time instant and secondly, by assuming uniform droplet spacing in the measurement locations. It was shown that G evaluated

via the 2nd approach is always overestimated by several orders of magnitude and thus, can be misleading in determining the mode of droplet evaporation. The mean values of G (from the 1st approach) at the measurement location was low (≈ 0.1) suggesting the mode of evaporation was in the intermediate regime of individual to group evaporation while its slightly increasing trend towards the spray axis indicated the increasing tendency of the droplets to evaporate as a group. Following the 2nd approach, $G \approx 1.0$ indicating the occurrence of the external group evaporation, which is not expected at the considered measurement locations in the spray.

5. The mean vapour concentration at $R = 45\ mm$ was far below the saturation level (mass fraction of vapour was about 2%) of the acetone vapour suggesting higher mixing with the entrained air. The ratio of the rms to mean vapour concentration showed a preferential decrease in that quantity in the radial inward direction indicating higher fluctuations towards the outer spray region.

6. Comparison of the mean vapour concentration distribution around a droplet with that obtained from a theoretically predicted trend indicated drastic reduction in the droplet evaporation rate due to simultaneously evaporating droplets in the vicinity of each other. The fluctuations of vapour concentration were observed to increase close to any droplet and found to be slightly asymmetric in the radial direction. These trend were independent of droplet size. The correlation between fluctuations in vapour concentration and droplet velocity was quite low and independent of droplet size.

Chapter 6

Conclusions and Scope for future work

6.1 Conclusions

Two phase characterizations of isothermal and evaporative sprays are the subject of the present investigation. The thesis describes the development and application of two novel experimental techniques for simultaneous characterization of droplet and gaseous phases in isothermal and evaporative sprays respectively. Both approaches use the out-of-focus imaging ILIDS technique for planar measurements of droplet size and velocity. The in-focus imaging techniques PIV and LIF are respectively combined with ILIDS for simultaneous measurement of gas flow characteristics in an isothermal spray and vapour concentration distribution in an evaporative spray. For the isothermal spray, the aim was to understand the underlying mechanism of interaction between the droplets and the entrained turbulent air through the estimation of the droplet-gas velocity fluctuations. For the evaporative spray, the aim was to estimate the instantaneous group evaporation number and relate the vapour concentration fluctuations around the droplets with droplet properties, which can provide fuhrer insight in to the collective behaviour of evaporating droplets in sprays. Specific conclusions arrived at are summarised in the following section.

6.1.1 Combined ILIDS and PIV technique

For the study of droplet-gas flow turbulence interaction in a spray, knowledge of droplet size is as important as the droplet and gas velocities. Combining ILIDS with PIV offers a unique opportunity for such measurements. ILIDS provides planar droplet size and velocity, while the gas velocity in the vicinity of individual droplets is obtained by PIV. The advantage of the approach is that the position of droplets in a spray, obtained by ILIDS beforehand, helps in identifying the images of the same droplets (as glare-points) in the focused PIV image, thus making it possible to associate the droplet size/velocity to the glare-points. The glare-points from the PIV image are removed retaining only 'seeding' particles, which follow the gas phase flow. The PIV images are then processed to obtain the gas velocity in the vicinity of each droplet. The important conclusions arrived at are described below:

1. Experiments with a stream of mono-sized droplets revealed that the defocusing of the ILIDS technique leads to a discrepancy between the centre location of the given droplet on the defocused and focused images. This can lead to the erroneous association of droplet size/velocity to glare points in PIV images eventually resulting in incorrect estimation of the droplet-gas spatial velocity correlation terms. A theoretical analysis, based on geometric optics, was performed by considering a simple optical configuration. Both the theory and measurements show that the discrepancy varies almost linearly with the position in object plane for a given degree of defocus and can be as large as 1,000 μm.

2. The estimated droplet centre discrepancy, obtained from experiments with a droplet generator, can be subtracted from the centre of fringe patterns in the ILIDS images, obtained from a polydispersed spray. This approach was shown to reduce the discrepancy from about 1,000 μm to about 100 μm and thus significantly enhance the probability of correctly identifying corresponding pairs of fringe patterns and glare points in a polydispersed spray. The remaining discrepancy was found to be mostly due to inaccuracy in locating the centre of

the fringe pattern during ILIDS processing.

3. Application of the conventional PIV algorithm (either FFT or integer based correlation estimation) to evaluate the gas velocity from the droplet-filtered PIV images is not advisable. This approach was proved to result in erroneous estimation of velocity for simulated PIV images (Okamoto *et al.*, 2000) where certain circular areas in each image were randomly cropped off to replicate the droplet removal. A modified PIV algorithm, based on evaluation of the direct correlation via FFT (Ronneberger *et al.*, 1998) in conjunction with a digital mask technique (Gui *et al.*, 2003), was found to result in higher accuracy for the considered non-ideal PIV images.

4. Simultaneous ILIDS and PIV measurements and results are reported for a mono-dispersed droplet stream with air, 'seeded' with particles, flowing around it and it is concluded that after elimination of the droplet centre discrepancy, the combined ILIDS and PIV technique can be applied in a spray for simultaneous two-phase measurements.

6.1.2 Droplet-gas interaction in sprays

The present study focused on evaluating the droplet-gas velocity correlation, which appear in the turbulent kinetic energy equation of the carrier phase and are essential to understand the momentum transfer between the two phases in the spray. For this purpose, the combined ILIDS and PIV technique was applied to measure at far downstream locations in a confined spray in the model spray dryer rig, where the interaction of droplets with the entrained air was expected. The effect of droplet size, anisotropy of the flow and gravitational force on the droplet-gas velocity correlation were studied. Specifically, the influence of the large scale flow structures in the carrier phase on the droplet-gas correlated motion were evaluated by applying POD over the gas velocity data and the turbulence modulation at specific length scales of the flow was studied. Apart from this, the presence of droplet clustering in the flow was examined by measuring the instantaneous droplet concentration.

The measurements were reported for five different cross-stream locations situated at 500 mm downstream from the atomiser and 125 mm off-axial position in the spray. At any measurement location, the mean droplet velocity was found to be low and independent of droplet size. The magnitude of the mean gas flow was found to be similar to that of the mean droplet flow and could be interpreted as due to the air surrounding the spray being entrained into the spray in a recirculating pattern. While the axial rms velocity slightly decreased away from the spray axis, the cross-stream rms velocity decreased by about 50% towards the outer spray. The correlation coefficients, based on droplet size classes, were determined as a function of the distance of separation between the droplets and gas or droplet velocity vectors. The conclusions emerging from this study are:

1. Closer to the spray axis, strong correlation was observed in both axial and cross-stream directions suggesting that the droplets faithfully follow the large scale gas motion. Also, the correlation coefficients were almost independent of the droplet size classes. This conclusion was expected from the low values of the turbulent Stokes number of droplets based on large eddy length scales of the flow ($St << 1$). The velocity correlations were always higher in axial direction than in the cross-stream direction. The difference between them increased from the spray axis towards the outer spray region, where the flow was more anisotropic and gravity dominated.

2. In axial direction, at any measurement location, the correlation in the spatial droplet-gas velocity fluctuations (R_{dg}), droplet-gas velocity fluctuations (R_{dd}) and gas velocity fluctuations (R_{gg}) were of similar order indicating low drag and so, negligible momentum transfer between the two phases. In cross-stream direction, away from the spray axis, R_{gg} decreased only slightly, while R_{dg} and R_{dd} were found to decrease considerably. At the outermost measurement location near the spray edge, especially for the larger sizes, R_{gg} was much larger than R_{dg} signifying increased drag in the cross-stream direction and the possibility of energy transfer from the fluid to the droplets. These results

indicates the gravitational force on the droplets and the anisotropy in the flow can cause considerable deviation in the behaviour of particle-fluid correlated motion in an isotropic flow as described by Ferrante and Elghobashi (2003).

3. For any measurement location, the first three POD modes of the gas velocity were found to contribute about 50% of the total turbulent kinetic energy of the gas flow and so, represented the large scale flow structures. Contributions of individual POD modes on the droplet-gas spatial correlation were determined. For the near axis location at $R = 0\ mm$, in axial direction, the 1st mode and in cross-stream direction, the 2nd mode were found to be the dominant contributors. For gaining further understanding on modification of turbulent kinetic energy by the droplets at various length scales of the flow, the gas velocity correlation coefficient was compared with the modified droplet-gas correlation coefficient at those length scales. It was found that, in the present case, the droplets tend to augment turbulence in the carrier phase at large length scales of the flow and attenuate it at small length scales so that the total change in the turbulent kinetic energy remains the same. The transition in the manner droplets modify turbulence was observed at Mode 4, where the droplet-gas velocity correlation reduced significantly compared to the gas velocity correlation due to poor response of the droplets to the gas motion. Thus, the turbulence enhancement by the droplets at the first three length scales of the flow (which contributes about 50% of the total TKE) is compensated by its attenuation at the other small scales.

4. In order to obtain the characteristic dimensions of the droplet clusters in the flow, the local droplet concentration probability density function were compared with that arising from a purely random process by dividing an image into boxes of a certain size and counting the number of particles inside each box. For box size equal to about one-fourth of the measurement area, maximum deviation from randomness was observed indicating particle clustering should be more prominent at this length scale. This was supported by the trend in the radial

distribution function (RDF), obtained conditional on droplet size classes. At small radius of separation, droplets of higher size classes had higher values of RDF. So the droplet clustering was more prominent for the larger droplets.

6.1.3 Measurement of evaporative spray

A novel approach for the evaporative spray measurement was described which combines ILIDS for droplet size and velocity measurement with LIF for simultaneous measurement vapour concentration. Similar to the combined ILIDS and PIV technique, in this case also, the discrepancy in droplet centre was noticed. The discrepancy in droplet centre was theoretically evaluated for different positions of the droplet in the CCD array for the considered optical arrangement. The theoretical prediction agreed well with the experimentally observed trend for a mono-sized droplet stream. Subtraction of the estimated error from the mono-sized droplet experiment resulted in reducing the positioning error in the spray measurements by about 90% and thus, increased the probability of locating the same droplets in both images. Application of the combined technique and the involved image processing details are first reported for a stream of mono-dispersed droplets (for two droplet sizes $235\mu m$ and $122\mu m$) with the objectives to demonstrate the potential of the combined technique for two phase measurement and to examine the influence of inter-droplet distance on the droplet evaporation. Then the combined technique was applied to an evaporative acetone spray with the objective of studying the group evaporation of droplets. Measurements were performed for four different radial locations situated at 350 mm downstream from the atomiser. Because of the difficulty in accounting for the laser energy absorption by the droplets while evaluating the instantaneous vapour concentration, the combined ILIDS and LIF results are presented only for the location at distance $R = 45\ mm$ from the spray axis. For the other radial locations only dispersed phase measurements by ILIDS are reported. Following conclusions have been arrived at in this work:

1. The smaller inter droplet spacing of the larger droplet sizes causes the vapour to

surround the droplet stream leading to group evaporation. For smaller droplet sizes, the large droplet spacing allowed interaction of the vapour field with the surrounding air modifying the vapour distribution. Thus, the inter droplet distance act as a deciding factor in determining the droplet evaporation rate.

2. Comparison of the droplet size distribution in the radial measurement locations for the evaporative acetone spray and a non-evaporating water spray indicated the effect of evaporation to be more prominent towards the edge of the spray. The evaporation was found to be occurring primarily from larger droplets ($>$ 40 μm). Large variation in instantaneous sauter mean diameter and inter droplet distance signified considerable fluctuations in the instantaneous droplet evaporation rate and so, the importance of estimation of the instantaneous group evaporation number.

3. The instantaneous group evaporation number was evaluated following two approaches. First, by considering the mean droplet size and inter droplet distance at the considered time instant and secondly, by assuming uniform droplet spacing in the measurement locations (similar to evaluating G while using single point techniques). It was shown that G evaluated via the 2nd approach is always overestimated by several orders of magnitude and thus, can be misleading in determining the mode of droplet evaporation. The mean values of G (from the 1st approach) at the measurement location was low (≈ 0.1) suggesting the mode of evaporation was in the regime of individual to group evaporation while its slightly increasing trend towards the spray axis indicated the increasing tendency of the droplets to evaporate as a group. Following the 2nd approach, $G \approx 1.0$ indicating the occurrence of external group evaporation, which is not expected at the considered measurement locations in the spray.

4. The mean vapour concentration at $R = 45\ mm$ was low. The mass fraction of acetone vapour (about 2%) of the acetone vapour in this experimental location suggesting higher mixing with the entrained air. The ratio of the rms to mean vapour concentration showed a preferential decrease in that quantity with the

radial inward direction indicating higher fluctuations towards the outer spray region.

5. The mean vapour concentration distribution around a droplet was compared with the theoretically predicted trend, which indicated drastic reduction in the droplet evaporation rate due to simultaneously evaporating droplets in the vicinity of any droplet. The vapour concentration fluctuations were observed to increase closer to any droplet, which was attributed to the relatively higher vapour velocity in the vicinity of any droplets. Also, the fluctuations of vapour concentration around any droplet were found to be slightly asymmetric in the radial direction. These trends were independent of the droplet size classes. The correlation between fluctuations in vapour concentration and droplet velocity was quite low and independent of droplet size.

6.2 Scope for future work

The present research emphasizes the potential of the two experimental techniques as powerful tools for two phase characterization of sprays. The findings presented here generate interesting possibilities for research that can lead to further understanding of the physics of interaction between the two phases in sprays, assist the development of models for numerical simulations and also, find application to combustion engines. There are quite a few interesting problems that can be addressed in future and are mentioned below:

1. Measurement of droplet-gas spatial velocity correlation close to the nozzle exit of a spray from a diesel or model gas-turbine injector can elucidate the importance of those terms in modelling the coupling between the dispersed and continuous phases. Also, for an evaporating environment, evaluation of the distribution of the fluctuations in vapour concentration around the droplets can provide insight into the variations in the droplet evaporation rate.

2. The mechanisms of turbulence modulation and their parametric dependence are

still poorly understood. Application of the combined ILIDS and PIV technique for flow conditions with higher mass loading (≈ 1) is important to assess the turbulence modulation in the carrier phase by droplets. Also, in such cases, it is important to examine if turbulence is attenuated or augmented at various length scales of the flow. Turbulence modification by large particles, especially due to their wake generation, has not been quantified yet and so, can be a subject of study.

3. Evaporation of polydispersed spray in a homogeneous and isotropic flow environment can be studied in detail. It is of greater practical significance to examine how the preferential concentration of droplets, in such flow conditions, lead to preferential evaporation of droplets and, investigate the prevailing mode of group evaporation. Also, the effect of droplet evaporation on droplet dispersion can be studied in detail.

4. Application of POD analysis on the instantaneous distribution of the group evaporation number can explore the existence of dominant modes of droplet evaporation and their frequency of occurrence.

5. Combination of ILIDS with OH-PLIF for flame detection can be a useful tool for studying the interaction between droplets and flames in liquid fuelled combustion. Also, further combining PLIF for droplet vapour measurement can indicate the generation of vapour from droplets, its consumption and flame behaviour while correlating with droplet size.

Bibliography

Aliseda, A.; Cartellier, A.; Hainaux, F.; and Lasheras, J. Effect of preferential concentration on the settling velocity of heavy particles in homogeneous isotropic turbulence. *Journal of Fluid Mechanics*, 468:77–105 (2002).

Aubry, N. On the hidden beauty of the proper orthogonal decomposition. *Theoretical and Computational Fluid Dynamics*, 2:339–352 (1991).

Bachalo, W.D. and Houser, M.J. Phase doppler spray analyser for simultaneous measurements of drop size and velocity distributions. *Optical Engineering*, 23:583–590 (1984).

Bauckhage, K.; Flogel, H.H.; and Schone, F. Simultaneous measurements of size, concentration and velocity of spherical particles by a laser doppler method. In *Proceedings of International Symposium on Optical Particle Sizing Theory and Practice*. Rouen (1987).

Bazile, R. and Stepowski, D. Measurements of vaporized and liquid fuel concentration fields in a burning spray jet of acetone using planar laser induced fluorescence. *Experiments in Fluids*, 20:1–9 (1995).

Berkooz, G.; Holmes, P.; and Lumley, J.L. The proper orthogonal decomposition in the analysis of turbulent flows. *Annual Review of Fluid Mechanics*, 25:539–575 (1993).

Birouk, M. and Gokalp, I. Current status of droplet evaporation in turbulent flows. *Progress in Energy and Combustion Science*, 32:408–423 (2006).

Boivin, M.; Simonin, O.; and Squires, K. Direct numerical simulation of turbulence modulation by particles in isotropic turbulence. *Journal of Fluid Mechanics*, 375:235–263 (1998).

Boree, J.; Ishima, T.; and Flour, I. The effect of mass loading and inter-particle collisions on the development of the polydispersed two-phase flow downstream of a confined bluff body. *Journal of Fluid Mechanics*, 443:129–165 (2001).

Castanet, G.; Lavieille, P.; Lebouche, M.; and Lemoine, F. Lif measurements of fuel vapour in an acetone droplet stream. *Experiments in Fluids*, 35:563–571 (2003).

Chen, C.P. and Wood, P.E. A turbulence closure model for dilute gas-particle flows. *The Canadian Journal of Chemical Engineering*, 65:349–360 (1985).

Chen, W. and Gomez, A. Dilute laminar spray diffusion flames near the transition from group combustion to individual droplet burning. *Combustion and Flame*, 110:392–404 (1997).

Chen, Y.; Starner, S.H.; and Masri, A.R. A detailed experimental investigation of well-defined, turbulent evaporating spray jets of acetone. *International Journal of Multiphase Flow*, 32:389–412 (2006).

Chigier, N.A. The atomization and burning of liquid fuel sprays. *Progress in Energy and Combustion Science*, 2:97–114 (1976).

Chiu, H. and Kim, H. Group combustion of liquid fuel sprays. *AIAA 21st Aerospace Sciences Meeting, Paper No:83-150* (1983).

Connon, C.; Dimalanta, R.; Choi, C.; and Dunn-Rankin, D. Lif measurements of fuel vapour in an acetone droplet stream. *Combustion Science and Technology*, 129:197–215 (1997).

Crowe, C.; Sommerfield, M.; and Tsuji, Y. *Multiphase Flows with Droplets and Particles*. CRC Press, Boca Raton, FL (1998).

Damaschke, N.; Nobach, H.; Nonn, T.; Semidetnov, N.; and Tropea, C. Multi-dimensional particle sizing techniques. *Experiments in Fluids*, 39:336–350 (2005).

Damaschke, N.; Nobach, H.; and Tropea, C. Optical limits of particle concentration for multi-dimensional particle sizing techniques in fluid mechanics. *Experiments in Fluids*, 32:143–152 (2002).

Dodge, L.G. Calibration of the malvern particle sizer. *Applied Optics*, 23:2415–2419 (1984).

Dombrowski, N. and Fraser, R.P. A photographic investigation into the disintegration of liquid sheets. *Philosophical Transactions of the Royal Society of London. Series A, Mathematical and Physical Sciences*, pp. 101–130 (1954).

Elghobashi, S. On predicting particle-laden turbulent flows. *Applied Scientific Research*, 52:309–329 (1994).

Ferrand, V.; Bazile, R.; Boree, J.; and Charnay, G. Gasdroplet turbulent velocity correlations and two-phase interaction in an axisymmetric jet laden with partly responsive droplets. *International Journal of Multiphase Flow*, 29:195–217 (2003).

Ferrante, A. and Elghobashi, S. On the physical mechanism of two-way coupling in particle-laden isotropic turbulence. *Physics of Fluids*, 15:315–329 (2003).

Fessler, J.R.; Kulick, J.D.; and Eaton, J.K. Preferential concentration of heavy particles in turbulent channel flow. *Physics of Fluids*, 6:3742–3749 (1994).

Fevrier, P.; Simonin, O.; and Squires, K. Partitioning of particle velocities in gassolid turbulent flows into a continuous field and a spatially uncorrelated random distribution: theoretical formalism and numerical study. *Journal of Fluid Mechanics*, 533:1–46 (2005).

Frackowiak, B.; Strzelecki, A.; and Lavergne, G. A liquidvapor interface positioning method applied to plif measurements around evaporating monodisperse droplet streams. *Experiments in Fluids*, 46:671–682 (2009).

Glantschnig, W.J. and Chen, W. Light scattering from water droplets in the geometrical optics approximation. *Applied Optics*, 20:2499–2509 (1981).

Glover, A.R.; Skippon, S.M.; and Boyle, R.D. Interferometric laser imaging for droplet sizing: a method for dropletsize measurement in sparse spray systems. *Applied Optics*, 34:8409–8421 (1995).

Golombok, M.; Morinyand, V.; and Mounaim-Rousselle, C. Droplet diameter and the interference fringes between reflected and refracted light. *Journal of Physics D: Applied Physics*, 31:59–62 (1998).

Golub, G. and Van Loan, C. *Matrix Computations*. Oxford: North Oxford Academic (1983).

Gui, L.; Wereley, S.T.; and Kim, Y.H. Advances and applications of the digital mask technique in particle image velocimetry experiments. *Measurement Science and Technology*, 14:1820–1828 (2003).

Hardalupas, Y. and Horender, S. Fluctuations of particle concentration in a turbulent two-phase shear layer. *International Journal of Multiphase Flow*, 29:1645–1667 (2003a).

Hardalupas, Y. and Horender, S. A method to estimate gas-droplet velocity cross correlations in sprays. *Atomization and Sprays*, 13:273–295 (2003b).

Hardalupas, Y.; Sahu, S.; Taylor, A.; and Zarogoulidis, K. Simultaneous planar measurement of droplet velocity and size with gas phase velocities in a spray by combined ilids and piv techniques. *Experiments in Fluids*, 49:417–434 (2010).

Hardalupas, Y.; Taylor, A.M.K.P.; and Whitelaw, J.H. Velocity and particle-flux characteristics of turbulent particle-laden jets. *Proceedings of the Royal Society of London. Series A, Mathematical and Physical Sciences*, pp. 31–78 (1989).

Hirleman, E.D. Modelling of multiple scattering effects in fraunhofer diffraction particle size analysis. *Particle Particle System Characterization*, 5:57–65 (1986).

Holmes, P.; Lumley, J.L.; and Berkooz, G. *Turbulence, Coherent Structures, Dynamical Systems and Symmetry.* Cambridge Monographs on Mechanics (Cambridge: Cambridge University Press) (1996).

Hotelling, H. Analysis of a complex of statistical variables into principal components. *Journal of Educational Psychology*, 24:417–441 (1933).

Karpetis, A. and Gomez, A. An experimental study of well-defined turbulent nonpremixed spray flames. *Combustion and Flame*, 121:1–23 (2000).

Kavounides, C. *Particle flows in spray dryers.* Ph.D. thesis, Imperial College London (2006).

Konig, G.; Anders, K.; and Frohn, A. A new light-scattering technique to measure the diameter of periodically generated moving droplets. *Journal of Aerosol Science*, 17:157–167 (1986).

Kosiwczuk, W.; Cessou, A.; Trinite, M.; and Lecordier, B. Simultaneous velocity field measurements in two-phase flows for turbulent mixing of sprays by means of two-phase piv. *Experiments in Fluids*, 39:895–908 (2005).

Kurosawa, R.; Hishida, K.; and Maeda, M. Combined measurement of lif and ilids for vapour concentration and droplets size and velocity in a spray. *11th International Symposium on Applications of Laser Techniques to Fluid Mechanics Lisbon, Portugal* (2002).

Lindken, R. and Merzkirch, W. A novel piv technique for measurements in multiphase flows and its application to two phase bubbly flows. *Experiments in Fluids*, 33:814–825 (2002).

Loeve, M.M. *Probability Theory.* Van Nostrand (1955).

Longmire, E. and Eaton, J. Structure of a particle-laden round jet. *Journal of Fluid Mechanics*, 236:217–257 (1992).

Lumley, J. The structure of inhomogeneous turbulent flows. In *Proceedings of International Colloquium on the Fine Scale Structure of the Atmosphere and its Influence on Radio Wave Propagation* (1967).

Maeda, M.; Akasaka, Y.; and Kawaguchi, T. Improvements of the interferometric technique for simultaneous measurement of droplet size and velocity vector field and its application to a transient spray. *Experiments in Fluids*, 33:125–134 (2002).

Maeda, M.; Kawaguchi, T.; and Hishida, K. Novel interferometric measurement of size and velocity distributions of spherical particles in fluid flows. *Measurement Science and Technology*, 11:13–18 (2000).

Okamoto, K.; Nishio, S.; Saga, T.; and Kobayashi, T. Standard images for particleimage velocimetry. *Measurement Science and Technology*, 11:685–691 (2000).

Orain, M.; Mercier, X.; and Grisch, F. Plif imaging of fuel-vapor spatial distribution around a monodispersed stream of acetone droplets: comparison with modeling. *Combustion Science and Technology*, 177:249–278 (2006).

Pergamalis, H. *Droplet impingement onto quiescent and moving liquid surfaces*. Ph.D. thesis, Imperial College London (2002).

Poelma, C. and Ooms, G. Particle-turbulence interaction in a homogeneous, isotropic turbulent suspension. *Applied Mechanics Reviews*, 59:78–90 (2006).

Prasad, A. Standard images for particle image velocimetry. *Current Science*, 79:51–60 (2000).

Prasad, A. and Jensen, K. Scheimpflug stereocamera for particle image velocimetry in liquid flows. *Applied Optics*, 34:7092–7099 (1995).

Prevost, F.; Boree, J.; Nuclisch, H.; and Charnay, G. Measurements of fluid/particle correlated motion in the far field of an axisymmetric jet. *International Journal of Multiphase Flow*, 22:685–701 (1996).

Raffel, M.; Willert, C.; and Kompenhans, J. *Particle Image Velocimetry, A practicle guide*. Springer Verlag Berlin Heidelberg, Germany (1998).

Ragucci, R.; Cavaliere, A.; and Massoli, P. Drop sizing by laser light scattering exploiting intensity angular oscillation in the mie regime. *Particle Particle System Charc.*, 7:221–225 (1990).

Risso, F. and Fabre, J. Diffusive turbulence in a confined jet experiment. *Journal of Fluid Mechanics*, 337:233–261 (1997).

Ronneberger, O.; Raffel, M.; and Kompenhans, J. Advanced evaluation algorithms for standard and dual plane particle image velocimetry. In *International Symposium on Applications of Laser Techniques to Fluid Mechanics* (1998).

Rottenkolber, G.; Gindele, J.; Raposo, J.; Dullenkopf, K.; Hentschel, W.; Wittig, S.; Spicher, U.; and Merzkirch, W. Spray analysis of a gasoline direct injector by means of two-phase piv. *Experiments in Fluids*, 32:710–721 (2002).

Saffman, M.; Buchhave, P.; and Tanger, H. Simultaneous measurements of size, concentration and velocity of spherical particles by a laser doppler method. In *2nd International Symposium on Applications of Laser Techniques to Fluid Mechanics*. Portugal, Lisbon (1984).

Sakakibara, J.; Wicker, R.; and Eaton, J. Measurements of the particle-fluid velocity correlation and the extra dissipation in a round jet. *International Journal of Multiphase Flow*, 22:863–881 (1996).

Salazar, J.; de Jong, J.; Cao, L.; Woodward, S.; Meng, H.; and Collins, L. Experimental and numerical investigation of inertial particle clustering in isotropic turbulence. *Journal of Fluid Mechanics*, 600:245–256 (2008).

Segawa, D.; Yoshida, M.; Nakaya, S.; and Kadota, T. Autoignition and early flame behaviour of a spherical cluster of 49 monodispersed droplets. *Proceedings of the Combustion Institute*, 31:2149–2156 (2007).

Silvermann, M. and Dunn-Rankin, D. Experimental investigation of a rectilinear droplet stream flame. *Combustion Science and Technology*, 100:57–73 (1994).

Sirignano, W. *Fluid Dynamics and Transport of Droplets and Sprays*. Cambridge University Press (1999).

Sirovich, L. Turbulence and the dynamics of coherent structures, part I, II, III. *Quarterly of Applied Mathematics*, 45:560–590 (1987).

Sirovich, L. Analysis of turbulent flows by means of the empirical eigenfunctions. *Fluid Dynamics Research*, 8:85–100 (1991).

Sornek, R.; Dobashi, R.; and Hirano, T. Effect of turbulence on vaporization, mixing, and combustion of liquid-fuel sprays. *Combustion and Flame*, 120:479–491 (2000).

Spalding, D. Combustion of fuel particles. *Fuel*, 30:121 (1951).

Squires, K. and Eaton, J. Particle response and turbulence modification in isotropic turbulence. *Physics of Fluids*, 7:1191–1203 (1990).

Sugimoto, D.; Zarogoulidis, K.; Kawaguchi, T.; Matsuura, K.; Hardalupas, Y.; Taylor, A.; and Hishida, K. Extension of the compressed interferometric particle sizing technique for threecomponent velocity measurements. In *International Symposium on Applications of Laser Techniques to Fluid Mechanics* (2006).

Sundaram, S. and Collins, L. A numerical study of the modulation of isotropic turbulence by suspended particles. *Journal of Fluid Mechanics*, 379:105–143 (1999).

Tanaka, T. and Eaton, J. Sub-kolmogorov resolution partical image velocimetry measurements of particle-laden forced turbulence. *Journal of Fluid Mechanics*, 643:177–206 (2010).

Tennekes, H. and Lumley, J.L. *A First Course in Turbulence*. MIT Press, Cambridge, Mass (1972).

Torrence, C. and Compo, G. A practical guide to wavelet analysis. *Bulletin of the American Meteorological Society*, 79:61–78 (1998).

van de Hulst, H.C. *Light Scattering by Small Particles*. Wiley, New York (1957).

van de Hulst, H.C. and Wang, R.T. Glare points. *Applied Optics*, 30:4755–4763 (1991).

Wang, L.P. and Maxey, M.R. Settling velocity and concentration distribution of heavy particles in homogeneous isotropic turbulence. *Journal of Fluid Mechanics*, 256:27–68 (1993).

Watanabe, H.; Kurose, R.; M., H.S.; and Akamatsu, F. Characteristics of flamelets in spray flames formed in a laminar counterflow. *Combustion and Flame*, 148:234–248 (2007).

Webster, D.R.; Roberts, P.J.W.; and Raad, L. Simultaneous dptv/plif measurements of a turbulent jet. *Experiments in Fluids*, 30:65–72 (2001).

Westerweel, J. Fundamentals of digital particle image velocimetry. *Measurement Science and Technology*, 8:1379–1392 (1997).

Wood, A.M.; Hwang, W.; and Eaton, J.K. Preferential concentration of particles in homogeneous and isotropic turbulence. 31:1220–1230 (2005).

Yang, T.S. and Shy, S.S. Two-way interaction between solid particles and homogeneous air turbulence: particle settling rate and turbulence modification measurements. *Journal of Fluid Mechanics*, 526:171–216 (2005).

Zarogoulidis, K. *Interferometric Laser Imaging for Droplet Sizing*. Ph.D. thesis, Imperial College London (2011).

Zimmer, L.; Domann, R.; Hardalupas, Y.; and Ikeda, Y. Simultaneous laser induced fluorescence and mie scattering for droplet cluster measurements. *AIAA Journal*, 41:2170–2178 (2003).

List of Publications from the Thesis

Journal

Hardalupas, Y.; Sahu, S; Taylor, A.M.K .P. and Zarogoulidis,K. Simultaneous planar measurement of droplet velocity and size with gas phase velocities in a spray by combined ILIDS and PIV techniques. *Experiments in Fluids*, 49:417–434 (2010).

Conference Proceedings

Hardalupas, Y.; Sahu, S; Taylor, A.M.K .P. and Zarogoulidis,K. Simultaneous planar measurement of droplet velocity and size with gas phase velocities in a spray by combined ILIDS and PIV techniques. *14th International Symposium on Applications of Laser Techniques to Fluid Mechanics*, Lisbon, Portugal, 07–10 July (2008).

Hardalupas, Y.; Sahu, S; Taylor, A.M.K .P. and Zarogoulidis,K. Simultaneous planar droplet size and droplet and gas velocity measurements in a confined spray. *American Institute of Aeronautics and Astronautics*, Florida, USA, 05–08 Jan (2009).

Hardalupas, Y.; Sahu, S; Taylor, A.M.K .P. and Zarogoulidis,K. Measurement of spatial correlation of droplet-gas velocity in a confined spray. *7th International Conference on Multiphase Flow*, Florida, USA, 30th May–4th June (2010).

Hardalupas, Y.; Sahu, S; Taylor and A.M.K .P. Measurement of vapour concentration and droplet size and velocity in an evaporative spray. *15th International Symposium on Applications of Laser Techniques to Fluid Mechanics*, Lisbon, Portugal, 05-08 July (2010).

Hardalupas, Y.; Sahu, S; Taylor and A.M.K .P. Experimental characterization of isothermal and evaporative sprays. *23rd Annual Conference on Liquid Atomization and Spray Systems*, Brno, Czech Republic, 06–08 September (2010).